Abstract

The search for oil gets more and more difficult and so the drilling for oil is. Having exact information on the drilled borehole formation and its geological structure is the key for successful reservoir management and converts complicated into workable deposits.
In doing so, borehole images play a decisive role and offer a unique view of the subsurface to geologists and petrophysicists [Ritter et al., 2004]. By the help of borehole images, it is possible to calculate dip parameters (azimuth and inclination) of declining geologic layers in the borehole and identify other geological features like fractures. Thereby a complex and high resolved reservoir characterization is made possible. Usually image log interpretation is performed manually by geologist and poses a time consuming and therefore expensive task.

The methodology of texture attribute extraction using a Gray Level Co-occurrence Matrix (*GLCM*) is adopted from digital photo analysis and was first applied to seismic and sonar data [Haralick et al., 1973]. By the help of this method, a regular raw data image is converted into a so-called *attribute image* considering different textural aspects like contrast, homogeneity or entropy within the raw data. A *contrast attribute image* for example emphasizes contrast changes while the *homogeneity attribute image* reflects the homogeneity distribution occurring in the raw data. With the knowledge how different attributes are characterized and how different geological features are represented by these attributes, it is possible to develop an automatic procedure to extract geological information automatically. Following applications are imaginable:

- Identification of geological boundaries and calculation of dip parameters
- Creation of a rock classification by combining different texture attributes
- Identification of other geological features like cracks, fractures, breakouts, etc.

Thereby either a helpful basis for reservoir geologist or a quick and approximate in situ interpretation is provided without any human help. The particular feature of this methodology researched in this thesis is up to the application. Neither this methodology using a GLCM was applied to high resolved borehole images nor is the automatic extraction of small-scaled features from an image well developed.

Zusammenfassung

Die Exploration auf der Suche nach Öl wird zunehmend aufwendiger und dem passt sich auch die Bohrtechnik an. Der Schlüssel für erfolgreiches Lagerstätten Management und manchmal sogar der ausschlaggebende Faktor zur Erschließung von profitablen Lagerstätten, liegt in genauen Information zur Formation und geologischen Struktur, in die gebohrt wird. Dabei spielen Borehole Images eine entscheidende Rolle, indem sie Geologen und Petrophysikern einen einzigartigen Einblick in das Bohrloch bieten [Ritter et al., 2004]. Mit der Hilfe von Borehole Images ist es möglich, Dip-Parameter (Inklination und Azimut) von geologischen Schichten zu berechnen, die das Bohrloch kreuzen, und andere geologische Strukturen, wie z.B. Klüfte, zu identifizieren. Damit ist eine komplexe und hoch aufgelöste Reservoir Charakterisierung möglich. Normalerweise wird eine Image Log Interpretation manuell von Geologen durchgeführt und ist zeit- und damit kostenaufwendig.

Die hier vorgestellte Methodik der Textur-Attribut-Extraktion mit einer Gray Level Co-occurrence Matrix (*GLCM*) ist der digitalen Photoanalyse entsprungen und wurde erstmals bei der Interpretation von Seismik- und Sonar-Daten angewandt [Haralick et al., 1973]. Mit Hilfe dieser Methode wird ein Rohdaten-Image in ein so genanntes Attribut-Image umgewandelt, das verschiedene Texturaspekte wie Kontrast, Homogenität oder Entropie innerhalb des Rohdaten-Images berücksichtigt. Ein Kontrast-Attribut-Image z.B. betont Kontrastwechsel, während ein Homogenitäts-Attribut-Image die Homogenitätsverteilung im Image widerspiegelt. Mit dem Wissen um die Charakterisierung und dem Verhalten dieser Attribute gegenüber geologischen Strukturen ist es möglich ein Verfahren zur automatischen Extraktion von geologischen Informationen zu entwickeln. Folgende Anwendungen sind denkbar:

- Identifikation von geologischen Schichtgrenzen und Berechnung der Dip-Parameter
- Entwicklung einer Gesteinsklassifikation durch Kombinierung von verschiedenen Textur-Attributen
- Identifikation von anderen geologischen Strukturen wie Rissen, Klüften, Ausbrüchen usw.

Potential dieser Methodik liegt entweder in der schnellen in-situ Interpretation ohne menschliches Zutun oder zur Unterstützung der Interpretationsarbeit von Geologen. Die Besonderheit des in dieser Arbeit angewandten Verfahrens bezieht sich auf seine Anwendung. Bisher wurde das Verfahren weder an hochauflösenden Bohrloch-Images angewandt noch ist die automatische Extraktion von geologischen Informationen überhaupt weit entwickelt bzw. überhaupt verfügbar.

Acknowledgement

Declaration

Hereby, I affirm on oath that I have completed this work without prohibited support of third parties and without use of sources other than indicated. Quotes have been explicitly highlighted.

Hiermit versichere ich, dass ich die vorliegende Arbeit ohne unzulässige Hilfe Dritter und ohne andere Benutzung als der angegebenen Hilfsmittel angefertigt habe. Die aus fremden Quellen direkt oder indirekt übernommenen Gedanken sind als solche kenntlich gemacht.

Stefan Jetschny

Contents

List of Figures

List of Tables

List of Abbreviations

A	amplitude of the acoustic wave; azimuth of the inclined sedimentological layer; cross section area of the electrical conductor
$\vec{B}$	magnetic flux density
CR	nuclear tool count rate
$\vec{D}$	electric flux density or dielectric displacement
$\vec{E}$	electrical field intensity
E	energy of gamma quantum
$\vec{H}$	magnetic field intensity
I	current; inclination of the inclined sedimentological layer (angle)
$\vec{J}$	electric current density
$\vec{M}$	magnetization
N_g	number of discrete value levels
$N_{x/y}$	size of the texel window in either horizontal or vertical direction
$\vec{P}$	electric polarization
R	electrical resistance; normalization factor, total number of possible times of co-occurrence
R_f	gage for reflection at the borehole surface
$S(i,j)$	element of GLCM G determined by row i and column j
$SAI_{x/y}$	size of the anomaly in the attribute image (in either horizontal or vertical direction)
$SSI_{x/y}$	size of the anomaly in source image (in either horizontal or vertical direction)
U	voltage
Z_m	mud impedance
Z_f	formation impedance
Y	Young's modulus (also called E-modulus)

α, B	tool specific parameters depending on tool design, standoff, source type, mud,… (determined by lab measurements)
c	speed of light
f	frequency
$f(surface)$	function of the borehole surface conditions (rugosity)
$f(T,p,r,\alpha)$	function of temperature t, pressure p, borehole radius r, mud attenuation coefficient α, mud composition MC …
h	Plank constant
k	complex vector in propagation direction of the planar wave
l	length of the electrical conductor
r	position vector; radius
t	time; acoustic travel time
v	velocity of the acoustic wave through formation
x	coordinate in x direction

α	attenuation term
$\varepsilon = \varepsilon_0 \varepsilon_r$	product of permittivity of the vacuum ε_0 and relative permittivity ε_r under conditions of isotropy, as a consequence piecewise homogeneity and thus ε being a constant and not a tensor
φ	porosity
λ	wave length
μ $\mu = \mu_0 \mu_r$	Shear modulus; product of magnetic permeability in vacuum μ_0 and relative magnetic permeability μ_r, under conditions of isotropy, as a consequence piecewise homogeneity and thus μ being a constant and not a tensor
v	velocity
ρ	density; electrical resistivity
σ	electric conductivity; standard deviation of
υ	Poison ratio
ω	angular frequency

1 Introduction

The search for oil gets more and more difficult and so the drilling for oil is. Having exact information about the drilled borehole formation and its geological structure is the key for successful reservoir management and converts complicated into workable deposits. In doing so, borehole images play a decisive role and offer a unique view of the subsurface to geologists and petrophysicists [Ritter et al., 2004]. By the help of borehole images, it is possible to calculate dip parameters (azimuth and inclination) of declining geologic layers in a borehole and identify other geological features like fractures. Thereby a complex and high resolved reservoir characterization is made possible.

Usually image log interpretation is performed by skilled geologist. For such a skilled human eye, measurement interpretation is almost easy to perform. Structures and textures within the raw data will be associated with already known structure and rock types. Sedimentological boundaries for example can be identified by visible changes in texture and more or less obvious drops in measurement values forming boundaries. On the other side, human interpretation is time-consuming and consequently expensive. Therefore, there is a need for automatic interpretation methods being either the basis for human reviewing at a later time or a situ interpretation without the presence of qualified interpreter. The *GLCM* method is one possible basic approach.

2 What is imaging?

Nowadays, Borehole drilling, searching for oil is not workable without borehole measurements and it is the other way round, as well. Even if borehole measurements are applied for other scientific field like the Ocean Drilling Program (ODP) to find out more about geological processes occurring on earth, dominant stimulus in research and investing money will be provided by Oil companies [Goldberg, 1997].

Not knowing where there is oil and not be able to see inside the ground without aid, scientists have had to developed physical measurement techniques to compensate this lack of knowledge. Measurable is almost every physical unit but only a few are capable for determining possible oil deposits (e.g. electric conductivity, acoustic velocity, porosity, density, permeability…) Often these units are not determined directly but by devious routes. Density for example can be determined by acoustic, neutron or gamma ray measurements. An overview of available downhole measurement techniques can be found e.g. in [Ellis, 1987; BakerHughes, 1992].

The earliest *logging tools* were lowered downhole hanging on a wire after the hole is drilled (following terms emphasized by italic font are explained in Table 1). That is why this class of probes is called *wireline* tools. Downhole, a bulk physical unit is measured representing 360° of the rocks surrounding the borehole (*formation*). In other words, only one measurement value per each depth is available. This might be sufficient for determining rock properties and therewith helps identifying rock types. By the need of far reaching information according to geological structures and features (e.g. angle of incidence of geological layers (*dip*), fractures, faults, beddings...) *imaging* techniques

were developed. The term imaging is derived by the ability to receive a photo like image of the borehole (see Figure 1).

Basis for each imaging tool is an orientation device (e.g. magnetometer) determining the position of tool-sensor relative to a specified coordinate system. Earths magnet field is a common reference coordinate system, parameters are *azimuth* and *inclination* ([Fulda, 2004a; Jetschny, 2004b]). Instead of measuring a bulk value, imaging tools do this for spatial sections of the borehole. The smaller these sections the more precise become information about geologic structures and features. It is understandable, that only one sensor and therefore only one measurement value is not sufficient to create an image. That is why wireline imaging tool bear a number of measurement sensors. This problem is not given for measurement while drilling (*MWD*) tools. This newer class of imaging tools is part of the rotating drill string and able to measure while drilling is in progress. Since the imaging tool *sub* is rotating, only one measurement sensor is needed for covering 360° degree in a spiral path and determining physical properties. Currently, imaging tools can be divided into three groups using different measurement techniques: acoustic, electric and nuclear imaging tools.

Term / Abbreviation	Explanation
Azimuth & Inclination	Actually, parameter of earths magnet field, in geological terms used to describe angle of incidence of geological layers
Dip	Notation for parameters of a declining geologic layer (azimuth, inclination) crossing the borehole
Formation	Surrounding of the borehole consisting of different rock types and formed by geological processes (see chapter 4.2.4)
Imaging	Subgroup of logging in order to acquire an image of the borehole (sometimes also called azimuthal measurement because of its ability to resolve objects horizontally)
Log	Downhole acquired dataset of measurement values representing different physical rock-properties
Logging	Process of acquiring borehole data (logs)
LWD	Logging while drilling; strictly speaking a subgroup of MWD; acquiring physical values suitable for geoscientifical purposes (formation properties like conductivity, radioactivity, density, permeability, …)
Mud	Borehole drilling fluid (see chapter 4.2.2)
MWD	Measurement while drilling; acquiring physical values related to all components of the borehole and considering different aspects (e.g. mud temperature, pressure, electrical formation properties, bit rotation speed, borehole geometry, inclination & azimuth (earth magnetic field), …)
Sub	Modular part of the drill string, e.g. measurement sub (tool), power supply sub, stabilizer sub, …
Tool	Borehole measurement device, can be a sub when using MWD
Wireline logging	Analogue to MWD, first the borehole is drilled, thereafter the drill string will be removed and a measurement tool is lowered downhole

Table 1 : Borehole related terms

3 Application and claims

Distinctive advantage and benefit of borehole images is related to the high resolution of acquired datasets. Not only one measurement value per each depth is taken but also several values distributed among 360° of the borehole. The more values are acquired the more the azimuthal resolution increases. Therefore, not only information can be gained about the presence of geological features but also about their position and type.

The main task for imaging logs is to provide a representative image of the borehole, not necessarily meaning to give absolute measurement values. In fact and as a matter of principle all imaging tools acquire relative values. E.g., resistivity values (see chapter 4.1) measured by an electrical imaging tool do not represent the true resistivity within formation. Instead, it is important that resistivity-contrasts are reflected correctly. For instance, an image log will reproduce a resistivity increase within the measured formation to a factor five in the same way.

The next chapters will give an overview of geological and borehole features can be identified by the use of the resulting high-resolution borehole images. These include planar features such as bedding, fractures, faults, stratigraphic features such as cross-bedding and ichnofabrics and borehole wall features like breakout and drilling-induced fracturing [BakerHughes, 2004].

3.1 *Sedimentological / depositional environments*

Sedimentological / depositional environments analysis comprises

- Description of facies and facies sequences
- Determination of paleotransport direction
- Analysis of reservoir geometry
- Characterization of depositional environment

The high-resolution data provided by imaging tools permits recognition of sedimentary structures and evaluation of bed contacts. Borehole image logs can be used for differentiation of facies, depositional environment interpretation, and stacking pattern analysis. Key features extracted from an image log and characterizing sedimentary structures would be thickness, shape and distribution of physical properties within respectively of a geological layer (see Figure 1). Additionally, borehole image logs are oriented. Therefore, the orientation of sedimentary features (e.g. cross bedding, scours, slump fold axial planes) can be determined. In combination with the structural dip analysis (see chapter 3.2), this may allow conclusions about dispersal vectors at the time of deposition (paleo-current and paleoslope direction). In turn, these can be used to constrain the trend and geometry of reservoir bodies away from the borehole. As a consequence a three dimensional model can be gained providing useful information for reservoir engineers.

Thin bed analysis is a specialized part of the sedimentological analysis, but very important because recent developed oil-bearing layers are getting thinner and thinner. For

e.g. thinly laminated turbidite sequences, borehole images are often the only practical method of determining thickness in the absence of borehole core.
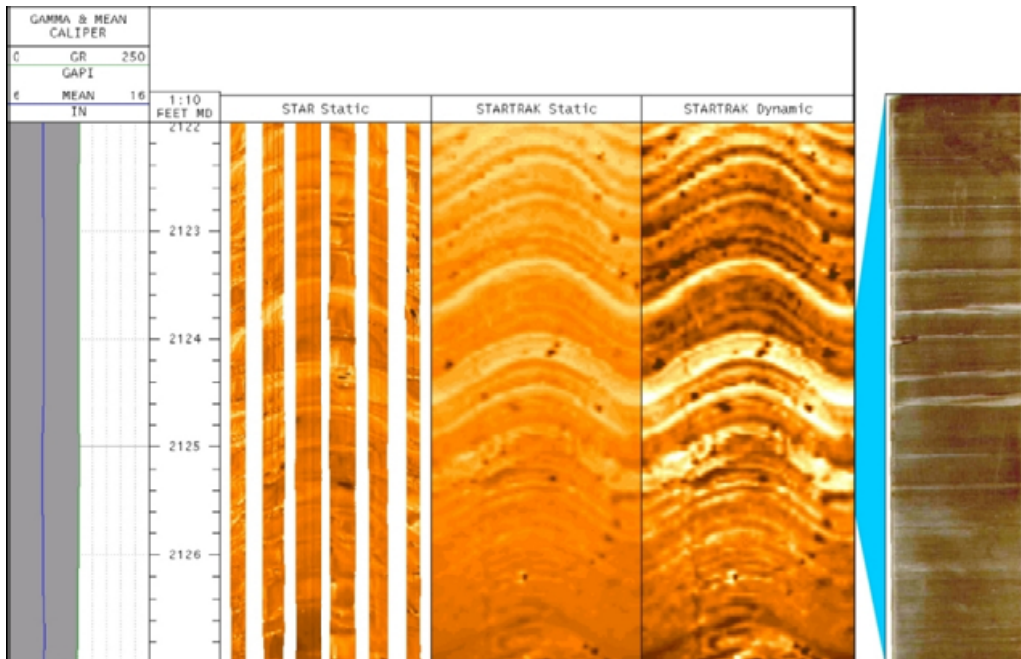
Figure 1 : Comparison of Gamma ray, StarImager™, StarTrak™ and core data of lamaniated formation; adapted from [Ritter et al., 2004]

3.2 Structural dip

The dip of a geological layer provides information about the direction and angle to which this layer is tilted relative to the borehole (see Figure 2, (A)). Due to its ability of acquiring high resolved and orientated images, borehole images are one of the main sources of information for describing structural features. Structural dip information is used for the following:

- Determining dip and strike directions
- Structural mapping and cross sections generation
- Well-to-well correlation
- Unconformity mapping
- Delineating other geological structures
- Up-scaling to seismic and verifying seismically derived structural dip

The appearance of a lithological border crossing the borehole is shown in Figure 2, (B). By unfolding the borehole-tube to a rectangle, the crossing layer becomes a sinusoid line. Amplitude and location of the maximum of the sinusoid determines the angle of incidence (*dip*, see Equation 23 and Equation 24).

18
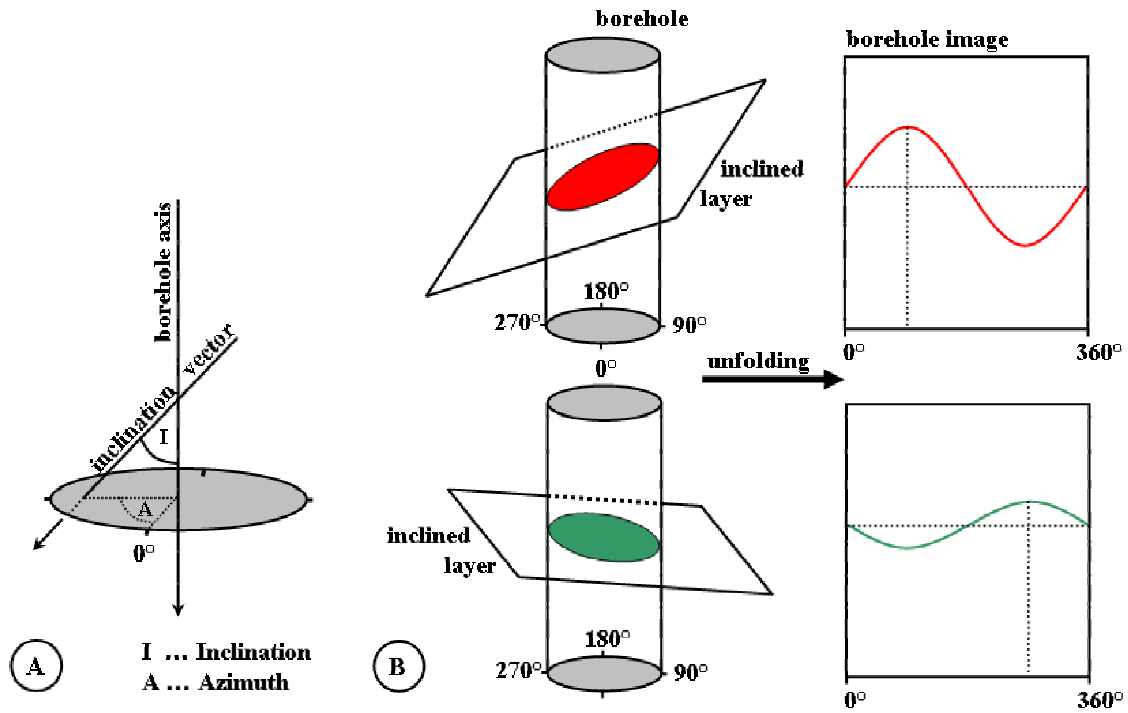
Figure 2 : Inclined geological layer crossing the borehole

3.3 Faults and unconformities

Faults are the result of the interaction between different rocks layers and stress related to geological processes. Vertical stress components will affect lifting or lowering while horizontal components lead to compression or relaxation. If the stress is high enough to exceed the elastically behavior, structures of layered rocks will break along faults and displacement will occur (see Figure 3).
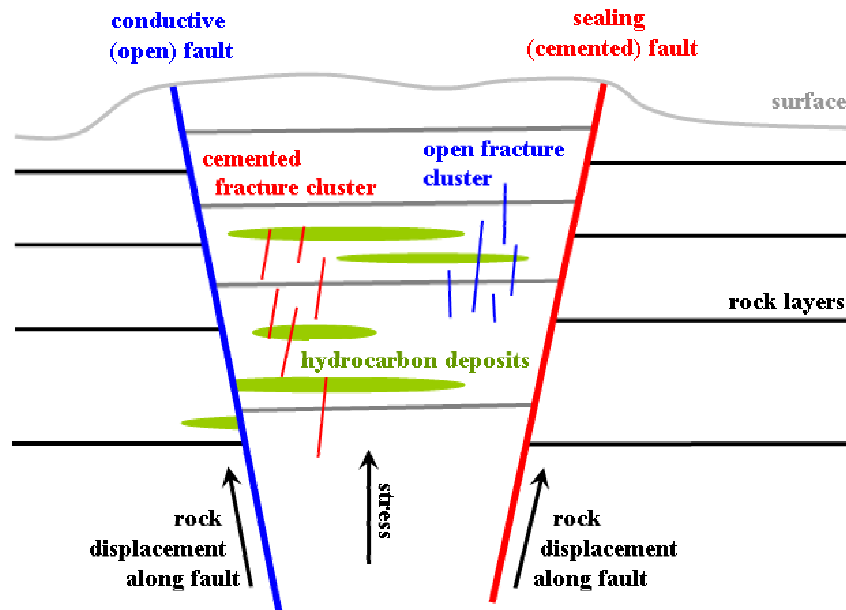
Figure 3 : Faults and fractures sketch

Borehole imaging tools can help in characterizing faulted reservoirs and unconformities. Analysis of high-resolution borehole image logs in these environments can be used to reduce uncertainties such as fault system geometry, fault spacing, rock displacement along the fault, and fault sealing capabilities. This information, including orientation and fault density, in conjunction with available seismic data, can improve future well placement and drainage pattern in faulted reservoirs.

Faults can be identified using one or more of the following observations:

- Change of dip direction and angle over large intervals
- Deformation of bedding due to fault related drag folds
- Discordant facies changes
- Higher fracture density (natural fractures) around the damage zone of faults
- Brecciation or mineralized fractures
- Local modifications of the regional stress field or drilling induced fractures that change orientation
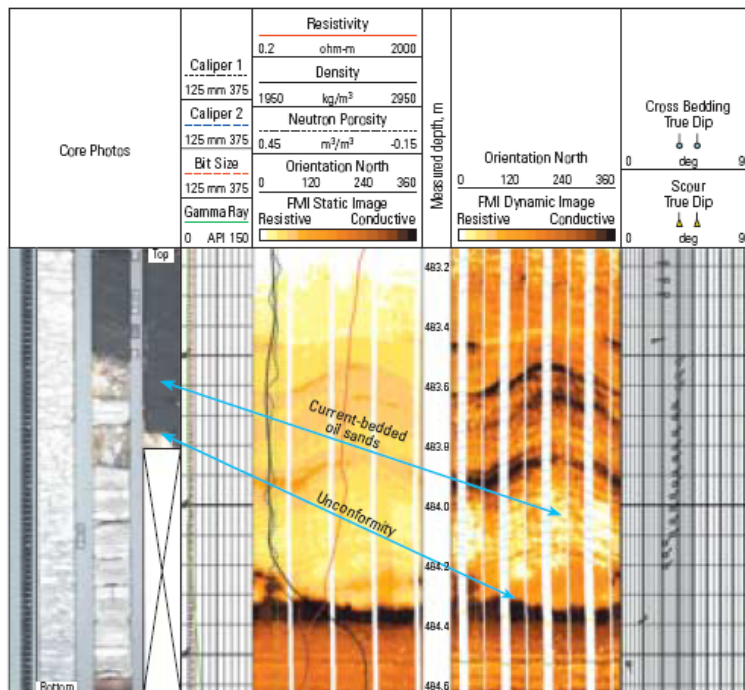
Figure 4 : Comparison of core, gamma ray and FMI™ data showing beddings and a unconformity; adapted from [Contreras et al., 2003]

3.4 Fractures

Fractures can be considered as small faults - both share the same origin. While faults muddle through structures of layered rocks, fractures appear at points of weakness within a rock layer (Figure 3). The description, distribution, and flow characteristics of fractures influence the producibility of reservoirs. Fractures can act as permeability barriers or as permeability conduits providing communication between reservoir zones. Borehole images allow a fracture model to be built in order to gain better reservoir permeability, which may result in enhanced production. Detailed fracture analysis includes:

- fracture typing
- fracture sets
- fracture length
- fracture frequency
- fracture filling

The appearance of a fracture is quite similar to that of a sedimentological boundary. To be able to differ between fractures and stratigraphic layers, fracture's shape and course in an image log has to be considered. A fracture rarely is a planar structure but irregular, so it creates no sinusoid typical for a boundary. If a fracture exhibits as a sinusoid its appearance will not be conform to the sinusoids representing the rock lamination. Furthermore fractures are open respectively filled with mud or cemented and haul out themselves by high contrasts in an borehole image (see Figure 5).
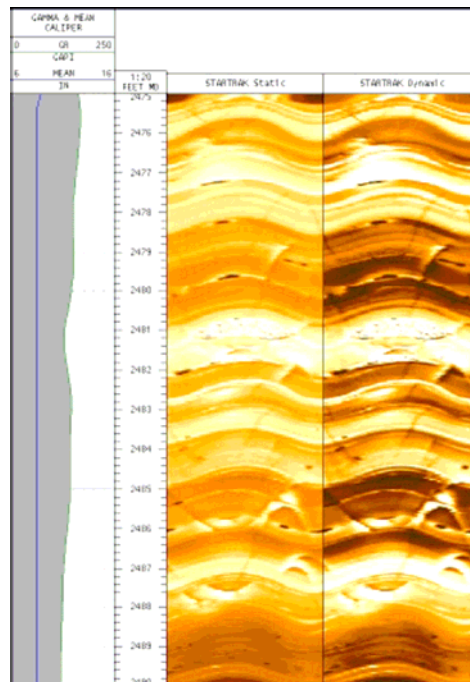
Figure 5 : Comparison of Gamma ray and StarTrak™ showing a cluster of 15-20 open/cemented fractures; adapted from [Ritter et al., 2004]

3.5   Geomechanical features

Geomechanical analysis comprises

- In-situ stress analysis
- Borehole stability analysis
- 3D borehole geometry analysis

Knowledge of rock mechanical properties and in-situ stresses is important for planning of both drilling and production. When a borehole is drilled, the stress around the borehole increases due to removal of the stress-bearing material that existed at this location. If the compressive stress around the borehole exceeds the compressive strength, borehole elongation (breakout) will occur (Figure 6). If the tensile stress exceeds the tensile strength, induced fractures will occur (Figure 6). Sand production, for example, is a form of local stress exceeding the rock strength. Therefore, knowledge of the mechanical properties of the rock and in-situ stresses is required to be able to counteract by e.g. adjusting the mud weight to balance stress or even the well trajectory.

The apparent easiest way of determining stress related effects would be in measuring the 3D borehole geometry (see Figure 9) because regional stress is transferred to near wellbore stress, which leads to the borehole cross-section becoming elliptical, or misshaped. Another possibility exists in measuring breakout orientation indicating the orientation of the present day horizontal stress field. All high-resolution imaging tools are able to detect such secondary effects. A more direct methodology of acquiring

22

information about the stress field present in the borehole is provided by acoustic imaging (see chapter 0). Both density variations in a uniform rock layer (as a consequence of compression or relaxation) and detailed analysis of the wavetrain especially the inserts of stonley waves can help determining stress fields.

During field development, knowledge of the principal horizontal stress orientation and propagation direction of hydraulic fractures may be used to optimize the placement of injector and producer wells. Further, borehole images in conjunction with hydraulic fracturing operations will help determine the extent of the propagation and the isolation of the hydraulic fracture in the zone of interest. The results can then be used to optimize the stimulation program and hydrocarbon recovery.
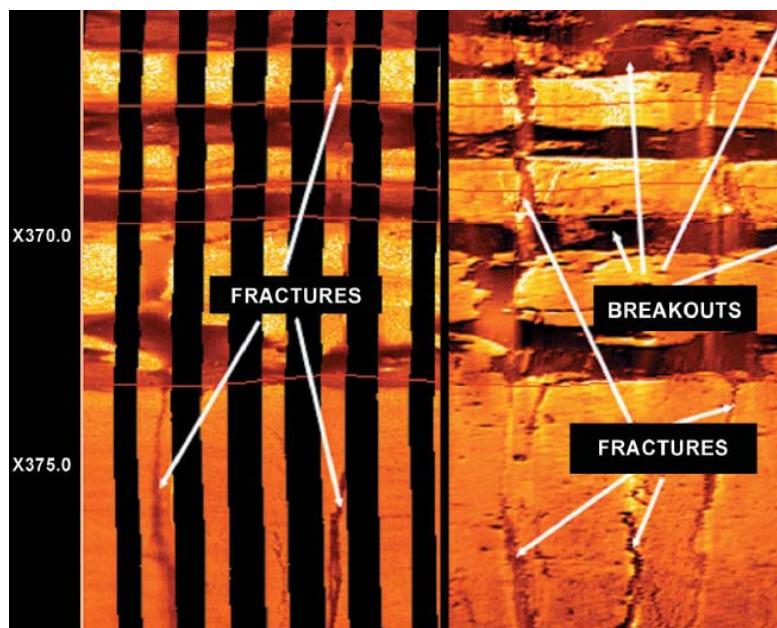
Figure 6 : Fracture and breakouts in both electric and acoustic image;
adopted from [BakerHughes, 2004]

3.6   Other geological features

Besides the features already mentioned there are several small scaling geological features possibly occurring in a borehole image. E.g., vugs and washouts can be related to chemical processes between borehole fluid and formation. Vugs are holes in the rock normally caused by dissolution of a carbonate rock and can be from mm scale to dm scale (Figure 7). If dissolution processes appeal to a whole layer of soluble rocks, washouts will occur and result in borehole radius anomalies.
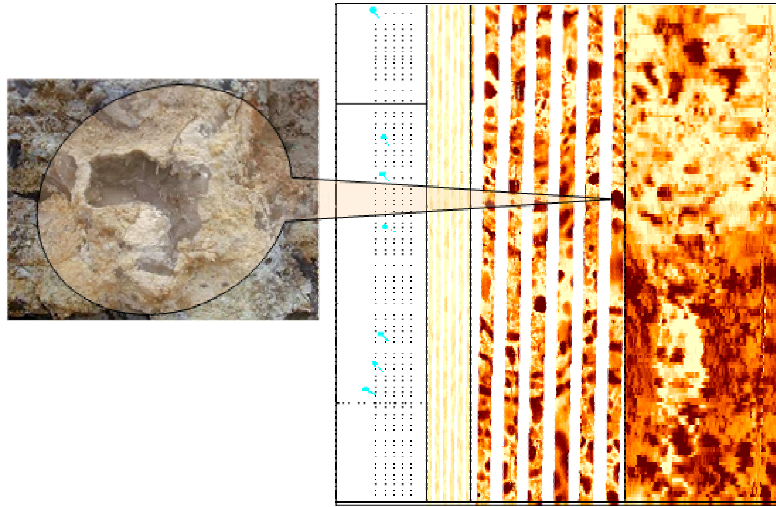
Figure 7 : A vug and its appearance in both electric and acoustic image log; adopted from [Dymmock, 2005]

4 Physical properties of the borehole environment

Determination of formation properties and detection of geological feature is the main and most important purpose of borehole imaging. Formation itself is characterized by its composition of different rock types. Standard procedure for in situ rock type determination used by field geologist comprises visual appearance, weighting by hand, hardness estimation. In a borehole – several thousand feet under the surface – this methodology is naturally not applicable. Therefore, measurement of physical rock properties is the only suitable possibility and an own scientific field deals with this topic: petrophysics.

Values measured by a geophysical imaging tool are determined by physical properties of the borehole environment and their distribution in this 3D space. Because of comprising different regimes like the tool itself, the borehole wall, the space between tool and formation filled with mud and the formation (Figure 8) these properties vary a lot and are addressed as well very different by geophysical methods.

As mentioned in the imaging introduction (chapter 2), imaging tools can be divided according to the applied measurement technique, namely acoustic, electric and nuclear imaging. Even if this thesis will focus mainly on electrical imaging, it will be dwelled more or less on all these three imaging techniques in the following chapters.
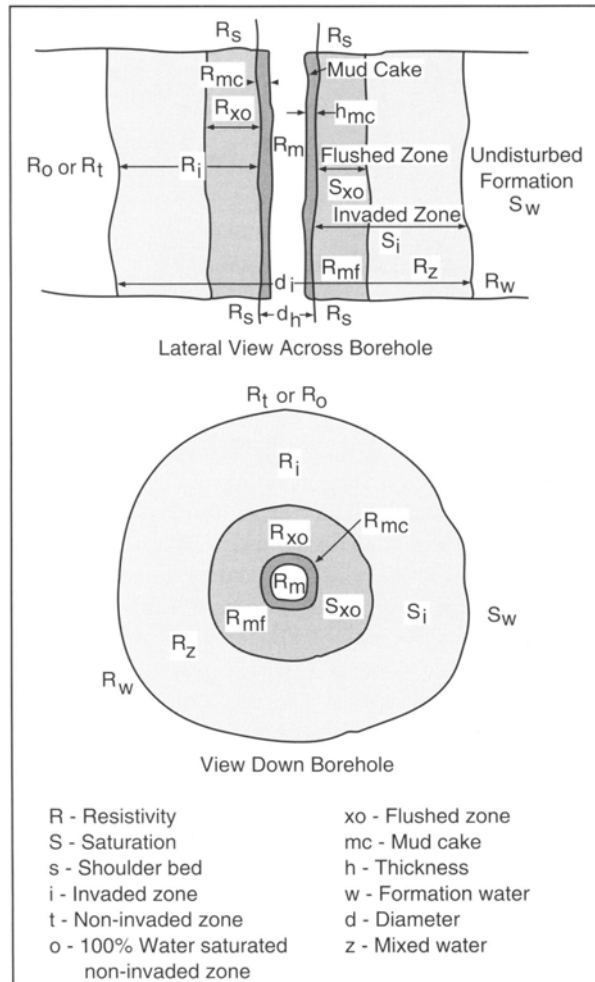
Figure 8 : Borehole environment adapted from [BakerHughes, 1992]

4.1 Physical parameters

For electrical, acoustic and nuclear measurements, relevant in this thesis, the performance characteristics are magnetic permeability, dielectric permittivity, electric conductivity (electrical measurements, [Beblo, 1997]) acoustic velocity and wave amplitude (acoustic measurement, [Ellis, 1987]) and count and energy analysis of gamma ray particles and neutrons, have been interacted with borehole environment.

Note that due to nuclear tool's bad resolution (only 4 to present 16 azimuthally density sectors) and the dropping importance, a detailed parameter description is foregone here. A more detailed brief method overview can be found in chapter 5.3. The remaining parameters according to electric and acoustic imaging are described detailed in the following chapters.

4.1.1 Magnetic permeability

Magnetic permeability influences the magnetic components of electromagnetic fields (see Equation 9) and only methods using alternating current are affected. For most of the rock types and minerals magnetic permeability is equal to the value measured in vacuum ($\mu=\mu_0$; $\mu_r=1.0$). So permeability can be neglected in most of the cases, only if ferromagnetic mineral occur consideration of magnetic permeability becomes important. Table 14 in the Appendix B shows some magnetic permeability values for different materials.

4.1.2 Dielectric permittivity

Dielectric permittivity is the gage for dielectric displacement (see Equation 9). Dielectric displacement occurs in every mineral when an electric field is applied and is a reversible displacement of charge carriers to a small stretch of way in phase to the time varying electric field. This causes a displacement current in addition to the applied current depending linear on the frequency of the electric field. Due to the electric displacement being almost lossless, attenuation of electromagnetic fields at higher frequencies becomes smaller. So propagation of electromagnetic waves is enabled and propagation velocity of the wave is determined by the dielectric permittivity. Table 15 in the Appendix B shows some dielectric permittivity values for different materials.

4.1.3 Electric conductivity and resistivity

First, it is important to point out the difference between resistance and resistivity. According to Ohm's Law (Equation 1), resistance is the quotient of voltage and current. The dependence of resistance to the length and the cross section of a conductor (two conductors of the same material and cross section differing in length have different resistance values) leads to the unit of resistivity. In other words, resistivity is the resistance of a conductor with defined length and cross section (impedance equation, Equation 1).

Equation 1
$$R = \frac{U}{I}$$
Ohm's law

$$\rho = \frac{R \cdot A}{l}$$
Impedance equation

with

- R = electrical resistance
- U = voltage
- I = current
- ρ = electrical resistivity
- A = cross section area of the electrical conductor
- l = length of the electrical conductor

Electric conductivity is a parameter relevant for every electromagnetic measurement techniques and can be assumed as a gage how much resistivity is opposed to an applied current (see Equation 2) for a specified electrical conductor. Furthermore, conductivity is responsible for the depth of investigation. The more the formation becomes conductive, the more an electromagnetic field is damped and therefore depth of investigation decreases. With a range of variation from 10^{-16} S/m (beryllium oxide) to about 10^8 S/m (sterling silver), conductivity belongs to physical units with one of the widest range of variation occurring in nature. This fact point out to different mechanisms contributing to the current flow: electronic semiconduction, metallic and electrolytic conduction [Beblo, 1997; Schön, 1998]. While measuring in the borehole, electrolytic conduction is dominant and even if conductivity is determined, primary the results are displayed as an image of resistivity values (Equation 2). Table 15 in the Appendix B shows some resistivity values for different materials.

Equation 2 $\qquad \rho = \frac{1}{\sigma}$

with

- ρ $\qquad$ = electric resistivity
- σ $\qquad$ = electric conductivity

4.1.4 Acoustic velocity

Another physical unit important for current imaging techniques is the acoustic velocity. It is determined by the time an acoustic wave needs for traveling a specified stretch of way. According to Wyllie's time average equation (see Equation 3), acoustic velocity through formation is only depending on porosity of a rock type and the velocities both of pure rock and fluid filling the pores. Actually, velocity of acoustic propagation is a rather more complex phenomenon than described by this simple equation [Ellis, 1987; Gilchrist et al., 2001].

Equation 3
$$\frac{1}{v} = \frac{1}{v_{solid}}(1-\phi) + \frac{1}{v_{fluid}}\phi$$
$$\Delta t = \Delta t_{solid}(1-\phi) + \Delta t_{fluid}\phi$$

with

- v $\qquad$ = velocity of the acoustic wave through formation
- v_{solid} $\qquad$ = velocity of acoustic wave through pure rock
- v_{fluid} $\qquad$ = velocity of acoustic wave through fluid filling the pores
- φ $\qquad$ = porosity (pure rock – pore ratio)
- t $\qquad$ = travel time of the acoustic wave through formation
- t_{solid} $\qquad$ = travel time of the acoustic wave through pure rock
- t_{fluid} $\qquad$ = travel time of the acoustic wave through fluid filling the pores

There are different types of acoustic waves, e.g. transversal (secondary wave) or longitudinal waves (primary wave) differing in their deformation behavior due to matter. Longitudinal waves for example are compression waves compressing or expanding rocks in direction of wave propagation, while transversal waves act as a shear force perpendicular to the direction of wave propagation. Equation 4 describes velocity for both types of acoustic waves.

Equation 4
$$v_p = \sqrt{\frac{Y}{\rho} \cdot \frac{1-\upsilon}{(1+\upsilon)\cdot(1-2\upsilon)}}$$
[Ellis, 1987]
$$v_s = \sqrt{\frac{\mu}{\rho}}$$

with

- v_p = velocity of the longitudinal wave
- v_s = velocity of the shear wave
- Y = Young's modulus (also called E-modulus)
- υ = Poison ratio
- μ = Shear modulus
- ρ = density

Note that Shear modulus μ, Lame constant λ (not mentioned in Equation 4) and Poison ratio υ are elastic constants used to describe elastic media while Young's modulus Y is also a physical property of an elastic media but not a constant. Table 17 in the Appendix B shows some velocity values of acoustic waves for different materials.

4.1.5 Acoustic wave amplitude

The second physical unit important for acoustic imaging measurements is wave amplitude being also very complex to handle because of depending on many influences. Wave amplitude itself is the maximum elongation of a wave's particle parallel (compression wave) or perpendicular (transversal wave) to direction of propagation.

Basis for describing acoustic amplitude is the equation for propagation of planar wave in homogenous matter:

Equation 5 $A(x,t) = A_0 \cdot e^{[i(k \cdot x - \omega \cdot t)]}$

with

- x = coordinate in x direction
- t = time
- $A(x,t)$ = amplitude of the acoustic wave at a specific time and space
- A_0 = source amplitude
- ω = source frequency depending angular velocity
- k = complex vector in propagation direction of the planar wave

28

Propagation vector k itself can be written as

Equation 6 $\quad k = k_{real} + k_{imag} = k_{real} + i\alpha$

By considering Equation 6 into account
Equation 5 becomes to

Equation 7 $\quad A(x,t) = A_0 \cdot e^{(-\alpha x)} \cdot e^{[i(k_{real}x - \omega t)]}$

The real term of Equation 7 is the attenuation term with attenuation coefficient α, while the imaginary term describes oscillation of the planar wave.

4.2 Parameters of borehole's components

The following chapters are used to explain and give a quantitative characterization of the parameters previously described within the different components of the borehole environment.

4.2.1 Tool

One component of the borehole environment can be easily dealt with, is the imaging tool itself. The physical properties of a tool are well known and designed to fit the desired purposes and in most cases, there is no interaction between the tool and the surrounding. To give an example, the body of an LWD electrical imaging tool is completely non-conductive, only the electrodes and anodes (also called return) are made of conductive materials. Therefore, it can be assumed there is no current flow trough the tool and therefore the tool can be neglected in interpretation and investigation of the measurement response. The single determining factor of measurement response is the tool geometry, e.g. the distance and arrangement of structural components. This geometry- influence is researched in detail during the engineering process of the tool e.g. via modeling to get the best possible response in a quantitative and qualitative way.

4.2.2 Mud

The influence of the component mud in the borehole is very complex due to the purpose of the mud and the interaction between mud and formation (Figure 8). In general, mud is a liquid pumped in the ground inside the stands, leaks at the end of the borehole, flows back to surface in the space between formation and stands and gets refreshed. Therefore, a mud-recycling circle is formed.

The main purposes of the mud are [BakerHughes, 2003c; Dingsoyr et al., 2004]

- stabilization of the borehole
- remove cuttings accrued during drilling process
- avoid falling of cuttings when drill string rotation stops
- cooling of the drill bit
- avoid discharge of fluids or gases (water, natural gas, hydrocarbons) into the borehole
- apply pressure at the end of the hole via a pillar of a dense fluid up to thousand of meter high
- being a media for data communication between tool and surface, e.g. via mud pulse telemetry.

To fit all these tasks and consider different borehole environments mud differs according to
- density (mud weight)
- viscosity
- oil-water ratio
- pH value
- special additives influencing the chemical reactivity.

Some simple notes illustrate the problem of inventing the "perfect" mud:

- If mud weight is too high, mud will leak in the surrounding formation. As a result, mud is lost, pore space is filled with mud and natural gas or hydrocarbons are extruded.
- If mud weight is too low natural gas or hydrocarbons will flow in the borehole forced by formation pressure. Apart from financial losses there is the great danger of having a highly inflammable fluid or gas under conditions of high pressure and heat when getting in contact with oxygen, e.g. at the surface
- If mud viscosity is to low, cuttings will fall down when rotation stops. While powering (rotating starts again) the drill string the next time there is the possibility of the drill-bit or drill string getting stick.
- If heat transport related properties of the mud are too poor drill bit will wear out faster and has to be replaced earlier.
- If water gets in contact with layers of clay or shale (included in almost all sediments) a chemical interaction will take place [Walker, 1999]. Because of highly chemical reactivity of clay-minerals in conjunction with water parts of the borehole wall can become instable, break out and fall in borehole providing risks of the drill string getting stick

Just the last statement is important for the distinction of mud in two types strongly differing in their physical properties. Drilling in areas like the Gulf of Mexico reveals the significance of this problem. Claystones overlying the target hydrocarbon reservoirs causes frequent reaming runs and unnecessary sidetracks to clean or elude impassable parts of the borehole. Taking the chemical reactivity of clay into account a type of mud using oil instead of water as a basis was invented [Walker, 1999; Wang et al., 2004].

Acoustic images can be acquired in both oil-based and water bused mud, so, following distinction considers mainly with electric properties. Note that there are no longitudinal waves in liquids because off shear forces are non-existing [Gilchrist et al., 2001].

4.2.2.1 Conductive mud, water-based mud (WBM)

Water-based mud (WBM) is the oldest and therefore most common type of mud used in the oil business. Due to its name, water is the largest component and because of water is very conductive this mud is often called conductive mud. The other way round, resistivity of the fluid, filter-cake and filtrate is low (see chapter 4 and Appendix B, Table 16). This means an electric current emitted by an electrode of a measurement tool can easily pass the mud before entering formation and signal response is generally of the highest quality when using WBM [Bloys et al., 1994; Laastad et al., 2000].

The major ingredients of a water-based mud are [Bloys et al., 1994; BakerHughes, 2003c]

- Water in its natural state or salt may be added to change filtrate reactivity with the formation
- Weighting agents (e.g. barite) to control formation fluid pressure
- Clay (e.g. bentonite) to provide viscosity and create a filter cake at the borehole
- Polymers to reduce filtration, stabilize clays, flocculate drilled cuttings and increase cutting-carrying capacity
- Thinners to reduce flow-resistance and avoid gel development
- Inorganic chemical to influence different chemical and physical properties like pH, hardness, salinity and density
- Bridging materials (e.g. calcium carbonate, cellulose fibers, asphalts) to build up the filter cake and lost circulation materials (e.g. walnut, mica, modified cellulose) to block large openings in the borehole
- Surfactants and specialized chemical

Typical physical properties for water-based mud are

Unit	Value range
Density	1 - 2,2 g/cm^3
Resistivity (depends on salinity)	0,015 – 3 Ωm
Plastic viscosity	15 – 35 cP
pH	8,5 – 10
Water content	%

Table 2 : Physical properties of WBM [BakerHughes, 1999; Baule, 2003]

4.2.2.2 Non-conductive mud (NCM), oil-based mud (OBM)

Due to the ingredients oil-based mud do not differ that much from water-based mud described above. In most cases, weight materials, viscosifiers, thinners and bridging materials are added as well. The main difference is the underlying basis of this mud. Oil-based mud is an invert emulsion with oil as the continuous phase while the aqueous phase consists of droplets of brines stabilized by emulsifiers [Dingsoyr et al., 2004]. That implies the far-reaching problem of oil is an insulator (see Appendix B, Table 16). Therefore electrical measurement techniques proved in WBM fail in OBM because coupling impedance is too high for direct injection of current into formation. Consequently, responses from "classical" resistivity logging tools are poor or non-existent [Laastad et al., 2000].

Even new electrical imaging tools have to be developed invert emulsion fluids are superior to conventional water-based muds. In many applications (e.g. extended reach and long horizontal wells) the advantages itemized in Table 3 especially the ability to stabilize reactive shale make OBM systems the only technical alternative and often usage of OBM is the criteria for distinction between economical and marginal field development [Laastad et al., 2000].

Advantages	Disadvantages
Shale stability and inhibition	High initial cost per barrel
Temperature stability	Pollution control required
Resistance to chemical contamination	High cost of lost circulation
Reduced tendency for stuck pipe	Disposal problems
Reduced fluid density drilling	Hole cleaning
Reduced corrosion	Hazardous vapors
High penetration rate	Fire hazard
Reduced cement cost	Special logging tools required

Table 3 : Advantages and Disadvantages of OBM adapted from [BakerHughes, 1999]

Typical physical properties for oil-based mud are

Unit	Value range
Density	0,9 – 2,63 g/cm^3
Resistivity	n/a
Plastic viscosity at 8°C	10 – 75 cP
pH	not applicable
Oil content	40% - 100%

Table 4 : Physical properties of OBM

Note that resistivity values for OBM are controversially discussed among experts and so no reliable values can be given. Furthermore, pH is not measured in OBM.

4.2.3 Borehole wall

Actually, borehole wall is not a real component of the borehole environment but more precisely the shape or surface of formation drilled in. For any imaging technique, there is no problem when borehole is assumed ideal. That means diameter of the borehole tube is constant for every depth, the tube is not tortuous and borehole wall is almost smooth. It is obvious that this can be hardly achieved, because drilling process can be complicated and formation rocks react very different. How a 3D plot of the borehole can look like is displayed in Figure 9 recorded by a six-arm caliper tool.

Following effects lead to borehole geometry anomalies:

- Breakouts
- Washouts
- Fractures
- Mudcake thickness
- Roughness (due to physical stress while drilling)
- Drilling related deformation of the borehole tube – tortuosity - (spiraling, rippling, hour-glassing) [Chen et al., 2002; Pastusek, 2002]
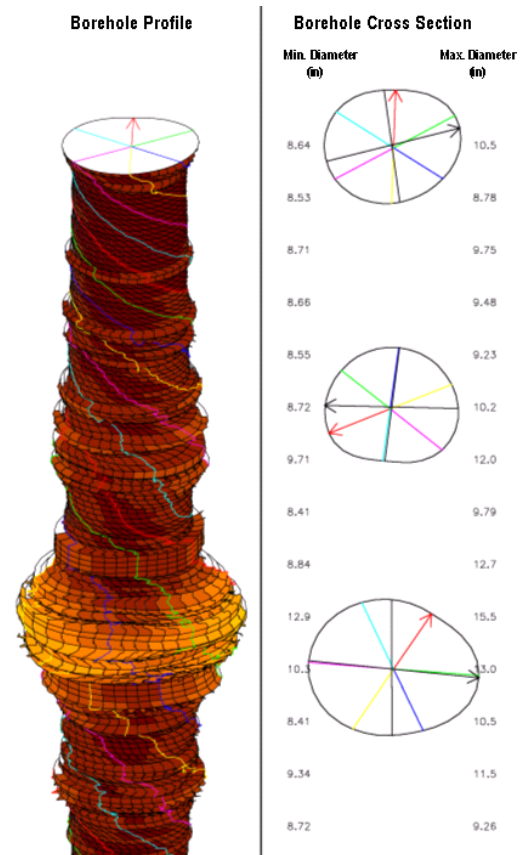
Figure 9 : 3D Borehole

Standoff, distance between measurement sensor and formation, is a very important influence for borehole imaging. E.g., acoustic logging (see chapter 0) needs standoff data to calculate wave velocity correct and depth of investigation of electrical measurements (see chapter 5.1) depends strongly on standoff. More precise, standoff for the StarTrak^{TM} tool (see chapter 5.1.4) is 1/8" (0.3 cm) in an 8.5" (21.6 cm) hole and depth of investigation is about several inches. If a breakout is larger than some inches, StarTrak^{TM} will measure resistivity of mud instead of formation.

In an ideal borehole tube and if tool is centered, standoff will be constant. In reality, standoff will vary according to borehole geometry anomalies. In the field of wireline imaging, this problem is partly solved by three or more articulated arms pressed against the borehole wall (see chapter 5.1.3). So larger standoff variations can be measured and taken into account. This procedure is not easily applicable for MWD imaging due to rotation of the whole drill string and therefore mechanical problems. So, standoff variations have to be determined differently (e.g. by the help of modeling).

Since wireline electrical imaging tools use sensors, attached to the arms pressed against the borehole wall, it is understandable that wireline tools measures only stripes along the borehole wall according to number of arms and borehole diameter. Common borehole sizes vary from 5" to 21" (12.7 – 53.3 cm). Figure 94 and Figure 95 in the Appendix B show some borehole coverage values for different borehole sizes. Note that e.g. borehole coverage increases from 30 % using the FMS^{TM} tool (4 arms, 4 pads) to 80% using FMI^{TM} tool (4 arms, 8 pads) for an 8" (20.3 cm) hole [Schlumberger, 1999]. In opposite and due to rotation MWD tool measurements cover 100% (360°) of the borehole.

Shape of the borehole is specifically important for acoustic measurements. Due to refraction and reflection of acoustic waves at boundary layers a lot of acoustic energy will be lost if the shape of a boundary layer is to rough. Acoustic waves being refracted deep into formation or being reflected back in the borehole cannot contribute to useful measurement response recorded in the tool's receiver.

4.2.4 Formation

Each rock type being a part of the formation can be characterized fundamentally by its chemical composition and compounds, the pore space and filling of these pores. Petrophysical units like density, electric conductivity or acoustic velocity are derived directly from these mentioned properties. With the knowledge of rock's petrophysical properties and their addressing by measurement tools (e.g. by lab measurements) it is possible to detect and identify rock types in the borehole.

Sometimes measurement response of one specific physical measurement principle is not unique but similar for different rock types. However, by combining different measurement principles clear rock identification is mostly possible. Due to the great variety of rock types, it is understandable that giving a full overview of rock types and their petrophysical properties is hardly possible in this thesis. Comprehensive information are provided by appropriate literature like [Schön, 1998]. A brief buildup of different petrophysical rock properties can be found in Table 14 to Table 17 in the Appendix B.

5 Measurement principles

Acoustic imaging measurements base on the propagation of acoustic waves and the interaction with borehole and formation (reflection, refraction, etc.), while electrical imaging measurements deal with the wide range of interactions between the electric and magnetic field and the borehole environment. Besides this, nuclear imaging extracts information by counting and analyzing of gamma ray particles or neutrons, have been interacted with formation. Not only measurement principle but also imaging technologies differ in azimuthally resolution and operational ability in different borehole environments. Acoustic and nuclear imaging can be performed in WBM as well in OBM, but provide only comparatively low resolution, while electrical imaging provides higher resolution, but currently there is no electrical imaging tool can be run in WBM as well as OBM. A brief comparison of imaging tools is provided in chapter 5.4.

5.1 Electrical imaging

Electric imaging is the newest imaging technique and many different approaches are used to make electric imaging applicable to both LWD and wireline (chapter 2) as well as OBM and WMB (chapter 4.2.2). Maybe that is way, scientists and scientific literature concerning with electrical imaging are divided on nomination and classification of the different electrical measurement methods. Terms like "galvanic", "capacitive", "induction" or "propagation" are widespread but often denoted different in aspects of interaction of magnetic and electric field with borehole environments. That is why an own classification is developed and used here and may be different to other classification can be found in scientific papers (Figure 11). As a criterion for delimitation, physical equations and parameters are called on. It is tried to develop these subdivisions as consequent as possible, but due to the great variety of properties of the borehole environment had to be considered by physical equations and the measurement devices, it is obvious to make compromises.

5.1.1 Theory

The basis for every effect relating to magnetic and electric fields is given by the Maxwell's laws (Equation 8). Among others, they describe the interaction between electric and magnetic field, the spread of each, electromagnetic waves and their interaction with different matters.

$$rot\vec{H} = \frac{\partial \vec{D}}{\partial t} + \vec{J}$$

Equation 8 $\quad rot\vec{E} = -\frac{\partial \vec{B}}{\partial t}$

$$div\vec{D} = \rho$$

$$div\vec{B} = 0$$

with

- $\vec{H}$ = magnetic field intensity
- $\vec{B}$ = magnetic flux density
- $\vec{E}$ = electrical field intensity
- $\vec{D}$ = electric flux density or dielectric displacement
- $\vec{J}$ = electric current density
- ρ = electric charge density
- t = time

Furthermore the basic relationship between current density J and electric field intensity E and electric (respectively magnetic) flux density D (respectively B) and electric (respectively magnetic) field E (respectively H) are:

Equation 9
$$\vec{J} = \sigma \vec{E}$$
$$\vec{D} = \varepsilon \vec{E} + \vec{P}$$
$$\vec{B} = \mu(\vec{H} + \vec{M})$$

with:

- $\vec{P}$ = electric polarization
- $\vec{M}$ = magnetization
- σ = electric conductivity
- ε = $\varepsilon_0 \varepsilon_r$ product of permittivity of the vacuum ε_0 and relative permittivity ε_r under conditions of isotropy, as a consequence piecewise homogeneity and thus ε being a constant and not a tensor
- μ = $\mu_0 \mu_r$ product of magnetic permeability in vacuum μ_0 and relative magnetic permeability μ_r, under conditions of isotropy, as a consequence piecewise homogeneity and thus μ being a constant and not a tensor

The complete mathematical derivation of Equation 8 in order to get a solution describing the dependences for the magnetic field intensity H can be found in the Appendix A. Combining Equation 29 and Equation 31 from Appendix A, following relation is obtained:

Equation 10
$$-\Delta \vec{H} = (i\varpi\varepsilon + \sigma)(-i\varpi\mu)\vec{H} = -(\varepsilon\mu\varpi^2 + i\sigma\varpi\mu)\vec{H}$$
$$\Delta \vec{H} = \vec{k}^2 \vec{H}$$

with

Equation 11 $\vec{k}^2 = -\varepsilon\mu\varpi^2 + i\sigma\varpi\mu = \alpha + i\beta$

It is obvious that k depends on three major parameters, namely conductivity σ, permittivity ε and frequency f (respectively ω). Permeability μ being nearly constant for the most types of rocks can be neglected (see chapter 4 ,[Beblo, 1997]).

Regarding to Equation 11 three different cases can be divided:

1) $i\omega\varepsilon >> \sigma$ that means either frequency of the electromagnetic (EM) wave or permittivity is exceeding the influence of the conductivity. So displacement current is dominant and Equation 11 becomes to $\vec{k}^2 = -\varepsilon\mu\varpi^2$

2) $i\omega\varepsilon << \sigma$ that means conductivity is exceeding the influence of frequency of the electromagnetic (EM) wave and permittivity. So displacement current is negligible and Equation 11 becomes to $\vec{k}^2 = \sqrt{i\sigma\varpi\mu}$

3) σ and $i\omega\varepsilon$ are of the nearly same magnitude. Neither displacement current nor current density J can be neglected and k depends still on all three parameters being of a low value. The critical frequency for this case is approximately 1 GHz estimating ε is 10 and σ is $\frac{1}{10}\frac{S}{m}$, respectively $\rho = \frac{1}{\sigma} = 10\,\Omega m$ [Fulda, 2004b].

Case 2) is commonly used in present WBM imaging tools and some detailed remarks should be given. As shown in Equation 11, k is a complex vector with two terms, α denotes phase shift and β attenuation (amplitude shift). If conductivity is dominating the influence of frequency and permittivity, the planar wave in k direction is strongly attenuated. This approximation is called quasi-static and its characteristic feature is that the signal is almost totally damped after one wavelength (Figure 10). The great advantage enabled by this scenario is the direct measurement of the value of interest: conductivity respectively resistivity.

The other way round in Case 1) conductivity is lower or influence of frequency/ permittivity is higher and so low attenuation takes place. Therefore real wave propagation can be observed and features of an interaction between wave and formation have to be taken in account (e.g. reflection, refraction…). In general, Case 1) and 2) are comparably easy to handle and well understood. Case 3) is more difficult, because no simplification can be applied and permittivity as well as conductivity is measured.
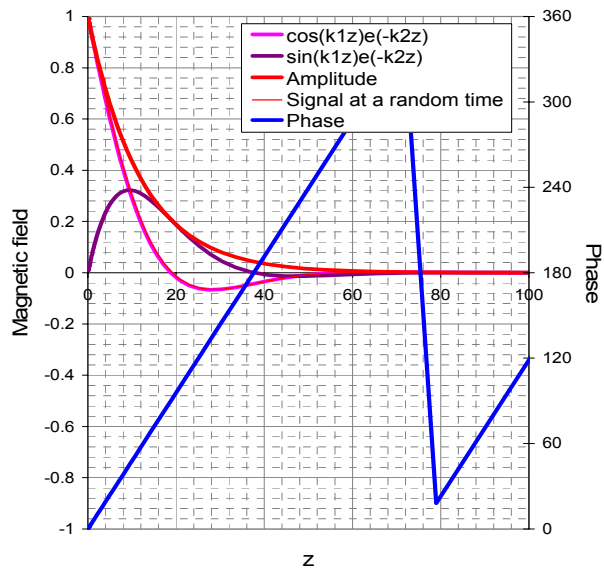
Figure 10 : Phase and attenuation for the quasi-static approximation; adapted from [Fulda, 2004b]

5.1.2 Classification

The flowchart of the developed classification of azimuthal resistivity tools is shown in Figure 11. The main difference is provided by the art of applying the current through the mud into formation –either direct (**galvanic**) or indirect (**inductive**).
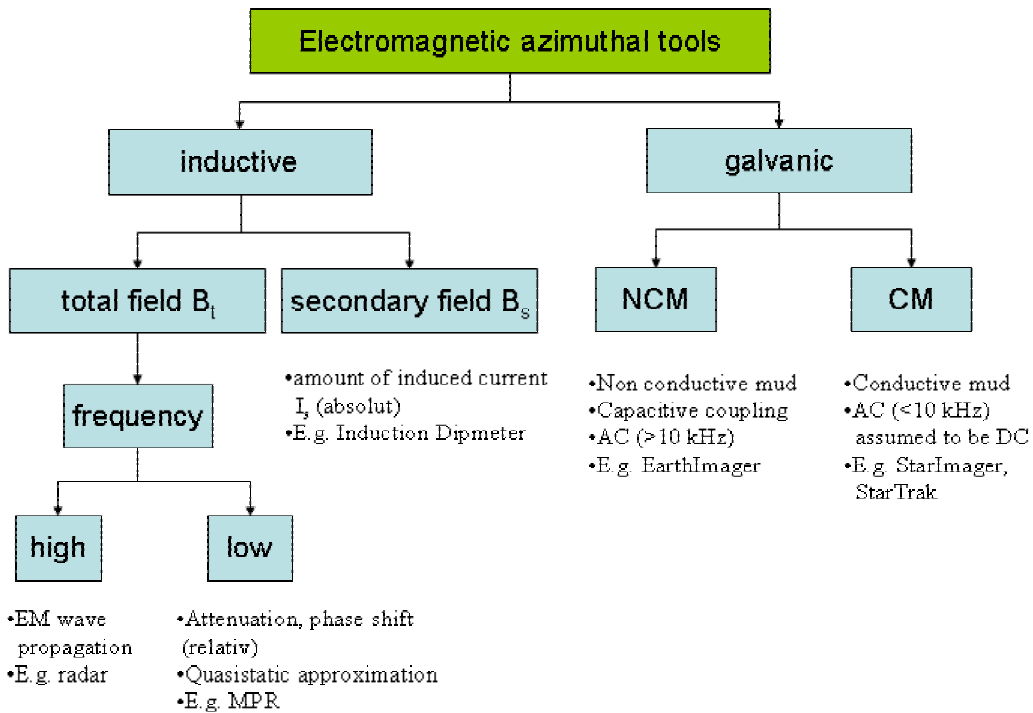
Figure 11 : Classification of electromagnetic azimuthally tools

38

5.1.2.1 Inductive devices

An inductive device consists of at least two coils, a transmitter and a receiver coil. The transmitter coil is excited by transmitter current I_P and produces a time varying electric field E_P with a specified frequency (according to Equation 29). This cause a time varying magnetic field H_p comprising both transmitter-coil and formation (Equation 29). According to the model drawn in Figure 12 formation behaves as a coil in which magnetic field H_p induces ground loop currents I_S. An electric field E_S respectively magnetic field H_S is set up in addition to E_P and H_P. Contrary to the transmitter coil formation "coil" is not spatial limited and the whole procedure of induction occurs between formation and receiver coil.
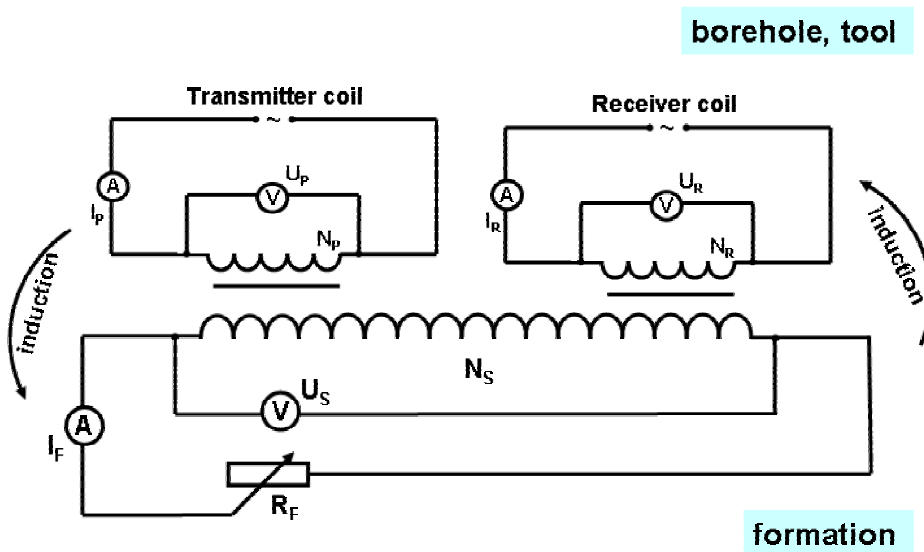
Figure 12 : Model of inductive devices

According to Figure 12 four different magnetic respectively electric fields have to be differed: magnetic field of the transmitter coil (H_P, primary field), magnetic field induced in formation (H_S, secondary field), total magnetic field ($H_T = H_P + H_S$) present in formation and magnetic field of the receiver coil (H_R). The magnetic field of interest is the secondary field determined by formation conductivity (symbolized by R_F in Figure 12). If formation is non-conductive ($\sigma = 0$) no current will be induced and therefore total field will be equal to primary field and secondary field will be zero ($H_T = H_P$; $H_S = 0$). Otherwise, there are two ways of determining the influence of conductivity, either, measuring secondary field (absolute) by annihilating primary field or measuring the total magnetic field depending on secondary field (relative).

Secondary field B_s

To be able to measure only the secondary magnetic field the receiver coil needs to be configured such that the primary magnetic field of the transmitter coil is cancelled. In other words signal output of the receiver coil must be balanced to yield zero response in a non-conductive media [Wurmstich et al., 1995]. The most common technique for annihilating the primary field is wiring two receiver coils in opposition. Details and other techniques are described in [Ellis, 1987; Johnson, 1989; Kaufmann et al., 1989; Wurmstich et al., 1995]. Finally the signal response describes the absolute value of conductivity respectively resistivity existing in formation. An example for a device that proceeds according to the described method would be the Induction dip-meter.

Total field B_t

To avoid the effort of canceling primary field, measuring the total magnetic field is a suitable approach. This method provides no absolute resistivity values only relative ones. Measured resistivity values are not comparable to formation's resistivity values but changes within resistivity distribution are expressed correctly. That means differences between resistivity values are of the same magnitude than present in formation. Signal response of the electromagnetic (EM) field is recorded at two different receiver coils and resistivity can be calculated by either phase or amplitude shift (attenuation) of the two recorded response of the time varying EM fields (Figure 13) [BakerHughes, 1998].
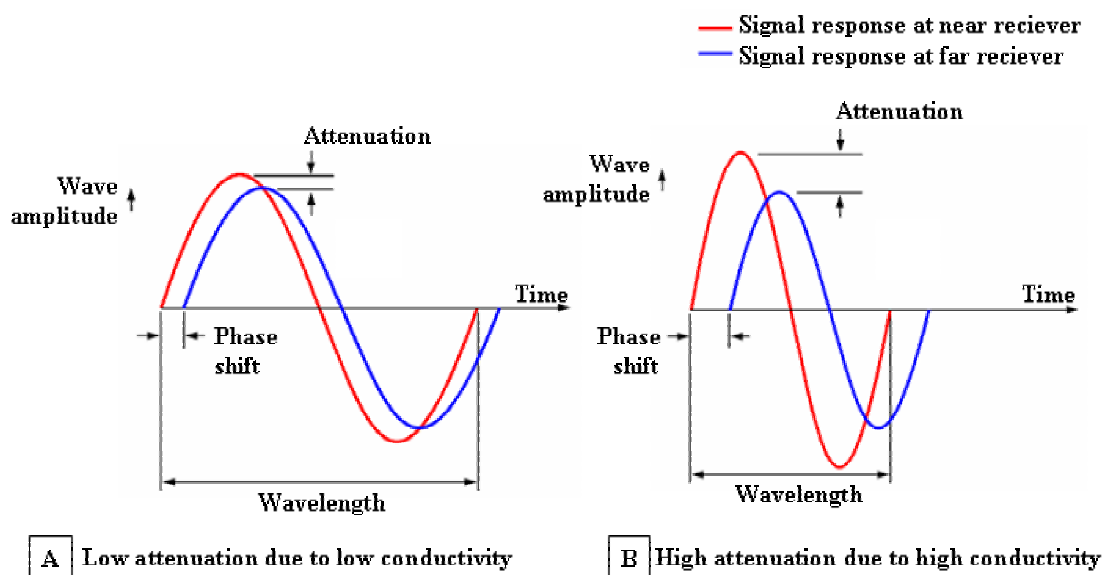
Figure 13 : Amplitude and phase shift for low and high formation conductivity

A further subdivision is provided by the amount of frequency. According to chapter 5.1.1 frequency is one of the parameters dividing the quasi-static approximation from real wave propagation. At lower frequencies (e.g. kHz – a few MHz,) the displacement current is negligible and the signal is almost totally damped after one wavelength. A tool proceeding due to this method is e.g. the MPR (Multiple Propagation Resistivity). High frequencies (e.g. MHz – GHz) invert this scenario. Displacement current is dominating and wave propagation occurs. This is used at downhole radar measurements and involves other problems like considering of the Skin effect and higher rate of attenuation because higher frequencies. Note that radar devices emit EM waves with no specific frequency but a range of different frequencies.

5.1.2.2 Galvanic devices

Galvanic devices are characterized by direct current flow from a measurement electrode through mud to a return electrode. Respecting the different physical properties of the mud (chapter 4.2.2), two wiring possibilities are offered: low frequency alternating current (AC, <10 kHz, can be idealized as direct current) in conductive mud and high frequency alternating current (AC, 10 kHz) in non-conductive mud (A and B in Figure 14).
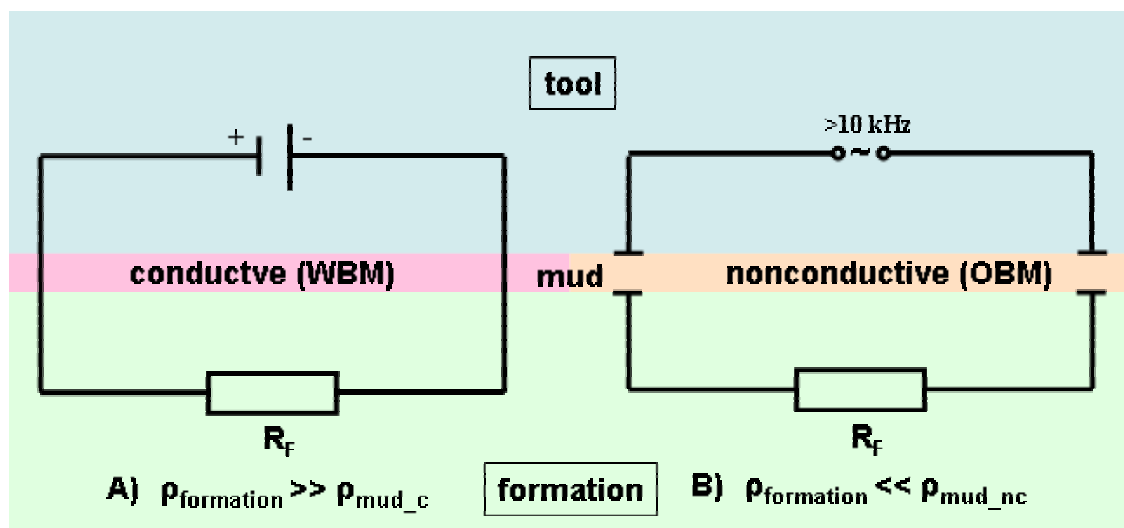
Figure 14 : Model for galvanic devices

Conductive mud

As implied by its name, water-based mud (WBM) is very conductive and so direct current from a tool's electrode can easily pass the mud. By measuring current and voltage of the return electrode and having the knowledge of the tool geometry, resistivity can be determined according to Equation 1 (see chapter 4.1.3). An imaging tool can be ranged in this category is e.g. the StarImager[TM] or FMS[TM] [Schlumberger, 1999; BakerHughes, 2004; Ritter et al., 2004].

Oil-based mud can nearly be considered as an insulator according to its high resistivity. That is why direct current cannot pass the mud easily. If an alternating current is applied, non-conductive mud will be seen as dielectric of a capacitor and a displacement current flow through mud into formation (and back) will occur. Finally, resistivity can be calculated by the same way described for conductive mud. A suitable example for this group of electric imaging tools is the OBMI[TM] or EarthImager[TM] [Evans, 2002; BakerHughes, 2004]. Note that new techniques for measuring in OBM are researched but not have been finished.

5.1.3 Implementation

As explained in the last chapter, different approaches for electrical imaging are used. To give an example, only one device is presented here more detailed. It is a wireline-imaging tool suitable for WBM developed by BakerHughes: StarImager[TM] (Figure 15). A principle sketch and the main components of the StarImager[TM] tool are displayed in Figure 16.

Figure 15 : StarImager[TM] here displayed with widened arms

A constant voltage difference between the return electrode and the pads mounted on six articulated arms and pressed against borehole wall is used to create a current flow through the formation. Return electrode and the pads are separated by an electrical isolator. Each pad contains a set of 24 measuring sensors (buttons) surrounded by a metal pad housings (guard electrode) which acts as a focusing electrode for the measuring sensors. Measuring button and guard electrode are of the same electrical potential, so no current flow between both electrodes takes place. Lines of flux cannot cross each other; therefore, lines of flux of measuring current have to arch around focusing current lines of flux. As a result, measurement sensor current flow is forced perpendicular to the tool into formation. This provides a higher depth of investigation and determines measurement values of a more specified spatial location (beam of measurement current is narrow and straight perpendicular into formation) [Evans et al., 2002].

| Measurement principle : Tool | Measurement principle : Pad | Picture : Pad |
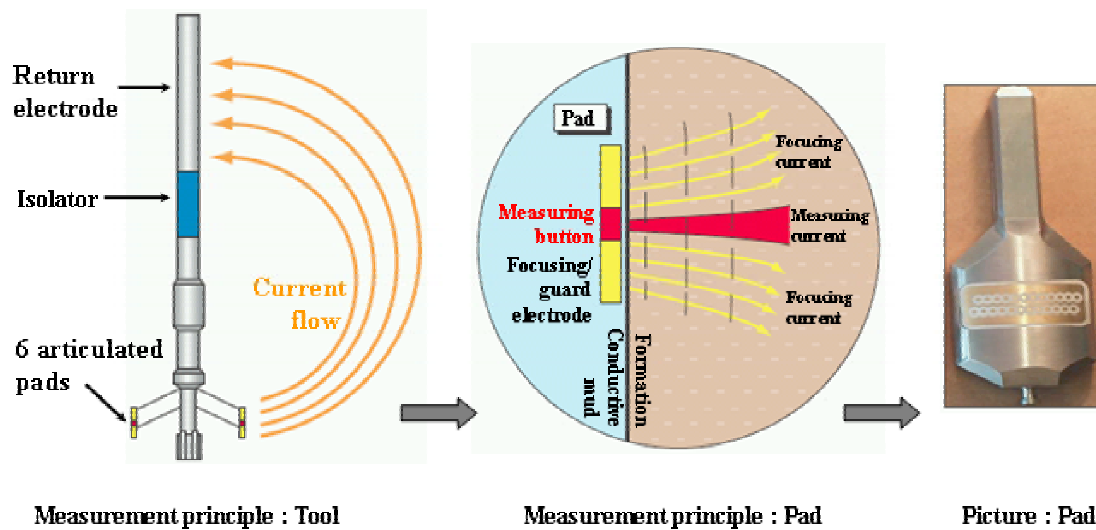
Figure 16 : Measurement principle StarImager^{TM}, adapted from [BakerHughes, 2004]

Each measurement button (StarImager^{TM} posses 24 buttons* six arms = 144 buttons) records a current depending on formation conductivity respectively resistivity (Equation 2). Consequently, the acquired image consists of six image stripes of each 24 resistivity values separated by a gap. The larger the borehole, the more the tool's arms are widened and therefore the larger the separation between the image stripes. Therefore, borehole coverage of the image log will varies [Gianzero, 1993; BakerHughes, 2003a; BakerHughes, 2004]. For more information and specification about StarImager^{TM,} see Figure 94 in the Appendix B.

By the way, a quite similar concept is implemented in the analog MWD tool StarTrak^{TM}. According to chapter 2 StarTrak^{TM} possess just one sensor at the surface of the measurement sub instead of amplified arms. By rotating of the drill string measurement response recorded by the sensor covers 360° of the borehole. Due to the more complicate drilling conditions, the first StarTrak^{TM} prototype acquired only 60 measurement values per revolution at moderate rotations speed (below 120 rotation per minute). Meanwhile, the azimuthal (horizontal) resolution was doubled to 120 measurement samples per revolution.

5.1.4 Tools

A build up of information and specifications of electrical wireline imaging tools can be looked up in Figure 94 and Figure 95 the Appendix B.

5.2 Acoustic imaging

Wireline acoustic imaging tools are commonly used and consequently an important imaging measurement technique. This can be traced to both its applicability in water and oil-based mud (chapter 4.2.2) and its high-resolution 360° borehole images, also under difficult wellbore conditions, including high-porosity and unconsolidated formations. Basic parameters are already described in chapter 4.1.4 and 4.1.5, afterwards tool measurement principles and implementation are in center of interest.

5.2.1 Theory

Basis for acoustic imaging as well as acoustic logging and seismics in general are elastic and inelastic properties of rock due to mechanical energy. Acoustic energy of a time and spatial propagating motion of particles (respectively wave) can be such a mechanical energy and comprises a frequency domain of 10 to 10^{15} Hz. It is emitted by a transmitter, propagates model-like as an oscillating particle-motion and is finally received by a receiver. If an assembly unit is designed to transmit and receive acoustic waves, it will be called a transducer. Analyzing acoustic wave-train through a specified material provides information about its petrophysical properties [Jetschny, 2003].

Even if standard acoustic logs and acoustic imaging tools share the same origin, their primary method of working differs principally. Primary source of information of an acoustic imager are acoustic waves reflected by the borehole while standard acoustic analyses refracted acoustic waves entering the formation. As can be seen in Figure 17 the emitted acoustic wave is also refracting within formation but never reach the receiver. Therefore, acoustic imagers belong to the field of refection seismics and standard acoustic tools to refraction seismics.

The two different applications of borehole imaging are 3D borehole geometry determination and formation imaging. The first application is achieved by acoustic travel time measurement. Acoustic velocity for both primary and secondary wave (chapter 4.1.4) in mud and mud density are unknown. So, at least acoustic velocity must be determined to be able to calculate borehole radius. A separate transducer located at the tool surface provides this (Figure 17, transducer B) task. Consequently, borehole radius can be calculated by picking the first arrival of the primary wave recorded in the tools receiver and by the simple equation

Equation 12 $r = r_T + v_p \cdot \dfrac{t}{2}$

with

- r = borehole radius
- r_T = tool radius
- v_p = acoustic velocity of the primary wave
- t = acoustic travel time (tool – borehole – tool)

44

According to Equation 4 acoustic velocity depends also on media density the wave travel trough, so, a raw estimation can be made due to mud density, too. The elastic properties (Poison ratio, Young's modulus …) can be assumed constant or at least slowly varying for specific sections of borehole. Therefore, changes in mud density will directly affect acoustic velocity.

Basis for understanding the principles of acoustic formation imaging is simplifying Equation 7 (chapter 4.1.5) in terms of dependences and considering only the wave propagation from tool to borehole wall (Figure 17). As a result, this leads to:

Equation 13 $\quad A = A_0 \cdot R_f \cdot f(surface) \cdot f(T, p, r, \alpha, MC, ...)$ **[Priest, 1994]**

with

- A_0 = source amplitude
- A = amplitude
- R_f = gage for reflection at the borehole surface
- $f(surface)$ = function of the borehole surface conditions (rugosity)
- $f(T,p,r,\alpha,...)$ = function of temperature t, pressure p, borehole radius r, mud attenuation coefficient α, mud composition MC …

Focusing on a partial spatial domain of the borehole $f(T,p,r,\alpha,...)$ at a specified depth interval can be assumed to be constant or at least slowly varying, while $f(surface)$ is mainly responsible for noise and can't be neglected. R_F is the gage of interest and is defined by

Equation 14 $\quad R_f = \dfrac{\rho_m v_m - \rho_f v_f}{\rho_m v_m + \rho_f v_f} = \dfrac{Z_m - Z_f}{Z_m + Z_f}$

with

- ρ_m = density of the mud
- ρ_f = density of the formation
- v_m = acoustic velocity within the mud
- v_f = acoustic velocity within the formation
- Z_f = formation impedance
- Z_m = mud impedance

Under the conditions of good borehole wall surface (rugosity is low and therefore noise is low) and low mud attenuation measuring acoustic wave amplitude provides information about formation density and acoustic velocity. Because of being unique parameters for each rock type, displaying wave amplitude can be therefore used as a borehole image. In this connection, it is understandable for high rugosity, high mud density (mud weight) and large borehole diameter being the worst case for acoustic imagers. This scenario causes a high noise level and the acoustic wave to be damped strongly.

As already mentioned in chapter 3, acoustic imaging as well as electrical imaging tools do not measure absolute formation values. Because of the absence of a possibility to determine exactly the missing mud density for Equation 14, only impedance contrast can be display correctly. This is adequate due to imaging claims of providing high resolved structural information of the borehole instead of exact petrophysical parameters (also see chapter 3).
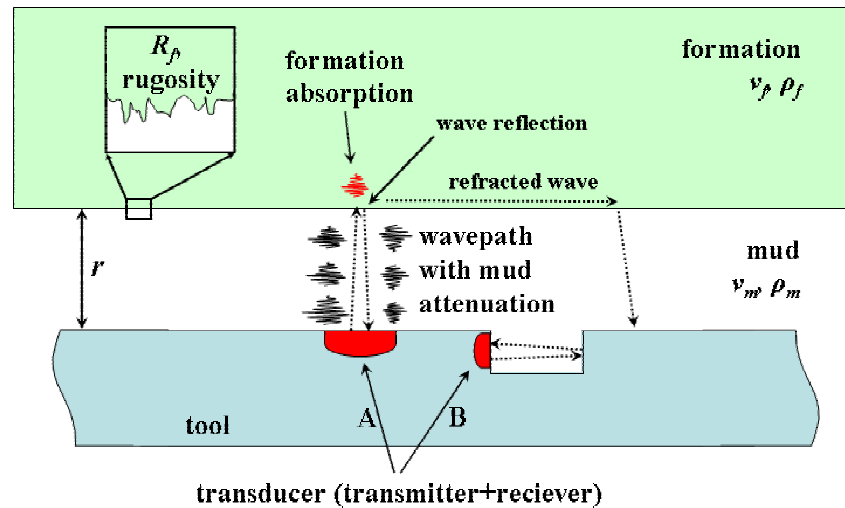
Figure 17 : Propagation of an acoustic wave [BakerHughes, 2003a]

5.2.2 Implementation

Representing the group of acoustic imaging, the Circumferential Borehole Imaging Logging (CBIL™) tool is described more detailed (Figure 18).

Figure 18 : CBIL tool; adapted from [BakerHughes, 2004]

The CBIL tool comprises an acoustic transducer mounted on a rotating section isolated in an oil-filled chamber from the drilling mud in the borehole. The transducer operates in a pulse echo mode meaning that it transmits and then detects the reflected acoustic pulse from the borehole wall every time it is fired. The transducer fires 125 or 250 times in each revolution, the amplitude and two way travel-time of the 125 or 250 reflected acoustic pulses are measured while the instrument is still moving in the borehole (Figure 19) [BakerHughes, 2004].

The measurement values can be drawn in two different images

- Reflectance amplitude image – this image shows contrasts in acoustic impedance of the borehole wall. Variations in lithology, bedding, lamination, or physical rock features such as fractures and vugs consisting of varying impedance can be seen (Figure 6, right image).
- Travel-time image – this image displays the borehole shape and size. Its shading is indicative of the distance of the transducer to the wellbore wall and is especially useful for the distinction between closed, open fractures, and mineralized fractures (Figure 9).
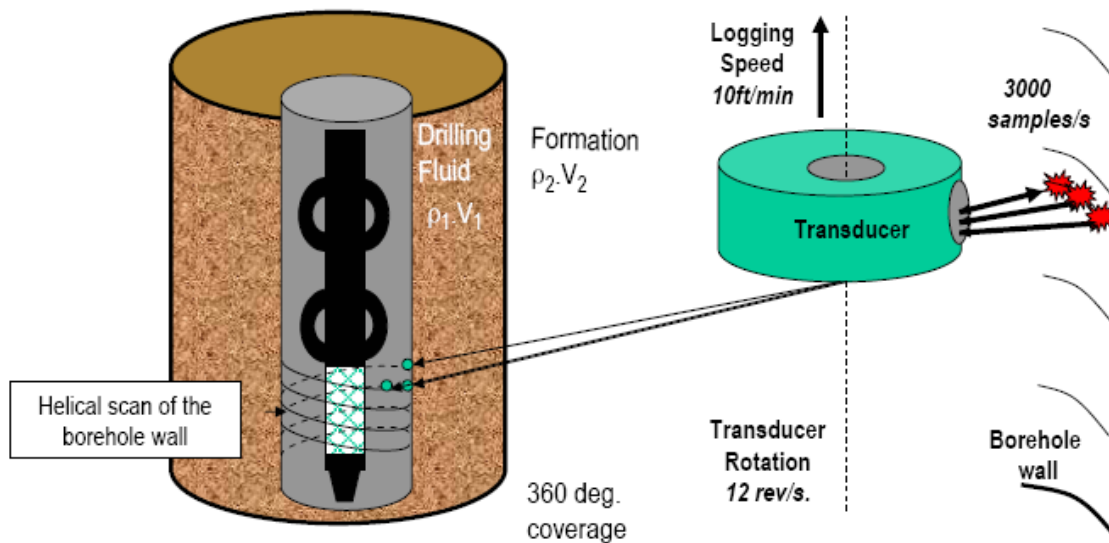
Figure 19 : CBIL tool sketch and measurement principle; adapted from [BakerHughes, 2003a]

Frequency of acoustic wave emitted by an acoustic imaging tool is an important key parameter. Higher frequencies results in higher resolution but unfortunately also in increased attenuation of the acoustic signal. The optimum frequency with moderate attenuation and good resolution is at about 250 kHz [Zemanek et al., 1969]. Hence the CBIL™ tool uses three different operation frequencies namely approximately 230, 250 and 300 kHz to achieve constant measurement quality under different borehole conditions.

Azimuthal spacing of data samples varies between 1.5 and 2.5 degrees depending on the exact tool and internal setup. The resolution of the acoustic imaging instrument is defined as its ability to distinguish between closely spaced formation features. Experimental data have shown that features separated by 0.3" (ca. 1 cm) can be resolved by the CBIL™ tool. Tests show that, the detection capabilities of the instruments are as small as 0.005" (0.0127cm) as fractures with these apertures have been detected [BakerHughes, 2003a].

Note, that the Ultrasonic Borehole Imaging tool (UBI™) by Schlumberger works principally the same way. The operation frequency is a little bit different to the CBIL™ tool (250 and 500 kHz) and the sonic beam is focused [Priest, 2005].

5.2.3 Tools

A build up of information and specifications of acoustic wireline imaging tools looked up in Figure 96 in the Appendix B.

5.3 Nuclear Imaging

LWD nuclear imaging is the oldest imaging technology on the market, but its importance is fading. Due to the measurement principle explained in the following, image resolution is very low, even if the resolution doubled recently (from 8 to 16 samples / 360°) and logging speed is far lower then provided by other imaging techniques. Nevertheless, density and porosity images, acquired by nuclear imaging tools, promise useful formation for enhanced formation evaluation.

5.3.1 Theory

The term nuclear measurement denotes not a single measurement but comprises different approaches using atomic particles (e.g. neutron) or radiation emitted by the decay of radioactive material or quantum mechanical processes (e.g. gamma radiation). Therefore, theory for each common nuclear measurement is described separately in the following chapters.

5.3.1.1 Gamma ray

Natural γ-radiation is caused by spontaneous decay of instable nuclei. Depending on occurring type of core reaction, α-, β- or γ-radiation is emitted. Primarily sources for gamma ray emission are daughter isotopes of the radioactive decay of uranium-238 and thorium-232 and radioactive potassium-40 [Telford et al., 2001]. These three radioactive elements are mainly accumulated in biomass deposited in rocks (U, Th) and shale respectively clay (K). Generally, radioactivity with γ-radiation is strongest in sediments, in metamorphic rock already narrowed and weakest in magmatic rocks [Jetschny, 2003].

Emitted gamma ray particles (quanta) are moving at speed of light and energy of one particle depends on its oscillation frequency. The lower the energy of a γ-quantum the lower is its frequency and therefore higher its wavelength (Equation 15).

Equation 15
$$E = h \cdot f$$
$$c = \lambda \cdot f$$

with

- E = energy of gamma quantum
- h = Plank constant
- f = frequency
- λ = wave length
- c = speed of light

Depending on gamma ray energy, different gamma ray interactions occur, when a gamma quant collides with an atom's core (also see Figure 20):

Energy of the gamma radiation	Dependence on atomic number Z (proportionality)	Interaction of gamma radiation with surrounding material	
		Notation	Description, if a γ-quantum collides with atom
>100 keV	Z^6	A) Photoelectric effect	γ-quantum transfers all its energy to an atom's electron being able to leave atomic shell and available as a free electron
75 keV – 2 MeV	Z	B) Compton effect	γ-quantum transfers only partial energy to an atom's electron (similar to an elastic impact) resulting in an emitted Compton-electron and deviated gamma quantum (with lower energy)
>1.2 MeV	Z^2	C) Pair production	γ-quantum is absorbed completely and an electron-positron-pair is emitted

Table 5 : Gamma ray interaction with material [Enyre, 1989; Telford et al., 2001]

Possible energy levels of a γ-quantum are not steady but discrete and each source (Th, U, K) posses characteristic discrete energy levels. Kalium-40 e.g. is mono-energetic, that means there is only one peak of 1.46 MeV in its energy spectrum. Measuring not only the count of gamma ray particles but also its energy (by a spectral gamma ray tool) provides information about the source and therefore the type of rock.

Besides the energy of the gamma ray quanta, the dependence of the mentioned interactions on electron density and therefore atomic number is very important, too. This fact allows density determination. Usually intensity of natural gamma radiation is too low for density measurement, so, an additional gamma ray source is used (gamma-gamma-density tool).
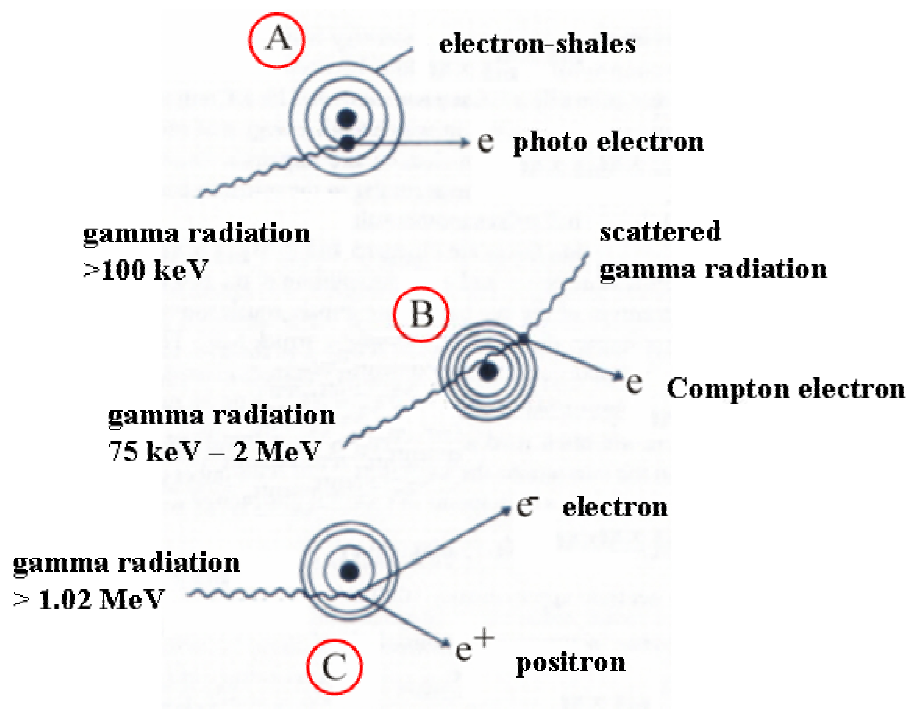
Figure 20 : Gamma ray interactions [Enyre, 1989]

As a summary following three types of gamma-ray-applications are possible (Table 6).

Tool notation	Benefit	Description
Natural gamma	Shale, clay and biomass determination within rock types	Measuring natural gamma radiation (counts of γ-quanta)
Spectral gamma	Assignment of gamma radiation to sources (U, Th, K), enhancement of natural gamma response	Measuring natural gamma radiation (counts and energy of γ-quanta)
Gamma-gamma-density	Density	Measuring natural and emitted gamma radiation (counts and energy of γ-quanta)

Table 6 : Gamma ray tools

5.3.1.2 Neutron

Quite similar to gamma ray measurements, basis for neutron measurements is the behavior of neutron within different materials. Therefore, some basics can be adopted from the previous chapter. High-energy neutrons (2-14 MeV) are emitted by a tool's radioactive source and invade formation. Within formation, neutrons collide with nuclei and depending on the impact angle, three different cases can be differed (also see Figure 21)[Enyre, 1989]:

- Central impact (impact angle is zero); neutron's energy is totally transferred to the nucleus (rarely occurring)
- Non central impact (impact angel is unequal zero); neutron transfers only partial energy to the nucleus, neutron's energy decreases (down to thermal level of <100eV) and neutron is deviated
- Impact of an already slowed down thermal neutron with neuron catcher (e.g. boron); neutron will be absorbed and a gamma quant is emitted

The more similar the mass of both colliding objects the more loss of energy increases. This is the case for neutron-proton collision and therefore ratio of energy loss (moderation) for fast neutrons is approximately proportional to density of protons. Because of consisting of only one proton in the nucleus hydrogen is most suitable for slowing down neutrons. It takes averagely 18 impacts to slow a neutron to thermal level, while there have to be 50 impacts for carbon, being the next common nucleus [Johnson et al., 2002]. Hydrogen occurs seldom elementary, but mostly bound in water or hydrocarbons. Water respectively hydrocarbons themselves fill the pore space within rocks. Therefore, neutron measurement is a porosity measurement, estimating all pores are filled with pore-fluid.

For porosity measurements, source-emitter distance becomes very important. The larger the distance, the higher the chance neutrons are getting scattered by hydrogen nuclei into formation or absorbed by a neutron catcher and therefore never reaching the detector. So, neutron log response with larger source-detector spacing is usually low, especially in high porous and water saturated rocks.
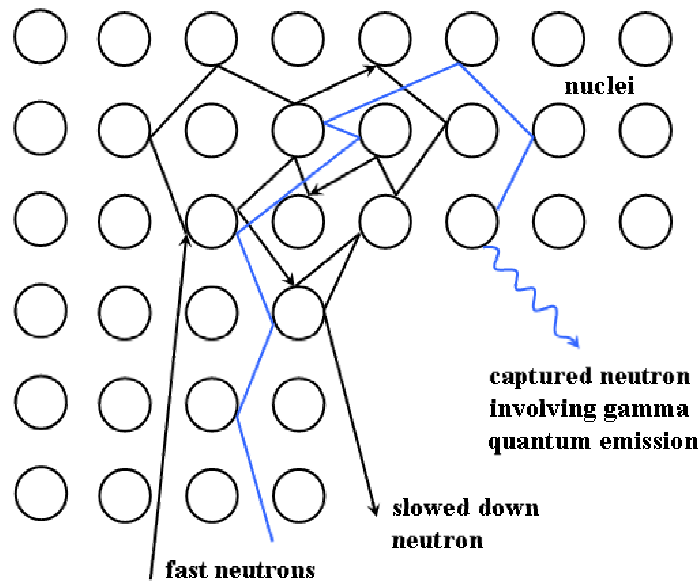
Figure 21 : Neutron moderation [Hallenburg, 1998]

5.3.2 Implementation

Exemplary for nuclear imaging tools the LWD advanced porosity logging service (APLS, also called azimuthal density imager) by BakerHughes Inc. is explained more detailed. The APLS tool comprises of three subs for each nuclear measurement method described in the previous chapter: natural gamma, density gamma (gamma-gamma density and spectral gamma) and neutron. The principle structure of such a sub is display in Figure 22. Both source and the two receivers are located beneath tool's surface joined by an isolated channel. This allows a focusing depending on the dihedral angle of the channel. Emitted particles leave the tool at a specific angle-range and only particles with a specific angle are enabled to enter tool's detectors. As a simplification, these focusing are drawn as different measurement beams in Figure 22. Therefore, the short space receiver is sensitive for mud while measurement response of the long space receiver covers mud and formation influence.

Note that focusing and bearing a nuclear source is valid only for density gamma and neutron measurements while the natural gamma sub manages in consequence of the measurement principle without any.
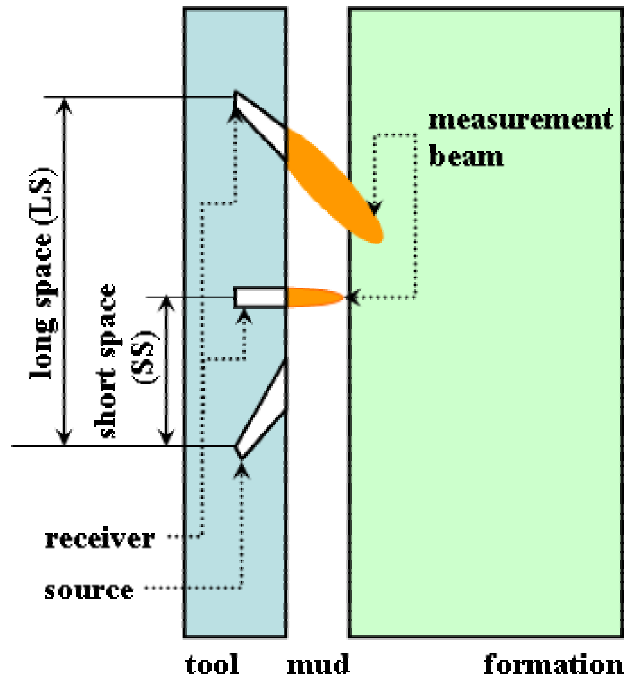
Figure 22 : Nuclear imaging tool sketch

According to the statements below e.g. for formation density determination using density gamma, a mud correction has to be applied. To explain measurement principle more detailed, following sections describe exemplarily density calculation from gamma count rate [Hassan, 2005].

Formation density is a function of both calculated density values from long-space (*LS*) and short-space (*SS*) receiver readings (sum for high mud density and difference for low mud weight):

Equation 16 $\qquad \rho = \rho_{LS} \pm f(\rho_{LS} - \rho_{SS}) = \rho_{LS} \pm \Delta\rho$

while ρ_{LS} and ρ_{SS} are calculated as follows:

Equation 17

$$\rho_{LS} = \frac{1}{\alpha} \cdot \log\frac{B}{CR_{LS}}$$

$$\rho_{SS} = \frac{1}{\alpha} \cdot \log\frac{B}{CR_{SS}}$$

with

- ρ = formation density
- ρ_{LS} = density calculated from long space (LS) receiver readings
- ρ_{SS} = density calculated from short space (SS) receiver readings
- α, B = tool specific parameters depending on tool design, standoff, source type, mud,… (determined by lab measurements)
- CR_{LS} = count rate read acquired form LS receiver
- CR_{SS} = count rate read acquired form SS receiver

$\Delta\rho$ itself is calculated by following equation:

Equation 18 $\Delta\rho = a \cdot (\rho_{LS} - \rho_{SS}) + b \cdot (\rho_{LS} - \rho_{SS})^2 + c \cdot (\rho_{LS} - \rho_{SS})^3$

with *a*, *b* and *c* are rock specific parameters determined by lab measurements. Therefore, nuclear measurements have to be calibrated. A quite similar procedure is applied for porosity determination by the help of neutron imaging sub. Just as the other imaging techniques nuclear images provides only relative values. Borehole environment and formation composition is too complicated to be described by just a few parameters determined in a lab.

While Baker Hughes Inteq introduced the APLS (advanced porosity logging service) [BakerHughes, 2003a] Schlumberger developed ADN (azimuthal density neutron) bearing besides neutron and density gamma an additional sensor for measuring photoelectric factor data[BakerHughes, 2003a].

5.3.3 Tools

A build up of information and specifications of nuclear LWD imaging tools looked up in Figure 97 in the Appendix B.

5.4 Brief comparison

It is almost impossible to give an objective ranking of imaging tools. Every kind of imaging tools has major advantages and disadvantages. Often it is a matter of the desired information and borehole environment that limits tool use and quality of acquired measurement data. In general, for each mud type (water-based / oil-based), but not for both logging techniques (wireline, LWD), there are acoustic, electric and nuclear imaging tools available. Up to now, there are electrical imaging tools for LWD and wireline, while a LWD acoustic and wireline nuclear imaging is not developed yet - due to either technical difficulties or missing necessity.

Usually electric images are preferred because of the high resolution in both water and oil-based mud providing many applications (see chapter 3) and electric resistivity offering a large measurement range (see Table 7). On the other side, electric imaging tools are comparatively new on the market and therefore expensive. So, acoustic images are often used as well, providing still excellent resolution and logging speed. Worst case for an acoustic imaging tool is the combination of heavy mud weight and large borehole and generally the tools are not used in these conditions.[BakerHughes, 2003a]. Even if nuclear imaging is a comparatively old technique, the measurement principle is limiting the tools resolution and logging speed to low values. Therefore, these imaging type features subordinate.

One of the main and maybe on of the most important difference between electric and acoustic imaging is the measuring method's rate of penetration. Electrical imaging tools measure electric properties of a volume element with a specified surface along the borehole wall and depth into formation. In opposite, acoustic imaging devices measure only surface but rock related properties. Therefore, surface texture features like fractures or borehole deformation (breakouts, washouts) should be displayed in an acoustic image more obvious, while electric image logs might emphasize lithological layers and boundaries better. To combine different measurement response and advantages with it, electrical and acoustic imaging tools are sometimes logged together. Even basic geomechanical analyses are possible, main application for nuclear images is lithology (dip) detection.

Imaging technology	Acoustic imaging	Electrical Imaging	Nuclear Imaging
Displayed physical unit	Amplitude of reflected wave	Resistivity	Density
Logging speed	up to 800 ft/hr	up to 1800 ft/hr	up to 150 ft / hr
Maximum horizontal (azimuthally) resolution	up to 250 samples / 360°	up to 192 samples / 360°	up to 16 samples / 360°
Availability	wireline	wireline + LWD	LWD

Table 7 : Imaging tool comparison (also see Figure 94 to Figure 96)

6 Interpretation of measurement results and GLCM methodology introduction

The most elaborate measurement technique is worthless without an appropriate display method in order extract the requested information. This chapter gives both a brief overview of present imaging display and interpretations methods and an introduction to the GLCM methodology as well.

6.1 State of the art in imaging processing business

Even if imaging tools are getting better and better there were only few improvements due to the actual measurement interpretations in the last years. Besides this, a lot of progress is done both according to corrections (tool speed, stand off) and post processing (filtering, interpolation) and methods were developed to avoid borehole, tool or measurement related artifacts [BakerHughes, 2003b]. The general procedure from acquired measurement data to measurement interpretation and state of the art in image processing business is (simplified) [Lofts et al., 1997; Ye et al., 1997; Contreras et al., 2003; Dymmock, 2003; BakerHughes, 2003b; Jetschny, 2004a]:

- different processing steps correcting drilling and logging related anomalies like tool speed, stand off (distance between measurement sensor and borehole wall), receiver shifting at multi receiver tools, …
- time-depth-correlation, because downhole tool electronic can only measure time but not correct depth
- image enhancement (filtering and tooth removal); if necessary interpolation of missing data
- static and dynamic normalization of log display
- structural dip calculation (manual, semi-manual, automatic)
- image artifacts recognition and if possible canceling (manual, semi-manual)
- extraction of geological features, facies identification (mainly manual)

The actual measurement interpretation (e.g. facies analysis, structural dip determination) is still performed by skilled human interpreters manually or by the help of semi-automatic software tool. This is natural for the interpretation results are usually basis for important and far-reaching decision due to potential new boreholes or the whole reservoir model. Hence, an automatic image log interpretation will not yet awhile replace human interpreters but can help save time and work or is a useful in situ and a priori interpretation.

Exemplarily static/dynamic normalization of electrical images and structural dip calculations from acoustic and pad-based images are described more detailed in the next two chapters.

6.1.1 Static/dynamic normalization of electrical image logs

Normalization is a common contrast enhancing procedure for imaging logs and the underlying idea is actually simple. It is all about the measurement range displayed in the image log. Instead of using the actual measurement resolution range (e.g. 0.2 – 2000 Ωm for the StarTrak™ tool), the minimum and maximum value occurring in a specific piece of the imaging log is picked. For the static normalization, this specific piece is the whole log and so, a minimum and maximum value is determined globally. Dynamic normalization uses a specific seized window covering the whole width and a specific length of the image, sliding over the image log and for each window minimum and maximum is picked locally for displaying of this image piece. This procedure allows local contrast enhancements and more structure is visible. In the static normalized image (Figure 23, right image) e.g. at depth 1400 – 1500 and depth 1700 – 1800 values are generally high and displayed by red color while the dynamic normalized data (Figure 23, left image) reveals more structure within the same depth interval. Therefore, by dynamic normalization relative contrast structures are gained while loosing absolute measurement value information.
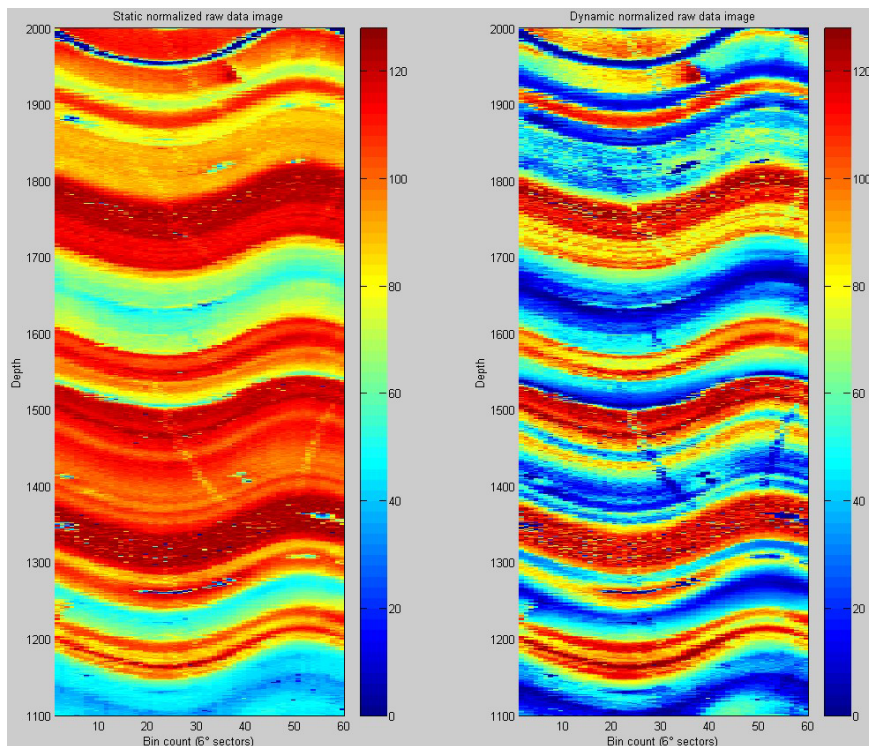
Figure 23 : Static and dynamic normalized raw data image (electric image log)

57

6.1.2 Dipex – statistical dip calculation approach

A different approach for automatic dip calculation is already available for internal use (Baker Hughes Incorporated) and implemented in an interactive dip computation, editing and interpretation system called Dipex. It processes image data for following imager types and uses a statistical approach, which is briefly described subsequently [Salafonov et al., 2004]:

Dual Imagers
- Simultaneous Acoustic and Resistivity Imager (Western Atlas), STAR

Resistivity Imagers (chapter 5.1)
- The Earth Imager (Baker Hughes)
- Formation Micro Scanner (Schlumberger), FMS
- Formation Micro Imager Tool (Schlumberger), FMI
- Electrical Micro Imaging Tool (Halliburton), EMI

Acoustic Imagers (chapter 0)
- Circumferential Borehole Imaging Log (Western Atlas), CBIL
- Ultrasonic Borehole Imager (Schlumberger), UBI
- Circumferential Acoustic Scanning Tool (Halliburton), CAST

Never mind which kind of imaging data is used for the automatic dip computation, the general procedure is the same. The measurement values are displayed in traces (e.g. acoustic traces; Figure 24) and according to chapter 3.1 and Figure 2 there is a typical sinusoidal curve along the time-shifted deflections of each trace when passing a sedimentological boundary. To determine the dip parameters (inclination and azimuth) the gradient curve is calculated for each trace. By varying azimuth and inclination within a user specified range, a correlation analysis is made. The best match for an assumed sinusoid according to the deflection of all traces is picked. A kind of correlation coefficient gives information about the quality of correlation between the assumed sinusoid and the deflections of each trace. So, only the best correlations are chosen. More detailed information referring to the Multi-channel Correlation algorithm can be found in the Appendix C, Figure 98. Data preparation and handling of Dipex is described in chapter 8.3.1.
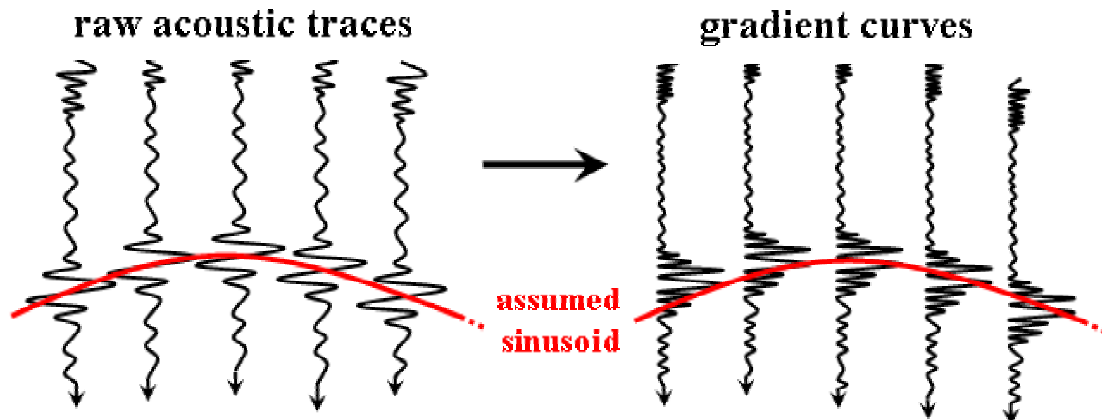
Figure 24 : Schematic trace correlation method used by Dipex

Several other automatic dip detection methods from borehole images have been proposed in literature, using

- edge matching for electric borehole images [Antoine et al., 1990]
- Hough Transform for acoustic [Torres et al., 1990] and electric images [Hall et al., 1996]
- edge matching and statistical analysis [Ye et al., 1997].

6.2 GLCM methodology

As already mentioned, human interpretation of acquired measurement data can be time consuming and expensive. Advances due to computer development offered possibilities to process this data in order to simplify manual interpretation or even extract geological features automatically. The *GLCM* as one possible basic approach is introduced in the following chapters.

6.2.1 Background

The here described methodology was first introduced by [Haralick et al., 1973] to extract textural features by using a gray-tone spatial-dependence matrix (*GTSDM*). These roots came from the arising processing of digital images. By searching of meaningful features for describing pictorial information spectral, textural and contextual features were found out to be three fundamental pattern elements used in human interpretation of color photographs. The attention of this thesis is focused on textural features describable e.g. as being fine, coarse or smooth, rippled, molled, irregular or lineated. For example in the humid tropics fine texture on radar images can be indicative of fine grained sedimentary rocks or sediments, a coarse texture for coarser grained sedimentary rocks, massive texture with high contrast for igneous rocks while hummocky texture can be characteristic of eroded igneous rock [Haralick et al., 1973].

In later literature the GTSDM is denoted gray level co-occurrence matrix (*GLCM*) and the methodology using this texture extraction was adopted for acoustic measurement like seismics, radar and sonar [Reed et al., 1989; Zhang et al., 1989; Gao et al., 1998]. This is natural for this kind of geophysical measurement is sampling wide areas and producing large images of measurement values. The methodology itself remains similar. Recent developments deal with the enhancement into the third dimension. [Gao, 2001; Gao, 2003] introduced the developed method of extracting structural features with the help of a voxel coupling matrix (*VCM*) – a by a additional dimension extended GLCM. This step takes into account, that "classical" 2D seismic measurements are being substituted by present 3D seismics. Up to now, the GLCM approach was primary used to describe rock texture and with it identify rock types.

Note that the term "texture attribute" is used differently for geological purposes. This may lead to confusions and therefore "texture attributes" are denoted "texel attributes" in this thesis.

6.2.2 Theory

Basis for the GLCM method is a 2D data matrix *M* filled with measured values *F(x,y)* (e.g. resistivity values) quantized to N_g discrete levels. A secondary matrix *G* (gray level co-occurrence matrix, *GLCM*) from which texel attributes are determined is calculated from this data matrix. First, a rectangular domain *T* (textural element, *texel*) T_x = 1,2,…N_x (horizontal spatial domain), T_y = 1,2…N_y (vertical spatial domain) is picked from *M*. Than this domain $T=T_x \times T_y$ is transformed into the GLCM $G = N_g \times N_g$ by defining *S(i,j)* $\in$ *G* is the total number of times a value *i* is directly neighbored by a value *j* (before and after value *i*). This procedure can be applied in different direction: horizontal, vertical or diagonal (see Figure 25). In other words, in a horizontal GLCM the number of times, a value *i* is neighbored horizontally by a value *j*, is counted and filled in *S(i,j)* [Haralick et al., 1973; Reed et al., 1989].
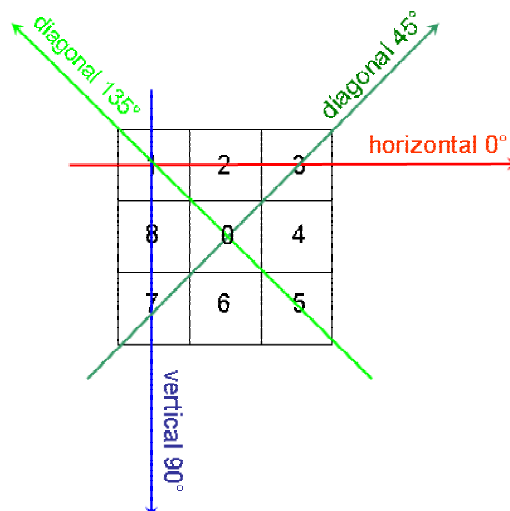
Figure 25 : Directions for evaluating a GLCM

As a simple example, if the selected texel *T* quantized to 4 discrete levels is given by

T(i,j)	1	2	3	4	5=Nx
1	1	1	2	3	3
2	1	2	2	3	4
3	2	3	3	4	4
4	1	2	4	4	4
5=Ny	1	1	3	3	3

Table 8 : Texel *T*

and the GLCM is to be evaluated in horizontal direction, then *G* would be

G(i,j)	1	2	3	4=Ng
1	4	3	2	0
2	3	2	3	1
3	2	3	8	2
4=Ng	0	1	2	6

Table 9 : Gray level co-occurrence matrix (GLCM) *G*

For a better understanding, some single calculation steps are given as follows: according to $G(1,1)$ the value "1" neighbored by "1" occurs 4 times, that means in detail $T(1,1) \rightarrow T(2,1)$; $T(2,1) \rightarrow T(1,1)$; $T(1,5) \rightarrow T(2,5)$ and $T(2,5) \rightarrow T(1,5)$ and according to $G(2,3)$ the value "2" neighbored by "3" occurs 3 times namely $T(3,1) \rightarrow T(4,1)$; $T(3,2) \rightarrow T(4,2)$ and $T(1,3) \rightarrow T(2,3)$. The residual values $G(i,j)$ are determined the same way. As can be seen, the evaluated matrix G is symmetric according to the diagonal (upper left to lower right corner).

Now the basis for calculating texel attributes is given. One of the important and easy to handle attribute is angular second moment, ASM (also called homogeneity) and defined as [Haralick et al., 1973]:

Equation 19
$$ASM = \sum_{i=1}^{N_g} \sum_{j=1}^{N_g} \left[\frac{S(i,j)}{R} \right]^2$$

with

- N_g = number of discrete value levels
- $S(i,j)$ = element of *G* determined by row *i* and column *j*
- R = normalization factor, total number of possible times of co-occurrence

Normalization factor *R* itself is depending on the direction *G* is evaluated and can be calculated by [Gao, 2003]

Equation 20 :
$$R_x = 2(N_x - 1)N_y \qquad \text{horizontal}$$
$$R_y = 2 \cdot N_x \cdot (N_y - 1) \qquad \text{vertical}$$

Following table gives another simple example for calculating the texel attribute Homogeneity (ASM) for a given texel in dependence of evaluation direction (horizontal, vertical, diagonal):

Texel

2	3	2	3
2	3	2	3
2	3	2	3
2	3	2	3

GLCM horizontal

0	0	0	0
0	0	8	0
0	8	0	0
0	0	0	0

GLCM vertical

0	0	0	0
0	12	0	0
0	0	12	0
0	0	0	0

GLCM diagonal

0	0	0	0
0	0	9	0
0	9	0	0
0	0	0	0

$$ASM = \left(\frac{8}{24}\right)^2 + \left(\frac{8}{24}\right)^2 \approx 0.222 \qquad ASM = \left(\frac{12}{24}\right)^2 + \left(\frac{12}{24}\right)^2 = 0.5 \qquad ASM = \left(\frac{9}{24}\right)^2 + \left(\frac{9}{24}\right)^2 = 0.28$$

Table 10 : Calculation example for texel attribute ASM

It is obvious that building a GLCM of a given texel and furthermore calculating a texel attribute is strongly depending on the evaluated direction. In vertical direction Homogeneity (ASM) is 0.5 and therefore relatively high while the horizontal and diagonal direction indicates a much lower homogeneity by ASM being approximately 0.222 respectively 0.28. In other words, the given texel is more homogeneous in vertical than in horizontal or diagonal direction.

Totally, there are 14 texel attributes calculable from a texel (Appendix C, Table 18) and being more or less correlating with each other [Haralick et al., 1973], three also important ones are

Contrast $$CON = \sum_{n=0}^{N_g-1} n^2 \left[\sum_{i=1}^{N_g} \sum_{j=1}^{N_g} {}_{|i-j|=n} \frac{S(i,j)}{R} \right]$$

Equation 21 Inverse difference moment $$IDM = \sum_{i=1}^{N_g} \sum_{j=1}^{N_g} \frac{S(i,j)}{R \cdot \left[1 + (i-j)^2\right]}$$

Entropy (randomness) $$ENT = -\sum_{i=1}^{N_g} \sum_{j=1}^{N_g} \frac{S(i,j)}{R} \cdot \log\left(\frac{S(i,j)}{R}\right)$$

[Gao et al., 1998] researched six important of the 14 texel attributes with respect to their correlation with each others. It was indicated that these attributes are correlated to varying degrees. Mathematical computations showed that angular second moment (*ASM*), contrast (*CON*) and inverse difference moment (*IDM*) explain approximately 92% of the variance according to seismic data and therefore these three components will explain most of the texel variations without losing much information. In the course of this thesis, it will be checked to which degree this statement can be transferred to imaging data basis.

7 Investigations on the GLCM method

For basic test of the method using a GLCM matrix and extracting texel attributes, three small programs were contrived in MatLab. One of them (*sycreate.m*) can create synthetic data due to specific guidelines and store this data into a textfile. The format of the stored synthetic data is geared to prototype StarTrak™ data (see chapter 5.1.3). In horizontal direction, the file comprises 60 data values representing the 60 bins measured by the prototype StarTrak™ [Holupirek, 2004; Jetschny, 2004a]. The length of the file representing the depth is variable but here fixed to 90 rows. So, the created synthetic data represents full 360° data acquired above a depth interval of 1.6 feet (≈0.5 m) at a constant rate of penetration (*ROP*) of approximately 160 ft/hr and more the 120 rotation per minute (*RPM*) (see chapter 7.1 and [Holupirek, 2004]).

The second program (*texelattrib.m*) read the stored file and calculates the GLCM and texel attributes by sliding the texel window (e.g. 10×10) within the data matrix by a defined step size starting with the $G(1,1)$ and ending at $G(80,60)$. Exemplarily, in Figure 26 a step size of "1" both in horizontal and vertical direction is used. Note that due to the unfolding of the borehole tube to a rectangle it is valid to take the first 9 entries into account by calculating the attribute of the texel with the upper left corner equal to G(x,60) (see Figure 26 rightmost). Finally, the third program (*syndisplay.m*) displays the resulting attribute images.
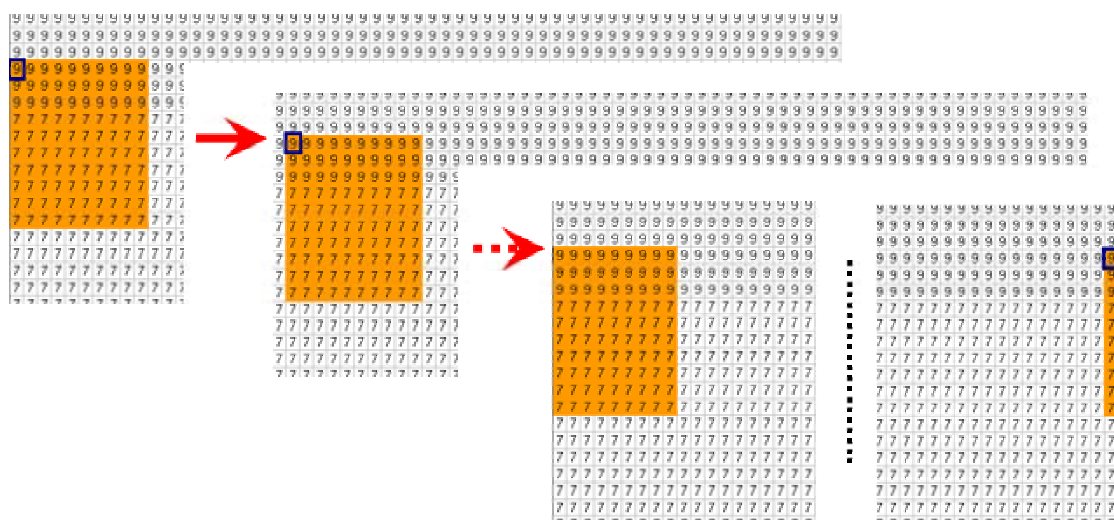
Figure 26 : Sliding texel window within data matrix

These three programs enable first basic tests using texel attributes extracted from synthetic resistivity data. Furthermore, it will be investigated how different texel attributes, texel sizes, texel shapes and the evaluation direction for calculating a GLCM interact with specified synthetic models. Note that even if investigation of size of the GLCM is a primary gage it will be investigates foremost in chapter 8.2.2. For further investigations GLCM size remains constant (16×16; N_g=16), that means possible entries in G range from "1" to "16".

7.1 Scaling consideration

To be able to reproduce the dimension of synthetic structures and geological features, some short scaling comments are given here. As already mentioned, the created synthetic data in the source matrix is geared to a typical StarTrak™ prototype image. Therefore, there are 60 synthetic measurement values per row in the source data matrix representing StarTrak™'s azimuthally resolution of 6°. That means, in an 8.5" (21.6 cm) hole one bin respectively 6° (each column) covers a 0.45" (1.1 cm) wide stripe of the borehole (6°/360° · π · 8,5"). A whole set of 60 bins covers a circumference of 26.7" (67.8 cm) in an 8.5" hole. The information for the vertical scaling conversion is extracted from a piece of a StarTrak™ image log acquired at the Baker Hughes Experimental Test Area (BETA), in Beggs, Oklahoma. At an assumed tool's rate of penetration of approximately 160 feet/hour and more than 120 RPM every ≈0.6 seconds a set of 60 measurement values per 360° of the borehole is acquired. By adding a time-depth correlation, 0.6 seconds respectively each row in the source data matrix represents a 0.21" (0.5 cm) section in vertical direction of the borehole.Putting the mentioned scaling conversions together one cell in the source data matrix comprises 0.45"×0.21" (1.1 cm × 0.5 cm) of the borehole. A few conversions can be looked up in Table 19.

7.2 Attribute image

Only a single value for a texel attribute is calculated from a given piece of the source image matrix (texel). Therefore, source image and attribute image will differ due to their dimension depending mainly on chosen texel size (see chapter 7.5) and step size (see chapter 7.4). Figure 27 displays step size, texel size and the position of the calculated texel attribute in the attribute image. As an example, a texel size of 9×9 (N_x×N_y) is chosen comprising 81 values in the source image (blue box). This is the underlying basis for creating the GLCM and calculating the texel attribute (blue number). Because of representing information of all 81 source values, the texture attribute is located in the middle of the box and there is an apparent offset of "4" (in general: [N_x-1]/2) in the attribute image to the top and side. The offset in horizontal direction can be compensated as already mentioned in chapter 7 (also see Figure 26) while the offset in vertical direction (both at the top and the bottom of the image) remains.

By sliding the texel window within source image to a specified step size – here a step size of "3" is chosen (red box) – another texel attribute will be calculated. The smaller the step size the smaller the apparent separation between two texel attributes. The maximum number of attributes can be calculated is achieved by a choosing a texel size of 2×2 and a step size of "1". These settings keep resolution of the source image as well as increase calculation expense. Minimum is represented by a texel covering the whole width (60 bins) and length (90 rows). So, only one attribute value would be calculated from the image piece.
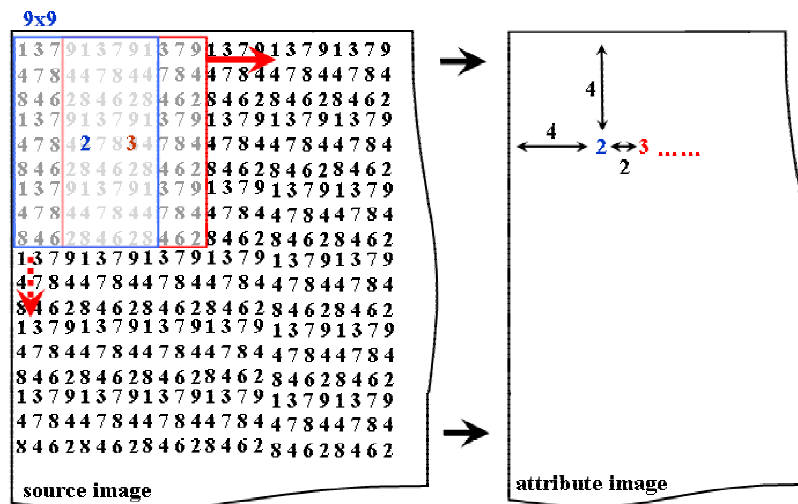
Figure 27 : From source to attribute image

7.3 *Influence of evaluation direction*

According to Figure 25, evaluation of a GLCM can be performed in different directions: horizontal (0°), vertical (90°) and diagonal (45° and 135°). For investigation regarding to evaluation direction, a synthetic model with horizontal and vertical layers and varying contrasts is chosen (Figure 28). The model consists of 90 rows (lines) each filled with 60 values (bins) ranging from "3" to "11". This format results in a attribute image of the same dimensions (minus boundary offset, see previous chapter) and remains constant for every model used in this chapter when not mentioned differently. The texel window is 10×10 bins (4.45"×2.13" respectively 11.3 cm × 5.4 cm), step size is "1" and exemplarily only the Contrast attribute images were calculated. Response images for the four possible evaluation directions are displayed in Figure 29 (A-D), additionally the difference image of horizontal and vertical evaluation is added (E). Contrast values range from "0" to "2".
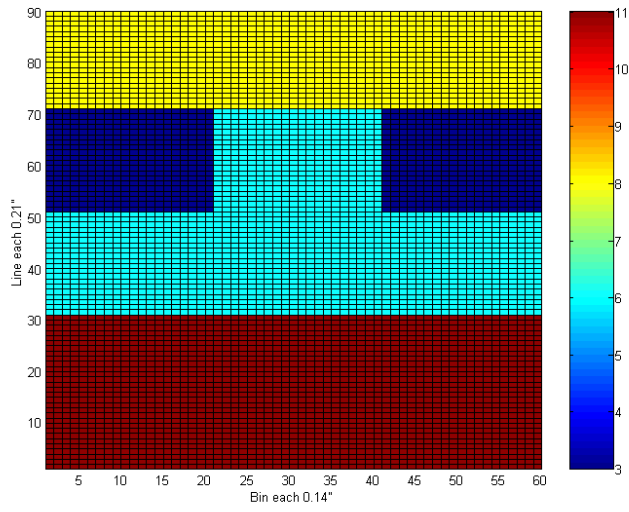
Figure 28 : Synthetic model with horizontal and vertical structures
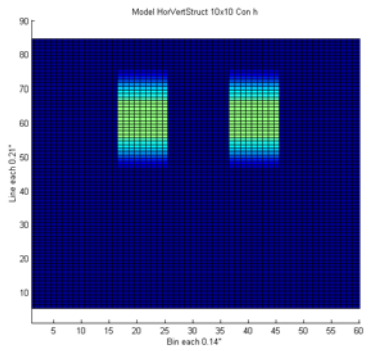
A) horizontal evaluation (0°)
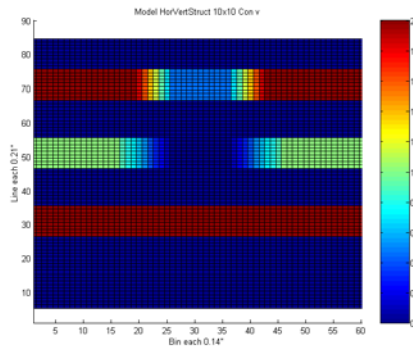
B) vertical evaluation (90°)
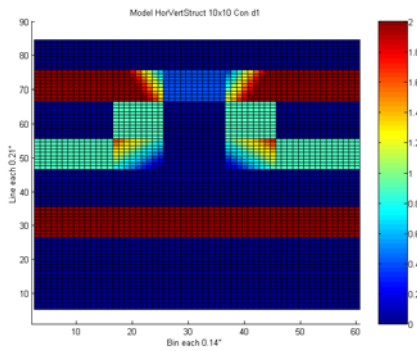
C) diagonal evaluation (135°)
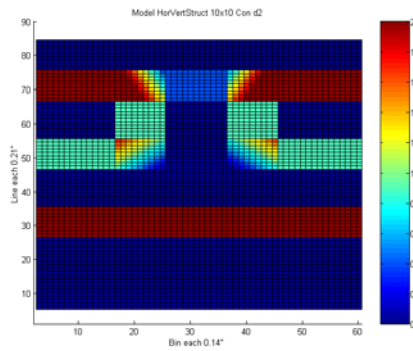
D) diagonal evaluation (45°)
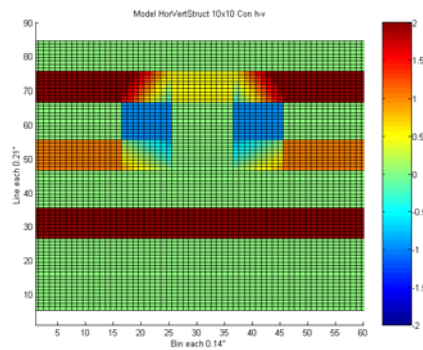
E) difference image horizontal-vertical

Figure 29 : Synthetic model response due to evaluation direction

It is obvious that orientation of structure and its appearance in the attribute image is strongly depending on evaluation direction. Texel attribute Contrast is most suitable for illustrating (see Equation 21 and chapter 7.8.4), because this attribute recognizes only contrast changes within each direction. E.g., texel window covering a horizontal structure (e.g., along change from aqua to maroon at depth line 30 in Figure 28; so, each texel row is filled with equal values) results in a Contrast attribute of zero when evaluating the GLCM in horizontal direction. Only evaluation of the GLCM in vertical or diagonal direction will detect this horizontal structure. This can be reproduced by the attribute images A and B in Figure 29. In the vertical evaluated attribute image (B) the horizontal borders of the synthetic model (Figure 28, line 30, 50 and 70) are expressed correctly, while the vertical borders (at Bin 20 and 40 in the depth interval 50-70) are missing. The other way round, this applies to the horizontal evaluated image (A) also. Foremost, drawing the difference image of horizontal and vertical evaluated image (E) results in all borders are reproduced correctly.

Instead of evaluating the GLCM in both horizontal and vertical direction, diagonal evaluations results in nearly equal response. This is natural for a diagonal can be considered as a vector sum of a horizontal and a vertical and therefore being sensitive to horizontal and vertical structures. Note that model response for both diagonals is approximately equal. Only at differently oriented diagonal structures, the two kinds of diagonal evaluations will differ.

67

7.4 Influence of step size

For determining the influence of step size the same model of chapter 7.3 is applied, but only the vertical evaluated attribute image is used. The texel size is still 10×10 and the Contrast attribute is drawn in the response images (Figure 30). As already explained in chapter 7.2 and Figure 27, step size is a gage how much two sequenced texel window are overlapping in horizontal or vertical direction. A low step size (minimum=1) increases resolution, a high step size (maximum=60) decreases calculating time. If calculating time plays no important role, a step size of "1" should be preferred. Step size of "2" and "3" may represent a good compromise on resolution and computing time. A larger step size rather results in a small geological feature (chapter 3) taken into account by only one texel window. The next texel will skip the feature und so determining of size, shape and kind of this feature is hardly possible. To give an example, a 4" (≈10 cm) wide geological feature is effecting nine bins and in the worst case will be recognized by only on 10×10 texel window at a step size of "10". At a step size of "5" the same feature will occur in two texel windows, at a step size of "1" in 10 texels.

A) step size 1   B) step size 3
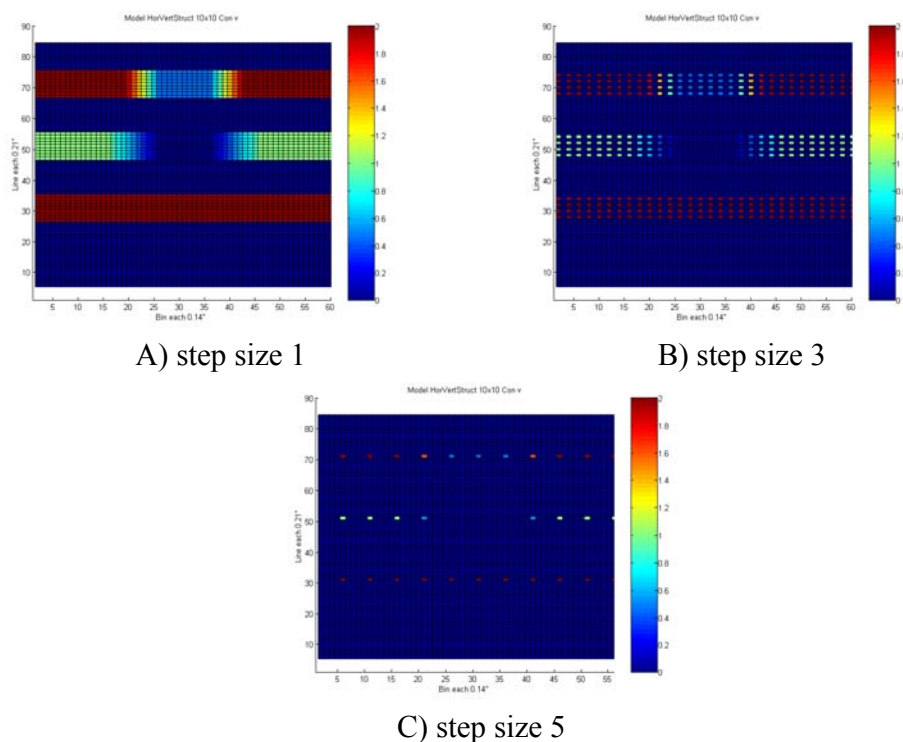
C) step size 5

Figure 30 : Synthetic model response due to different step sizes in both vertical and horizontal direction

Note that is also possible to use different step sizes in horizontal and vertical direction (e.g. step size$_x$ = 1 and step size$_y$=5) to keep resolution in a specified direction while decreasing resolution in the other direction (also see 7.6). This can be useful for one dominant feature orientation. To achieve maximum resolution in every direction a step size of "1" is used in the further course of this thesis unless it is explicit mentioned differently.

7.5 Influence of texel size

To determine influence of the texel size for calculating GLCM and texel attributes another synthetic model goes into action (Figure 31). It consists of three vertical lines with varying width and emphasized by a value contrast of 1:10 (fracture: background). As a simplification, these structures can assume to be open fractures of low resistivity. The first fracture's width is five bins (≈2.2" / 5.7 cm), the other two fracture are each one bin (≈0.45" / 1.1 cm) wide separated by three bins (≈1.3" / 3.4 cm). Note that width of the first fracture and the set of the next two fractures including the separation is the same. By doing so, it can be checked whether it is possible to differ between a wider fracture and two thin fractures close together. Because of being sensitive to high contrast differences, the texel attribute Contrast was chosen (see chapter 7.8). The GLCM was evaluated only in horizontal direction respecting the vertical orientation of synthetic fractures (see Figure 25). The response due to varying texel size starting with a texel window of 2x2 ending with 10x10 is displayed in Figure 32. All attribute images are calculated with a constant step size of "1" both in horizontal and vertical direction.
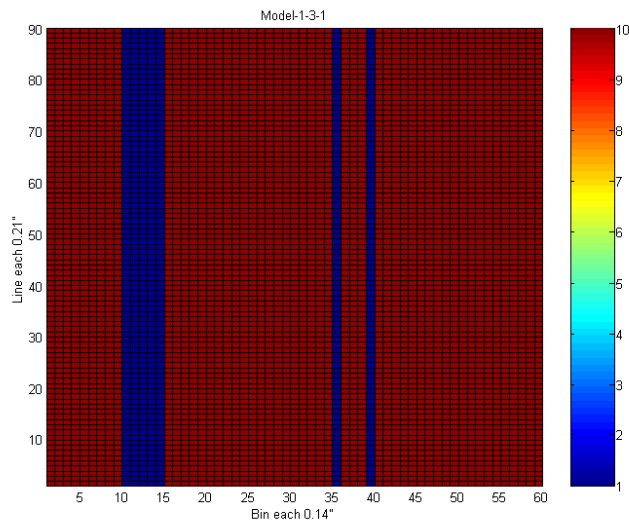
Figure 31 : Synthetic model with three assumed fractures

2x2   3x3   4x4

| 5x5 | 6x6 | 7x7 |
| 8x8 | 9x9 | 10x10 |
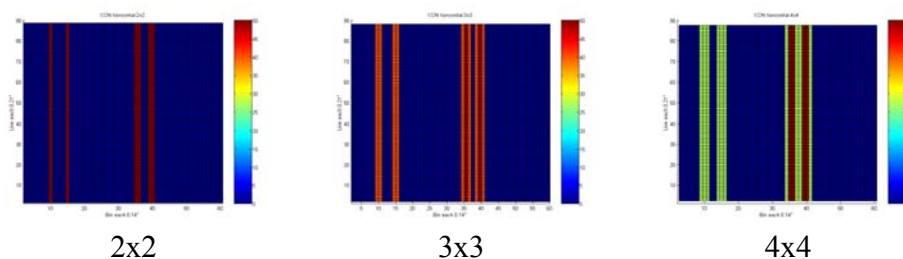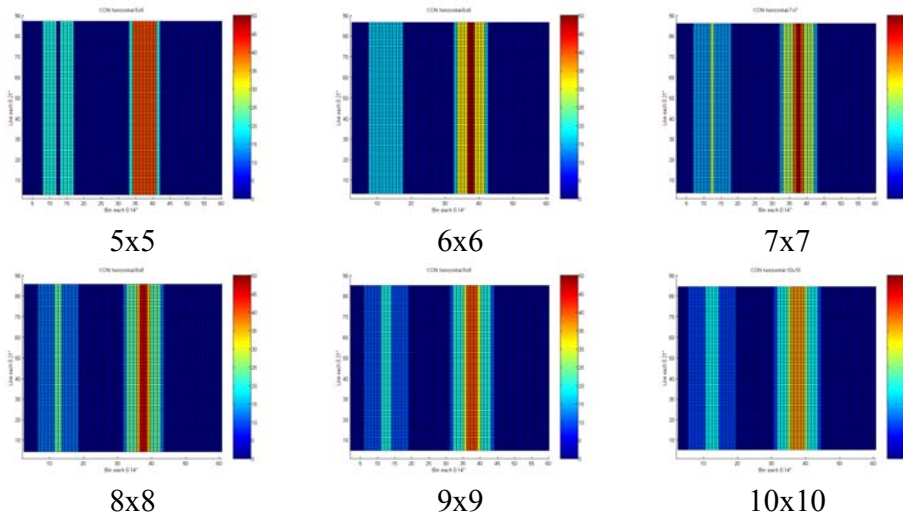
Figure 32 : Synthetic model response due to different different texel sizes

It is obvious that increasing texel size results in larger responding anomalies according to structures and features in the attribute image. E.g. a horizontal structure with a width of one bin (≈0.45" / 1.1 cm) and being investigated by a texel size of 5x5 (≈2.2"x 2.2" respectively 5.7 cm × 5.7 cm) will affect five successive texture attributes while a texel size of 10x10 will influence 10 successive texture attributes. In general, size of the anomaly in the attribute image can be estimated by following equation:

Equation 22 $SAI_{x/y} = SSI_{x/y} + N_{x/y} - 1$

with

- $SAI_{x/y}$ = size of the anomaly in the attribute image (in either horizontal or vertical direction)
- $SSI_{x/y}$ = size of the anomaly in source image (in either horizontal or vertical direction)
- $N_{x/y}$ = size of the texel window in either horizontal or vertical direction

By focusing on the wider fracture and its response in the calculated Contrast attribute images (Figure 32), two scenarios has to be differed: the texel size is smaller than (respectively equal to) to be investigated structure or larger. Regarding the first scenario following procedure takes place while texel window is sliding within source data matrix:

1) Texel window is in front of the structure resulting in a low Contrast attribute because of comprising only equal background values
2) Texel window enters structure and covers background as well as structure resulting in a high Contrast attribute
3) Texel window is within structure resulting in low Contrast attribute because of comprising only equal values of the structure
4) Texel window leaves structure and covers background as well as structure resulting in a high Contrast attribute
5) Texel window is in behind the structure resulting in a low Contrast attribute because of comprising only equal background values

This can be reproduced by Contrast attribute response of the five bin wide first fracture due to texel sizes ranging from 2x2 to 5x5: two sharp Contrast peaks are separated by a low Contrast. Two emphasize this, one row of each calculated Contrast image with varying texel sizes is displayed in Figure 33. Note that for clearer representation only even texel sizes are drawn. The dark blue and yellow line in the left part of the image shows the mentioned behavior of two high peaks.

Increasing texel size results in following procedure (texel size is larger than structure):

1) Texel window is in front of the structure resulting in a low Contrast attribute because of comprising only equal background values
2) Texel window enters structure and covers background as well as structure (first boundary: background $\rightarrow$ fracture) resulting in a high Contrast attribute
3) Texel window covers both boundaries (background $\rightarrow$ fracture and fracture $\rightarrow$ background) resulting in a Contrast attribute higher than 2)
4) Texel window proceeds within structure and covers only the second boundary (fracture $\rightarrow$ background) resulting in a high Contrast attribute equal to 2)
5) Texel window is in behind the structure resulting in a low Contrast attribute because of comprising only equal background values

The light blue and green line in the left part of Figure 33 reproduces this sequence: a high level of Contrast topped by a higher Contrast peak. The texel window 6x6 is a exception due to the five bin comprising fracture. It is obvious that a texel window with a six bin length won't be able to cover the background in front, the five bin wide structure and the background after the structure. Therefore, only a high level Contrast saddle occurs without a topping peak.
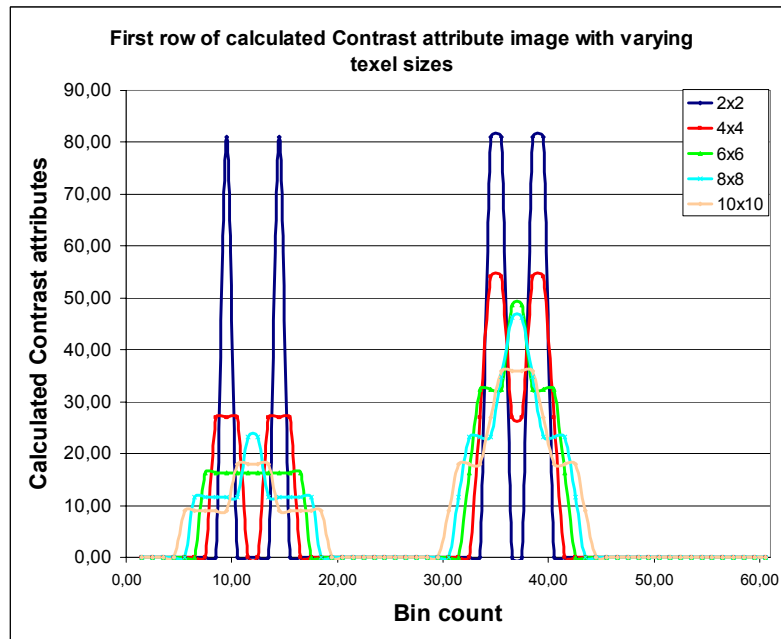
Figure 33 : First row of calculated Contrast attribute image with varying texel sizes

The response of the two separated fractures displayed in the right part of Figure 33 pose a more complicated extension of the just described scenario of texel windows cover a whole structure. Depending on texel size and number of covered background-structure boundaries different combinations of high Contrast saddles and peaks can occur.

7.6 Influence of texel shape

Varying the texel shape is a combination of different texel sizes. Therefore, this chapter is strongly related to the previous chapter. Up to now, a square texel size was used (e.g. 2×2 or 10×10), but it is also possible to vary texel dimension without keeping the ratio $T_x / T_y = 1$ (e.g. 5×2 or 10×5). This may be useful to emphasize resolution in one specified direction. As researched in the previous chapter, geologic feature size in an attribute image depends among others on texel size (Equation 22). Besides varying step sizes independently for horizontal and vertical direction, texel shape is another way to reduce calculation time without loosing much resolution, but just for the case of one dominant feature orientation.

The already used model in chapter 7.3 and 7.4 is basis for determining texel shape influence (Figure 34). The GLCM was evaluated in diagonal direction at a texel size of 10×10 to emphasize both horizontal and vertical structures (chapter 7.3), a step size of "1" for horizontal and vertical direction was used and the Contrast attribute was calculated for displaying response images (Figure 35).
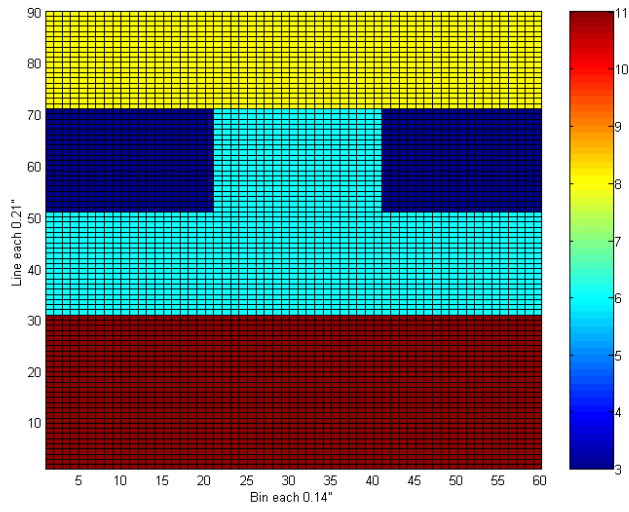
Figure 34 : Synthetic model with horizontal and vertical structures
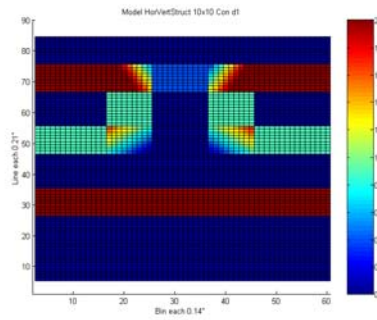
A) 10x10 (square)
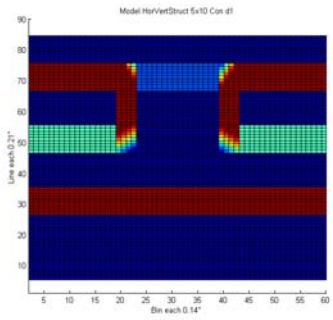
B) 5x10 (vertical rectangle)
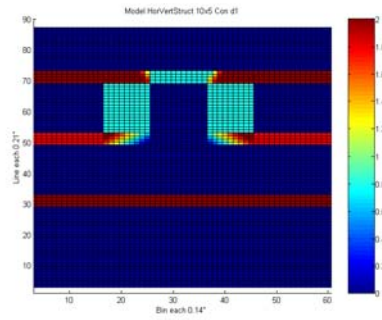
C) 10x5 (horizontal rectangle)
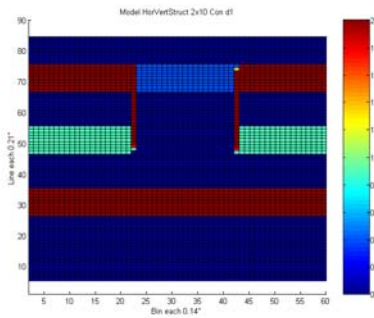
D) 2x10 (vertical rectangle)   E) 10x2 (horizontal rectangle)
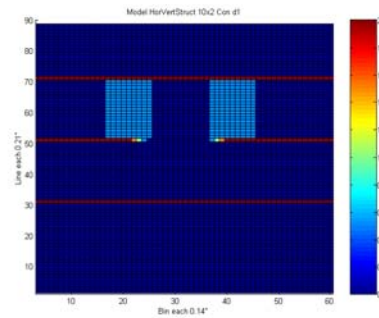
Figure 35 : Synthetic model response due to different texel shapes

Figure 35 (B-E) provides a quit similar conclusion than that of the previous chapter, only separated to horizontal or vertical direction. Decreasing of N_x (horizontal texel size) will result in sharper appearance of vertical structures in the attribute image and vice versa. The same happens to horizontal structures when decreasing N_y (vertical texel size).

7.7 Brief summary of influence gages

As shown during the previous chapters, there are many parameters influencing the attribute images without considering attribute characteristics. Therefore, some simple relations should be given here:

- Evaluation of the GLCM in diagonal direction considers both horizontal and vertical structures, while horizontal evaluation is only sensitive to vertical structures and vise versa
- the smaller the texel size the clearer the appearance of a feature respectively structure in the attribute image
- the larger the texel size the more stable the attribute image regarding the influence of noise
- increasing step size and texel window in one direction reduces calculation time without loosing to much information when there is a dominant orientation of the features respectively structures

For optimal attribute images calculated from synthetic models, following parameters seem to be favorable, but it remains to be seen, whether these parameters are suitable for acquired imaging data, too:

- evaluation direction : diagonal, vertical/horizontal at signalized feature orientation
- step size : "1" in both horizontal and vertical direction
- texel size : either 3×3 or 4×4
- texel shape : square, $T_x : T_y$ ratio equal to 1

7.8 Characteristics of texel attributes

For determining characteristics of texel attributes and especially the range in which the calculated attribute values are varying, two synthetic data models are used (Figure 36 and Figure 37). These two extremes (layered model without noise and a pure noise model of random distributed values) may help describing behavior of different texel attributes regarding different scenarios. To reduce the calculation time and the amount of displayed pictures the GLCM was evaluated in only horizontal direction. For all attribute images texel size 10×10 and step size "1" in both horizontal and vertical direction remains constant.
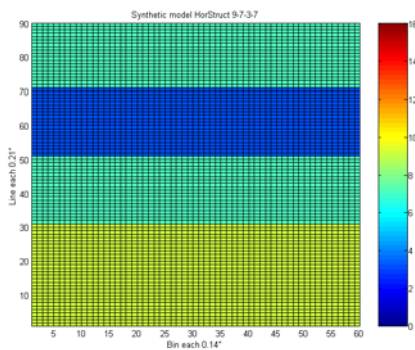
Figure 36 : Synthetic model with discrete horizontal layered levels (below to above : 9–7–3–7)
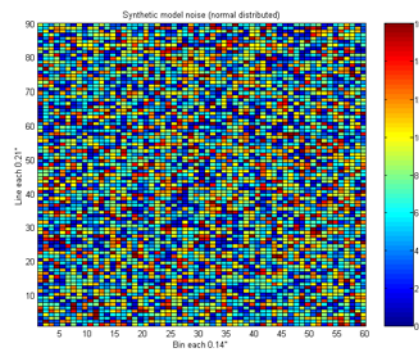
Figure 37 : Synthetic model with normal distributed numbers from 1-16

Besides the four texel attributes already mentioned in chapter 6.2.2 (Equation 19 and Equation 21), the original list of all 14 attributes [Haralick et al., 1973] (Appendix C, Table 18) was researched in order to find other attributes maybe suitable according to the main focuses of this thesis. Altogether, the following attributes have been chosen: Homogeneity/Angular Second Moment, Contrast, Correlation, Variance, Inverse Difference Moment and Entropy. A detailed investigation of the other eight texel attributes is foregone here, because some attributes are obviously enhancements of the six researched attributes (e.g. Sum Entropy and Difference Entropy -> Entropy; Appendix C, Table 18).

7.8.1 Homogeneity (*HOM*) / Angular Second Moment (*ASM*)

As the name already implies, Homogeneity (notation used in [Gao, 2003]) respectively Angular Second Moment (notation used in [Haralick et al., 1973]) is a gage how homogenous the given texel taken from the data matrix is. In other words, Homogeneity describes how much equal values neighboring each other are there in a texel.

According to Equation 19 this texel attribute can be calculated by

$$ASM = \sum_{i=1}^{N_g} \sum_{j=1}^{N_g} \left[\frac{S(i,j)}{R} \right]^2$$

and due to this formula minimum and maximum are determined by

Minimum   1/R;   all values in a texel are different; $R*(1/R)^2$
Maximum   1;   all values in a texel are equal; $1*(R/R)^2$

Note that Homogeneity is not sensitive to high or low contrasts at all; values in the texel must only differ to cause low Homogeneity. A synthetic model with two layers filled each with the same specified values will always result in the same homogeneity attribute even if the values per each layer are varying.

The response due to the two models (Figure 36 and Figure 37) is displayed in Figure 38 and Figure 39. The differences are quit obvious. The Homogeneity response of the noise free model is always "1" (dark red) within the layers, only when the texel window covers two different layers (at a synthetic sedimentological boundary) calculated Homogeneity decreases to a minimum of "0.5" (blue). Contrary to the noise free model response, Homogeneity attribute calculated from the noise model is always very low (0.0088-0.02) and therefore apparent Homogeneity-peak spots should not be overrated. Nevertheless, as can be seen e.g. below the upper left corner, there are still parts (yellow to red) where there Homogeneity is higher than in other parts of the texel attribute image, hardly recognizable in the original model image.
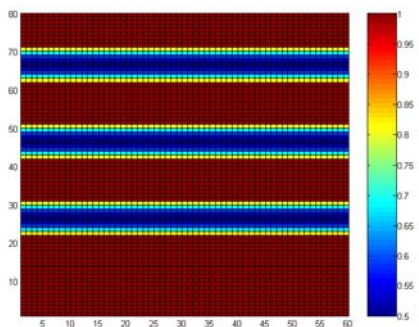
Figure 38 : Homogeneity response image of the noise free model
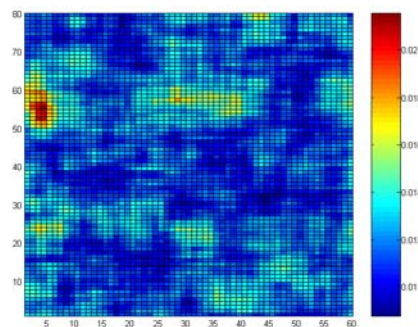
Figure 39 : Homogeneity response image of the noise model

7.8.2 Entropy (ENT) / Randomness (RAN)

Randomness (notation used in [Gao, 2003]) respectively Entropy (notation used in [Haralick et al., 1973]) is a gage to which degree values of a given texel taken from the data matrix are distributed randomly. According to Equation 21 this texel attribute can be calculated by

$$ENT = -\sum_{i=1}^{N_g}\sum_{j=1}^{N_g}\frac{S(i,j)}{R}\cdot\log\left(\frac{S(i,j)}{R}\right)$$

Therefore, Entropy behaves reverse to Homogeneity described in the previous chapter. If Homogeneity is high, Entropy will be low and vice versa. Chapter 7.9.1 will deal with correlation analyses of Entropy and Homogeneity. In general minimum and maximum are determined by

Minimum   0;   all values in a texel are equal 1*(R/R)*log(R/R)
Maximum   -log(1/R);   all values in a texel are different; R*1/R*log(1/R)

Model response displayed in Figure 40 and Figure 41 is quit similar to that of texel attribute Homogeneity, but reverse. This can be reproduced by the apparent Homogeneity peak spot below the upper left corner of Figure 39 resulting in an Entropy minimum in Figure 41. Entropy of the noise free model is zero (dark blue) when the underlying texel is absolutely homogenous and increases to approximately 0.7 at the layer boundaries (dark red). The noise model consisting of randomly distributed values shows on the other hand higher Entropy values up to 4.8 (dark red).
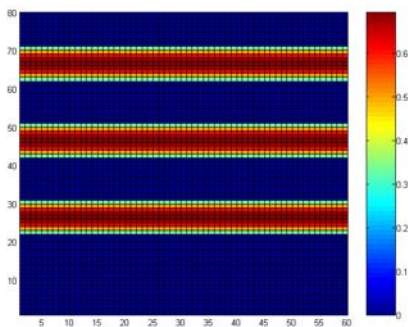
Figure 40 : Entropy response image of the noise free model
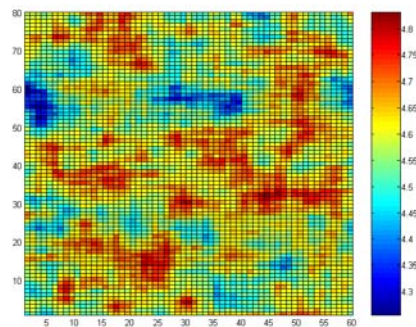
Figure 41 : Entropy response image of the noise model

7.8.3 Inverse Difference Moment (*IDM*)

The texel attribute Inverse Difference Moment (IDM) is in opposite to the texel attributes of Homogeneity and Entropy sensitive for occurring contrasts. Therefore, position of a co-occurrence entry in the GLCM towards to diagonal is taken into account, too. As a reminder, in the GLCM diagonal only values neighbored by equal values can be found. The farer away from the diagonal the lesser its contribution of a value in the GLCM to the IDM attribute. In a simple sense, entropy is an extension of Homogeneity by a contrast weighting. According to Equation 21 this texel attribute can be calculated by

$$IDM = \sum_{i=1}^{N_g} \sum_{j=1}^{N_g} \frac{S(i,j)}{R \cdot \left[1 + (i-j)^2 \right]}$$

and due to this formula minimum and maximum are determined by

Minimum: $1/(1+(N_g-1)^2)$;   lowest and highest values $\in N_g$ are alternating in a texel (only the upper right and lower left corner of the GLCM are filled); $C/(R*(1+(i-j)^2)$ with $C = S_{1,N_g} + S_{N_g,1} = R$ and therefore i-j=(N_g-1)

Maximum: 1;   all values in each texel-row (horizontal) respectively texel-column (vertical) are equal (only the diagonal in the GLCM is filled); $D/(R*(1+(i-j)^2))$ with $D = \sum_{i=j} S(i,j) = R$ and therefore i-j=0 and

By the help of this maximum and minimum consideration and chapter 7.3, it is understandable that horizontal evaluation of the GLCM is not suitable for calculating the IDM attribute according to a horizontal layered model. Each line is filled with the same values and therefore IDM of an evaluated GLCM will always be "1". Therefore, signal response of the noise free model is represented by the vertical evaluated attribute image (Figure 42) while the pure noise model is still evaluated in horizontal direction (Figure 43) to be comparable to the previous noise model response.

The IDM attribute image (Figure 42) for the layered model detects layer boundaries clearly and contrast dependent. The first boundary at depth line 30 between layer filled with values of "9" and layer filled with values of "7" results in an IDM attribute of approximately 0.92 while the both boundaries (depth line 50 and 70) between layer of "7" and "3" are emphasized by an IDM attribute of approximately 0.9. Note that only absolute contrasts between layers are taken into account. It does not matter whether texel window comprises border crossing from "7" to "3" (depth line 50) or "3" to "7" (depth line 70), both will result in the same IDM attribute value.

The response of the IDM attribute to the noise model (Figure 43) is similar to that of homogeneity. Due to the contrast weighting during the attribute calculation some Homogeneity-peak spots may be emphasized or attenuated (Homogeneity-peak spot below upper left corner and in the middle of the upper half).
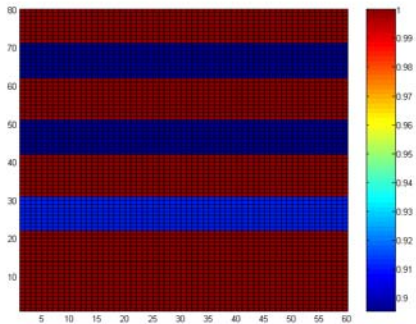
Figure 42 : IDM response image of the noise free model (vertical evaluation)
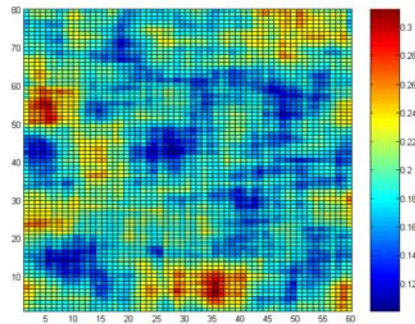
Figure 43 : IDM response image of the noise model (horizontal evaluation)

7.8.4 Contrast (*CON*)

Contrast is a texel attributes able to detect and quantifies assumed sedimentological boundaries and features, distinguishing themselves by a high contrast towards their surrounding. Contrast seems very similar but reverse to the IDM attribute. However, values in the texel neighbored by itself are not taken into account, that means the diagonal in the GLCM is cancelled. The farer the entries in the GLCM are located towards the diagonal the more they are emphasized. In other words, a bigger difference (contrast) between neighboring values in a texel results in a higher contrast value calculated for the texel. According to Equation 21 this texel attribute can be calculated by

$$CON = \sum_{n=0}^{N_g-1} n^2 \left[\sum_{i=1}^{N_g} \sum_{j=1}^{N_g} |i-j|=n \frac{S(i,j)}{R} \right]$$

and due to this formula minimum and maximum are determined by

Minimum: 0; all values in each texel-row (horizontal) respectively texel-column (vertical) are equal (only the diagonal in the GLCM is filled); $0 * \sum\sum S(i,j)$ with i-j=0

Maximum: $(N_g-1)^2$; lowest and highest values $\in N_g$ are alternating in a texel (only the upper right and lower left corner of the GLCM is filled); $n^2 * C/R$ with $C = S_{1,Ng} + S_{Ng,1} = R$ and n=(N_g-1)

The remarks given for model response of IDM are valid for the Contrast attribute, too. All values per each row in the noise free model are equal so no contrast is detected for horizontal evaluation and therefore attribute response is always zero. That is why noise free, layered model has been evaluated in vertical direction, too (Figure 44). Border crossings (depth line 30, 50 and 70) in the Contrast image for the noise free model are represented in the same way than the IDM attribute, but reverse. Only contrasts along layer boundaries result in high Contrast values. Both boundaries between the two layer of "7" and the layer of "3" are displayed by high Contrast values (≈1.8) while the boundary at depth line 30 with lower value-contrast results in a Contrast value of 0.6. The space between the boundaries without any contrast is represented by Contrast attribute values of zero. Figure 45 shows the calculated contrast attributes for the noise model being always very high (20 to 50). This is understandable for the model consisting of normal distributed values including more or less a contrast between each neighboring entry in the underlying model. Hence, apparent structures in the contrast image should not be overrated.
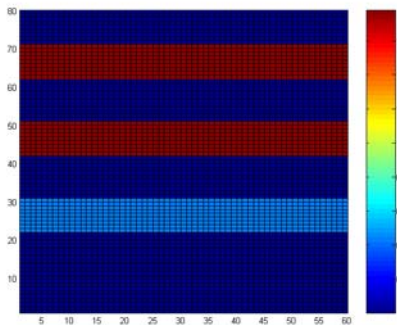
Figure 44 : Contrast response image of the noise free model (vertical evaluation)
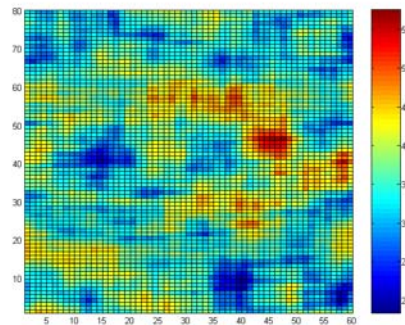
Figure 45 : Contrast response image of the noise model (horizontal evaluation)

7.8.5 Variance (Var)

Besides Contrast and Inverse Difference Moment, Variance is also a gage for contrasts within a texel. However, while the two already described attributes are providing absolute contrast information, Variance emphasizes only deviations of the texel values towards texel's mean value. That means, the larger the difference of a texel entry to the mean value of the whole texel, the more this value is emphasized. Values equal to the mean value are not taken into account. By the way, referring to texel's mean provides sensitivity of Variance according to both horizontal and vertical orientated structures. Therefore attribute image response of different evaluation directions for a GLCM will not differ that much.

Variance is calculated in the following way:

$$Var = \sum_{i=1}^{N_g} \sum_{j=1}^{N_g} (i - \mu)^2 \frac{S(i,j)}{R}$$

with texel's mean μ. Due to this formula minimum and maximum are determined by

Minimum: 0; all values in the texel are equal to texel's mean μ or located in the same column (same i) than texel's mean μ; $\sum\sum$ (i-μ)^2·S(i,j) with i-μ=0

Maximum: $((N_g+1)/2)^2$ Texel is filled with the same number of both the highest and lowest possible values (alternating or homogenous distributed), that means difference between all values and texel's mean value is always the same and maximal; $((N_g+1)/2)^2$*C/R with $C = \sum S(i,j) = R$ and $S(i,j) \in \left[1,\, N_g\right]$

Variance attribute image response for the horizontal layered and noise free model (Figure 46) looks familiar when comparing to IDM and Contrast image response. When texel window is covering an assumed lithological boundary a lot of values will more or less differ from texel's mean value and therefore Variance will be high. In opposite, Variance will be zero when texel window is comprising homogenous noise free values. All texel values are equal to texel's mean and will be cancelled. Image response for the noise model is also approximately the same than according to the Contrast attribute (Figure 45), even the Variance image seems to be more structured. However, it has to be kept in mind, that structures in the image response for the noise model are misleading. Only irregularities within the normal distributed noise are emphasized.
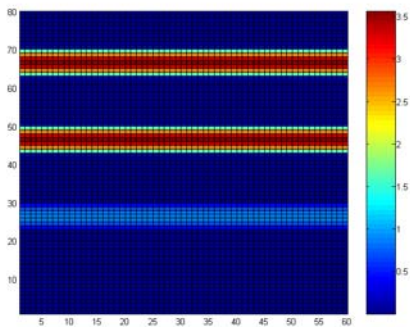
Figure 46 : Variance response image of the noise free model
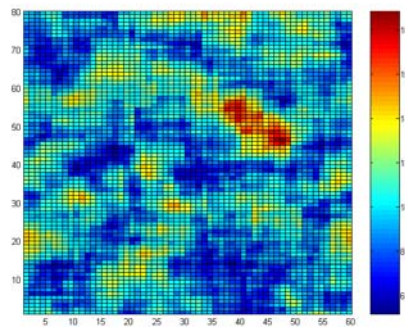
Figure 47 : Variance response image of the noise model

7.8.6 Correlation (Cor)

Texel attribute Correlation is similar to Variance; instead of texel's mean value the mean and standard deviation of texel's column respectively row sum (resulting in the vectors S_x and S_y) are taken into account. The more equal the values within the texel are, the smaller the standard deviation and therefore the higher the Correlation value. According to Equation 21 Correlation can be calculated by

$$Cor = \frac{\sum_{i=1}^{N_g}\sum_{j=1}^{N_g}(i \cdot j)\frac{S(i,j)}{R} - \mu_x\mu_y}{\sigma_x\sigma_y}$$

with

- μ_x = mean of S_x
- μ_y = mean of S_y
- σ_x = standard deviation of S_x
- σ_y = standard deviation of S_y

while S_x and S_y are vectors representing texel's column respectively row sum (also see Appendix C, Table 18) calculated in the following way

$$S_x = \sum_{i=1}^{N_g} S(:,i) \ \ and \ \ S_y = \sum_{i=1}^{N_g} S(i,:)$$

Minimum and maximum determination is difficult in comparison to the other attributes, because of considering of texel's mean and standard deviation. In general Correlation is negative, because product of mean μ_x and μ_y is greater than the product of normalized number of co-occurrence and row and column number ($S(i,j) \cdot (i \cdot j)$). The more similar the texel-values in either each column or row or just all values of S_x or S_y (column or row sum vector) the smaller gets the standard deviation σ_y or σ_x and with it the Correlation attribute. When standard deviation is zero and even division by zero results in infinity, per definition Correlation is set to "0". Therefore, maximum Correlation is actually below "0" for a texel rich in contrast and minimum is above "-∞" for a homogenous texel. Unfortunately, Correlation is not unique. It was found out that at least two constructed texel examples shown in Table 11 break the uniqueness. Both 3×3 texel are very different but both result in the same Correlation. Generally, both texel scenarios should not occur so often in real acquired imaging data.

(i,j)	1	2	$N_x=3$
1	1	4	3
2	2	5	1
$N_y=3$	2	3	3

$S_y = (8,8,8)$ $S_x = (5,12,7)$
$\mu_y = 8$ $\mu_x = 8$
$\sigma_y = 0$ $\sigma_x = 3,6056$
Correlation = 0

(i,j)	1	2	$N_x=3$
1	2	2	2
2	2	2	2
$N_y=3$	4	4	4

$S_y = (6,6,12)$ $S_x = (8,8,8)$
$\mu_y = 8$ $\mu_x = 8$
$\sigma_y = 0$ $\sigma_x = 0$
Correlation = 0

Table 11 : 3×3 texel example and Correlation calculation

Minimum and maximum Correlation can be reproduced by attribute response according to the noise free (Figure 48) and noise model (Figure 49). Within the layered noise free model, at least the row or column sum vector consist of equal entries and therefore Correlation is "0" all the time. Correlation attribute value regarding the noise model range between -2000 and -16.000 indicating a varying standard deviation, but besides some spots of very low values (-16.000), Correlation is always relatively high (-2000).
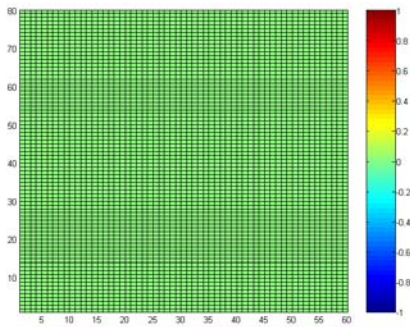
Figure 48 : Correlation response image of the noise free model
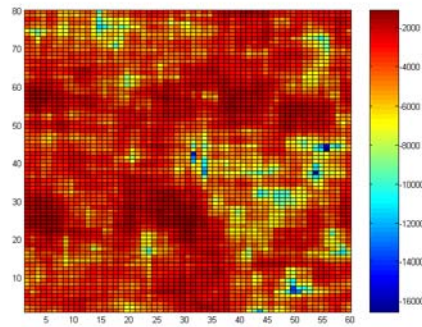
Figure 49 : Correlation response image of the noise model

7.9 Correlations between texel attributes

Some texel attributes behave quite similar but oppositional to one and the same model or are similar according to their equations; namely Homogeneity vs. Entropy, Contrast vs. IDM and Variance vs. Correlation. Therefore, a correlation analysis is made here using texel attribute response due to the same model with different amount of applied relative noise (10% and 90%, Figure 50). From each attribute image, the 60th row was extracted and cross-plotted (e.g. 60th line of Homogeneity image versus 60th line of the Entropy image).

The term "Noise" can be ambiguously, so it should be briefly elaborate how noise was applied here. During the course of this thesis, two different kind of synthetic noise has to be differed:

- relative noise; depends on the actual input value. A specified percentage (10% - 90%) of the input value is used for the standard deviation (STD) determining the range of the normal distributed output value (Figure 51). 20% relative noise regarding a value of "10" means the random distributed output value ranges from "9" to "11", while 90% relative noise results in an output range of "5.5" – "14.5". This procedure is applied to each value of the input matrix.
- absolute noise; depends not on actual output value. A matrix of the same size than the input matrix is filled with normal distributed values with a specified range (e.g. "1" – "2") and added to the input matrix.

Note that after applying noise, each value is rounded to the next whole-numbered value in order to keep discretization. Relative noise influences mostly high values, while low values are less affected. 90% relative noise towards a value "2" results in a rounded output range of 2±1, 90% applied to a value "12" to a rounded range of 12±5. On the other hand, absolute noise affects low and high values likewise.

Figure 50 : Models for attribute correlation analysis at 10% (left) and 90% noise (right)

Figure 51 : Normal distributed noise scheme
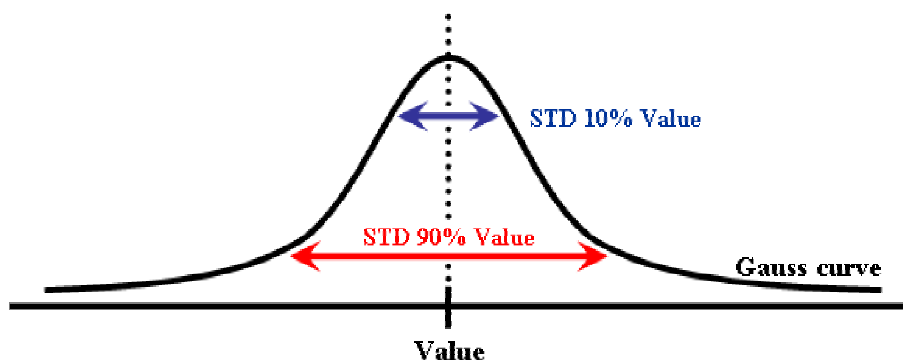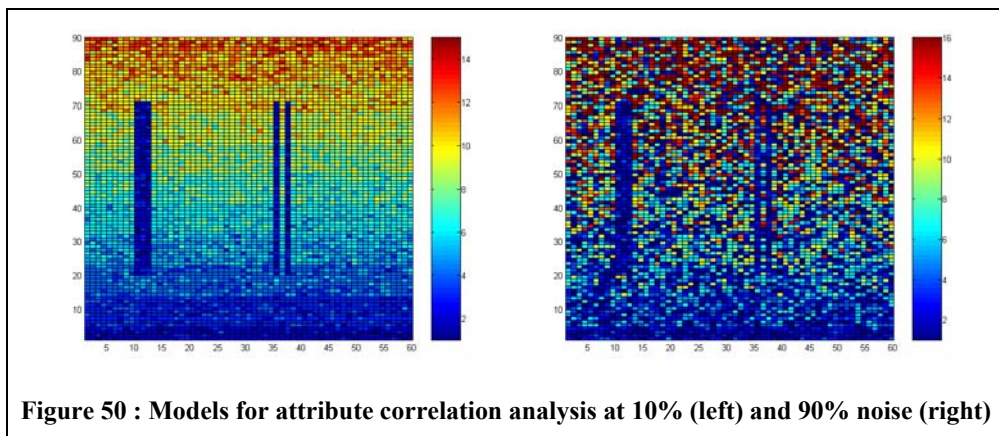
7.9.1 Homogeneity versus Entropy

Cross plots for Homogeneity versus Entropy are displayed in Figure 52 (10% noise – low noise model) and Figure 53 (90% noise – high noise model). It is obvious that there is not only the trend but also a very good correlation between Homogeneity and Entropy according to the correlation coefficient R. For both cross plots R is about 0,9 and therefore Homogeneity can be calculated from Entropy (and vice versa) without loosing much information. For further investigations, it may enough to consider just one of these two texel attributes instead of both.
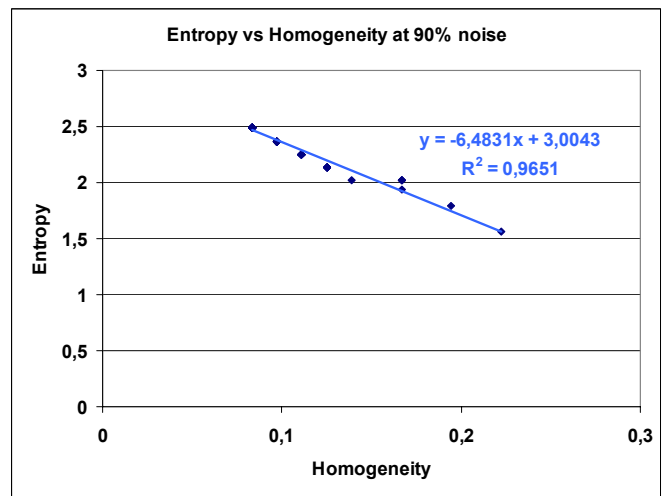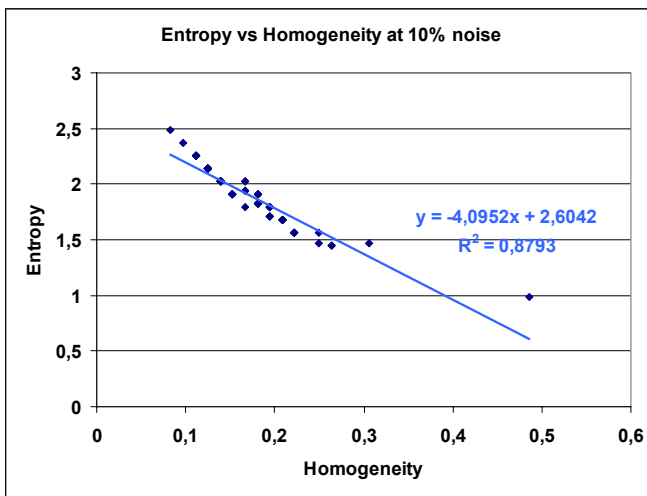
Figure 52 : Homogeneity vs. Entropy for a low-noise model **Figure 53 : Homogeneity vs. Entropy for high-noise model**

7.9.2 Inverse Difference Moment versus Contrast

Cross plots of IDM versus Contrast in Figure 54 (10% noise – low noise model) and Figure 55 (90% noise – high noise model) visualize differences in comparison to the Entropy versus Homogeneity plots. A general trend is visible for both plots but the correlation coefficient R is low (blue trend line), especially for the high noise model. After neglecting some outliers, the trend for the 10% noise model is slightly better, but still to low for a good correlation (red trend line). Therefore, IDM and Contrast attribute are so far independent even when the general behavior is similar.
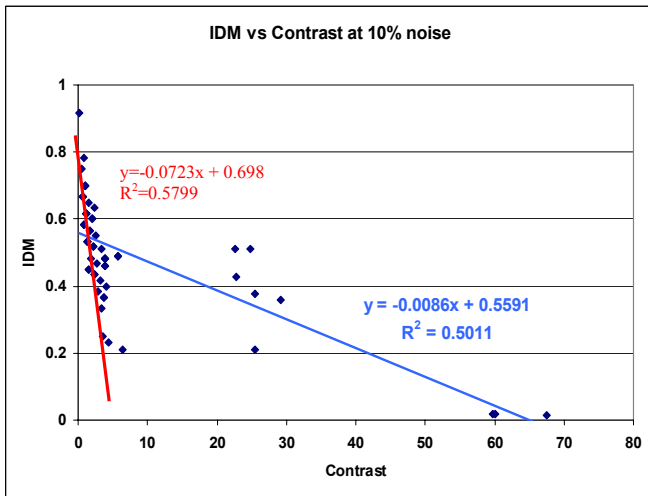
Figure 54 : IDM vs. Contrast for a low-noise model
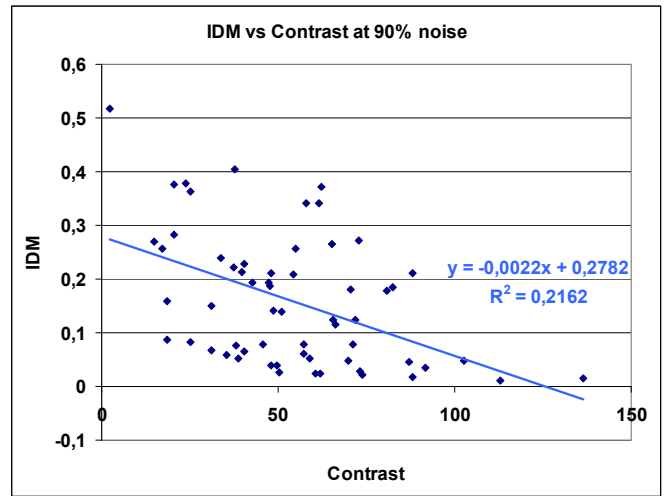
Figure 55 : IDM vs. Contrast for a high-noise model

7.9.3 Variance versus Correlation

Even if both equation for calculation of Correlation and Variance include statistical values (mean, standard deviation) attribute image response is quite different. Cross plot of Variance versus Correlation for both models (low noise - Figure 56 - and high noise - Figure 57) show not even a trend, that's why no correlation analysis is applied here. Eye catching is the ambiguity of Variance being zero and Correlation varying from "-16" to "-217". Therefore, Correlation and Variance are absolutely independent - at least according to the two models used here.
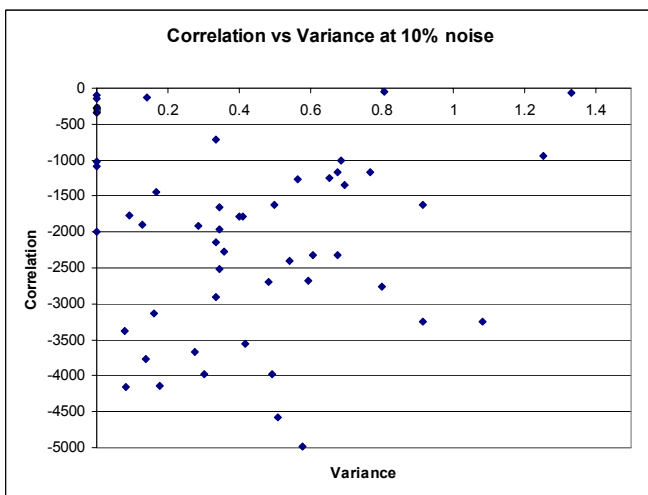
Figure 56 : Variance vs. Correlation for a low-noise model
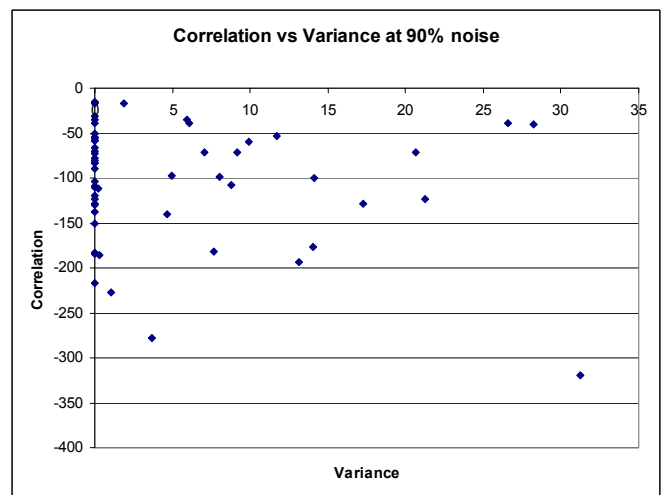
Figure 57 : Variance vs. Correlation for high-noise model

7.10 Brief summary of attributes properties

Attribute	Min / Max for a 10×10 texel and GLCM size of 16	Short description
Contrast	0 / 225	Gage for contrast within the texel; all texel values neighbored by itself are cancelled; the higher the difference between two neighboring values, the higher the contribution to Contrast attribute
Correlation	$> -\infty$ / 0	Complex gage for variance regarding texel's mean; standard deviation is taken into account, too; the more equal the values in the texel, the higher the Correlation attribute
Entropy	0 / 2,255	Gage for randomness within the texel; the more the texel-values are randomly distributed the higher the Entropy value
Homogeneity	0,0056 / 1	Gage for homogeneity within the texel; the more equal the values in the texel, the higher the Homogeneity attribute
Inverse Difference Moment	0,0044 / 1	Gage for contrast within the texel, the higher the difference between two neighboring values, the higher their contribution to IDM attribute
Variance	0 / 72,5	Gage for the variance due to texel's mean; values equal to the mean are cancelled; the more a texel is differing from the mean value the higher the contribution to Variance attribute

Table 12 : Summary of attributes properties

8 Dip calculation from imaging logs

One of the main purposes within this thesis is to determine geological features especially parameters of an inclining sedimentological layer (dip). As already mentioned in chapter 3.2, dip information is important for geologist in order to create a geological model of the borehole environment. Therefore, it is researched in the next chapters if dip calculation using attribute images will be possible and whether there are advantages in comparison to present dip calculation methods exemplarily described in chapter 6.1.2. First basic investigations are made with synthetic (self created) data before applying the method to real acquired imaging data.

8.1 Synthetic data

8.1.1 Synthetic sinusoids with high contrasts

In preparation for dip-calculation from real acquired imaging data, a model with two thin sinusoids (one Bin respectively 0.21" / 0.5 cm) and a linear varying background (in vertical direction, values ranging from "1" to "16" reached at the middle back to "1") was taken into action (Figure 58, A). To provide comparable results both sinusoids show approximately the same value-contrast to the background (1:14). Additionally relative noise ranging from 10% to 50% and constant absolute noise (a equal sized matrix with normal distributed entries around "1" and a standard deviation of 0.5 is added) is applied (see chapter 7.9)

By considering chapter 7.7 and the attribute characterization in chapter 7.8, following parameters were chosen for calculating the attribute image assumed to be the best one:

- Texel size 3x3 to detect contrast changes in the synthetic data as fine as possible
- Step size 1x1 to keep source image resolution
- Vertical evaluation; unless sine's amplitude is moderate, sine can be considered to be a horizontal structure, so vertical evaluation was chosen. Research on all evaluation directions showed, that vertical evaluation provides best results especially according to exact amplitude determination, even if amplitude of the sine wave is larger
- Contrast attribute; since there is a large contrast between modeled sines waves and background (1:14), Contrast attribute seems to be most suitable, with the side effect that the background in the attribute image is more structureless

Therewith, a Contrast image was calculated from the synthetic image (Figure 58, B) and correlation analysis was applied to determine parameters of the synthetic sinusoids in the raw image, namely vertical position and amplitude (Equation 23). Generally, a sinus wave is also characterized by a phase shift, but to simplify the dip calculation at the first stage, phase shift is neglected. As can be seen in (Figure 58, B) both sinusoids stand out against the background and any contrasts within the background are too small to be apparent. Therefore, background appears almost uniform. One of the major advantages of the attribute images (especially for the Contrast attribute) is to emphasize relative

contrasts in the raw data image no matter whether the values changes from high to low or the other way round. A model with sinusoids of value "10" and a varying background from "16" to "1" and back to "16" (compare to Figure 58, A) would result in an approximately equal attribute image.

As already described in chapter 3.2, geological layer crossing the borehole cause typical sinusoidal structures in an unwrapped image. Detecting parameters of a geological layer is therefore reduced to determine parameters of a sine curve representing layer boundaries. A sine wave mathematically described by:

Equation 23 $y = a * \sin(x + b)$

with

- y = vertical position ranging from 1 to 90
- x = horizontal position ranging from 1 to 60
- a = amplitude of the sinusoid
- b = phase shift of the sinusoid (neglected here)

According to chapter 3.2 and Figure 2, amplitude is a gage for the inclination while phase shift determines the azimuth of the inclined layer. The basic relationships between these gages are

Equation 24 $$a = \tan(I)$$
$$b = \tan(A)$$

with

- I = inclination of the inclined sedimentological layer (angle)
- A = azimuth of the inclined sedimentological layer

The dip correlation analysis works in the following way and is performed by a MatLab script: for each depth (vertical position), a sinusoid is created with a ranging inclination from 10° to 70° and along the sine line, values were extracted from the Contrast attribute image. Than the mean value of this data row is calculated and acts as a kind of correlation coefficient. When covering the sine wave in the attribute image completely, the mean value is highest (maximum correlation), while an estimated sinusoid results in a very low mean value when covering only the background (minimum correlation) or partly background and sinusoid (low correlation). Mean correlation for each inclination (angle) and vertical position is displayed in Figure 58, C.

Cleary to identify are the high correlations at the vertical positions 25 and 60 fraying to a fan by increasing inclination angle. By increasing the amplitude and therefore inclination angle, values of the estimated sinusoid are covering both sine and background instead of only the sinusoid. Now, peaks form the correlation plot have to be picked in order to determine vertical position (depth) and inclination angle of well correlating sines. To do so, for each vertical position the maximum correlation-value (best matching inclination angle) is picked and plotted in Figure 58, D. Two peaks at vertical position (depth) at 25 and 60 are striking.

To be able to pick the exact vertical position automatically a difference plot is calculated by subtracting each value of the data row of Figure 58, D with its previous value resulting in Figure 58, E. Benefit of this kind of gradient filter is a typical zero-crossing course of a peak (positive value, zero-crossing, negative value). Than, a window based threshold filter is applied, canceling all values below a multiple of the mean of a sliding window with a specified window length (Figure 58, F). Here, all values below "1.0 · mean" of a 10 value comprising window are cancelled in order to filter small variations. To suppress larger scaled variations not belonging to the major peaks, a global filter is canceling all value below the multiple of the mean (here 1.0 · mean is used) of the whole data row (Figure 58, G). Picking the two peaks is now simple: a positive value in the data row immediately followed by a negative value or a positive and negative value separated by a zero-value indicates the exact vertical position of a correlation-peak (Figure 58, H).. Finally, the best matching inclination for the determined vertical position has to be extracted from Figure 58, C) by picking the maximum of the specific data row. The results can be seen in the screenshot of the MatLab command window (Figure 58, I).

Note that according to this specific example, a single threshold filter would have been sufficient to detect correlation peaks, too. In respect to further research (real acquired images data), this signal processing was developed to pick peaks even under rougher conditions like low contrasts and less uniform background.

A) Model image (two sinusoids of value "1", angle=30°, width=1 and at depth (vertical position) 25 and 60; background linear from "1" at depth line 1 to "16" at depth line 45 and back to "1" at depth line 90, 10% relative noise, constant absolute noise)

B) Contrast attribute image, vertical evaluation, step size 1x1, texel size 3x3

90
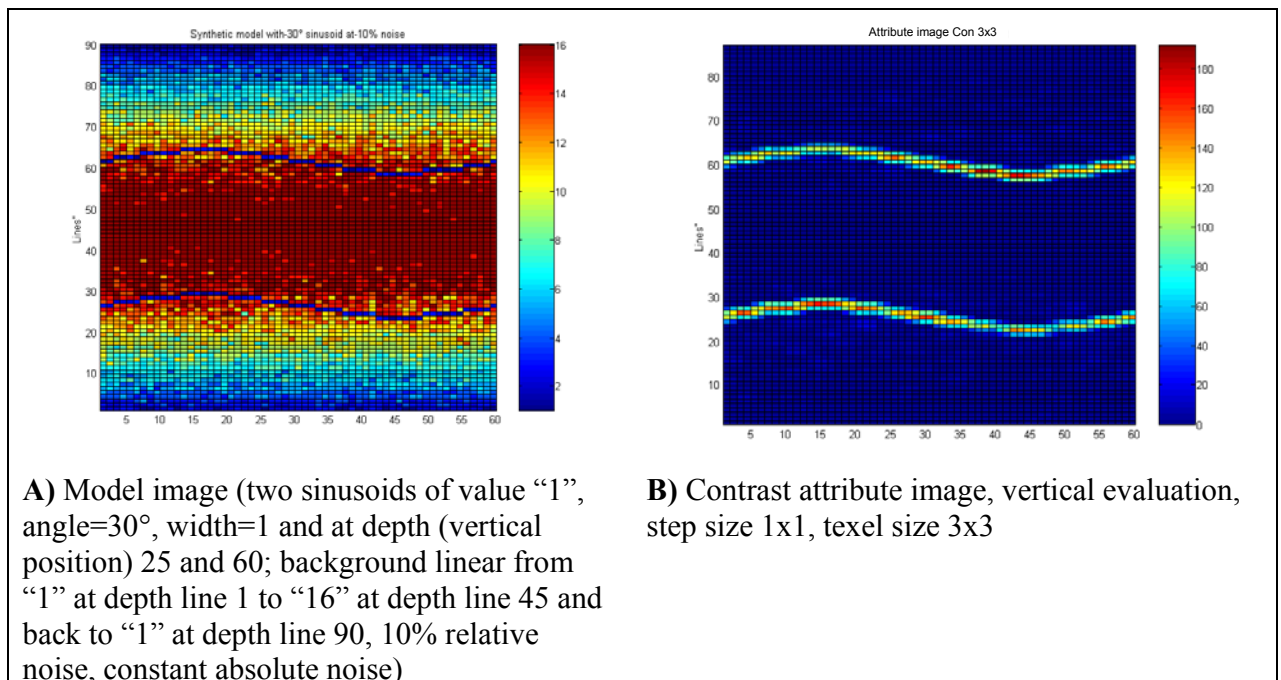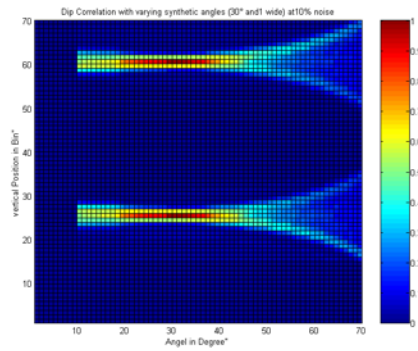
C) Calculated correlation image of assumed sinusoids with varying angles and vertical position and the sinusoids of the attribute image
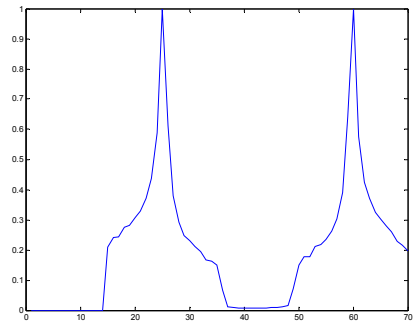
D) picked maximum angle correlation of synthetic sinusoids and image sinusoid versus vertical position (depth) – from **C)**
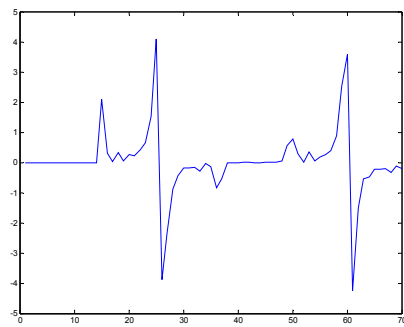
E) stretched difference plot of two neighboring values from **D)**
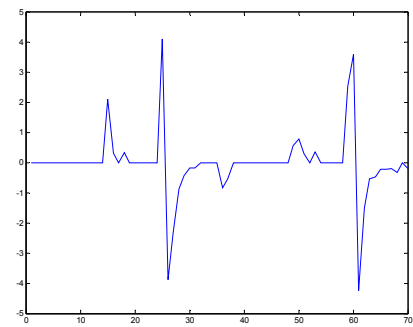
F) window based filtering of plot **E)** with a window size of 10
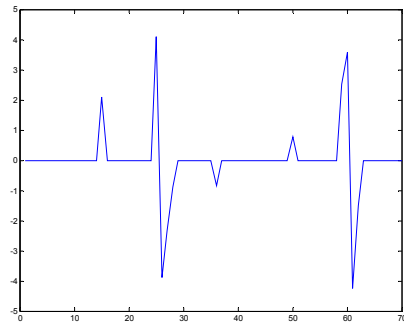
G) global filtering of plot **F)**
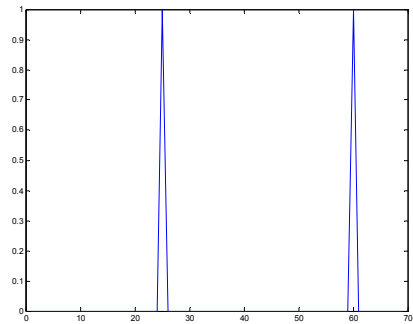
H) picked peaks from plot **G)**

I) screenshot of the calculated maximum correlating angel and vertical position (depth)
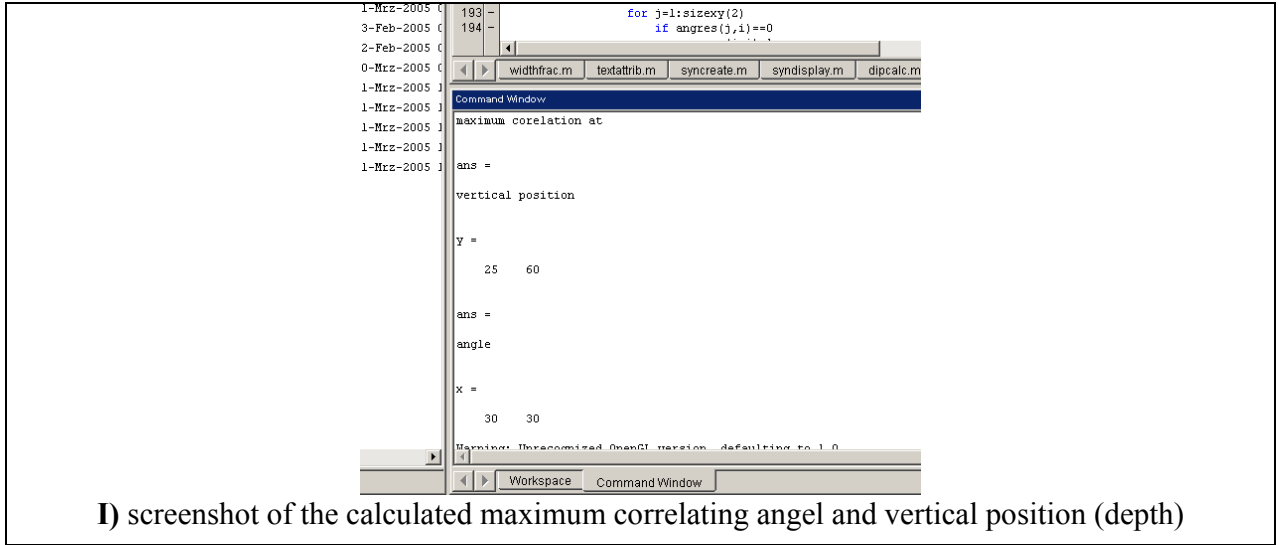
Figure 58 : Dip calculation procedure from the Contrast attribute image

The same dip computation procedure was performed for a second, slightly different model. Instead of thin sinusoids (one Bin, 0.21" / 0.5 cm), five Bin wide sines (1.07" / 2.7 cm) were created at the same depth positions. Background as well as parameters for the attribute image calculation remain the same. The results of the described correlation analysis for the two models bearing thick and thin sinusoids are displayed in Figure 59 and Figure 60.

Determination of inclination angle and vertical position regarding the thin sinusoid model is not only possible, but almost perfect, even at high noise. Calculated angel and depth correspond to the model parameters completely (angle : 30° and depth: 25 and 60). This is understandable for 60% relative noise applied to the sine values of "1" results after discretization in values of "1" or "2". Thus, high noise affects primary the background and the contrast between sinusoids and background is always high resulting in high and continuous Contrast attribute values – a good basis for dip calculation.
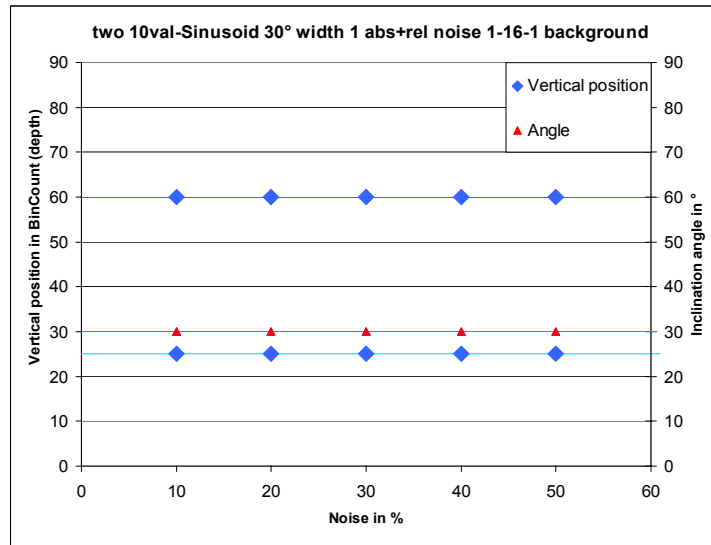
Figure 59 : Build up of calculated angle and vertical positions versus noise ratio for two 0.21" (0.5 cm, one Bin) wide sinusoids for the attribute image

Calculated angle and vertical positions regarding the thick sinusoid model in Figure 60 reveals a possible advantage of dip calculation using the texel attributes. Not only can the sinusoid be detected, but also the upper and lower boundary of a thicker sinusoid. Note that in this context "thick" means more than three Bins wide (0.64" / 1.6 cm) according to a 3x3 texel window size (see chapter 7.5 and Equation 22), in a geological context it would be a very thin bed. The calculated angle is accurate at 30° with only small variations (±1°) while there are two vertical positions per each sinusoid at 25 and 30 respectively 60 and 65, indicating lower (25 respectively 60) and upper boundary (25 respectively 60 + width of the sinusoid of "5" = 30 respectively 65).
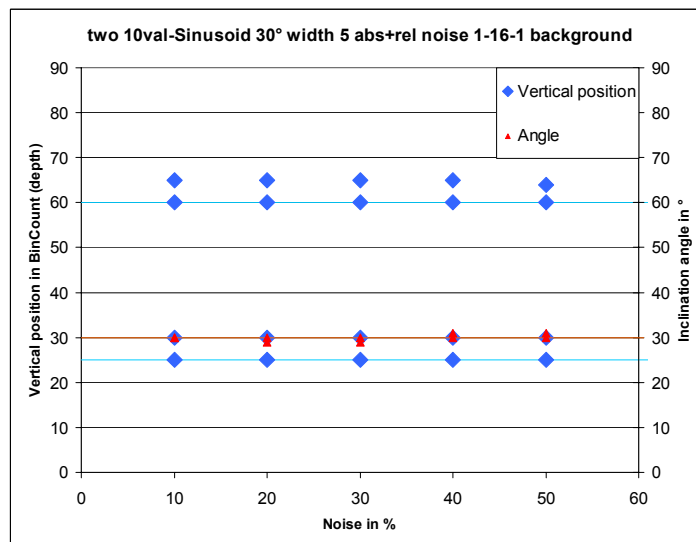
Figure 60 : Build up of calculated angle and vertical positions versus noise ratio for two 1.07" (2.7 cm, five Bins) wide sinusoids for the attribute image

Consequently, dip calculation (inclination and depth position) from a synthetic data by the help of attributes is possible and provides very accurate results when there is a high sine-background-contrast (>1:10), even at high noise ratios. The same procedure with a model containing sine waves at 60° inclination provides approximately the same quality of calculated dip-parameters. A comparison of dip calculation using other contrast-sensitive texel attribute (IDM and Variance) and only raw data is performed in the next chapter.

8.1.2 Synthetic sinusoids with high and low contrasts

For a validation and further development of the so far acquired cognitions a quit similar model than that of the previous chapter is used. This time, the synthetic sinusoids consist of values of "10" and the background varies from "1" at the beginning of the synthetic image log to "15" at the end. Thus, sine-background for the lower sinusoid at depth 25 is much higher (≈11:4) than for the upper one at depth 60 (≈11:9). Exemplarily, two models with five Bin wide sines (1.07" / 2.7 cm) at 10% (A) and at 50% relative noise (B) are displayed in Figure 61. The method for dip-calculation remains the same.

| **A)** Model image (two sinusoids of value "10", angle=30°, width=5; background linear from "1" at depth line 1 to "15" at depth line 90, 10% relative noise, constant absolute noise) | **B)** Model image (two sinusoids of value "10", angle=30°, width=5; background linear from "1" at depth line 1 to "15" at depth line 90, 50% relative noise, constant absolute noise) |
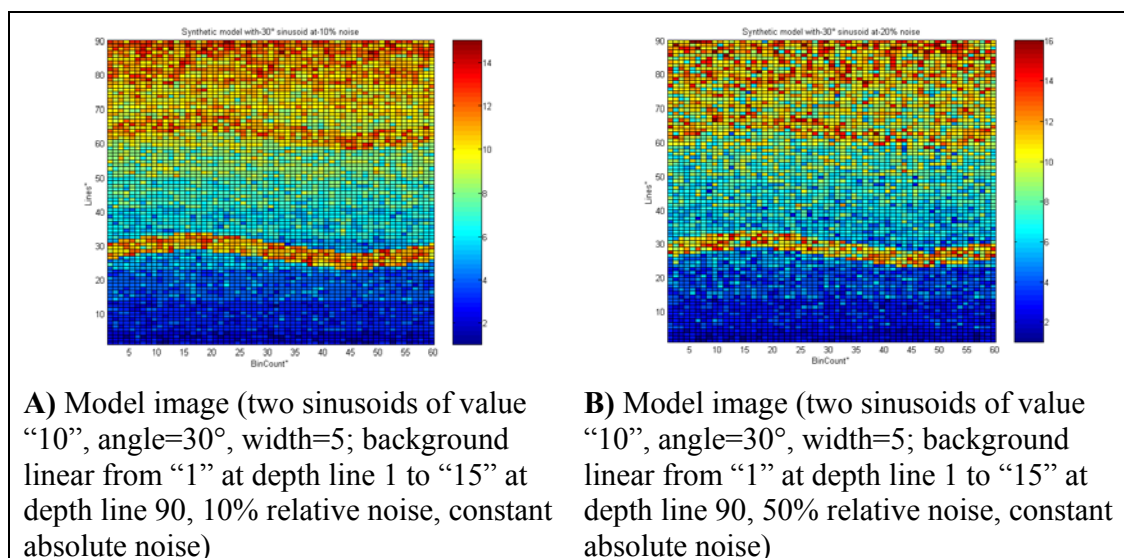
Figure 61 : Model images for calculated angle/depth comparison using raw data and IDM and Contrast images

Results of calculated dip parameters (inclination angle and vertical position) from synthetic image models (Figure 61) are displayed in Figure 62 to Figure 65. For each model, dip is calculated from the Contrast attribute, Inverse Difference Moment (IDM) attribute and the raw data image. Note that only since both sinusoids are emphasized by its positive contrast to the background (high values of the sinusoids to lower values of the background), dip calculation from the raw data is possible. So, an estimated sine wave covering an original sinusoid in the raw data image implies also a correlation maximum. Also, note that correlation analysis for the Variance attribute is performed, too, but result quality is comparable to that of the IDM attribute and therefore results are not displayed

to improve legibility of the diagrams. To avoid overloading, the calculated vertical positions and angles are separated in two diagrams. Figure 62 shows the vertical positions and Figure 63 the inclination angles versus applied noise for the one Bin (0.21" / 0.5 cm) wide sinusoids, while Figure 64 and Figure 65 display the same separated parameters for the five Bin (1.07" / 2.7 cm) wide sinusoids.

The first two diagrams indicates, that all three image types are suitable for accurate calculating vertical position and angle up to 20% of relative noise. At 30% and more relative noise, either additional correlation peaks (Figure 63, IDM30 and Con30 at 30% noise) or incorrect values are picked (Figure 62, IDM30 for the upper sinusoid at 60). Note that assignment between the inclination and vertical position diagram are not clear. Mostly, improper calculated vertical positions imply improper angles, too. All together, following basic assumptions can be made:

- for high sine-background-contrast (≈11:4) all three source images provides mostly accurate dip parameters
- for low sine-background-contrast (≈11:9) best results are provided by the raw data image, at least one approximately correct pair of dip and a second additional correlation peaks are calculable by the Contrast image, while Variance and IDM image provide no reliable results at higher relative noise amount (>20%)

Note that even if dip calculation from the raw data image provides best matches, commonly there are two different kinds of contrasts, namely high to low to high (Figure 58, A) and low to high to low (Figure 61), resulting in minimum correlation for the first case and maximum correlation for the second case. Differing between these two cases is one of the major problems in current dip calculation methods when performing a correlation analysis. In comparison with this, the contrast sensitive attributes images of Variance and Contrast emphasizes contrast changes always in the same way: as a maximum, no matter what kind of contrast. IDM response is reverse, contrast changes always result in minimum attribute values, but inverting the IDM image (highest value becomes the smallest and vice versa) lead back to the same case. Therefore, there are obviously advantages that may improve dip calculation from real acquired imaging data.

Figure 62 : Comparison of calculated vertical positions of two 0.21" (0.5 cm, one Bin) wide sinusoids using raw data and IDM and Contrast images
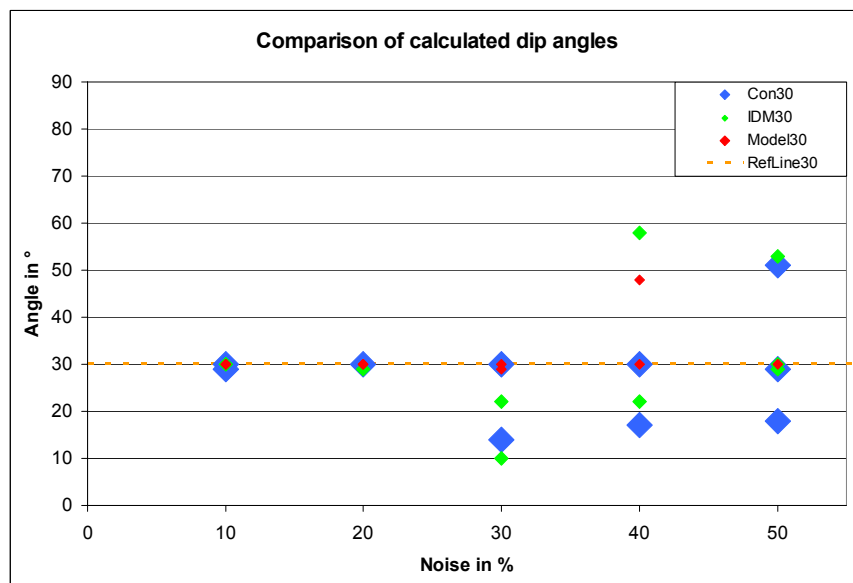
Figure 63 : Comparison of calculated angles of two 0.21" (0.5 cm, one Bin) wide sinusoids using raw data and IDM and Contrast images

The already mentioned advantage of calculating dip parameters of both boundaries of a thicker sinusoid by the help of attribute images can be retrieved in Figure 64 and Figure 65. For both Contrast and IDM attribute image, a pair of two dip parameters is calculated - at least for the lower high-contrast sinusoid, where vertical position and inclination angle is determined accurately up to a noise amount of 40%. Quite different results are gained from the raw data image regarding the lower sinusoid. While attribute images emphasizes both boundaries (when chosen texel size is smaller than thickness of the sinusoid) and thus correlation analysis results in maximum at these boundaries (Figure 66, gold sine), sine correlation regarding the raw data image is maximum in the middle of the

sine structure (Figure 66, green sine). At this vertical position, a range of inclination angles results in approximately equal correlation values, but only one correlation maximum is picked by the described signal processing procedure (Figure 58). Therefore, vertical position is determined between both boundaries (25-30 respectively 60-65) and the corresponding inclination is too low (<30°).

Worse results are displayed for the upper sinusoid. Due to the low sine-background contrast, only one sinusoid boundary is clearly determined by the help of attribute images. At 30% of noise and more, only determination of the vertical position provides reliable values, even if especially vertical position calculated by the Contrast image is drifting from the lower sine boundary to the middle of the sinusoid. Inclination calculation fails more or less.

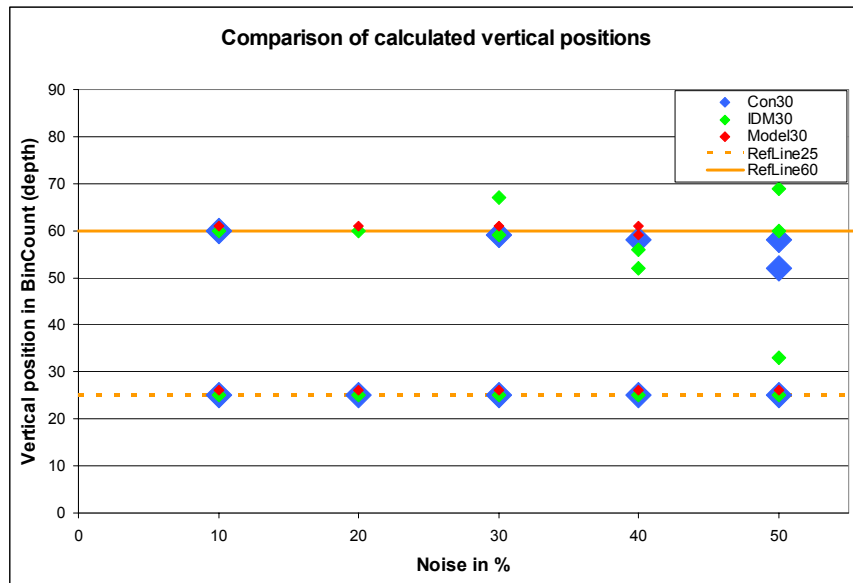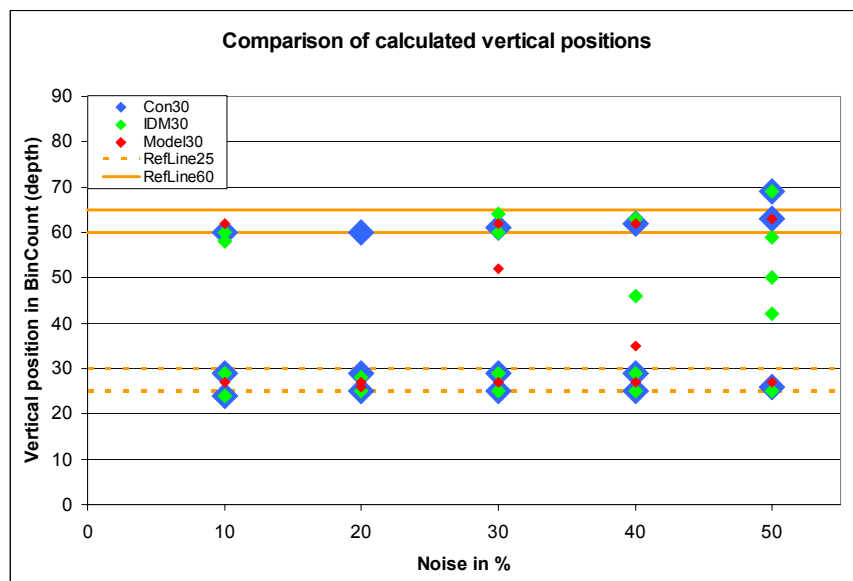**Figure 64 : Comparison of calculated vertical positions of two 1.07" (2.7 cm, five Bin) wide sinusoids using raw data and IDM and Contrast images**
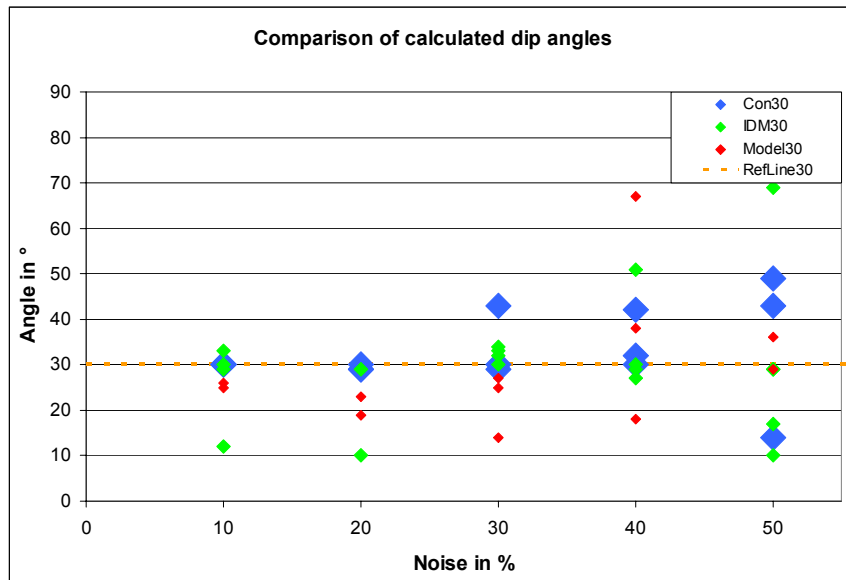
Figure 65 : Comparison of calculated angles of two 1.07" (2.7 cm, five Bin) wide sinusoids using raw data and IDM and Contrast images
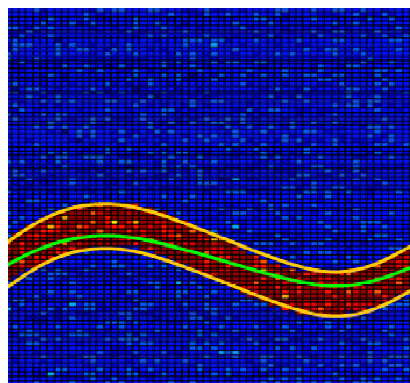
Figure 66 : Comparison of dip calculation by attribute image (gold sine) and raw data image (green sine)

8.2 Acquired electrical imaging data

According to horizontal and vertical resolution and the 360° borehole coverage imaging (continuous images), data acquired by the StarTrak™ tool seems most suitable for first investigations. Currently, four different data sources are available: logging data acquired

- at the rotational lab-test in Celle, Germany during Spring 2003.[Clausen, 2003; Fulda, 2004c]
- at the Baker Experimental Test Area (BETA) from May 19, 2003 till June 6, 2003 [Baule, 2003; Holupirek, 2004]
- in the North Sea in the field of Alba from October 26, 2003 till October 28, 2003 [Morris, 2004; Jetschny, 2004a]
- at the Baker Experimental Test Area (BETA) from April 26, 2005 till May 17, 2005 [Bethge, 2005] (data not released)

Rotational test data comprises only one sedimentological border with very low Rate of Penetration (ROP) and the tool run in the field of Alba acquired data in a horizontal well without any clear geological structures (only a few fractures), therefore the 2003 BETA data was chosen for further research.

8.2.1 Data preparation

Exemplarily two pieces of the imaging log of the 5th StarTrak™ run (29.05.2003 – 02.06.2003) were prepared to fit input requirements (continuous image log without gaps and discrete value-levels depending on the size of the GLCM) for the GLCM texel feature extraction:

- BETA1, 30.05.2003 10:01:14 – 10:03:19 (Figure 100 in the Appendix C)
- BETA2, 30.05.2003 10:09:09 – 10:12:04 (Figure 101 in the Appendix C).

Unfortunately, rotation speed of the drill string while data acquisition was lower than 120 RPM and therefore not a full set of 60 value covering 360° of the borehole were measured during the time stamp of 0.5 s [Holupirek, 2004]. Thus, vertical gabs occur in the raw data matrix (see Figure 67) had to be filled with interpolated values (linear interpolation between two values within one bin). To convert StraTrak™ measurement range (0.2 – 2000 Ωm [Holupirek, 2004]) into 16 discrete levels a logarithmic conversion scale (Table 13) was used. When increasing the number of discrete levels (e.g. Level=32 or Level=64), the logarithmic scale is changing by changing A in the exponential equation. For 32 discrete levels, A is 3.858 and for 64 levels, A is 7.716.
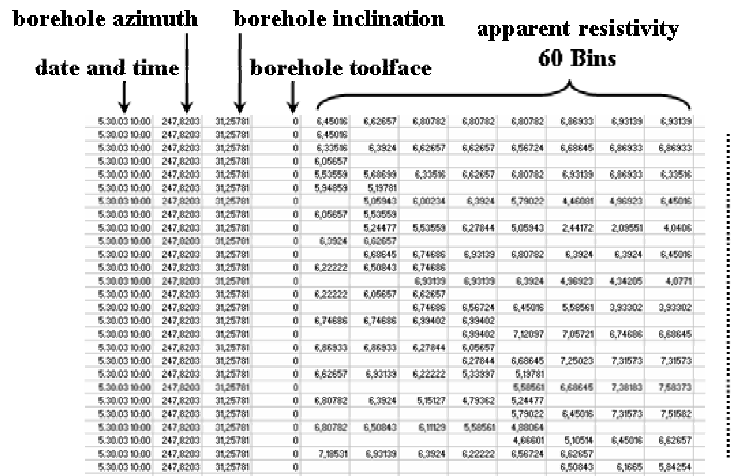
Figure 67 : Raw BETA field test data

Discrete Level	max Resistivity value = $\frac{1}{2} \cdot e^{\frac{Level}{A}}$ wit A= 1.929
1	0,84
2	1,41
3	2,37
4	3,98
5	6,68
6	11,22
7	18,83
8	31,63
9	53,12
10	89,20
11	149,80
12	251,56
13	422,46
14	709,46
15	1191,42
16	2000,81

Table 13 : Logarithmic conversion scale for discretizion and GLCM size of 16

8.2.2 Influence of GLCM size ($N_g \times N_g$)

Another influence gage up to now not mentioned, but also important for the GLCM method, is the size of the GLCM equal to the number of discrete levels of measurement values. To investigate the influence, the process of data preparation of image piece BETA1 is repeated with varying GLCM sizes (N_g =16, 32, 64). Than the Entropy image was calculated for each discretized BETA1 raw image (Figure 68). It is obvious that information content of the discretized raw data is increasing by raising the number of levels for discretization. More details are visible, structures show more texture and border crossings tend to be smoother. This can be easily reproduced by the attribute images (Figure 69, each calculated with a texel size of 3x3 and evaluated in vertical direction).

100

Areas appearing homogenous in the 16 level-discretized image gain structure and assumed sedimentological boundaries are emphasized more obvious in images with more levels. Unfortunately not only requested structures appear clearer in the discretized raw data and attribute image, but also structures within geological layer and other irregularities maybe disturbing the actual dip calculation. Especially the smoothing of contrasts boundaries results in lower attribute response (e.g. for contrast sensitive attributes). It was investigated that 32 levels for discretization is a good compromise between increasing information content of the raw data and hiding structure not belonging to sedimentological boundaries. Therefore a GLCM size of 32×32 is used for further consideration.

| discrete levels :16 | discrete levels :32 | discrete levels :64 |
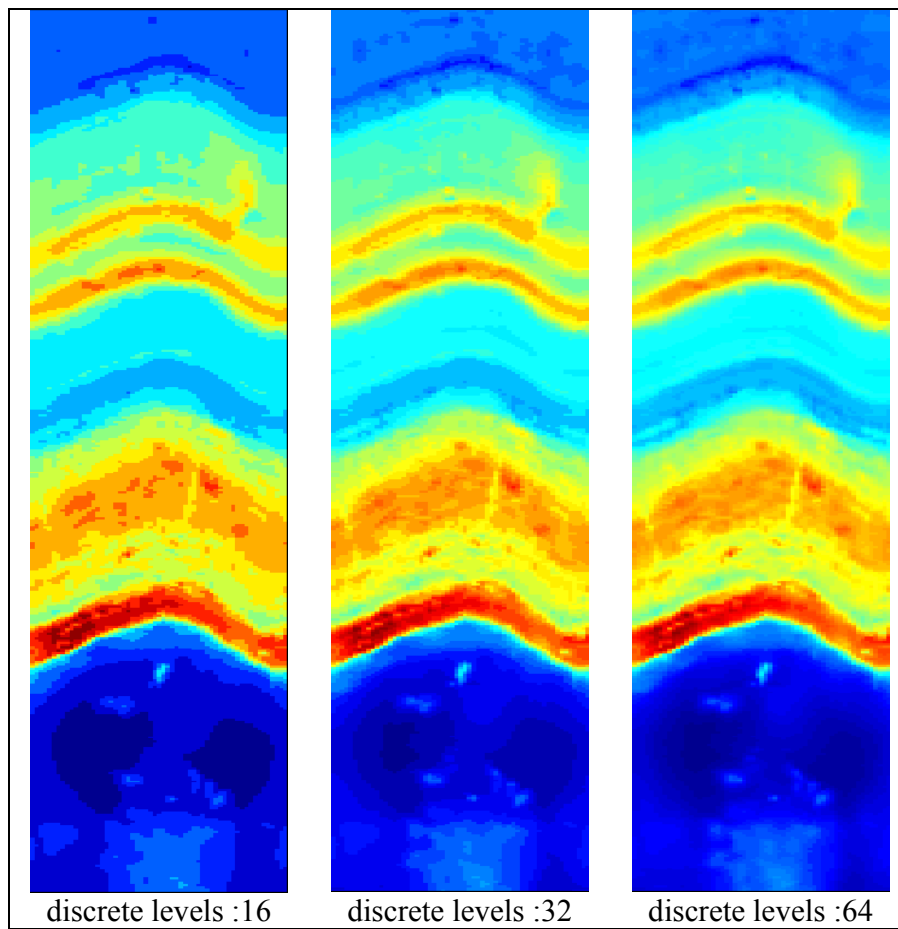
Figure 68 : Raw data image (BETA2) with different number of discretization levels

| GLCM size $N_g=16$ | GLCM size $N_g=32$ | GLCM size $N_g=64$ |
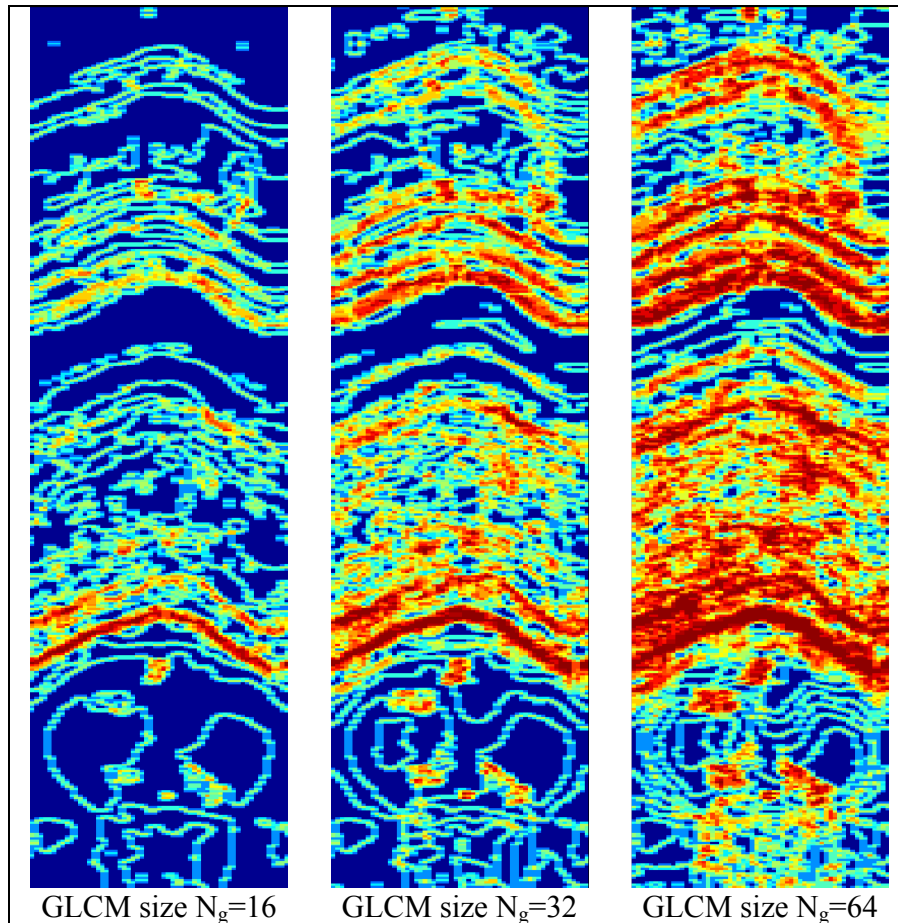
Figure 69 : Entropy attribute image with different GLCM sizes due to BETA1

8.2.3 Improvements in the process of Dip calculation

Even if some basic cognition have been gained during research on synthetic data, the step towards real acquired imaging data requires some essential adjustments will be described in the next chapters.

8.2.3.1 Texel attributes besides IDM and Contrast

According to the discretized raw data BETA1, three different attribute images are displayed in Figure 70 (texel size 3x3, step size 1x1, vertical evaluation). Even the Contrast attribute image - the most promising attribute (see chapter 8.1) – shows the worst response. The detected contrast boundaries are low in value and very thin. Besides a few major sinusoidal structures, not much structure is visible. The comparison in retrospective to the synthetic models reveals the flaw. The synthetic models point out high and sharp contrasts not really existing in acquired imaging data.

That's why all texel attributes described in chapter 7.8 are researched due to their suitability for dip calculation, namely Homogeneity, Entropy, Inverse Difference Moment, Contrast, Variance and Correlation. Determining criteria were:

- all major sinusoidal structure have to be emphasized by high attribute values; if possible continuous
- sedimentological boundaries have to be reproduced as thicker sinusoids to have clearance for the correlation analysis
- few clear structures besides the requested sine structures or at least of low attribute values
- background as much unstructured (homogenous) as possible, described by low attribute values

For that investigation some attribute images (IDM, Homogeneity) had to be inverted, because contrast changes are attribute-related emphasized as a minimum. It was found out that Entropy is most suitable, even if not being a typical contrast sensitive attribute. Hence, texel attribute Entropy was chosen for dip calculation.

| Contrast image | IDM image | Entropy |
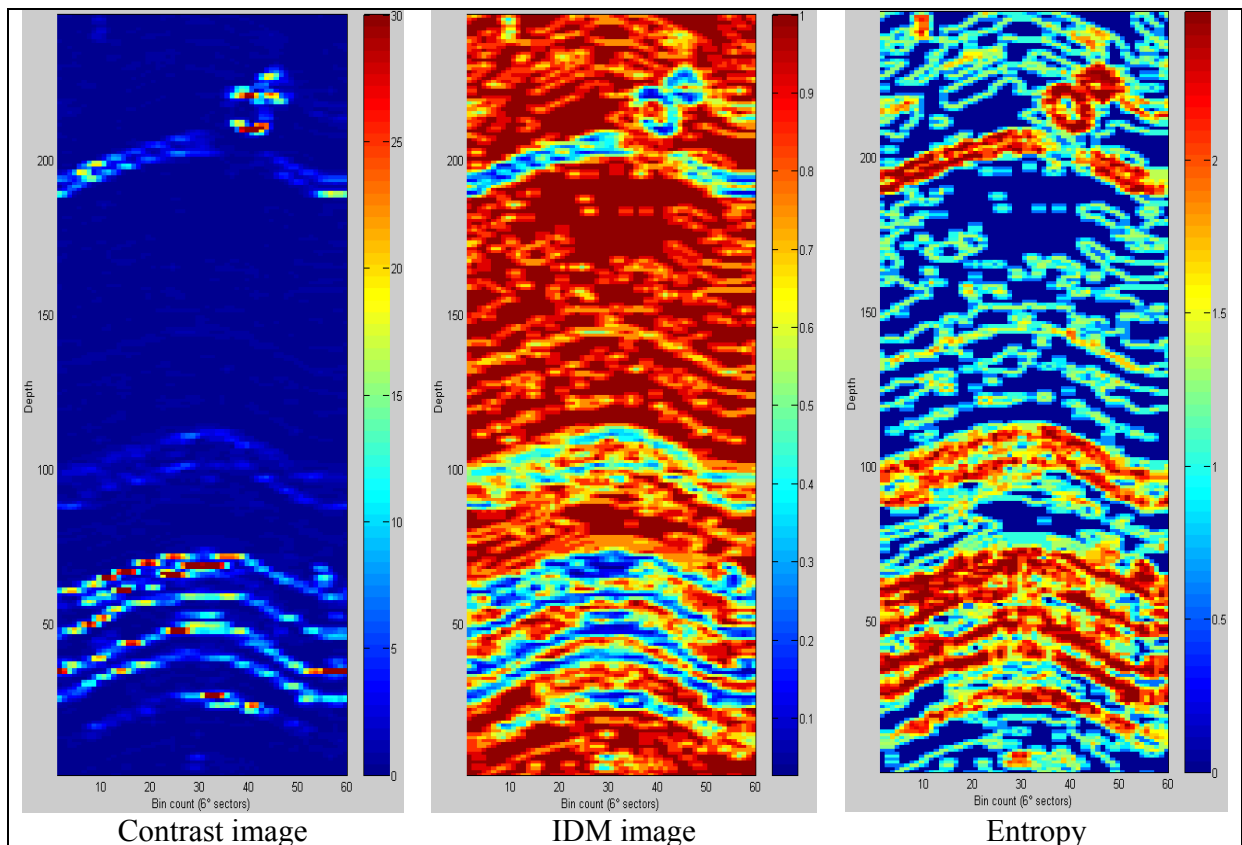
Figure 70 : Contrast, IDM and Entropy attribute due to BETA1

8.2.3.2 Image enhancements

To simplify correlation analysis and improve quality of calculated dip parameters, image enhancement is applied to the attribute image before doing the correlation analysis. Therefore, a dynamic normalization and a band pass filter are used. Process of image enhancement is displayed in Figure 71. The first picture (left) shows the discretized raw data image (32 levels) and the second the calculated Entropy image with a texel size of 3x3, a step size of 1x1, GLCM (N_g=32) was evaluated in vertical evaluation. The rightmost picture displays the processed Entropy image and following processing steps were applied:

- window based filtering (threshold filter); around each single Entropy row a window is defined comprising 100 rows respectively depth lines (50 rows to the bottom and top). Figure 72 shows this procedure for a nine-row comprising window. From this window, the mean is calculated and each value within the row (e.g. "2" – for the blue window) is filtered by the help of this mean (e.g. "5.3" for the blue window). If the value is below a multiple of mean (usually raging from 1.0 … 1.5 times of the mean), the value will be cancelled and if being above three time of the mean, it will be set to three times the mean. This filtering makes sure, that low contrast structure disappear (e.g. Figure 71, row 60-80) and local high contrast peaks are not overpowering regular high contrast changes of a sinusoid (e.g. the two circular artifact at row 220, right).

- window based normalization; around each single Entropy row a window is defined comprising 20 rows respectively depth lines (10 rows to the bottom and top). From this window, the maximum value is determined and each value within the row is divided by this maximum. Figure 72 shows this procedure for a nine-row comprising window. This procedure normalizes each contrast changes within the Entropy image, so that each apparent sedimentological boundary is emphasized in the same way (e.g. Figure 71, sinusoidal structures at row 30-60). Thus, lower contrast boundaries are emphasized and more desired structure is visible (e.g. .the sine at row 130). A quit similar normalization (according to the median value) is displayed in Figure 74 (A to B)

| discretized raw data image | Entropy image | processed Entropy image |
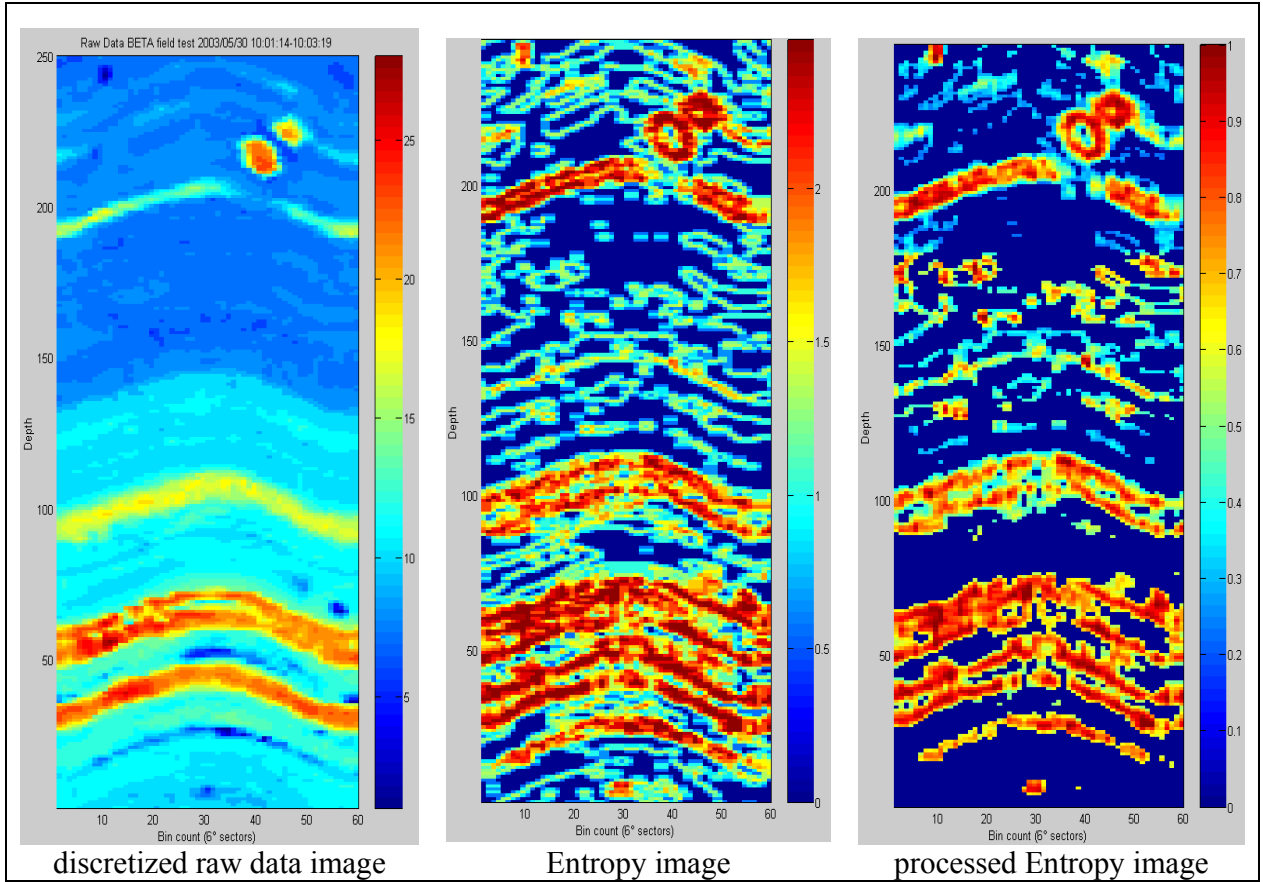
Figure 71 : Image enhancement of the Entropy image (BETA1)
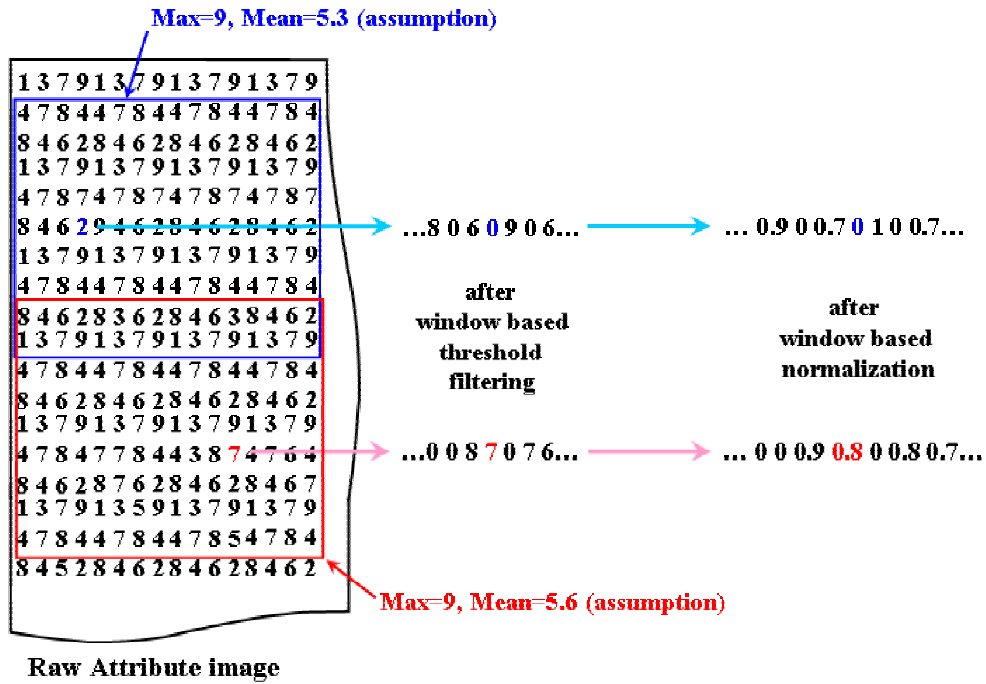
Figure 72 : Image enhancement scheme

8.2.3.3 Correlation analysis

Only a few improvements due to the correlation analysis have been made. Not only the vertical position and the angle are varying but also the phase shift. For every vertical position angle is varying from 10° to 70° and phase from "0" to "60". Then values along the assumed sinusoid are picked and the mean value of this data set is calculated. Additionally the mean value is divided by the standard deviation of the data set. This small change improves the correlation analysis and takes into account the scenario exemplarily displayed in Figure 73. When there are some contrast changes very close together both sinusoids (green and gold) results in a higher correlation peak, but only the gold sine covers the original sinusoid. The standard deviation helps distinguishing because of green sine is covering both low values from the background and higher values from the two original sinusoids. Hence, standard deviation for the green sine is higher than that for the gold sine. Dividing the mean value, acting as a correlation, coefficient by this standard deviation will emphasize the correlation peak for the gold sinusoid while damping the green one.

This improvement does not only affect very close contrast changes but also sedimentological boundaries neighbored by high contrast artifacts (e.g. BETA1, Figure 100 top right). Finally, a matrix is the output of the MatLab script, responsible for the correlation analysis, containing correlation coefficient, amplitude (inclination angle) and phase shift (azimuth) of the best matching sinusoid for each vertical position (depth).
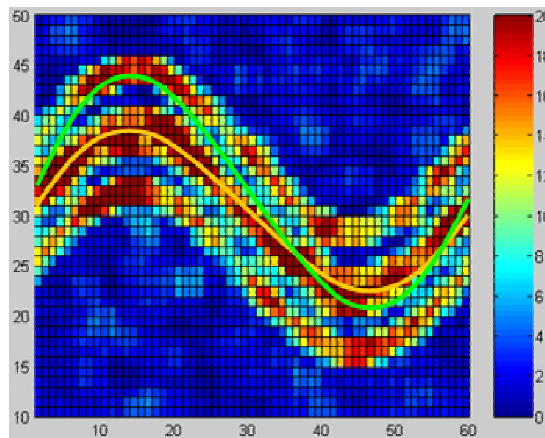
Figure 73 : Example for correlation-improvements due to correlation analysis

8.2.3.4 Signal processing of the correlation plot

The principal sequence of signal processing in order to pick correlation peaks remains the same than described in chapter 8.1.1, only normalization is added as a first processing step. Figure 74 (A) is the result of the correlation analysis described in the previous chapter, displayed is the maximum correlation for each vertical position (depth). For each correlation value, the mean value within a 30-value comprising window (15 values to the right and left) is calculated and the value is divided by this mean. So, local peaks are emphasized cautiously (Figure 74, B). Than, the difference plot is created by subtracting each value of the data set by its previous neighbor (Figure 74, C) and a window based filter is applied canceling each value below the multiple of mean of a 100 value

comprising window ((Figure 74, D; similar to the filter used for image enhancement in chapter 8.2.3.2). This threshold value (multiple of mean) usually ranges from 1.0 to 1.5. Finally the correlation peaks are picked by searching for a positive value followed immediately (or separated by a zero) by a negative value (Figure 74, E). Because of containing not only the correlation but also angle and phase shift of the best matching sine for each depth position, displaying the results is very easy by extracting all dip parameters from the output matrix gained by the correlation analysis.

A) Correlation vs. depth plot for due to the processed Entropy image (Figure 71)

B) normalized plot (**A**) due to the median of a 30 value comprising window

C) difference plot; subtraction of each value by its previous neighbor

D) filtered plot (**C**) due to the median of a 100 value comprising window

E) picked peaks
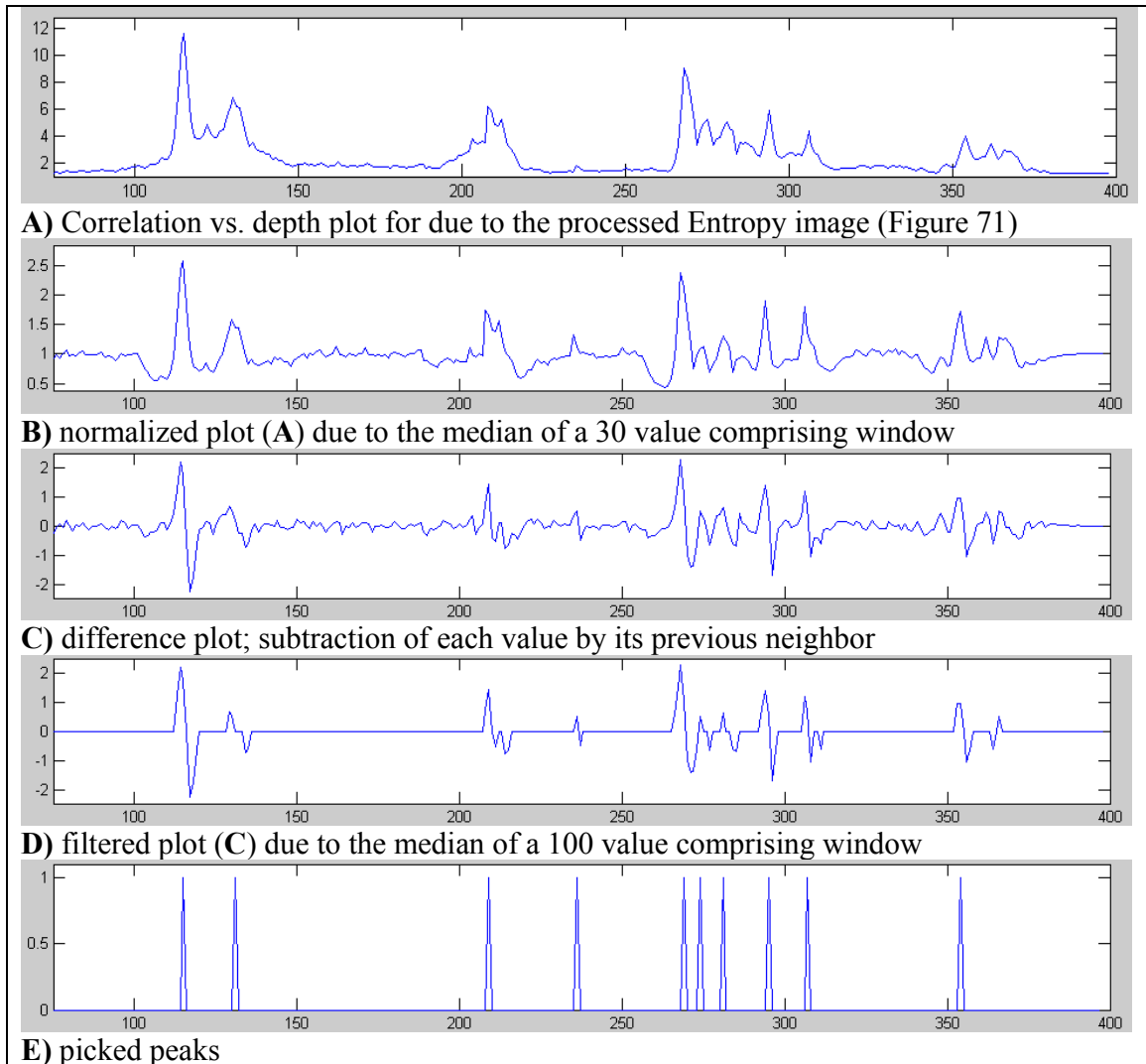
Figure 74 : Signal processing in order to pick correlation peaks

107

8.2.4 Results and problems of the Dip calculation

Results of the dip parameter calculation according to pieces of BETA image log (BETA1 and BETA2) are displayed in Figure 75. Detected sines are drawn as blue lines and inserted in the original discretized raw image. Clearly visible are the good matches at high contrast boundaries (e.g. (1) at BETA1 and BETA2). Sometimes it seems, that the detected sinusoids do not align perfectly with original sinusoids in the raw data image (e.g. (2) at BETA2). A view in the attribute images reveals that thick Entropy anomalies (2a), blurry contrasts (2b) or structures slightly differing from the sine-shape can cause these shifts. Besides this, some additional detected sinusoids occur (e.g. (3) at BETA2) or an apparent sine is missing (e.g. (4) at BETA1). Both dip calculation examples are unaffected by artifacts (high resistivity spots at BETA 1 (5) and high resistive flare at BETA 2 (6)).

Comparatively, dip calculation was performed for the Contrast, IDM and Variance image, too. After image enhancement, each of the attribute images is in principle suitable for dip calculation. However, either more additional sines are picked not corresponding with the original sinusoidal structures or major contrast changes are not clearly reproduced in the attribute image and therefore correlation is filtered. Best result according to quality and quantity of the detected dip parameters is still provided by the Entropy attribute image.

As a remark, it should be mentioned here, that the described methodology is only tracing sinusoidal structures within the image log. Whether the detected sine is really such a layer has still to be checked by a human viewer.
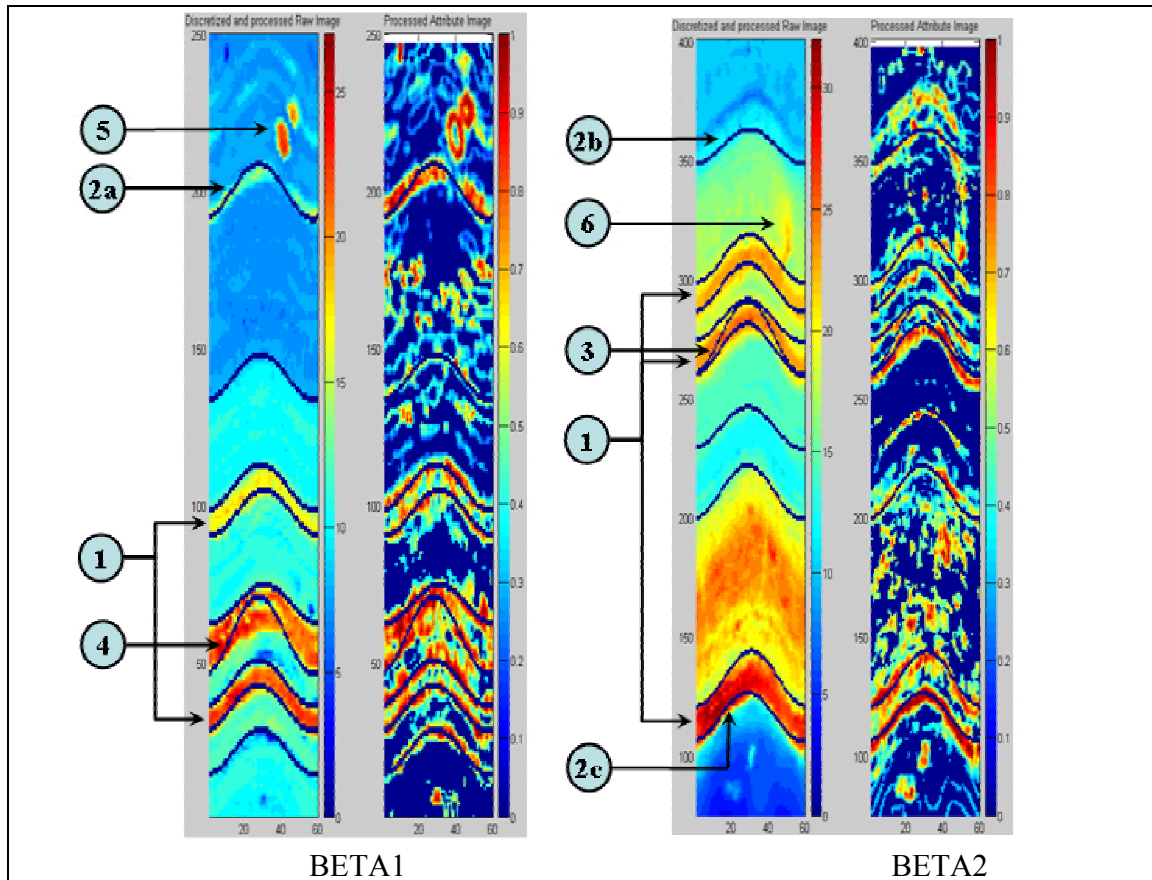
Figure 75 : Discretized BETA raw data and attribute image with detected sinusoids (for enlarged images see Appendix C, Figure 102 and Figure 103)

Some of these obvious mistakes and other problems occurring during the process of dip parameter calculation should be explained below:

- Determination of filter coefficients; currently filter coefficients are determined manually by review of processed attribute image. Setting the filter coefficient to high, sines are getting to thin and possibly non continuous while setting the coefficient to low, sinusoids emphasize themselves not clearly from the background or a sinusoid is not clearly separated by another close sinusoid (Figure 76, A, yellow arrow). Both scenarios result in a worse correlation analysis and in incorrect detected sines.
- Correlation analysis; if there are two original sinusoids close together and not well separated in the attribute image, correlation analysis can result in an additional detected sine covering both sines (Figure 76, B). Differing between a correlation peak according to an original sinusoid and an assumed sinusoid comprising two or more sine structures can be very difficult. The same can happen for a sedimentological layer with internal structures.

- Rough boundaries; if an assumed sedimentological layer is characterized by rough borders or a smooth transition (e.g. Figure 76, C), the attribute image will not be able to allow a continuous tracing along the boundaries. Hence, correlations analysis will not provide high correlations at this location and probably no sine will be detected.
- Signal processing; one weak point of the developed signal processing procedure is picking flat correlation maxima without a sharp peak and small local peaks very close to major peaks (Figure 76, D). The former kind of peaks shows no characteristic zero-crossing when calculating the difference plot, the second kind is damped too much by the window based normalization.

A) determination of filter coefficients

B) correlation analysis

C) rough boundaries

D)
signal processing, picking peaks close to major peaks or flat peaks
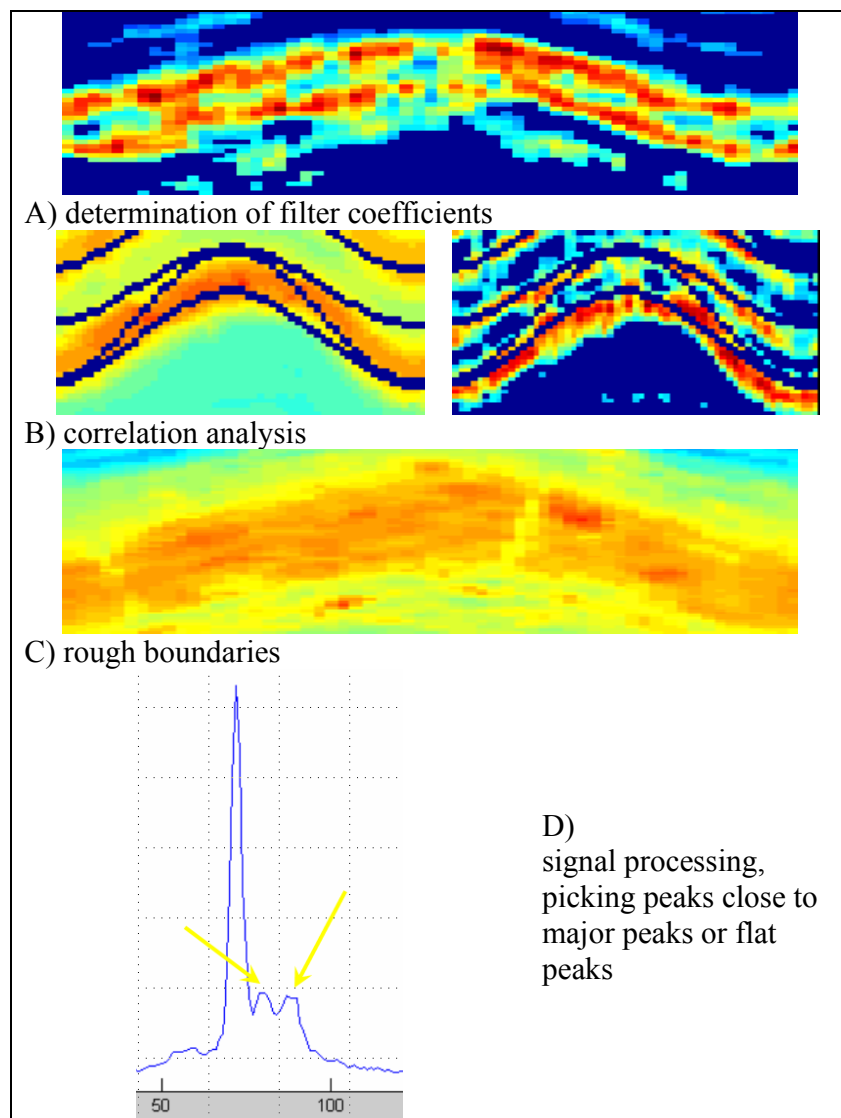
Figure 76 : Problems during the process of dip parameter calculation

8.3   GLCM vs. Dipex

As mentioned in chapter 6.1.2, there is already an in-house software called Dipex being capable of calculating dips automatically, too. A comparison of dips calculated by Dipex and the introduced approach using a GLCM is therefore obvious and will be described in the next chapters. By the way, in the following methodology comprising conversion of raw into attribute image data, pre and post-processing and self-developed correlation analysis is called *GLCM method*.

8.3.1 Data preparation for Dipex

Actually, handling of Dipex is very intuitive but the data preparation is a little bit tricky. Dipex requires "*.xtf" files – a binary data format - for data input, so the raw data had to be converted. This was done by the help of "LogManager" an integral part of the Baker Hughes Inteq software package "Case" used for log display and editing. One major problem due to the data conversion is the vertical resolution. The xtf file format provides a vertical resolution of only 0.05 feet when creating a depth based image plot while the vertical resolution of the original data can be 0.01 feet or below. Instead of averaging the data to fit input requirements, a stretched depth scale was used. In order to keep the vertical resolution the scale doesn't represent the original depth any more. Furthermore, the automatically calculated dip parameters will be wrong, as well. Nevertheless, the main points are brought out by the quality of dip's computed by Dipex and not by absolute dip parameters.

For e.g. prototype StarTrak™ data, 60 measurement curves were created and the original raw data was inserted. Afterwards a waveform is calculated from these single curves. Once managed to convert the data, a radius matrix sized like the image data waveform and three additional curves (borehole deviation curve, borehole drift azimuth, tool orientation azimuth) had to be created. These curves are required by Dipex (see Figure 77) but not necessary for the already incorrect dip calculation (according to the absolute dip parameters). Therefore, they can be filled with constant values. Finally, xtf header entry for the borehole orientation type had to be set to "gnorth" (geographic north) otherwise Dipex will refuse the image data. Unfortunately, LogManager is not able to edit the full xtf header; this is done by the DOS program XTFManager.
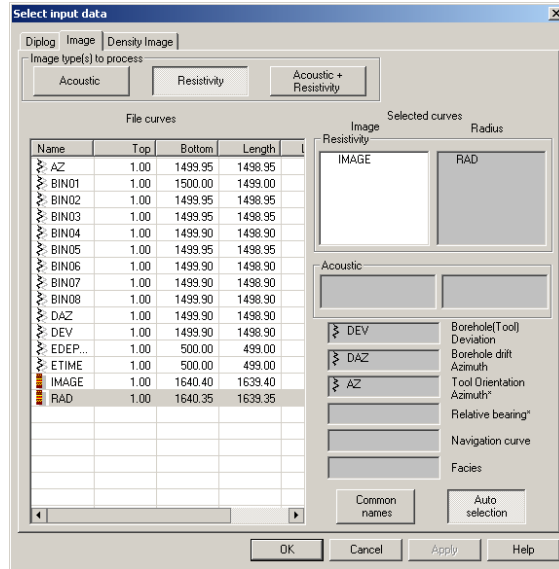
Figure 77 : Dipex input data dialog

After selecting the single curves and the image and radius waveform as input data, confirming some error messages due to the faked curves and determining of a depth interval, Dipex can perform automatic dip calculation. There are several settings, for explanations due to the different parameters see Appendix C, Figure 99. Parameters were set as displayed in Figure 78 providing the best results and sometimes being the only working possibility at all (especially according to BETA 1 and BETA 2).
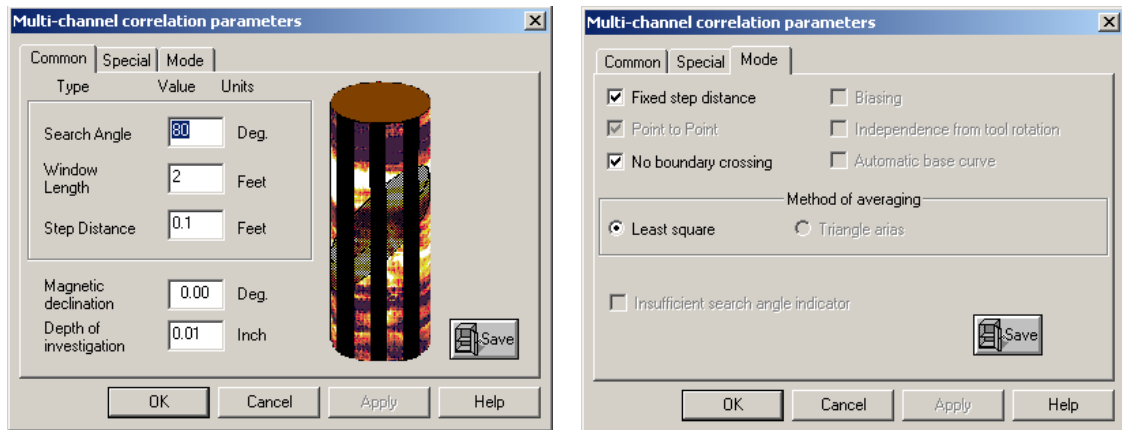
Figure 78 : Dipex parameters (common and mode page)

8.3.2 Results

In order to perform a comparison of both methods (Dipex and GLCM), the image examples BETA 1 and BETA 2 were called on again. Dip calculation results using the GLCM method were adopted from chapter 8.2.4. Because of considering both the attribute image and the pre and post-processing applied to the raw and attribute image before calculating dips (described in chapter 8.2.3), only the BETA 1 and BETA 2 raw image data were converted into xtf files (see chapter 8.3.1). Neither filtering nor discretization was applied to this data, only a dynamic normalization (with a window size of 7) was performed by Dipex in order to increase visual contrasts.

A buildup of already presented dip calculation results according to the attribute images and the dips calculated by Dipex from BETA 1 and BETA 2 are displayed in Figure 79 and Figure 80 (for enlarged images see Appendix C, Figure 102 and Figure 103). To sum the results, Dipex:

- provides excellent dips. Calculated sinusoids fit very well along assumed sedimentological layers and are almost unaffected by artifacts (e.g. high resistivity spots at BETA 1 (1)). Only at the beginning and the end of image piece BETA 2 there are additional sines and one sine is caused by the high resistive flare (2).
- calculates more sinusoid than provided by the GLCM method. In opposite to Dipex, the GLCM method determines sinusoids mainly along assumed sedimentological boundaries while Dipex calculates dips were there are no boundaries. Therefore, it might be possible to extract additional information about the absolute layer thickness when computing dips with the GLCM method.
- works very fast (apart from the data preparation), it takes only a couple of minutes to load the data and calculate the dips while it takes at least half an hour to perform the same piece of image log with the GLCM method.

All together, it obvious that the GLCM method provides slightly better dip calculations results than Dipex does – at least for these to image log examples and when time is not relevant. The dips calculated by the GLCM method reflect the geologic structure described by the borehole image better and additional information may be offered. There are advantages especially for exact boundaries and layer thickness determination.
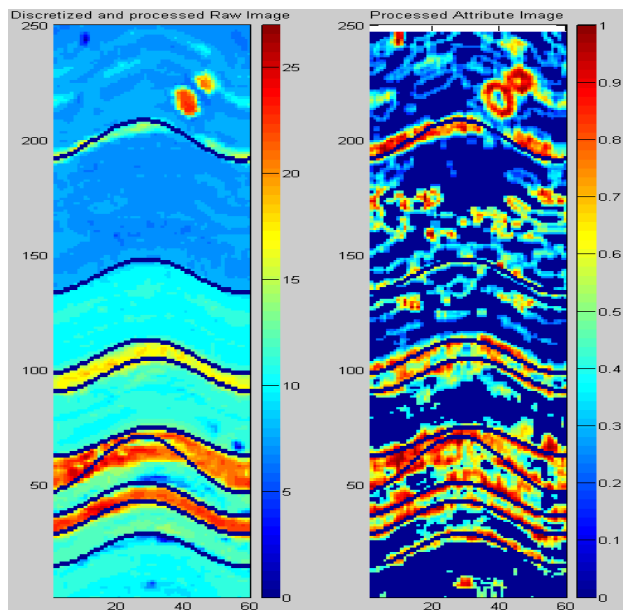
Electric raw data image with sinusoids detected
by the GLCM method
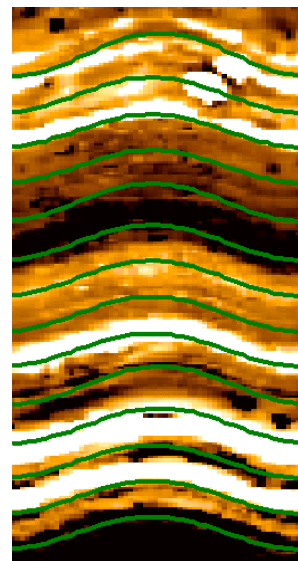
Electric raw data image with
sinusoids detected by Dipex

Figure 79 : Dip calcualtion comparison, electrical image, BETA 1
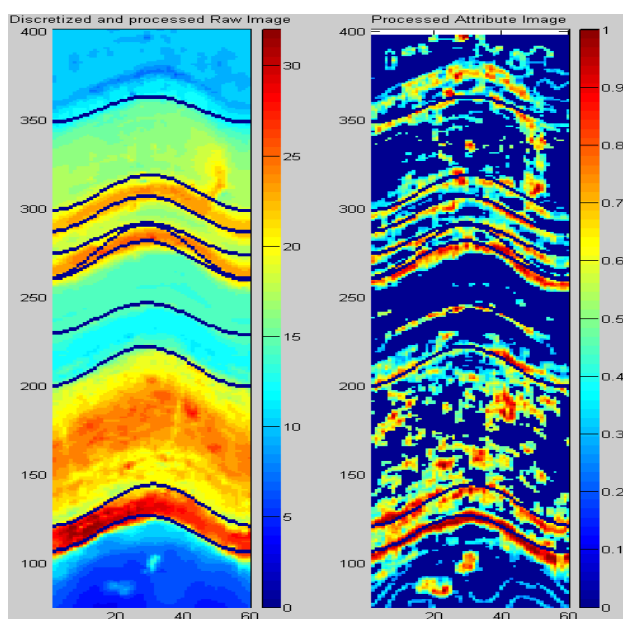
Electric raw data image with sinusoids detected
by the GLCM method
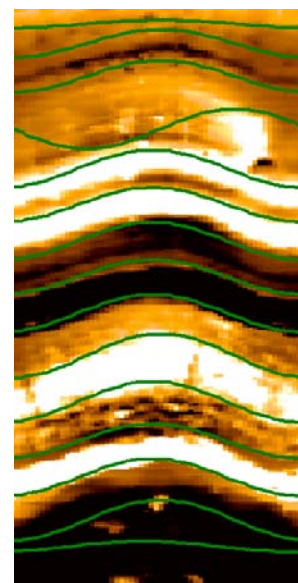
Electric raw data image with
sinusoids detected by Dipex

Figure 80 : Dip calculation comparison, electrical image, BETA 2

In addition to BETA 1 and BETA 2, other image logs were called on both to investigate the practicalness and stability of the GLCM method and to get comparable dip results by Dipex and the GLCM method. Following image pieces were chosen:

- Electrical image log, acquired by the prototype StarTrak™ at BETA in May 2003 (BETA 3), depth range 2522 – 2530 ft, dynamic normalized (Appendix C, Figure 104). BETA 3 is in comparison to BETA 1 and BETA 2 more complicated in structure. Geological layer are not so clearly and distinctive, fractures are crossing the lamination
- Nuclear image log, acquired by the LWD tool APS™ (advanced porosity service); according to confidential aspects there are no information regarding depth, time, well or field (Appendix C, Figure 105). The original nuclear image was available in only 8 measurement Bins and has been interpolated to 60 Bins to increase visibility of assumed geological structures.

Both dip calculation results provided by Dipex and the GLCM method can be seen in Figure 81 respectively Figure 82 and enlarged in the Appendix C (Figure 104, Figure 105).

At least two large and several smaller fractures disturbing the lithology can be found in BETA 3 (e.g., white dotted lines; Figure 104, (1)) and lithological boundary in general are less sharp but sometimes rough (e.g. Figure 81, (2)). Both factors will affect negatively the correlation analysis and will result in slightly imprecise or no detected sinusoids. Therefore, a pre-processing in terms of a soft low pass filter was applied to the raw data before being converted into an attribute image in order to smoothen the lithological borders by removing saw-teeth effects. Hence, contrast changes become clearer and as a side effect areas more homogenous. Both raw image and processed raw image are displayed in Figure 81. The affiliated processing of the attribute image and the correlation analysis remains the same (see chapter 8.2.3).

Following problems or distinctive features occurred during the dip detection in detail

- when using the GLCM method
    - as already described in chapter 8.2.4, two sinusoidal structures close together can result in a assumed sinusoid jumping from one sine to a second one and therefore covering both original sines (Figure 81, (3))
    - thick and continuous contrast boundaries in the attribute image involves several high correlating sinusoids with slightly different amplitude and phase shift values forming a high correlation peak for each of this boundaries. Due to the signal processing only one correlation value is picked per peak (see chapter 8.2.3.4), maybe not the perfect one as can be reproduced by a detected sine shifted a little bit from the original sine structure (Figure 81,(4))
    - irregularities in the attribute image, like high attribute spots (Figure 81,(5)), are just processing related artifacts occurring either at the beginning or end of the log not influencing the actual dip calculation

- – when using Dipex:
  - Dipex detects sines falsely at high resistivity flares as already mentioned in a previous paragraph (Figure 81, (6))
  - the effect of an assumed sine covering to similar and closely neighbored sinusoid in the raw data, recognized in the GLCM results, is occurring in the Dipex results as well (Figure 81, (7))

All together and despite of the mentioned weak points the summary gained according to BETA 1 and BETA is still valid. Both methods provide excellent detected sines, but strictly compared, quality and quantity of detected dips is slightly better when using the GLCM method.
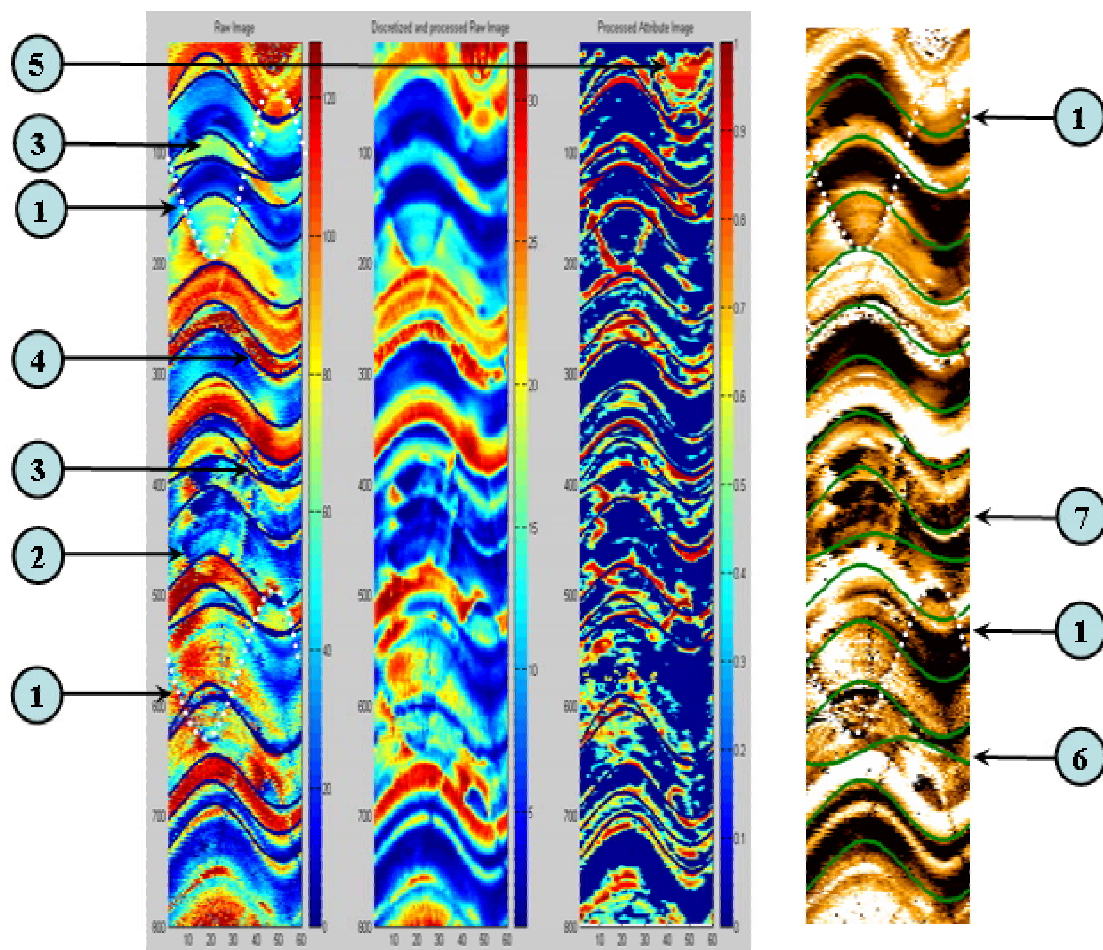
Figure 81 : Dip calculation comparison, electrical image, BETA 3

116

Even if horizontal resolution (8 respectively 16 measurement-values per 360° of the borehole) is low, nuclear image are sufficient for dip calculation. In the absence of better images, nuclear images are still used for dip determination (also see chapter 5.4).

At first, a low-pass filter was applied to the raw data as already done for BETA 3. In order to increase the horizontal resolution, finally, the original raw data (8 Bins) was interpolated to 60 Bins (60 measurement values per 360°).

Focusing on Figure 82 and in opposite to previous results, it is obvious that the chosen nuclear image piece turns out to be different, especially according to the dip calculation results. Even if both method have detected correct sinusoids successfully (e.g. Figure 82, (1)), dip calculation in general was difficult. Because of the interpolation, assumed sedimentological boundaries appear blurry and low in contrast (e.g. Figure 82, (2)). Sometimes boundaries do not even have a good sinusoidal shape, which makes it difficult for the correlations analysis to correlate with a sine (e.g. Figure 82, (3), two other possible sines are displayed as dotted lines). Furthermore, areas are bearing lots of inhomogeneity causing unwanted structures in the attribute image (e.g. Figure 82, (4)).

Following problems or distinctive features occurred in detail:

- when using the GLCM method:
    - contrast change at blurry boundaries (e.g. Figure 82, (2)) is so low involving no continuous attribute anomalies along this border. Therefore, a possibly calculated dip at this position is of low correlation and is filtered.
    - dip calculation along non-sine structures (e.g. Figure 82, (3)) results understandably in incorrect dips. So, amplitude, phase shift or both parameters can more ore less differ from the original dip of an inclining layer.
    - the already mentioned effect of calculated sines covering two close neighbored structures can be found here as well (e.g. Figure 82, (5))
    - even it is possible for a human interpreter to identify inhomogeneous structures of low contrast (e.g. Figure 82, (6)), attribute image response is so noisy eliminating the chance of calculating meaningful dips

- when using Dipex
    - The mentioned problem of calculating a dip along a non-sine structure effects Dipex as well, but the result is slightly better (e.g. Figure 82, (7); amplitude of the sine is more precise)
    - Dipex as well is influenced by inhomogeneity within assumed geological layers. This can be reproduced by e.g. Figure 82, (8). The first sine directly marked by (8) is completely wrong, while the other three (counted bottom up) are only slightly differing in phase and amplitude representing actually no geological boundary.
    - Even Dipex proofs to be able to detect low contrast and blurry structures (e.g. Figure 82, (9)), this not working all the time like e.g. Figure 82, (10)
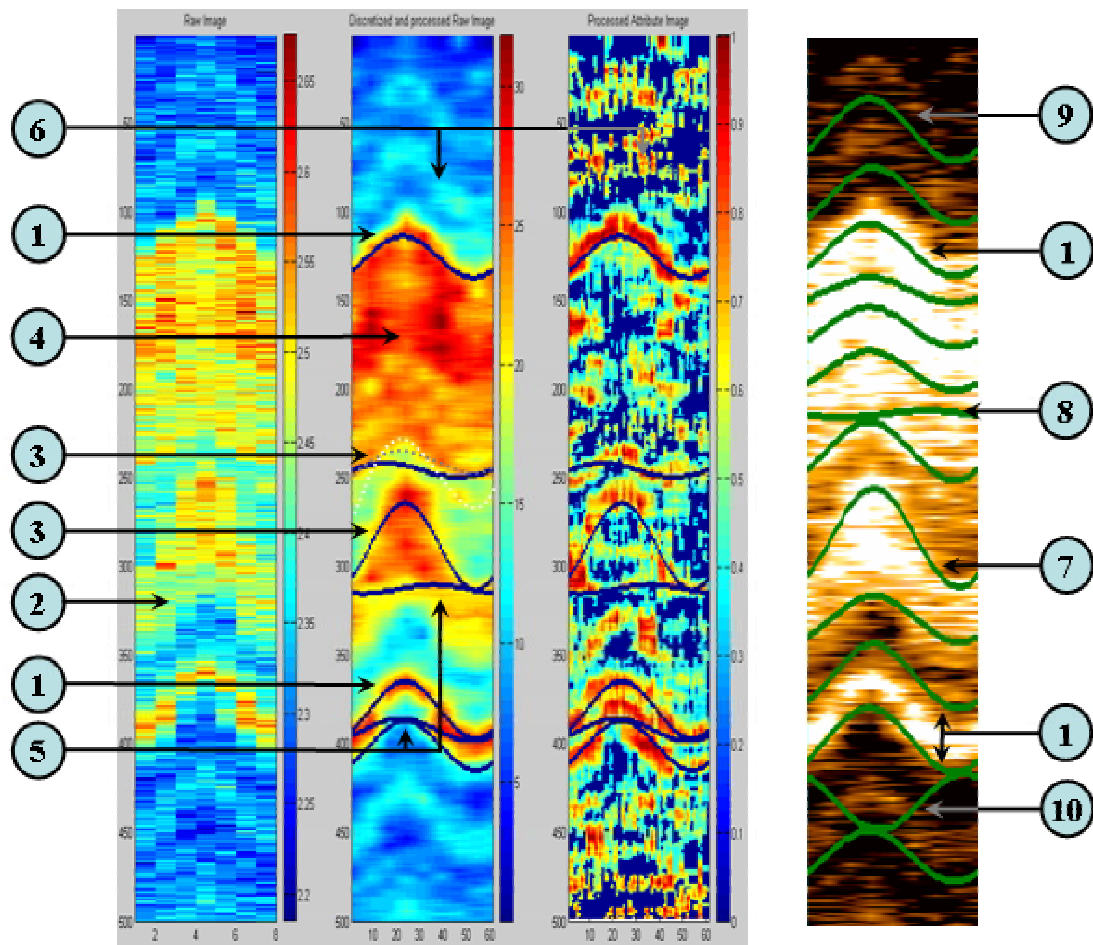
Figure 82 : Dip calculation comparison, nuclear image

This last example is excellent for showing limitations especially according to the GLCM method. Depending on the image quality, the GLCM method provides slightly better or worse results. Nuclear images are of lesser horizontal resolution and therefore the assumed lithological boundaries are less clear in contrast and shape. Under this condition, the GLCM method is not able to outdo all advantages. Hence, Dipex is in contrast to the previous described image pieces slightly predominant. Low contrast and blurry structures are detected by Dipex while the GLCM method fails. On the other hand, Dipex results show some mistake as well in terms of calculating wrong or slightly incorrect dips.

As a remark, it should be mentioned here, that attention was turned primary on calculation of as much as possible correct dips. It was tried to find the right balance between filtering incorrect dips and keeping correct determined dips, e.g. along major boundaries. According to both methods, it would have been possible to increase the correlation-threshold value in order to pick only a few almost "perfect" matches.

118

9 Facies Classification

Facies are characteristics of a rock mass that reflect its depositional environment. These characteristics enable the rock mass to be distinguished from rocks deposited in adjacent environments [Geology-Dictionary, 2005]. With the absence of a core, determining facies types from borehole images actually means investigating rock texture. Texture itself can be defined differently. From a geological point of view, texture is connected to the spatial relationship of geological objects observed on an image, at a given scale and method. As already mentioned in chapter 2, borehole images do not directly correspond to visible light cores images and the lack of core calibration makes it difficult to define geological objects seen on images. In opposite, from an image analysis standpoint, the texture is considered as spatial organization of color levels on an image [Ye et al., 1998]. Many attempts were made to formulate and create texture model using mathematically relations in order to quantify the texture. Therefore, several automatic facies (respectively texture) analysis methods have been proposed in literature:

- [Rivest, 1992] used mathematically morphology [Serra, 1982] and zonation by decision trees
- [Harris et al., 1993] used features extracted from a GLCM [Haralick et al., 1973] and multi-layer neural network classification [Rummelhart et al., 1986]
- [Luthi, 1994] used Laws texture engines [Laws, 1980] and Wards hierarchical clustering [Ward, 1963]
- [Hall et al., 1996] used feature extracted from a GLCM and a self-organizing map classification [Kohonen, 1984]
- [Ye et al., 1998] used statistical texture models [Ma et al., 1983], texture synthesis and a self-organizing map

In most of these works, image texture analysis and segmentation is considered a discrimination issue. First, typical textures observable from image logs are identified, and then characterizing features were found. By the help of these features, a so-called *feature space* is created (e.g. cross plot of two texture-describing features) and subdivisions are carried out. This classified feature-space is finally used as a reference in order to make comparisons with other to be classified image textures (respectively the extracted texture features). A quite similar procedure will be applied here, but in opposite to most of these methods, the main objective is not to develop an absolute or extensive rock classification, but a rough facies distinction. Instead of trying to differ between almost infinite natural geologic textures, a simple way will be researched to distinguish approximately 10 different and representative texture types for a rough classification, such as lamination low or high in contrast, structureless or irregular formation , pebbled structures or almost homogenous cementation. By doing so, two major objectives have to be considered:

- Uniqueness: each different texture should be described uniquely
- Uniformity: same texture should be detected independently of absolute measurement values.

9.1 Feature activity and continuity

As can be seen from the previous chapter, major problem in facies classification is finding parameter describing different facies types and extraction of the parameters from image logs. One possible set of parameters can be:

- Feature activity; describes feature contrasts towards surrounding structures/background, the larger the measurement value contrast between two neighbored structures, the larger the activity is
- Feature continuity; describes traceability of features within the 360° of the borehole surface. A continuous feature, (from the right to the left side in an image log) will result in a high continuity while discontinuous structures are of low continuity.

According to feature activity and continuity, following rough classification can be developed (Figure 83). It is marked by four extreme extremes (clockwise, starting up left):

1) High activity, low continuity, such as carbonates and conglomerates
2) High activity, high continuity, such as deep water sand-shale laminations
3) Low activity, high continuity, such as mudstone alternations
4) Low activity, low continuity, such as cementations and fine grained basal

Of course, there will be transitions between these four extreme scenarios, how much and to which degree they can be distinguished has to be researched. It is expected to find at least 10 different and unique texture types.
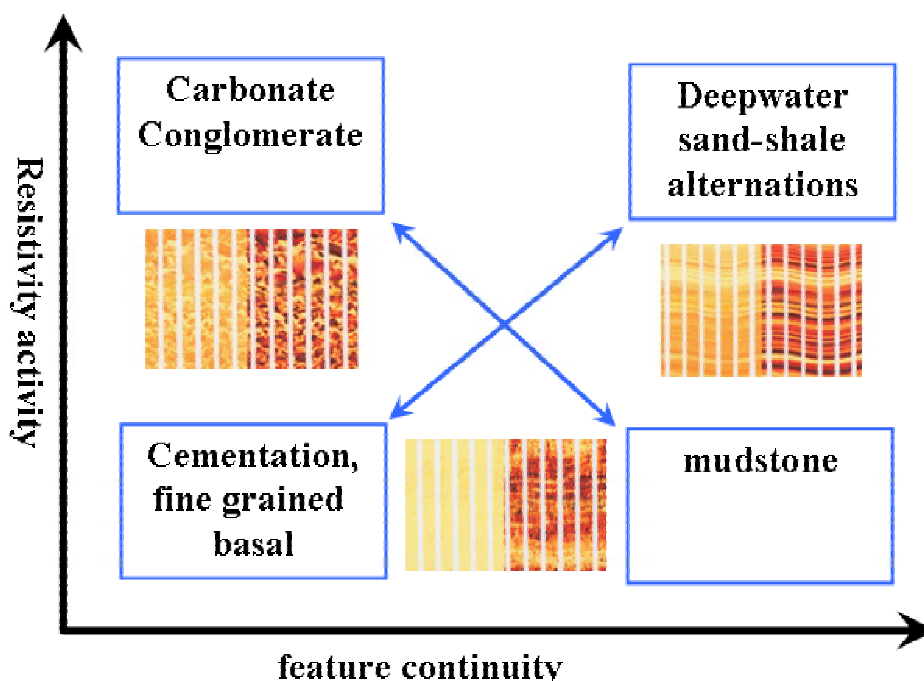
Figure 83 : Feature activity vs. feature continuity

Main purpose within this chapter will be to find synonyms of feature activity and continuity extractable by the help of image logs. With the knowledge of attributes behaving along contrast boundaries gained during the dip calculation (chapter 8), it is likely to use this boundary effect of attributes to describe the activity. The first approach dealt with different shaped texel windows. The underlying idea is demonstrated schematically by Figure 84. A thin vertical rectangle (red) was used for determining the feature continuity while a thin horizontal rectangle (blue) was called on as a gage for feature activity. In theory, it works like this:

- feature continuity; while sliding horizontally along the assumed sinusoidal boundary (Figure 84, left image), the red window will comprise the boundary all the time. Therefore, the attribute response will be continuously high (thick red dotted line). In opposite, attribute response regarding Figure 84, right image, will be only high when sliding over the assumed pebble-like structure (thick red dotted line). By calculating e.g. the standard deviation along this attribute line, it should be possible to differ between both scenarios.
- feature activity; similar to the feature continuity a window comprising either the whole width of the image or at least being very wide (blue), is sliding vertically over the assumed sine-shaped boundary respectively pebbled structure (Figure 84, left and right image). Since the contrast (1:10) and vertical dimension is equal for both examples, attribute is approximately equal, as well (thick blue dotted line).

So far, the theory, unfortunately, in the course of the research use of different texel sizes to describe continuity and activity turned out to be of less practical use. The larger the texel window, the more structure is covered by the texel and therefore the smoother the attribute image gets. As a result, facies classes were separated poorly like illustrated in Figure 88 and Table 21, 1). Hence, a new approach had to be developed.

| High continuity, high contrast | Low continuity, high contrast |
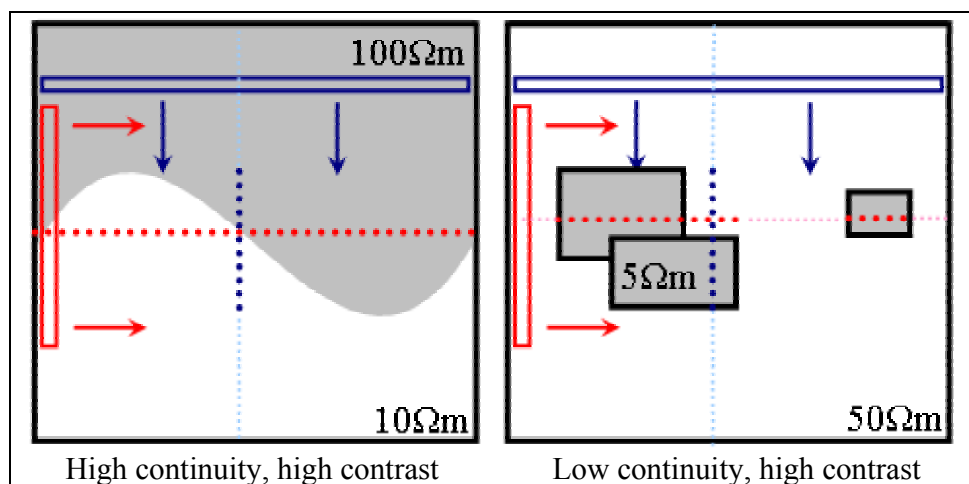
Figure 84 : Different texel windows to describe activity and continuity

One step back and being more basic, the next approach does not try to focus on continuity and activity while converting the raw into the attribute image. Instead, the attribute image should reproduce contrast distribution and shape within the raw data as detailed as possible. Then, for each row (depth) the mean and standard deviation is simply calculated. Figure 85 helps to understand the methodology. Four extreme schematic texture types are displayed corresponding to Figure 83 (first row: schematic raw images, second row: schematic attribute image). Similar colors (e.g. red tones) indicate low contrasts, while different colors represent larger or different contrasts. As found out in previous chapters, attribute images are mainly sensitive to contrast changes, homogenous areas result in lower attribute values. Therefore, only the contour of raw image's structures is drawn in the attribute image. Picking a line (depth level, Figure 85, light green dotted line) from each attribute image scheme and calculating mean and standard deviation (STD) leads to following:

- low contrast lamination is characterized by low STD and low mean (Figure 85, first left image column)
- high contrast lamination is characterized by low STD and high mean (Figure 85, second left image column)
- low contrast pebbles are characterized by high STD and low mean (Figure 85, second right image column)
- high contrast pebbles are characterized by high STD and high mean (Figure 85, first right image column).

Of course, picking a line between to lamination boundaries will result in still a low STD but also a low mean value. In reality, lamination is rarely flat, but bent. Hence, attribute image response according to a lamination will appear as more area-like anomalies with STD is low and mean is higher while covering the lamination. Since attribute image reproduce only relative contrasts disregarding absolute values, both objectives (uniformity and uniqueness) seem to be fulfilled. Therefore, standard deviation (STD) is used in the following for representing feature continuity and mean for describing feature activity.
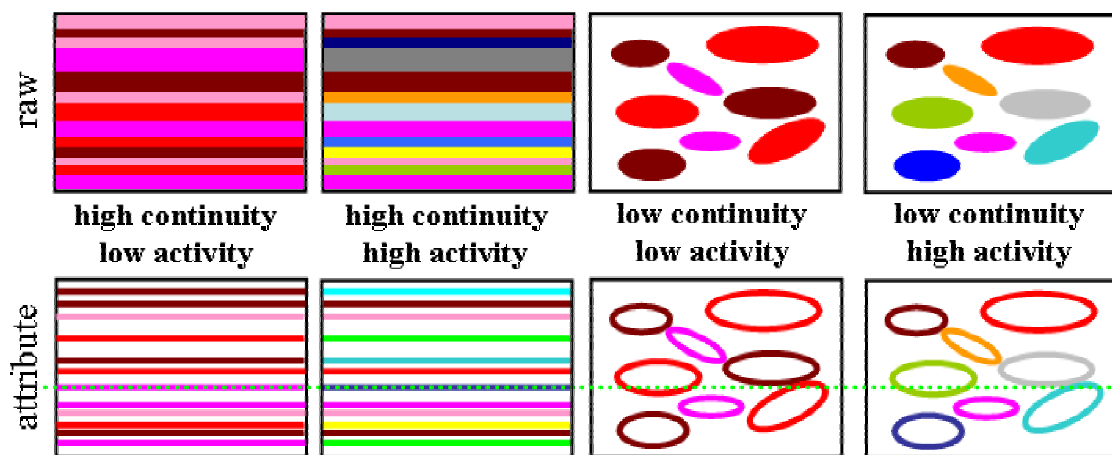
Figure 85 : Feature activity & continuity, schematic

9.2 Data Processing

For developing the classification different image logs were called on. Theoretically, it should not matter which image tool is used or in which well the data was acquired, as long as measurement range is similar. Hence, three different well logs were chosen, namely:

- ALK-45, field Al Khalij, operated by Total E&P Qatar, depth interval 4675 – 8167ft, acquired by Star Imager™
- BHD-7, field Mounds, Baker Hughes Experimental Test Area (BETA), depth interval 2264 – 2284 ft, acquired by Star Imager™
- BHF-13, field Mounds, Baker Hughes Experimental Test Area (BETA), May-June 2003, depth interval, acquired by StarTrak™

Optically, eight image pieces of the same size were chosen (Table 20, each consisting of 600 rows respectively depth levels) and following data processing was applied, similar to some processing steps described in chapter 8:

- interpolating of gaps or acquisition related stripes in order to get a continuous image (Figure 86, second left image)
- applying a soft low-pass filter to smooth interpolation related artifacts, discretization of measurement range into 64 instead of 32 levels used for the dip calculation to keep structural details (Figure 86, third left image)
- conversion of the processed raw image into several attribute images (Contrast, Correlation, Entropy, Homogeneity, Inverse Difference Moment, Variance) using a texel size of 4x4, a step size of 1x1, a GLCM of 64 and both horizontal and vertical evaluation. All together, 12 attribute images are gained (Figure 86, third right image, exemplarily, Entropy is displayed).
- for each attribute image row (depth level) mean (Figure 86, second right curve) and standard deviation (STD, Figure 86, rightmost curve) is calculated.
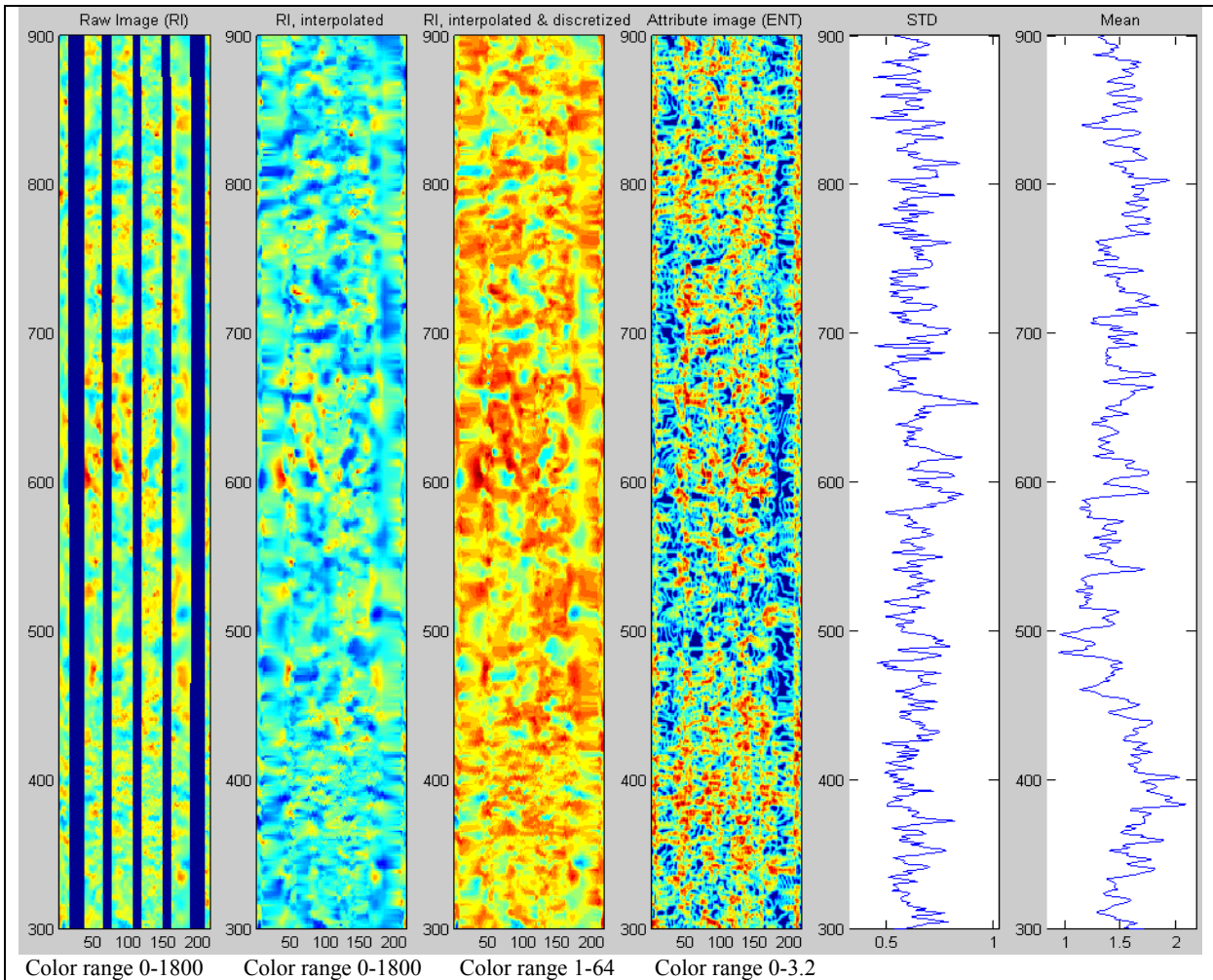
Figure 86 : Image processing for facies classification (here: Al Khalij 4755 – 4765 ft)

In theory, the cross plot of mean (representing feature activity) and STD (representing feature continuity) should form a unique cluster for each different texture type (e.g. Figure 87). Combining cross plots for each chosen image piece should result in a feature space with well-separated texture types being basis for the texture classification. Overlaps or covers would be indicators for similar or same texture types. In this context, it is now demonstrable why using large but thin horizontal (respectively vertical) texel window results in worse separated texture types. Figure 88 shows an Entropy cross plot using a 4x4 and 30x4 texel window according to the Star Beta image piece. The cluster becomes more compact when using a small texel instead of a larger one. This can be even reproduced by using an 8x4 instead of a 30x4 texel window – of course with less effect. A classification using a texel size of 4x4 and 8x8 can be found in Appendix, Table 21, (1) and (2).
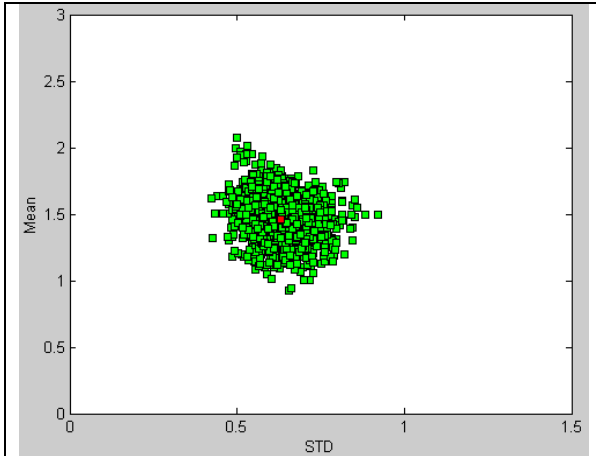
| Figure 87 : Mean vs. standard deviation (STD (here: Al Khalij 4755 – 4765 ft) | Figure 88 : Mean vs. STD for different texel sizes (here: Star Beta) |
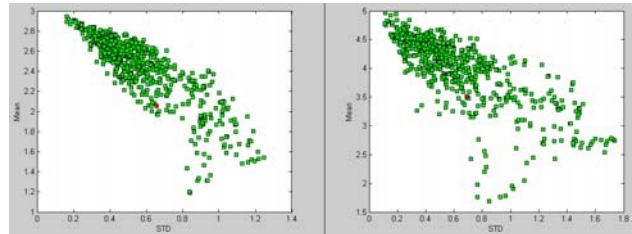
9.3 Results

The processing described in the previous chapter was applied to all of the eight image-pieces; so, eight clusters are available for each of the six attributes and for both evaluation directions ($8 \cdot 6 \cdot 2 = 96$). Main task is therefore to find the most suitable attribute respectively attribute-combination to describe feature continuity and activity. As implied, a single attribute must not necessarily be the perfect match, but possibly, there is one attribute ideal for reflecting activity and another one for continuity. A second basic assumption is referring to a possible assignment of vertical evaluation to STD and horizontal evaluation to the Mean value. To review chapter 7.3, horizontal evaluation is sensitive to vertical structures and vice versa. Because of focusing mainly on vertical contrast changes and horizontal continuity, it is obvious to use STD of a vertical evaluated attribute image and Mean of a horizontal evaluated attribute image.

A brief facies classification history can be found in Appendix D, Table 21, and indeed, the IDM clusters (Table 21, (2) and (3)) show a better separation, when using vertical STD vs. horizontal Mean. On the other hand, using an attribute combination can improve the classification, as can be seen by the change from IDM (vertical STD vs. horizontal Mean, Table 21, (3)) to IDM STD vs. Entropy mean (Table 21, (4)). Especially image pieces of higher activity (higher mean, e.g. Star Beta, StarTrak Beta 530-560 and Al Khalij 5825-5835) are more focused. After researching possible attribute-combinations, Correlation STD vs. Entropy mean turned out to provide the best classification. More detailed, the standard deviation calculated from the vertical evaluated Correlation attribute is plotted vs. the mean from the horizontal evaluated Entropy image. The final classification is displayed in Figure 89, the connection between cluster and image piece are emphasized in terms of color. Feature continuity is represented by the STD along the x-axis ranging from "0" (high continuity) to 250.000 (low continuity), while feature activity is represented by the mean along the y-axis ranging from "0" (low activity) to "3" (high activity).

Generally, the classification can be divided in three groups described by:

1) High continuity (STD of 0 - 30.000) and activity ranging from low to high (mean of 0.5 – 3)
2) Medium continuity (STD of 50.000 – 150.000) and activity ranging from medium to high (mean of 1 – 2.5).
3) Low continuity (STD of 70.000 – 250.000) and low activity (mean of 0.2 - 1)

The first group is represented by the three laminated image pieces (Star Beta and StarTrak Beta), sorted correctly by their activity. The StarTrak Beta image 1790-1820 shows clear laminations, but the activity (respectively contrast) is very low. The difference between minimum and maximum measurement values is small. In opposite, StarTrak Beta 530-560 and Star Beta are of more distinctive lamination and the contrast is much higher. Min-Max range is at least twice. Consequently, the last two image examples are located within the classification where there is high continuity and high activity (dark blue and pink markers), while continuity is still high for the StarTrak Beta 1790-1820, but activity is low (yellow markers).

The other extreme comprises Al Khalij 5050-5060 and Al Khalij 5170-5180 (third group). Both images are of low structure and most measurements values are ranging in a small band, resulting in both low feature continuity and activity. Actually, both image pieces are quit similar, the entropy image response, too. Anyway, especially the attribute image reveals more internal structure in the Al Khalij 5050-5060 and therefore it is possible to follow some assumed horizontal structure through the whole image, resulting in a higher continuity in comparison to Al Khalij 5170-5180. Some of these structures are gained by the interpolation of the gaps between the pads, so the continuity-difference between both image pieces should not be overrated.

The last major cluster group consists of the remaining image pieces, namely Al Khalij 5825-5835, 7730-7740 and 4755-4765 (second group). All three images distinguish oneself by more or less irregular structure and medium to higher contrast. That is why they are located in middle of the classification, described by low to medium continuity and medium to higher activity. Al Khalij 4755-4765 and 7730-7740 are almost equal in texture, so, overlap of both clusters is large. Feature continuity is similar to that of the second cluster group (Al Khalij 5050-5060 and 5170-5180), but the activity is much higher. Al Khalij 5825-5835 looks to be a hybrid within the image piece. There are apparent sine-like structures of partly high contrast, but the continuity is quite low respectively feature characteristic is rough. Hence, both feature continuity and activity is significant higher than for the other two images pieces within this group, even there is an overlap.

All together, the eight image texture pieces were placed within the classification quite consequently. In other words, position of the clusters according to feature continuity and activity and texture characteristics correlated well. The laminated image pieces are distinctively separated from the images containing irregular structure, and so these are from the examples low of structure. Large overlap of clusters means almost equal texture types and can be reproduced by the image texture appearance. One obvious weak point is due to the interpolation of the gabs between each pad. As can be seen by the help of Table 20, along these former gaps, attribute image response is usually very low. This is natural, for the 1D linear interpolation creates smooth change from one pad to the next. Therefore, both mean and STD for each depth level is slightly affected. It is expected, that either a two dimensional interpolation or neglecting of the interpolation for mean and STD calculation, will result in better compaction of each cluster.
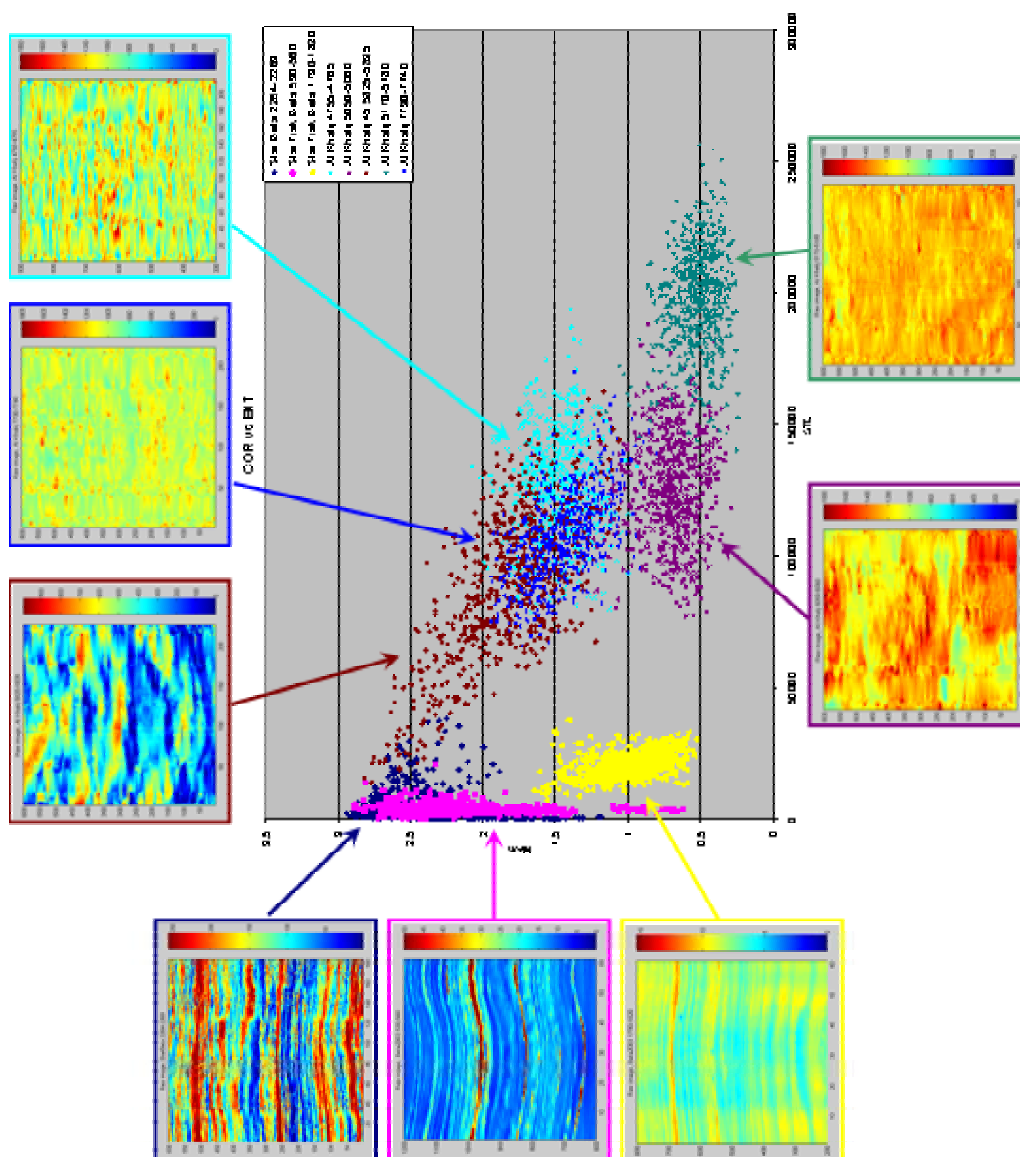
Figure 89 : Facies classification (feature space) for different image pieces

127

9.4 Application

For verification of the introduced facies classification procedure, a whole image log was called on, namely: Bill Stribling well #3, field Johnson City, depth interval 223 – 1274ft, acquired by Star Imager™ (Figure 91). This logs is characterized by its small well diameter and therefore small gaps between the separate pads and the variety of different texture types occurring in the image. Hence, there is no necessity of gap interpolation and images acquired by each Star Imager™ pad were directly joined together. This eliminates low attribute image response along the interpolation, negatively influencing the classification. Besides this, processing in order to create facies classification remains the same. First, a soft low-pass filter was applied and then the image log was converted in a vertical evaluated Correlation and a horizontal evaluated Entropy image using a texel size of 4x4 and a step size 1x1. To decrease calculation expense, instead of using 64 discrete levels, GLCM size (respectively number of discrete measurement levels) was set to 45, still providing enough accuracy for texture distinguishing. Finally, both standard deviation (STD) from each Correlation image row (depth level) and mean from each Entropy image row was calculated and cross-plotted in Figure 90. By doing so, feature space (range of both feature continuity and activity represented by STD and mean) is created according to the Johnson City well. To be able to differ between texture types, subdivisions within the feature space has to be made. This was done as displayed in Figure 90, considering visual striking apparent clusters. Now, each pair of mean and STD for each depth level denotes a facies type ranging from "1" to "6" and this facies curve was attached to the original image (Figure 91, red curve).
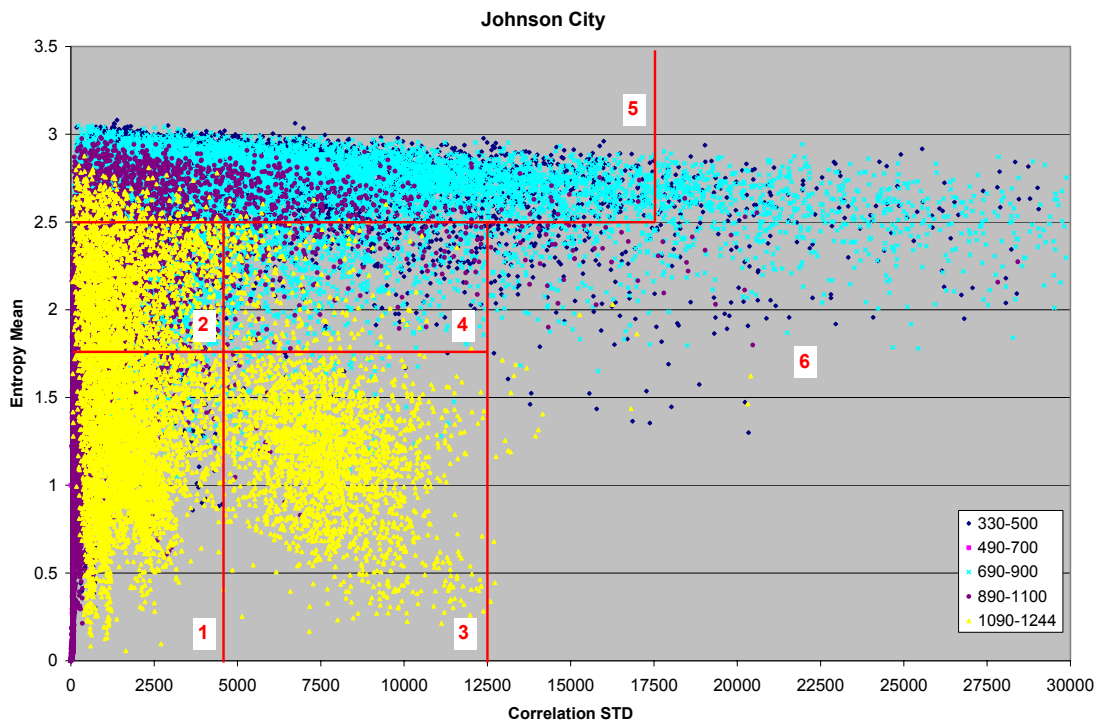
Figure 90 : Feature space from the Johnson City well (1st subdivision approach)
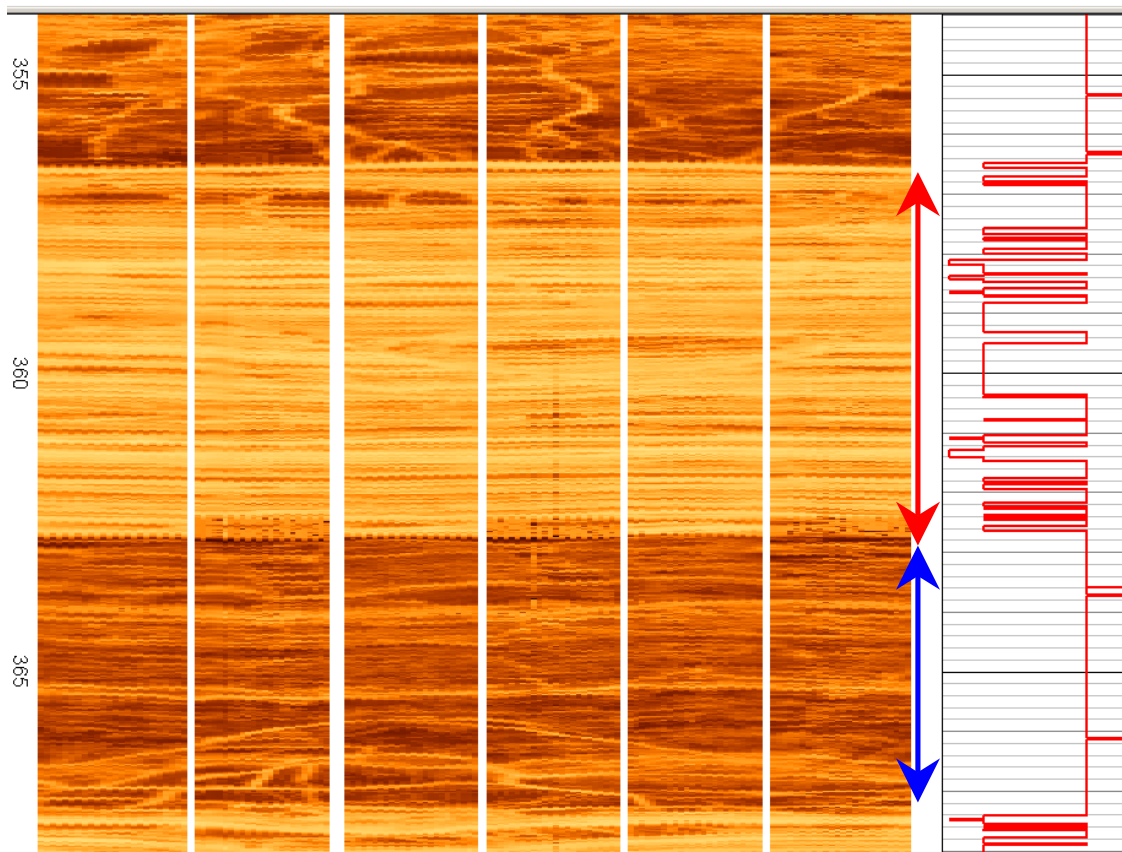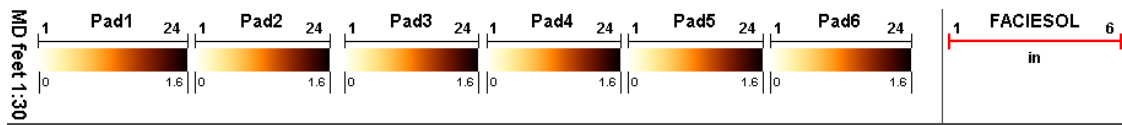
Figure 91 : Electric image log Johnson City I including facies classification curve (1st subdivision approach)

Since it is not possible to analyze the whole image log and the corresponding facies curve here, only two typical examples (Johnson City I, 355 – 368ft and Johnson City II, 897 – 907ft)) are extracted and the first one is exemplary discussed detailed in the following (Figure 91 - Figure 93). The second example (Johnson City II) is displayed in Appendix D, Table 22. Johnson City I comprises two apparent facies types, marked by the red and blue arrow in Figure 91. The red facies is characterized by very fine and continuous lamination and a range of contrasts (e.g. lower contrasts at depth level 358ft and higher contrasts at level 362ft). Therefore, feature continuity is expected to be always very high, while feature activity can vary from medium to high. In opposite, blue facies seems to be more homogenous in contrasts while the feature continuity varies. Especially the lower part (e.g. depth level 367ft) shows obvious disturbance within the lamination. Thus, feature continuity will range from high to medium while activity is constantly high.

Detailed feature space according to the red and blue facies shows exactly this behavior (Figure 92). The red facies cluster is characterized by a small range of STD (representing feature continuity) and a mean ranging mainly from 1.5 – 3.0 (medium to high activity), while the blue facies is always high on activity (high mean) and the STD varies from high to medium. Consequently and according to the subdivisions in Figure 89, the red facies is classified by facies type "1", "2", and "5" and the blue facies by facies type "5". A few STD-mean pairs from the blue facies (high mean, lower STD) were hidden to increase display range and result in some single facies peaks of type "6".

| 357-362ft (red range), facies type 1, 2, 5 | 363-367ft (blue range), facies type 5 |
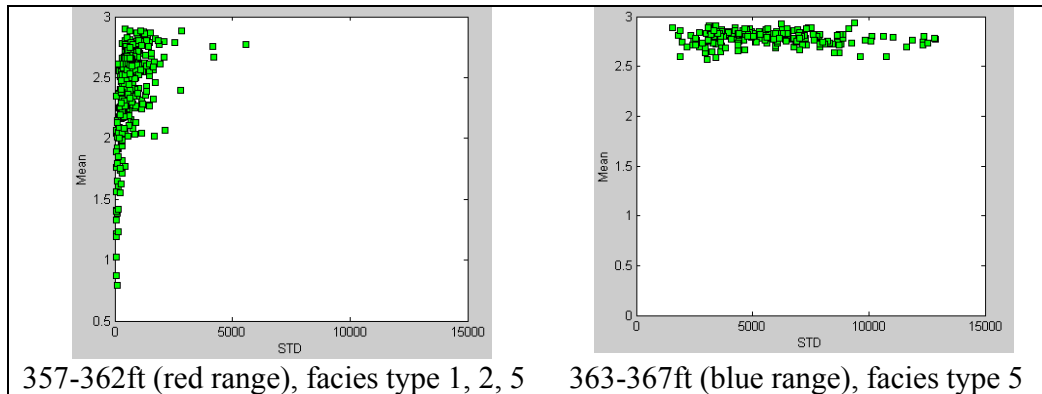
Figure 92 : Feature space for two selected facies

The more detailed facies curve from image example Johnson City I can be found in Figure 93 (top). Clearly visible is the facies curve within the red facies jumping from facies type "2" to "5" and back, there are some peaks of type "1" too. In contrast, facies type within the blue facies remains stable at type "5", only a few type "6" peaks occur. Even if both red and blue facies show a unique behavior along the facies curve, there is a large overlaps of both feature spaces (mean 2.5-3 and STD 0-4500). Hence, both different facies types are not well separated by different facies types. Small changes at the subdivisions produce relief. Shifting the vertical border separating facies type "1", "2" and "3", "4" from 4500 to 2500 provides lesser overlaps. Additionally, the large facies type "5" has been split in two different types. The new facies subdivisions are displayed in Appendix D, Figure 106; while the resulting facies curve according to Johnson City I, is drawn in Figure 93 (middle) and Figure 107, red curve. Now, red facies types range from "2" to "3" with only single peaks of type "5" and the blue facies is predominantly characterized by facies type "5". Only few overlaps occur and both facies types are well separated.

Final stage is an average filter in order to smoothen the facies curve by eliminating outliers. Instead of the original value, the median of a 51 value comprising window (25 previous values and 25 following) is drawn in Figure 93 (bottom) and Figure 107, black curve. This way, each whole facies type is more distinctive and represented by only one or two facies types.
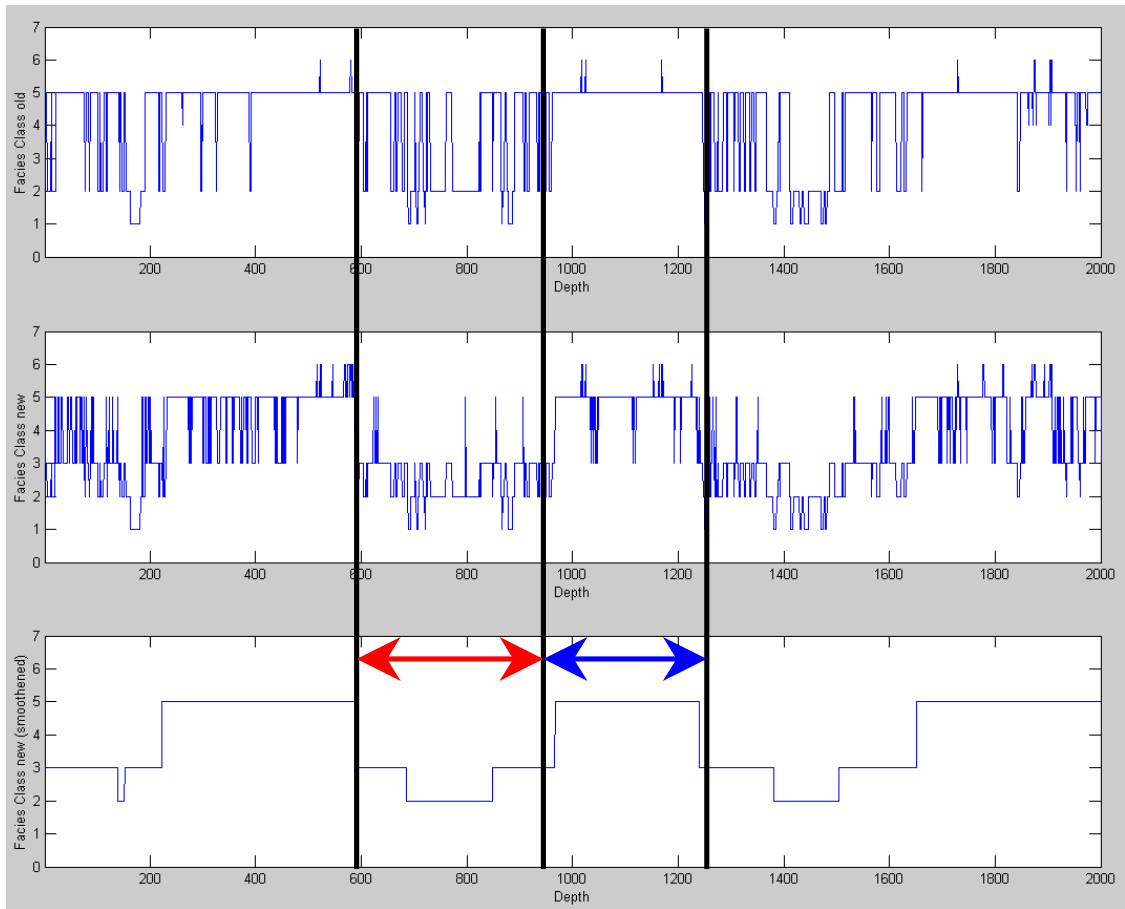
Figure 93 : Facies curve Johnson City I, according to subdivisions in Figure 90 (top), facies curve (middle) and smoothened facies curve (bottom) according to subdivisions in Figure 106

Both image examples Johnson City I and II reveal possibilities and difficulties according to the introduced facies classification procedure. Pre-processing, conversion from raw into attribute image as well as feature space creation can be performed completely automatic. Challenge is to distinguish the facies-type-subdivisions within the feature space. As shown so far, visual determined subdivisions are providing quite satisfying results. Each facies type shows unique response in the facies curve and similar facies types are reproduced similar. Unfortunately, the unique behavior is sometimes limited to unique scattering instead of only a single facies type. In other words, the facies curve jumps between two or more facies types. Picking two different facies types from the image log, researching each single feature space and determine subdivisions by the help of these feature spaces improves uniqueness. On the other side, focusing on a single case of two facies type to be differed can involves disturbing a second case. Assigning subdivisions is therefore not trivial. A possible solution would be to implement interactivity between visually determined facies types and the facies curve attached to the image log. Thus, changes in subdivision limits would immediately result in different facies curve response. Corrections and fine-tuning could be easily performed this way.

131

Once found a stable basis, facies classification extension is easily possible at any time. Each new log is processed in the previous described way and its STD mean couples are added to the feature space cross plot. When a new cluster appears there, new subdivisions can be assigned, so, by time, the classification is completing itself. This can be reproduced by comparing feature space Figure 89 and Figure 90. According to the continuity-axis range (STD 0 - 30.000), the Johnson City well represents actually only a piece of the Figure 89 (STD 0 – 300.000). This is naturally for mostly fine laminated or at least continuous facies types occur in the Johnson City well, e.g. unstructured types with low activity or low continuity are missing.

10 Summary & Conclusion

First, both synthetic and real acquired imaging data were used to investigate the possibility of extract geologic features in terms of dip parameters of inclining geological layers. On synthetic data basis, setting-characteristics according to the *Gray Level Co-occurrence Matrix* (GLCM) approach were created. Influence of evaluation direction, texel size and shape as well as step size for creating a GLCM were determined. As a next step, major attributes, calculated by the GLCM and representing different textural aspects of a given texel were researched, namely Contrast (CON), Correlation (COR), Entropy (ENT), Homogeneity (HOM), Inverse Difference Moment (IDM) and Variance (VAR). Limitations, dependencies, possible applications and general understanding regarding these six attributes were adopted.

As a first application, detectability of inclination and vertical position of two synthetic sinusoids with varying width and contrast to the background were researched. Therefore, synthetic data was created, converted into different attribute images and a self-developed correlation analysis was applied. By the help of this correlation analysis, a synthetic sinusoid with varying amplitude is sliding on the attribute image in order to detect sines there. Such a synthetic sine covering a sinusoid in the attribute image (representing e.g. a sedimentological boundary of an inclining layer) will result in a good correlation (respectively correlation coefficient). By filtering and picking only good correlations, the original sine structure in the image are determined quite steady. Not only the sine itself is detected, but in case of a sinusoid thicker than the chosen texel size, both the lower and upper sine's boundary too. Dip detection was successful from synthetic image data even after adding different amount of noise in terms of normal distributed random numbers up to a specified threshold value. The contrast sensitive attributes Contrast and Inverse Difference Moment (IDM), a square texel size of 3x3 to 4x4, a step size of 1x1 and the vertical evaluation shaped up as most suitable.

In the following, the gained experiences according to the synthetic images were applied to real imaging data. For first tests, two electrical images were chosen. Both image pieces show clear sinusoidal structures. The original correlation analysis was enhanced by varying azimuth, as well. Therefore, it was possible to determine sine's amplitude (gage for inclination) and phase (gage for azimuth). An additional image enhancing processing was applied to the attribute images in order to normalize anomalies and suppress unwanted structures. Unfortunately, the promising attribute Contrast was figured out to be not very suitable for real imaging data, because of being too sensitive to contrast

changes. Usually there are not so sharp contrasts resulting in lower Contrast values not standing clearly against the background. So, other attributes besides Contrast and IDM were researched and Entropy was detected to be capable of providing good results instead. Finally, the combination of texel attribute Entropy respectively IDM, texel size of 3x3 to 4x4, step size of 1x1 and vertical evaluation of the GLCM was found out to provide optimal dip calculation results.

Further investigations were performed on additional imaging data. Besides a different electric image, a piece of nuclear imaging data was used. In opposite to the previous used image data examples, these additional images are more complex in structure an appearance (e.g. fractures disturbing the lamination, low resolution regarding the nuclear image). Because of showing more artifacts like saw-tooth effects along boundaries or blurry structures, a pre-processing was applied in terms of a low pass filter in order to increase contrasts and smooth contours. Finally, the gained dip calculation results according to all image pieces were compared to dip results provided by the in-house software Dipex using a different statistical approach.

One of the main advantages of the GLCM method is the conversion of a raw data image into a texture property related attribute image. Using contrast sensitive attributes, focuses primary on contrast boundaries, which can be a criteria for sedimentological boundaries. In the course of this comparison, it becomes obvious that the GLCM method offers more geological information than using Dipex. Not only dip parameters are computed – sometimes slightly more correct than Dipex – but the exact position of assumed lithological boundaries and the thickness as well. Of course, partly dip quality is strongly depending on the underlying image quality. Especially the nuclear image example showed that the GLCM method has problems with blurry or non-sinusoidal shaped boundaries and inhomogeneous areas. Other problems are related to sine structures close together and not separated distinctively, resulting in detected sines covering both features. All together, while Dipex is faster and more robust due to image quality, the GLCM method can calculate dips more accurate and offers more geological information, like exact boundary detection and layer thickness.

Finally, the here introduced GLCM method comprises of

- "pre-processing"; interpolation of missing data, an image enhancement of the raw data image (low pass filter); discretization into a specified number of levels
- converting the discretized raw image into an attribute image by the help of a GLCM
- "post-processing"; low-pass, band-pass filtering and normalization of the attribute image
- correlation analysis
- determining high correlation peaks by filtering (low-pass, kind of gradient filter)

and is expected to be principally applicable to every kind of imaging technology and tool. Primary developed for electrical imaging, the GLCM method works for nuclear imaging also, just by adjusting some filter and discretization settings. Even if detailed fine-tuning of these settings can provide optimal dip calculation results, imaginable are presets for each imaging technology.

As a second application, the possibility of creating a rough facies classification by the help of attribute images was researched. In opposite to existing approaches, aim is to develop a simple and rough classification in order to differ approximately 10 major facies, like lamination, cementation, pebbled structure or structureless facies. Basis for facies classification is finding suitable feature uniquely describing different facies types. Here, feature continuity, describing continuous horizontal traceability of structures in the borehole image, and feature activity being a gage for the measurement value contrast between a geologic object (respectively structure) and the surrounding. Standard deviation (STD) and mean calculated from each attribute image depth level were found out to be suitable synonyms to describe continuity (STD) and activity (mean). To extract both parameters, the original raw image is converted into several attribute images, using a texel size of 4x4, a step size of 1x1 and a GLCM size of 45. Best results are provided by the STD calculated from the vertical evaluated Correlation image and the mean computed from the horizontal evaluated Entropy image. It was estimated that, cross plot of STD and mean form a unique cluster for each facies type.

As a first application, eight different image pieces assumed to represent different facies types were chosen. Then, STD and mean is calculated from each depth level and single image, as described and all mean vs. STD clusters are combined to create a feature space. As guessed, each cluster is located in respect to their texture characterized by feature activity and continuity. For example, the three laminated image example distinguish themselves by high continuity and low to high activity – depending on the layer contrasts. The other pieces are put in its proper place correctly, too. Overlaps occur only, when texture is similar, otherwise texture types are consequently separated. The two major objectives of uniqueness and uniformity are fulfilled.

After successfully creating a classification from different wells and by different electric images, a completely electric image log was called on. The log was converted in a vertical evaluated Correlation image for feature continuity determination as well as a horizontal evaluated Entropy image for feature activity. All mean vs. STD couples computed from both attribute images form the feature space. Visually, subdivisions were assigned respecting apparent clusters within the feature space. Therefore, a range of mean-STD couples will be signed to a specific facies type. Detailed investigation on the subdivisions and carefully adjusting can improve the classification significantly in terms of uniqueness and separation of each texture type occurring in the image log. Detected facies types correlate well with visual different facies types in the image log. Similar facies results in same types.

All together, results gained during the first application using different image pieces can be confirmed. By the described methodology, it is possible to extract feature continuity and activity by the help of attribute image converted from electric image logs. Furthermore, the two parameters can be used for a rough automatic facies (respectively texture) classification – once suitable subdivisions within the feature space are assigned. In principle, any number of facies types can be defined, but only a rough classification of approximately 10-20 types provides apparent textures in image logs described by a single facies type.

11 Outlook

In general, improvements of the pre-processing are expected to increase quality of detected dips additionally. In opposite to the background, sine structure is of low frequency, so, separation of desired structures and background variations by improved filtering methods is possible. Suppressing background structure produces more distinctive sedimentological boundary characteristics resulting in more unique attribute anomalies along these boundaries. Consequently, Correlation analysis will provide better dips.
Such a background-removing-proceeding is described among others in [Ye et al., 1998].

Automatic dip calculation from image logs by the GLCM method is only one application of using a GLCM for emphasizing structural features. By simply replacing the correlating geometric object used during the correlation analysis by other structures such as circles or ellipsoids, it is almost possible to detect every imaginable structure in the borehole (e.g. vugs, breakouts, intrusions…). In other words, instead of correlating a sinusoid with the image, a correlating ellipsoid with varying parameters (length of axes, position of centroid and angle of rotation) can detect geological structures forming a typical ellipsoidal area when crossing the borehole, such as vugs (see chapter 3.6). Main challenge will be to find suitable parameters to define a geometric object for converging with real geological structures.

Another possible continuation of the investigated structural analysis in this thesis is referring to downhole just-in-time interpretation. Resolution of imaging tools especially from electric imaging is getting higher and higher, and so the amount of acquired data gets. Unfortunately, real time transmission of this data to the surface is not keeping up with this development. Either resolution has to be downscaled for data transmission or only relevant data can be sent uplink. Relevant data can be e.g. dip parameters, because of being one of the most important parameters for deposit geologists. Thus, further research can focus on optimizing the developed GLCM method to fit downhole requirements. Even if the whole dip calculation is time consuming up to now, there are approaches for accelerating the computation like larger texel size, smaller image pieces, focusing on only one attribute image, etc …

Additional research can be done regarding the facies classification, too. In theory, feature activity and continuity have proven to be able to distinguish facies types. Improvements according to find synonyms by the help of attribute images might be possible, even if standard deviation and mean turn out to be a good first approach. Furthermore, several image logs comprising different texture types, especially marked by lower continuity, have to be processed in order to complete the feature space. Finally, additional and reasonable subdivisions have to be made to distinguish distinctive major facies types.

References

Antoine, J. N. and J. P. Delhomme (1990), "A Method to derive Ddips from Bed Boundaries in Borehole Images", SPE 20540, pp. 121-130.

BakerHughes (1992), "Introduction to Wireline Log Analysis", internal publication of BakerHughes WesternAtlas International Inc. (now BakerAtlas).

BakerHughes (1998), "Multi Propagation Resistivity (MPR) Technology Guide", internal publication by BakerHughes Inteq.

BakerHughes (1999), "Fluid Facts - Engineering Handbook", internal publication by BakerHughes Inteq.

BakerHughes (2003a), "Introduction to Borehole Imaging", Borehole Imaging, Product Knowledge Training, Advanced Technologies, Chapter 3, internal publication by BakerHughes BakerAtlas.

BakerHughes (2003b), "Processing and Artifacts", Borehole Imaging, Product Knowledge Training, Advanced Technologies, Chapter 6, internal publication by BakerHughes BakerAtlas.

BakerHughes (2003c), "An Introduction to Drilling Fluids", internal publication by BakerHughes Inteq.

BakerHughes (2004), "Borehole Imaging Services and Applications", internal publication by BakerHughes BakerAtlas.

Baule, A. (2003), "6 3/4" StarTrak™ Electrical Imaging while Drilling - Field Test Report for BETA", Internal publication by BakerHughes Inteq.

Baule, A. (2003), "Mud and Formation Resistivity", internal publication by BakerHughes Inteq, PowerPoint presentation.

Beblo, M. (1997), "Umweltgeophysik", Ernst & Sohn Verlag für Architektur und technische Wissenschaften GmbH.

Bethge, J. (2005), "6 ¾" StarTrak Version 2 Electrical Imaging LWD Field Test Report BETA BHD-8", Internal publication by BakerHughes Inteq.

Bloys, B., N. Davis, et al. (1994), "Designing and Managing Drilling Fluids", Oilfield Review, 04/1994.

Boortz, G. (1998), "Formeln und Tabellen, Physik, Astronomie, Arbeitslehre/Technik", Volume 1.

Chen, D. C.-K., T. Gaynor, et al. (2002), "Hole Quality: Gateway to Efficient Drilling", Offshore Technology Conference 2002 Houston, OTC 14277.

Clausen, L. (2003), "Evaluation of the rotational test measurement 2003 for development of the MWD resistivity imager StarTrak™", Internal publication by BakerHughes Inteq, Technical Report 25/03 - 28/03.

Contreras, C., H. Gamero, et al. (2003), "Invastigating Clastic Reservoir Sedimentology ", Oilfield Review, Spring 2003.

Dingsoyr, E., E. Pedersen, et al. (2004), "Oil Based Drilling Fluids with Tailor-Made Rheological Properties: Results from a Multivariate Analysis", Annual transactions of the Nordic Rheologic Society, 12.

Dortmann, N. B. (1976), "Fiziceskie Svoistva Gornich Porod i Polesnich Iskopamych", Izdat. Nedra, Moskva.

Dymmock, S. (2003), "Borehole Image Processing and Quality Control Manual", Internal publication by BakerHughes BakerAtlas.

Dymmock, S. (2005), "Geolological Features and their Appearance in Image Logs", Internal publication by BakerHughes BakerAtlas, PowerPoint Presentation.

Ellis, D. V. (1987), "Well Logging for Earth Scientists", Elsevier Science Publisging Co., Inc.

Enyre, L. M. (1989), "Finding Oil and Gas from Well Logs", Van Nostrand Reinhold, New York.

Evans, M. T. (2002), "Apparatus and Method for Wellbore Resistivity Determination and Imaging Using Capacitive Coupling", United States Patent Application Publication No. US 2002/0166699 A1.

Evans, M. T. and A. R. Burt (2002), "Image Focusing Method and Apparatus for Wellbore Resistivity Imaging", United States Patent No. US 6,348,796 B2.

Fulda, C. (2004a), "Toolface Measurement for StarTrak(TM)", Internal publication by BakerHughes Inteq, Technical Report.

Fulda, C. (2004b), "EM Theory", Internal publication by BakerHughes Inteq, Technical Report.

Fulda, C. (2004c), "Evaluation of the laboratory, real condition simulating measurement "3", April 7th 2003 for development of the MWD resistivity imager StarTrak™", Internal publication by BakerHughes Inteq, Technical Report 13/03.

Gao, D. (2001), "Method for Analyzing and Classifying Three Dimensional Seismic Information", United States Patent No. 6,226,596 B1.

Gao, D. (2003), "Volume Texture Extraction for 3D Seismic Visualization and Interpretation", Geophysics Vol 68 (July-August 2003).

Gao, D., S. D. Hurst, et al. (1998), "Computer-Aided Interpreatation of Side-Looking Sonar Images from the Eastern Intersection of the Mid-Atlantic Ridge with Kane Transform", Journal of Geophysical Research, Vol. 103, No. B9.

Gebrande, H., H. Kern, et al. (1982), "Elasticity and Inelasticity", Pysical Properties of Rocks, Springer Verlag Berlin.

Geology-Dictionary, I. (2005), "http://geology.com/dictionary/glossary-f.shtml".

Gianzero, S. C. (1993), "Logging Apparatus for Measurment of Earth Formation Resistivity", United States Patent No. 5,191,290.

Gilchrist, A., D. Patterson, et al. (2001), "Acoustic Logging Methods - Principle of Measurements - Theory and Application", Internal publication by BakerHughes Inteq.

Goldberg, D. (1997), "The Role of Downhole Measurements in Marine Geology and Geophysics", Reviews of Geophysics, 35, 3, August 1997, American Geophyscial Union.

Hall, J., M. Ponzi, et al. (1996), "Automatic extraction and characterization of geological features and textures from borehole images and core photographs", SPWLA 37th Annual Logging Symposium.

Hallenburg, J. K. (1998), "Standard Methods of Geophysical Formation Evaluation." Lewis Publishers.

Haralick, R. M., K. Shanmugam, et al. (1973), "Textural Features for Image Classification", IEEE Transactions on Systems, Man and Cybernatics, Vol. SMC 3, No. 6.

Harris, D. A., J. J. M. Lewis, et al. (1993), "The Identification of Lithofacies Types in Geological Imagery using Neural Networks", Eurocaipep 93, 20-22. September 1993.

Hassan, G. (2005), "Personal Communication concerning Density Calculation from Nuclear Image Logs".

Holupirek, J. (2004), "First evaluations of StarTrak™ data from Field Test at BETA, May 2003", internal publication by BakerHughes Inteq, Technical Report 02/04.

Jetschny, S. (2003), "Tongehaltsbestimmung an verschiedenen Logs der Bohrung Boetersen Z5a", Bachelor Thesis, TU Bergakademie Freiberg.

Jetschny, S. (2004a), "Development of StarTrak™ data from the Alba field, North Sea", Internal publication by BakerHughes Inteq, Technical Report 07/04.

Jetschny, S. (2004b), "Determination of high-side toolface while drilling for StarTrak(TM) service by means of magnetometer measurement -dataflow-", Internal publication by BakerHughes Inteq, Technical Report 08/04.

Johnson, D. E. and K. E. Pile (2002), "Well Logging in Nontechnical Language", PennWell Publishing Company.

Johnson, W. (1989), "Microinduction Diplog Instrument Development", AWS Report.

Kaufmann, A. A. and G. V. Keller (1989), "Induction Logging: Elsevier".

Kohonen, T. (1984), "Self-Organization and Associative Memory", Volume 8 of Springer Series in Information Science, Springer-Verlag, New York.

Kopf, M. (1977), "Fortschritte der Petrophysik", Physik der Erdkruste, Akademie-Verlag Berlin.

Kurkoski, P. (2005), "LWD Nuclear Tools", Internal publication by BakerHughes Inteq, PowerPoint Presentation.

Laastad, H., E. Haukefaer, et al. (2000), "Water-Based Formation Imaging and Resistivity Logging in Oil-Based Drilling Fluids-Todays Reality", Society of Petroleum Engineers 62977.

Laws, K. I. (1980), "Texture Image Segmentation", Technical Report USCIPI Report 940, Department of Electrical Engineering, Image Processing Institute, University of Southern California, Los Angeles.

Lofts, J. C., J. Bedford, et al. (1997), "Feature Recognition and the Interpretation of Images Acquired from Horizontal Wellbores", Developments in Petrophysics, Geological Society Special Publication No. 122.

Luthi, S. M. (1994), "Textural Segmentation of Digital Rock Images into Bedding Units using Texture Energy and Cluster Labels", Mathenatical Geology, Vol.26, No.2, 181-196.

Ma, S. D. and A. Gagalowicz (1983), "Natural Texture Synthesis with the Control of Correlation and Histogram ", 3rd Scandinavian Conference on Image Analysis, Copenhagen, Denmark, July 1983.

Morris, S. (2004), "StarTrak™, Azimuthal resistivity imaging-while-drilling: Data quality and interpretation", Internal publication by BakerHughes Inteq.

Pastusek, P. (2002), "Dynamic Model of Hole Oscillations - Rippling, Spiraling, and Hour-glassing", Internal publication by BakerHughes HughesChristensen.

Priest, J. (1994), "Image Logging under Difficult Conditions", PowerPoint Presentation held at Advances in Borehole and Core Imaging Conference, Aberdeen Formation Evaluation Society, March, 1994.

Priest, J. (2005), "Personal Communication concerning basic principles of the CBIL Acoustic Imaging Tool".

Reed, T. B. and D. Hussong (1989), "Digital Image Processing Techniques for Enhancement and Classification of SeaMarc II Side Scan Sonar Images", Journal of Geophysical Research, Vol. 94, No. B6.

Ritter, R. N., R. Chemali, et al. (2004), "High Resolution Visualization of near Wellbore Geology Using While-Drilling Electrical Images", SPWLA 45th Annual Logging Symposium.

Rivest, J. F. (1992), "Analyse Automatique d'Images geologiques: Application de la Morphologie Mathematique aux Images Diagraphies", PhD. Thesis, Ecole Nationale Superieure des Mines de Paris.

Rummelhart, D. E., G. E. Hinton, et al. (1986), "Learning internal Representation by Error Propagation", PDP Research Group, Eds. Cambridge, Mass.: MIT Press, p. 318-362.

Salafonov, O. and M. Salafonova (2004), "Dipex, Advanced Petrophysical Environment, User / Reference Resource", Internal publication by BakerHughes BakerAtlas.

Schlumberger (1999), "Borehole Image Measurements", internal publication by Schlumberger Oilfield Services Version 9.2.

Schön, J. H. (1998), "Physical Properties of Rocks, Fundamentals and Principles of Petrophysics", Handbook of Geophysical Exploration, Volume 18.

Serra, J. (1982), "Image Analysis and Mathematical Morphology ", Academic Press.

Telford, W. M., L. P. Geldart, et al. (2001), "Applied Geophysics", Cambridge University Press.

Torres, D., R. Strickland, et al. (1990), "A new Approach to Determining Dip an Strike using Borehole Images", SPWLA 31th Annual Logging Symposium, June 24-27, paper K.

Walker, M. J. (1999), "Advances in Wireline Data Acquisition in Synthetic-Based Mud Systems and Strategies for Improved Formation Evaluation", APPEA Journal.

Wang, T., S. Fang, et al. (2004), "Borehole Imaging in Nonconductive Muds: Resolution, Depths of Investigation and Impact of Anisotropy", SPWLA 45th Annual Logging Symposium.

Ward, J. H. (1963), "Hierarchical Grouping to optimize am Object Function", JASA, v.58.

Wurmstich, B., S. Forgang, et al. (1995), "Oil Based Mud Dipmeter: Evaluation of Different Approaches", internal publication by Western Atlas Logging Service.

Ye, S.-J., P. Rabiller, et al. (1997), "Automatic High Resolution Sedimentary Dip Detection on Borehole Imagery", SPWLA 38th Annual Logging Symposium, June 15-18, 1997.

Ye, S.-J., P. Rabiller, et al. (1998), "Automatic High Resolution Texture Analysis on Borehole Imagery", SPWLA 39th Annual Logging Symposium, May 26-29, 1998.

Zemanek, J. and e. al. (1969), "The Borehole Televiewer - A New Logging Concept for Fracture Location and Other Types of Borehole Inspection", Journal of Petroleum Technology, V.21, No.6.

Zhang, Z. and M. Simaan (1989), "Knowledge Based Reasoning in SEISIS - a Rule Based System for Interpretation of Seismic Sections Based on Texture", Geophysical Development Series, Volume 3, 3.

Appendix A

The basis for every effect relating to magnetic and electric fields is given by the Maxwell's laws (Equation 8). Among others, they describe the interaction between electric and magnetic field, the spread of each, electromagnetic waves and their interaction with different matters.

Equation 25

$$rot\vec{H} = \frac{\partial \vec{D}}{\partial t} + \vec{J}$$

$$rot\vec{E} = -\frac{\partial \vec{B}}{\partial t}$$

$$div\vec{D} = \rho$$

$$div\vec{B} = 0$$

with

- $\vec{H}$ = magnetic field intensity
- $\vec{B}$ = magnetic flux density
- $\vec{E}$ = electrical field intensity
- $\vec{D}$ = electric flux density or dielectric displacement
- $\vec{J}$ = electric current density
- ρ = electric charge density
- t = time

Furthermore the basic relationship between current density J and electric field intensity E and electric (respectively magnetic) flux density D (respectively B) and electric (respectively magnetic) field E (respectively H) are:

Equation 26

$$\vec{J} = \sigma\vec{E}$$

$$\vec{D} = \varepsilon\vec{E} + \vec{P}$$

$$\vec{B} = \mu(\vec{H} + \vec{M})$$

with:

- $\vec{P}$ = electric polarization
- $\vec{M}$ = magnetization
- σ = electric conductivity
- ε = $\varepsilon_0\,\varepsilon_r$ product of permittivity of the vacuum ε_0 and relative permittivity ε_r under conditions of isotropy, as a consequence piecewise homogeneity and thus ε being a constant and not a tensor
- μ = $\mu_0\,\mu_r$ product of magnetic permeability in vacuum μ_0 and relative magnetic permeability μ_r, under conditions of isotropy, as a consequence piecewise homogeneity and thus μ being a constant and not a tensor

If the geological formation is assumed not to be ferromagnetic (respectively ferroelectric) and charged (have a source), P and M will be neglected and $div\vec{D} = 0$. Thus, the Maxwell equations simplify themselves to:

$$rot\vec{H} = \varepsilon \frac{\partial \vec{E}}{\partial t} + \sigma \vec{E}$$

Equation 27 $\quad rot\vec{E} = -\mu \frac{\partial H}{\partial t}$

$$div\vec{E} = 0$$

$$div\vec{H} = 0$$

A differential equations system is now obtained and can be solved by choosing a harmonic changing electric field intensity E (respectively H) as a basic approach for a planar wave.

$$\vec{X}_0(\vec{r}, t) = \vec{X}_0(\vec{r})e^{i\omega t} \text{ with } \vec{X}_0(\vec{r}) \text{ is a vector with complex components}$$

Equation 28
$$E = E_0 e^{i(\omega t - \vec{k}\vec{r})} = E_0 e^{i\omega t} \cdot e^{-i\vec{k}\vec{r}}$$
$$H = H_0 e^{i(\omega t - \vec{k}\vec{r})} = H_0 e^{i\omega t} \cdot e^{-i\vec{k}\vec{r}}$$

Note that Equation 28 consists of a start field intensity, a time depending term ($e^{i\omega t}$) and a position depending term ($e^{-i\vec{k}\vec{r}}$), due to its complex character being in charge for a shift in amplitude (attenuation) and phase.

Now the first two Maxwell equations can be written as

Equation 29
$$rot\vec{H} = i\omega\varepsilon\vec{E} + \sigma\vec{E} = (i\varpi\varepsilon + \sigma)\vec{E}$$
$$rot\vec{E} = -i\omega\mu\vec{H}$$

with:
- ω = angular frequency and $\omega = 2\pi f$
- f = frequency of the oscillating field.
- k = complex vector in propagation direction of the planar wave
- r = position vector

Using the relationship between differential operators

Equation 30 $\quad rotrot\vec{H} = graddiv\vec{H} - \Delta\vec{H}$

and Equation 27, the first equation of the Equation 29 can be transformed into

Equation 31 $-\Delta\vec{H} = \text{rotrot}\vec{H} = (i\omega\varepsilon + \sigma)\cdot\text{rot}\vec{E}$

Combining Equation 29 and Equation 31 following relation is obtained

Equation 32 $-\Delta\vec{H} = (i\varpi\varepsilon + \sigma)(-i\varpi\mu)\vec{H} = -(\varepsilon\mu\varpi^2 + i\sigma\varpi\mu)\vec{H}$

$\Delta\vec{H} = \vec{k}^2\vec{H}$

with

Equation 33 $\vec{k}^2 = -\varepsilon\mu\varpi^2 + i\sigma\varpi\mu = \alpha + i\beta$

Appendix B

Material	μ_r
Gold	0,999971
Water	0,999991
Zinc	0,999986
Aluminum	1,00002
Chromium	1,00028
Air	1,00000037
Platinum	1,0002
Cobalt	80 – 200
Iron	250 – 680
Nickel	280 – 2500
Special alloys	up to 900000

Table 14 : Magnetic permeability for different materials [Boortz, 1998]

Material	ε_r
Dolomite	8 - 10
Calcite	8 - 12
Quartz	5 - 7
Sand	
dry	3 - 5
wet	20 - 30
Shale	5 - 15
Clay	5 - 40
Granite	4 - 8
Mica	5 - 9
Rock salt	5,5 – 6,5
Amber	2,8
Soil	
sandy	2,6 – 25
loamy	2,5 – 19
clay	2,4 – 15
Water (20°C)	80,4
Ice	3 - 3,5
Ethanol	25
Air	1,0006
Hydrogen	1,0003

Table 15 : Dielectric permittivity for different materials [Beblo, 1997; Boortz, 1998]

Material	ρ in Ω
Atmospheric air	10^{14}
Water	
distilled	10^{10}
58,5 mg/l NaCl	89,4
585 mg/l NaCl	9,34
5850 mg/l NaCl	1,03
Oil	$10^9 - 10^{16}$
Soil	
sandy	$150 - 7 \cdot 10^3$
loamy	$50 - 9 \cdot 10^3$
clay	$20 - 4 \cdot 10^3$
Sand	
dry	10^5
wet	$10^3 - 10^4$
Clay	
dry	$30 - 10^3$
wet	$1 - 30$
Rock salt	$10^5 - 10^7$
Marl	$5 - 200$
Shale	$10 - 10^3$
Silt	$10 - 10^3$
Iron	$1 \cdot 10^{-4}$
Copper	$1.7 \cdot 10^{-5}$
Silver	$1.6 \cdot 10^{-5}$
Granite	$300 - 3 \cdot 10^4$
Quartzite	$3 \cdot 10^3 - 10^5$
Quartz	$2 \cdot 10^{14}$
Calcite	$9 \cdot 10^{13}$
Mica	$10^{10} - 10^{14}$
Feldspar	$10^{11} - 10^{12}$
Dolomite	$4 \cdot 10^{13}$

Table 16 : Resistivity for different materials [Beblo, 1997; Boortz, 1998; Baule, 2003]

Material	v_p in km/s	v_s in km/s
Water		
Distilled	1.497	-
0,1% NaCl	1.565	-
0,2%	1.689	-
Drilling mud	1.830	-
Oil	1.280	-
Sandstone	3.63	2.26
Rock salt	4.57	
Marl	5.41	
Shale	3.66	
Silt	4.42	
Granite	5.01	
Quartzite	4.01	2.56
Gneiss	5.68	3.05
Gabbro	6.42	
Basalt (dry)	5.41	3.06
Dolomite	5.0	2.75

Table 17 : Mean velocity of elastic waves [Dortmann, 1976; Kopf, 1977; Gebrande et al., 1982; Ellis, 1987]
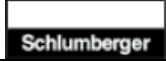
	Vertical resolution	Logging speed	Hole size	Hole coverage	Button-number	Resistivity contrast range Rt/Rm
STAR (Baker Hughes)	0.2"	600 ft/hr	6.0" – 21"	60% in 8"	144	4000 (STARIII)
FMI (Schlumberger)	0.2"	1800 ft/hr	6.25" – 21"	80% in 8"	192	20.000
FMS-B (Schlumberger)	0.25"	1800 ft/hr	4.5" – 15"	30% in 8"	64	20.000
EMI (Halliburton)	0.2"	1800 ft/hr	6.25" – 21"	62% in 8"	150	20.000
XRMI (Halliburton)	0.2"	1800 ft/hr	6.25" – 21"	62% in 8"	150	100.000
HMI	0.2"	1800 ft/hr	6.25" – 21"	62% in 8"	150	20.000

Figure 94 : Competitor analysis electric imaging in WBM (wireline); adapted from [BakerHughes, 2003a]
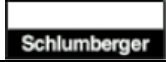
	Vertical resolution	Logging speed	Hole size	Hole coverage	Button-number	Max BHT
EARTH (Baker Hughes)	0.3"	19200 pixels/min	6.0" – 21"	63% in 8"	48	350 °F
OBMI (Schlumberger)	1.2"	8000 pixels/min	7" – 21"	32% in 8"	20	320 °F
OBMI-2 (Schlumberger)	1.2"	16000 pixels/min	7" – 21"	32% - 64% in 8"	40	320 °F
OBMI Slimhole (Schlumberger)	1.2"	8000 pixels/min	5.8" – 15"	32% in 8"	20	400 °F

Figure 95 : Competitor analysis electrical imaging in OBM (wireline); adapted from [BakerHughes, 2003a]
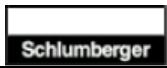
	Vertical & azimuthal resolution	Logging speed	Hole size	Mud weight	Max BHT
CBIL	0.3" at 250 samples	600 ft/hr	4.5" – 16"	< 18 lb/gal	400 °F
UBI	0.2" (0.4") at 180 samples	400 (800) ft/hr	4.5" – 12"	< 16 lb/gal	350 °F
CAST-V	0.3" at 200 samples	600 ft /hr	5" – 12.5"	8 - 15 lb/gal	350 °F
AST	0.35" at 250 samples	600 ft/hr	4.5 - 12"	8 - 15 lb/gal	300 °F

Figure 96 : Competitor analysis acoustic imaging (wireline); adapted from [BakerHughes, 2003a]

	BAKER HUGHES	HALLIBURTON	Schlumberger	Precision Drilling
Density	available	available	available	available
Porosity	available	available	available	available
Caliper	available	available	available	available
Azimuthal (image) Density	available	available	available	n/a
Azimuthal (image) Porosity	n/a	available	available	n/a
Azimuthal (image) Caliper	pending	available	available	n/a
Density image	available	available	available	n/a
Caliper image	pending	available	available	n/a
"Sourceless" density	n/a	n/a	available	n/a
Mineralogy	n/a	n/a	available	n/a

Figure 97 : Competitors nuclear imaging (LWD); adapted from [Kurkoski, 2005]

Appendix C

Attribute name	Abbreviation	Equation	Related attribute
Angular Second Moment Homogeneity	HOM	$$ASM = \sum_{i=1}^{N_g}\sum_{j=1}^{N_g}\left[\frac{S(i,j)}{R}\right]^2$$	SAV
Contrast	CON	$$CON = \sum_{n=0}^{N_g-1} n^2 \left[\sum_{i=1}^{N_g}\sum_{j=1}^{N_g}{}_{|i-j|=n}\frac{S(i,j)}{R}\right]$$	
Correlation	COR	$$Cor = \frac{\sum_{i=1}^{N_g}\sum_{j=1}^{N_g}(i\cdot j)\frac{S(i,j)}{R} - \mu_x\mu_y}{\sigma_x\sigma_y}$$	IMC, MCC
Variance (Sum of Squares)	VAR	$$Var = \sum_{i=1}^{N_g}\sum_{j=1}^{N_g}(i-\mu)^2\frac{S(i,j)}{R}$$	SVAR, DVAR
Inverse Difference Moment	IDM	$$IDM = \sum_{i=1}^{N_g}\sum_{j=1}^{N_g}\frac{S(i,j)}{R\cdot\left[1+(i-j)^2\right]}$$	
Sum Average	SAV	$$SAV = \sum_{i=2}^{2\cdot N_g} i\cdot S_{x+y}(i)$$	HOM
Sum Variance	SVAR	$$SVAR = \sum_{i=2}^{2\cdot N_g}(i-ENT)\cdot S_{x+y}(i)$$	VAR + ENT
Sum Entropy	SENT	$$SENT = -\sum_{i=1}^{N_g}\sum_{j=1}^{N_g} S_{x+y}(i)\cdot\log\left[S_{x+y}(i)\right]$$	ENT
Entropy Randomness	ENT	$$ENT = -\sum_{i=1}^{N_g}\sum_{j=1}^{N_g}\frac{S(i,j)}{R}\cdot\log\left(\frac{S(i,j)}{R}\right)$$	SVAR, SENT, DENT
Difference Variance	DVAR	$$DVAR = \text{variance of } S_{x-y}$$	VAR
Difference Entropy	DENT	$$DENT = -\sum_{i=1}^{N_g}\sum_{j=1}^{N_g} S_{x-y}(i)\cdot\log\left[S_{x-y}(i)\right]$$	ENT
Information Measures of Correlation	IMC	$$IMC1 = \frac{HXY - HXY1}{\max(HX,HY)}$$	COR
		$$IMC2 = (1 - e^{[-2\cdot(HXY2-HXY)]})^{1/2}$$	COR
Maximum Correlation Coefficient	MCC	$$MCC = (\text{second largest eigenvalue of } Q)^{1/2}$$	COR

Table 18: Texel attributes [Haralick et al., 1973]

with

$$S_y(i) = \sum_{i=1}^{N_g} \left[\frac{S(i,j)}{R} \right]$$

$$S_x(i) = \sum_{j=1}^{N_g} \left[\frac{S(i,j)}{R} \right]$$

$$S_{x+y}(k) = \sum_{i=1}^{N_g} \sum_{j=1}^{N_g} {}_{i+j=k} \left[\frac{S(i,j)}{R} \right] \qquad k = 2,3,...,2 \cdot N_g$$

$$S_{x-y}(k) = \sum_{i=1}^{N_g} \sum_{j=1}^{N_g} {}_{|i-j|=k} \left[\frac{S(i,j)}{R} \right] \qquad k = 0,1,...,N_g - 1$$

$$HXY = -\sum_{i=1}^{N_g} \sum_{j=1}^{N_g} \left[\frac{S(i,j)}{R} \right] \cdot \log \left[\frac{S(i,j)}{R} \right]$$

$$HXY1 = -\sum_{i=1}^{N_g} \sum_{j=1}^{N_g} \left[\frac{S(i,j)}{R} \right] \cdot \log \left[S_x(i) \cdot S_y(j) \right]$$

$$HXY1 = -\sum_{i=1}^{N_g} \sum_{j=1}^{N_g} \left[S_x(i) \cdot S_y(j) \right] \cdot \log \left[S_x(i) \cdot S_y(j) \right]$$

$$Q(i,j) = \sum_k \frac{S(i,k) \cdot S(j,k)}{R \cdot S_x(i) \cdot S_y(k)}$$

μ_x, μ_y = mean of S_x and S_y

σ_x, σ_y = standard deviation of S_x and S_y

Direction						
horizontal				vertical		
BinCount	**Degree**	**Inch**	**cm**	**Line**	**Inch**	**cm**
1	6	0.45	1.13	1	0.21	0.54
2	12	0.89	2.26	2	0.43	1.08
3	18	1.34	3.39	3	0.64	1.63
4	24	1.78	4.52	4	0.85	2.17
5	30	2.23	5.65	5	1.07	2.71
6	36	2.67	6.78	6	1.28	3.25
7	42	3.12	7.91	7	1.49	3.79
8	48	3.56	9.04	8	1.71	4.33
9	54	4.01	10.17	9	1.92	4.88
10	60	4.45	11.30	10	2.13	5.42
12	72	5.34	13.57	12	2.56	6.50
14	84	6.23	15.83	14	2.99	7.59
16	96	7.12	18.09	16	3.41	8.67
18	108	8.01	20.35	18	3.84	9.75
20	120	8.90	22.61	20	4.27	10.84
22	132	9.79	24.87	22	4.69	11.92
24	144	10.68	27.13	24	5.12	13.00
26	156	11.57	29.39	26	5.55	14.09
28	168	12.46	31.65	28	5.97	15.17
30	180	13.35	33.91	30	6.40	16.26
35	210	15.58	39.57	35	7.47	18.97
40	240	17.80	45.22	40	8.53	21.67
45	270	20.03	50.87	45	9.60	24.38
50	300	22.25	56.52	50	10.67	27.09
55	330	24.48	62.17	55	11.73	29.80
60	360	26.70	67.83	60	12.80	32.51
				65	13.87	35.22
				70	14.93	37.93
				75	16.00	40.64
				80	17.07	43.35
				85	18.13	46.06
				90	19.20	48.77

Table 19 : Scaling conversion model - 8.5" borehole

Multi-channel Correlation Algorithm
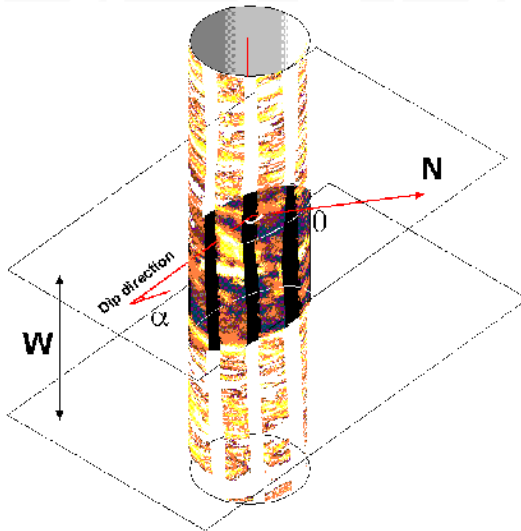
Picture for explanation of multi-channel correlation

Input

1. Window length in samples - W
2. Base curve number - NB (the bound points of the base curve have been chosen for correlation).
3. Total pad curve number - N.
4. Intervals of button data -Xij (i - pad curve number, j - sample number)
5. Pad curve space level - Xlev
6. Intervals of radius data Rij (i - arm number, j - sample number)
7. Radius curve space level - Rlev
8. Search angle - San
9. Dip angle step - Anlev
10. Dip azimuth step - Azlev
11. Array of bound points - Zi,j (i - pad curve number, j - point number)
12. Current base curve point -i (current depth)

Output

The output for the multi-channel correlation algorithm is the dip angle and azimuth of the best fit plane and maximum correlation function value.

1. Using search angle and dip angle step, compute the number of the possible dip angle - Nan and dip azimuth - Naz steps.

$$Nan = San/Anlev$$
$$Naz = 360/Azlev$$

2. Set the current bedding plane angle at $\alpha = 0$ and the azimuth at $\theta = 0$
3. Compute the difference (displacement) between the current base curve point depth and the depth of the bedding plane and tool axis intersection.

$$d_{NB} = R_{NB,ir}\cos(\theta + \phi)tg\alpha$$

where ϕ is a base sensor curve azimuth and $ir = \dfrac{Z_{NB,i}}{Rlev}$.

The crossing bedding plane and tool axis depth z0 is computed

$$z_0 = Z_{NB,i} - d_{NB}$$

154

4. Compute displacements for the other pad curves.

$$d_k = \widehat{R}_k \cos(\theta + \phi_k) \quad k = \overline{1, N} \quad k \neq NB$$

where $\widehat{R}_k$ is the radius distance minimizes

$$\min_R \; |R_{k, index} - R\cos(\theta + \phi_k)tg\alpha|$$

where

$$index = ir - \frac{R\cos(\theta + \phi_k)tg\alpha}{Rlev}$$

5. For each pad curve, calculate the sample numbers corresponding to displacements.

$$m_k = \frac{z_0 + d_k}{Xlev} \qquad k = \overline{1, N}$$

6. For the current dip value compute the correlation function $S(\alpha, \theta)$.

$$S(\alpha, \theta) = \frac{\sum\limits_{p = -W/2}^{W/2} \left[\frac{1}{N} \sum\limits_{k=1}^{N} (X_{k, m_k + p} - \bar{X}_k) \right]^2}{\frac{1}{N} \sum\limits_{p = -W/2}^{W/2} \sum\limits_{k=1}^{N} (X_{k, m_k + p} - \bar{X}_k)^2}$$

where $\bar{X}_k$ is the signal average on the interval $[m_k - W/2, m_k + W/2]$.

Save the current correlation function value as the element of the two-dimensional array (matrix) E[Nan][Naz]. Row and column numbers of this element are $\overline{\frac{\alpha}{Anlev}}$ and $\overline{\frac{\theta}{Azlev}}$, respectively.

7. Set the current dip angle at $\alpha = \alpha + Anlev$. If $\alpha \leq San$ go to Step 3, otherwise $\alpha = 0$.

8. Set the current dip angle at $\theta = \theta + Azlev$. If $\theta \leq 360$ go to Step 3.

9. Find the array E's maximum element and transform its row and column numbers to an evaluation of the dip components $\widehat{\alpha}, \widehat{\theta}$. If E[m][n] is a maximum element,

$$\widehat{\alpha} = mAnlev \qquad and \qquad \widehat{\theta} = nAzlev$$

Figure 98 : Excerpt of Dipex users manual; Multi-channel-Correlation Algorithm

155

Common Parameters Page

The common parameters are very similar to the parameters of pair interval correlation. On the Common Parameters page there are several edit boxes to be filled in:

Search Angle

The search angle is the maximum apparent dip angle you want to get as a result of processing and its value can vary from zero to 80 degrees (see Pair Correlation Parameters Dialog). Multi-channel correlation has the additional ability to detect an insufficient search angle in run-time. If the correlation surface maximum (see Correlation Surface View) often lies on the bottom of the multi-channel function plot, you need to expand the surface window by increasing the search angle. Moreover, you can first process data using a small search angle and then reprocess some interesting intervals with an increased search angle. The units used in this process are degrees.

Correlation Window

The correlation window is the thickness of the correlation disk. The correlation disk space shape is formed by the borehole wall and two parallel planes crossing this wall. All pad curves' samples that belong to the shape participate in the correlation function calculation. All notes about correlation window length listed below for pair correlation apply to multi-channel correlation as well, except:

- The random noise influence should be significantly lower. The number of signals taking part in the correlation function calculation is significantly greater than two (6 or even 8 for 8-arm dipmeter tools).
- Geometric noise can be detected easily if we have two or more meaningful peaks in the correlation function surface (do not forget that this surface has two coordinates: dip angle and azimuth). The correlation disc may have captured at least two geologic features.
- The above changes should allow you to shorten the correlation window length to 1 foot or less and obtain more detail in the final dip distribution, even in the face of noisy data and rapidly changing dip.

Step Distance

Depths change as the correlation disk is moved between two successive rounds of correlation. Usually, the step distance is equal to 25 or 50 percent of the correlation disk thickness. This parameter is used when processing runs with the fixed step distance mode (see Mode Parameters Page below). The units required for this procedure are feet or meters.

Magnetic Declination

Magnetic declination is the horizontal angle from true north to magnetic north. The value of magnetic declination is read from the XTF file, but if it is zero, you can set it manually. The units required for this procedure are degrees.

An animated figure is drawn to the right of the parameter field, which explains the principle of the multi-channel correlation process. The variation of the correlation disk position and thickness depends upon the current values of the search angle and correlation window.

Mode Parameters Page

Fixed Step

There are currently two options for multi-channel correlation that you can use. A checked *Fixed Step Distance check* box means that processing will use a fixed-length depth shift between successive positions of the correlation disk. Otherwise, processing will use a variable step distance.

Point-to-Point

The Point-to-point mode allows you to find curve points corresponding to geological boundaries that lie inside the tolerance of the multi-channel-found plane and use the points' coordinates for dip computation. Note that the number of points found for one boundary may be less than or equal to the number of sensors. If the number of points is greater than 3, the Least Squares method of averaging is used to calculate plane depth, dip angle, and direction. Obviously, if the number of points is less than 3, no dip is computed.

It is possible to use the fixed step distance and point-to-point modes simultaneously but the interpretation results may be unclear.

No Boundary Crossing

The No Boundary Crossing mode allows to eliminate all calculated plane boundaries if they cross the previous one.

Save

Save feature allows you to write current parameter values for all pages to the registry.

Note: If you open several XTF files, you can set correlation parameters independently for each.
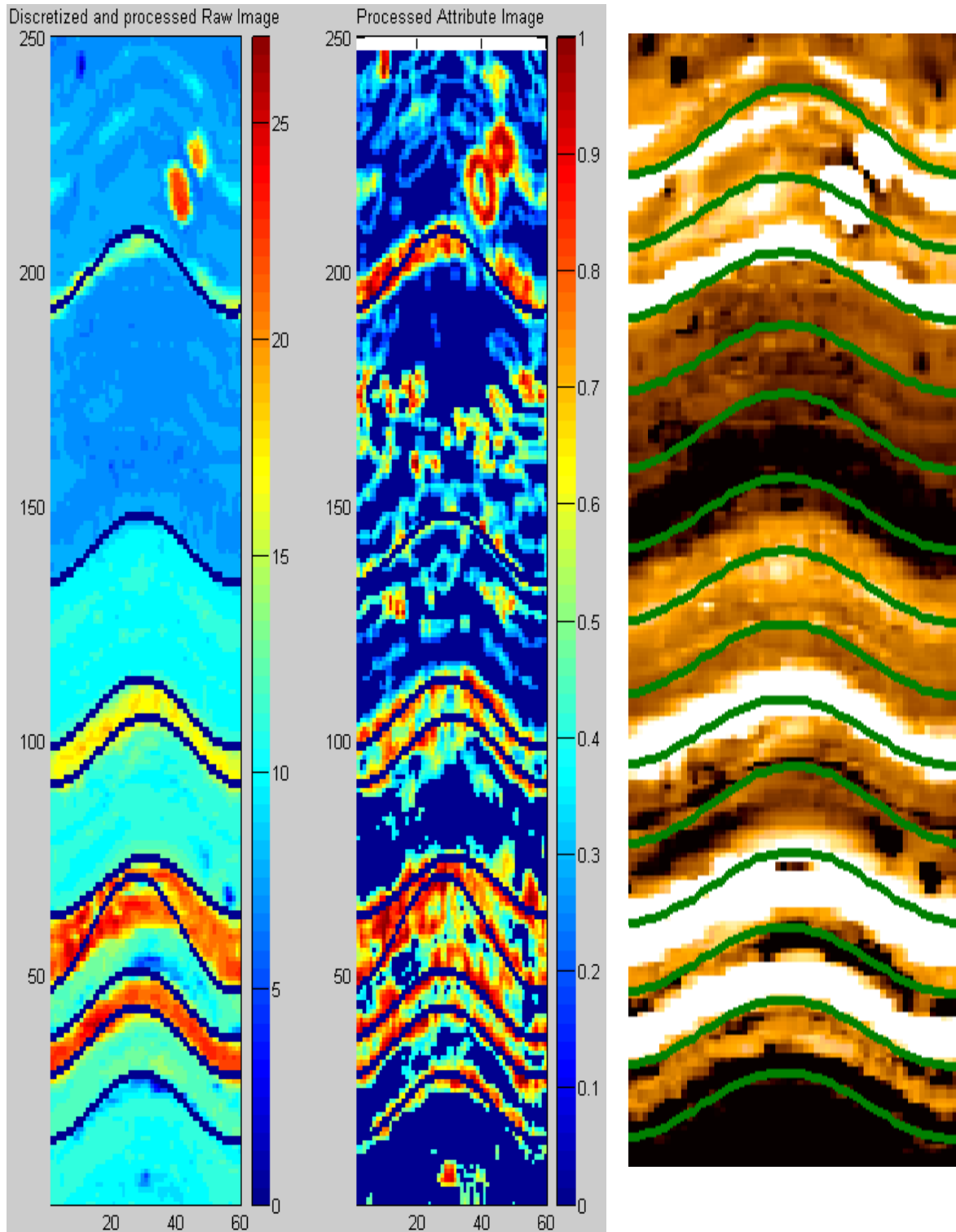
Figure 99 : Excerpt of Dipex user's manual; Common and Mode parameter page for Multi-channel dip computation

156
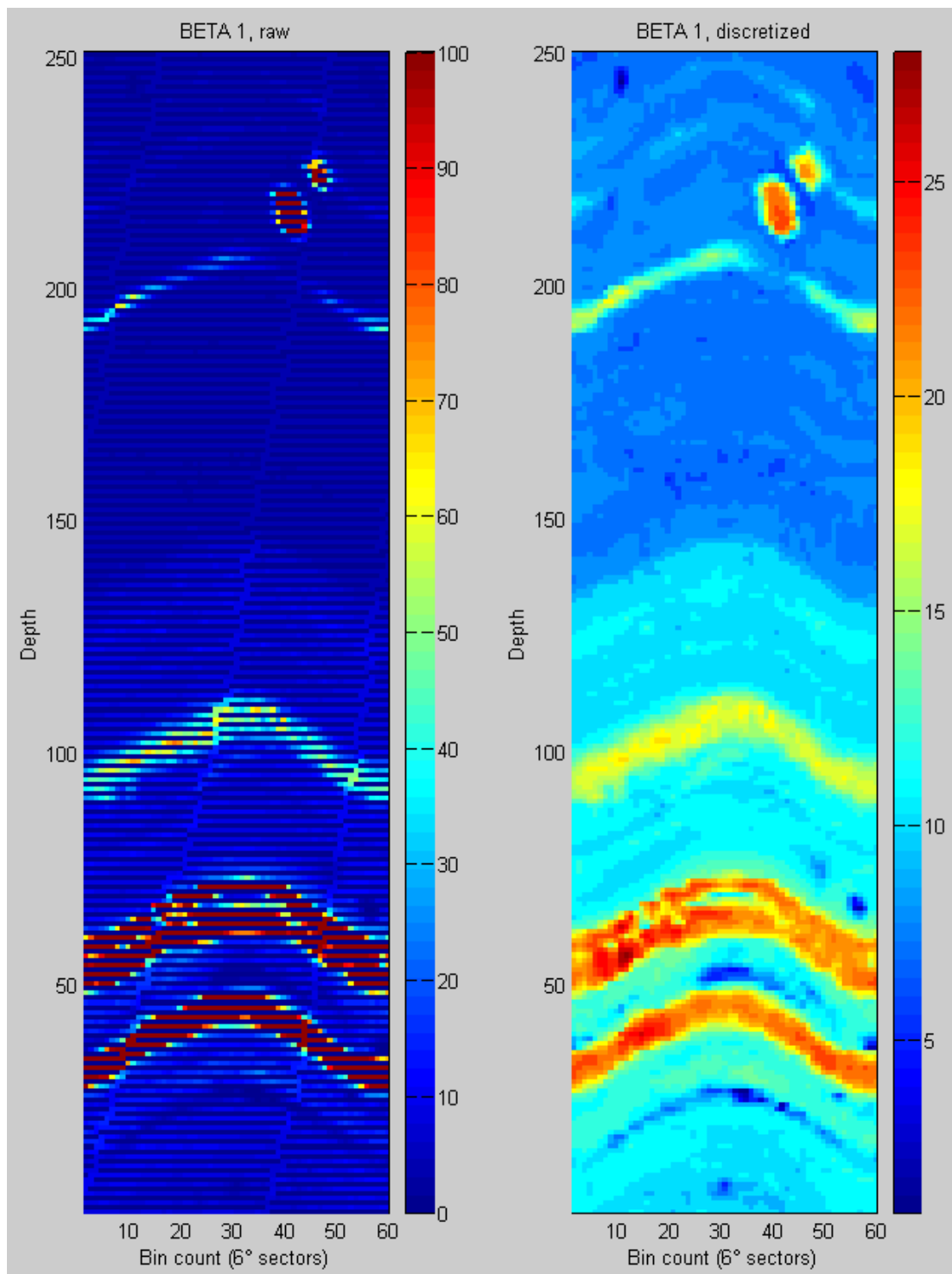
Figure 100 : raw and discretized (32 levels) BETA field test image
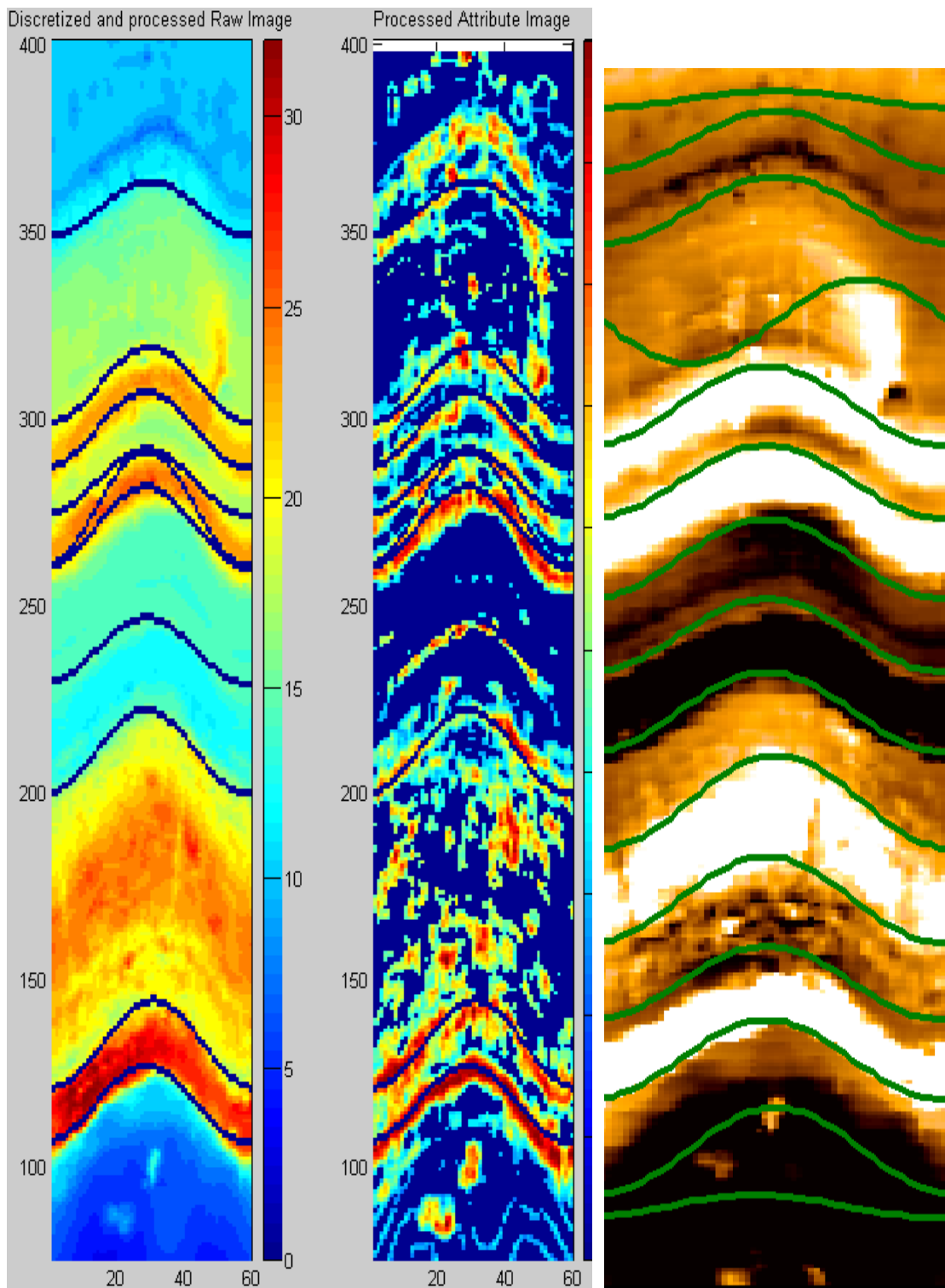   **2003/05/30 10:01:14 - 10:03.19 (BETA1)**
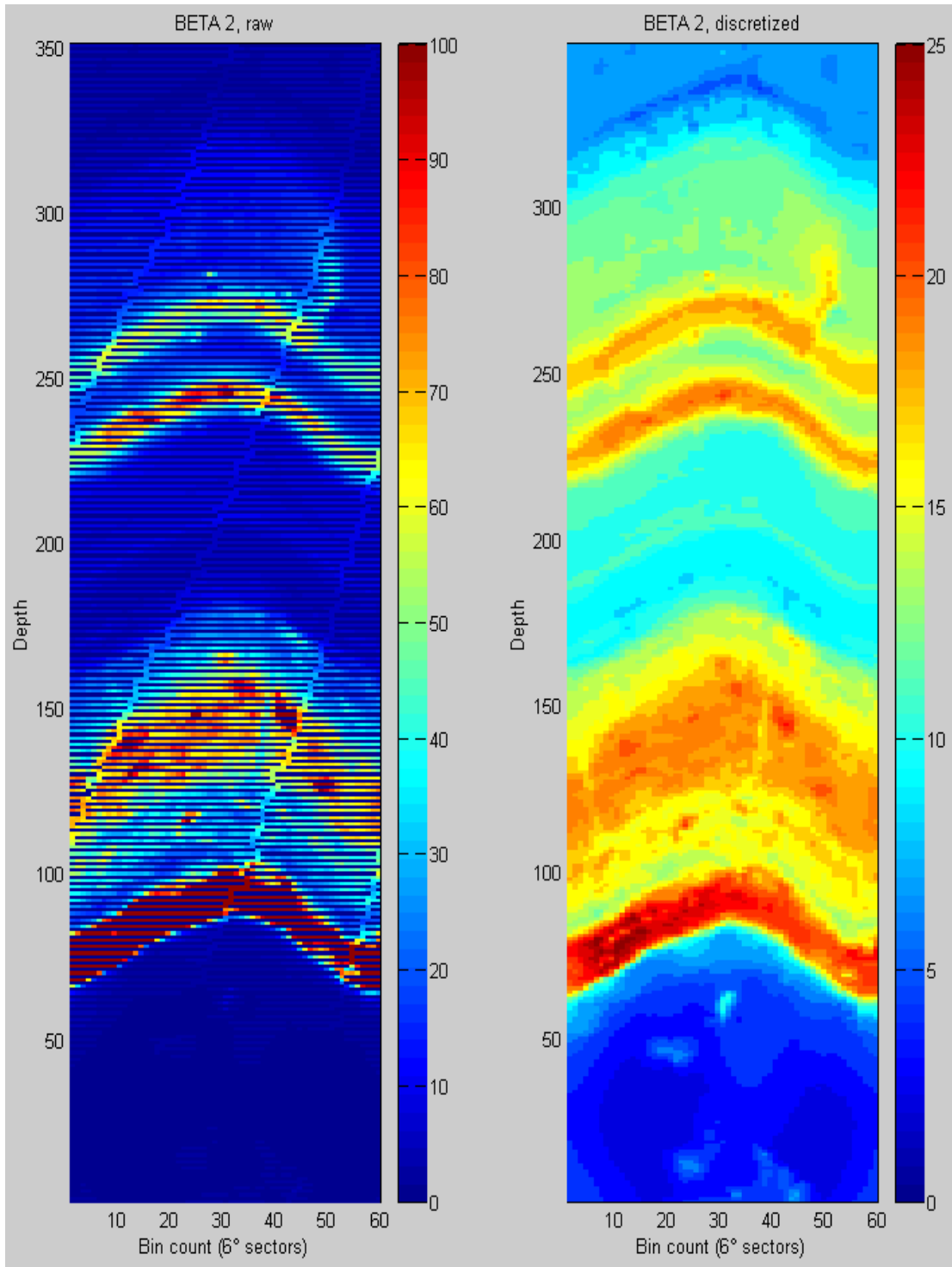
Figure 101 : raw and discretized (32 levels) BETA field test image
     2003/05/30 10:09:09 - 10:12:04 (BETA2)

158

electrical raw and IDM attribute image with sinusoids detected by the GLCM method
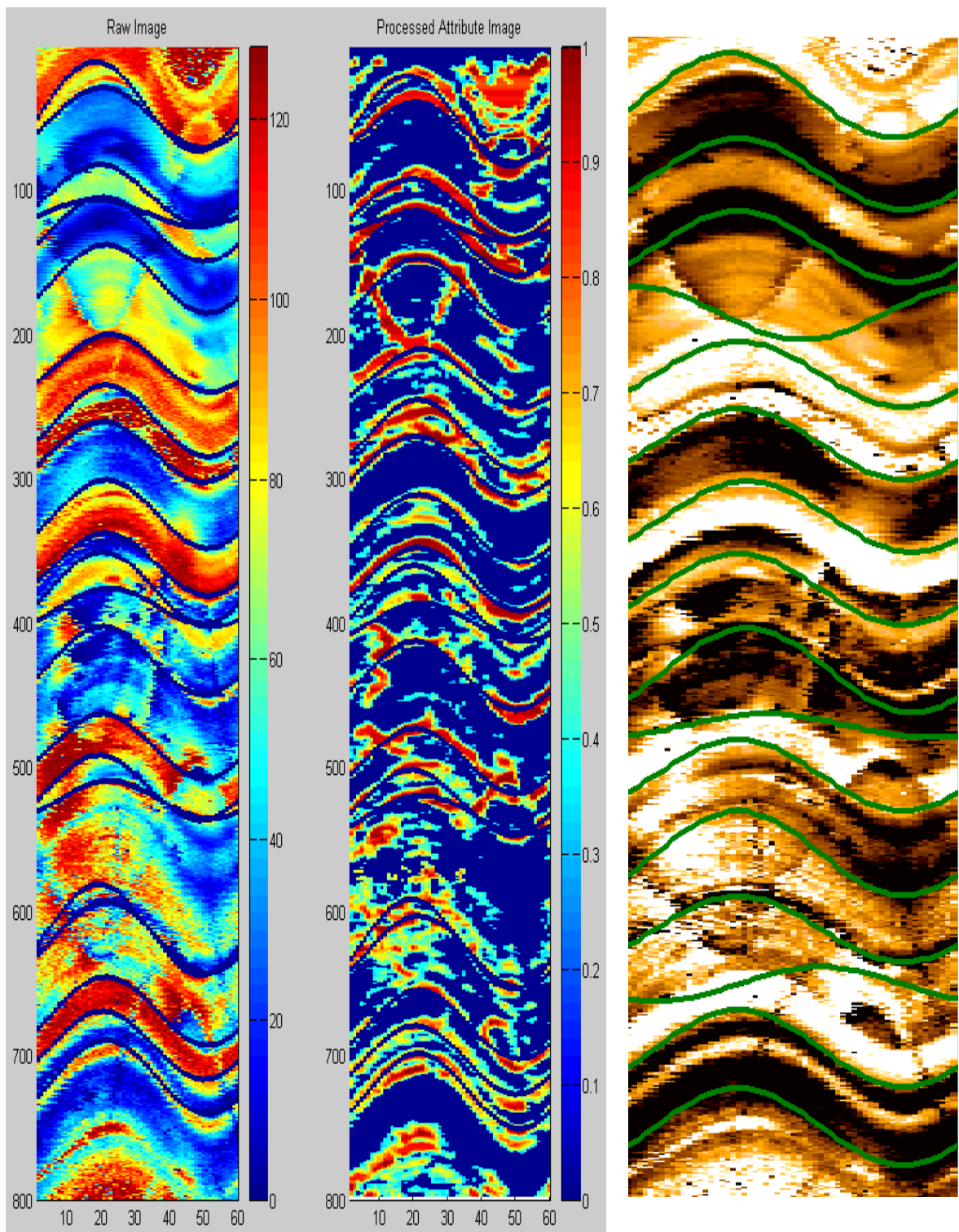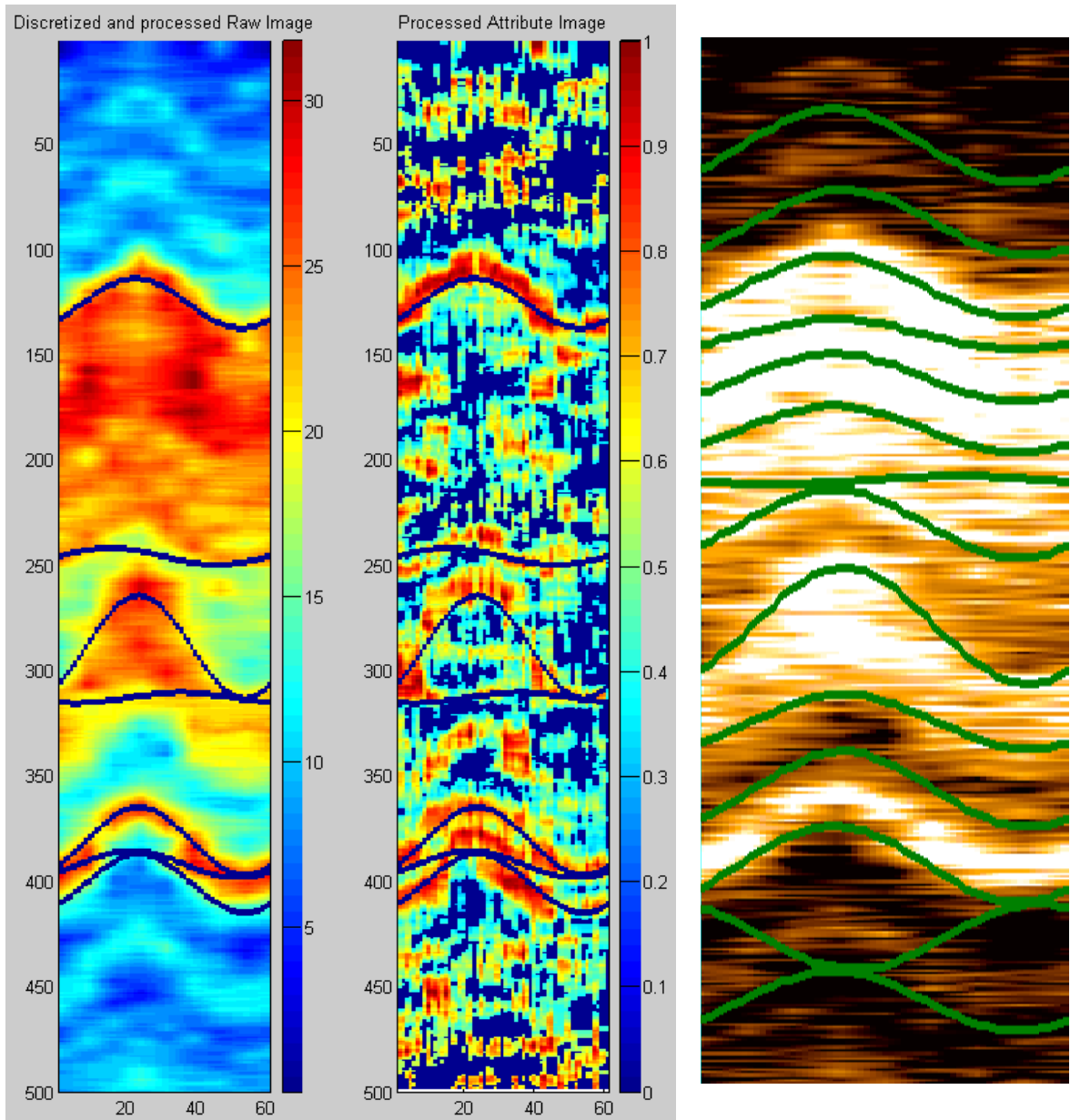
Electrical raw image with sinusoids detected by Dipex

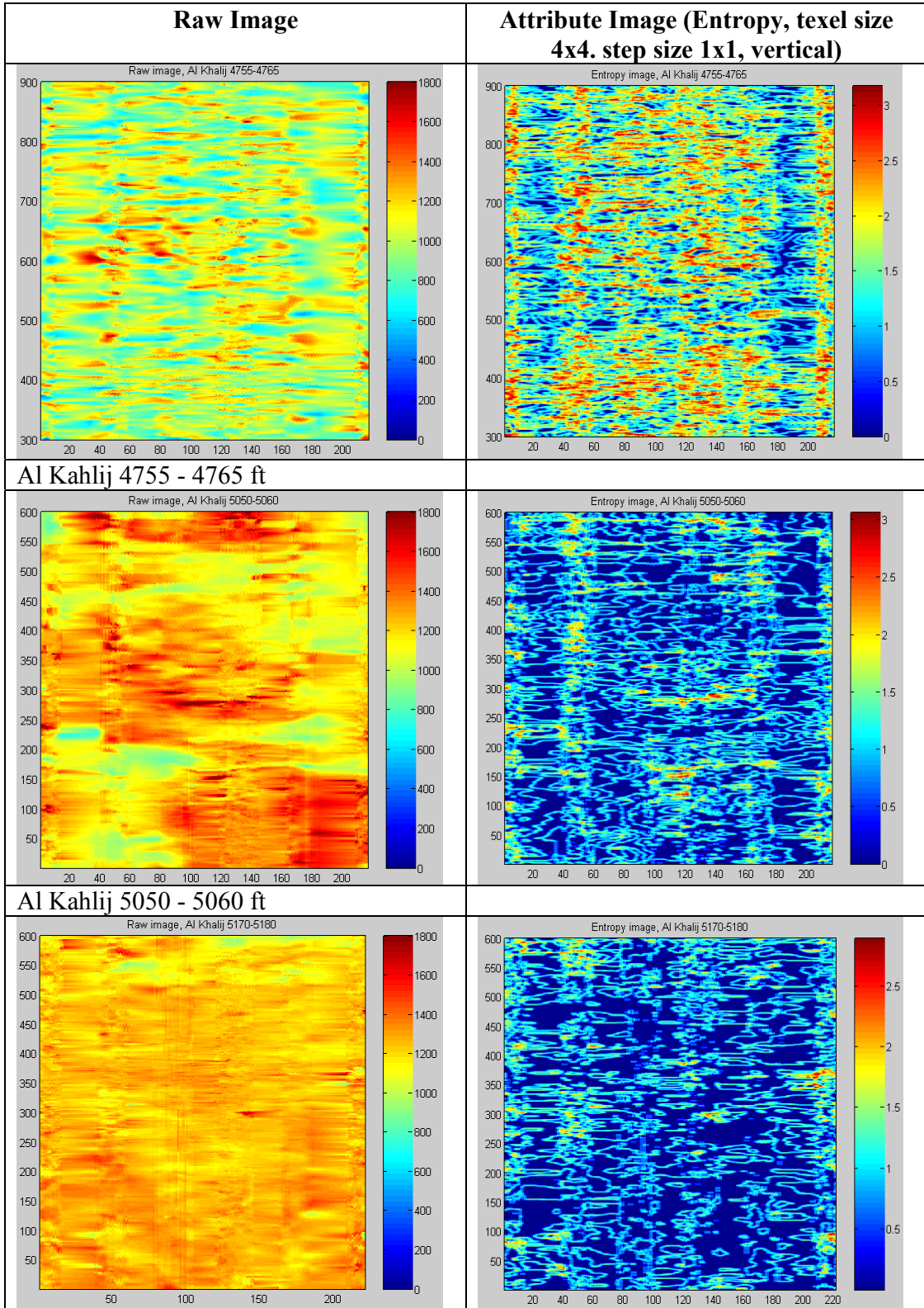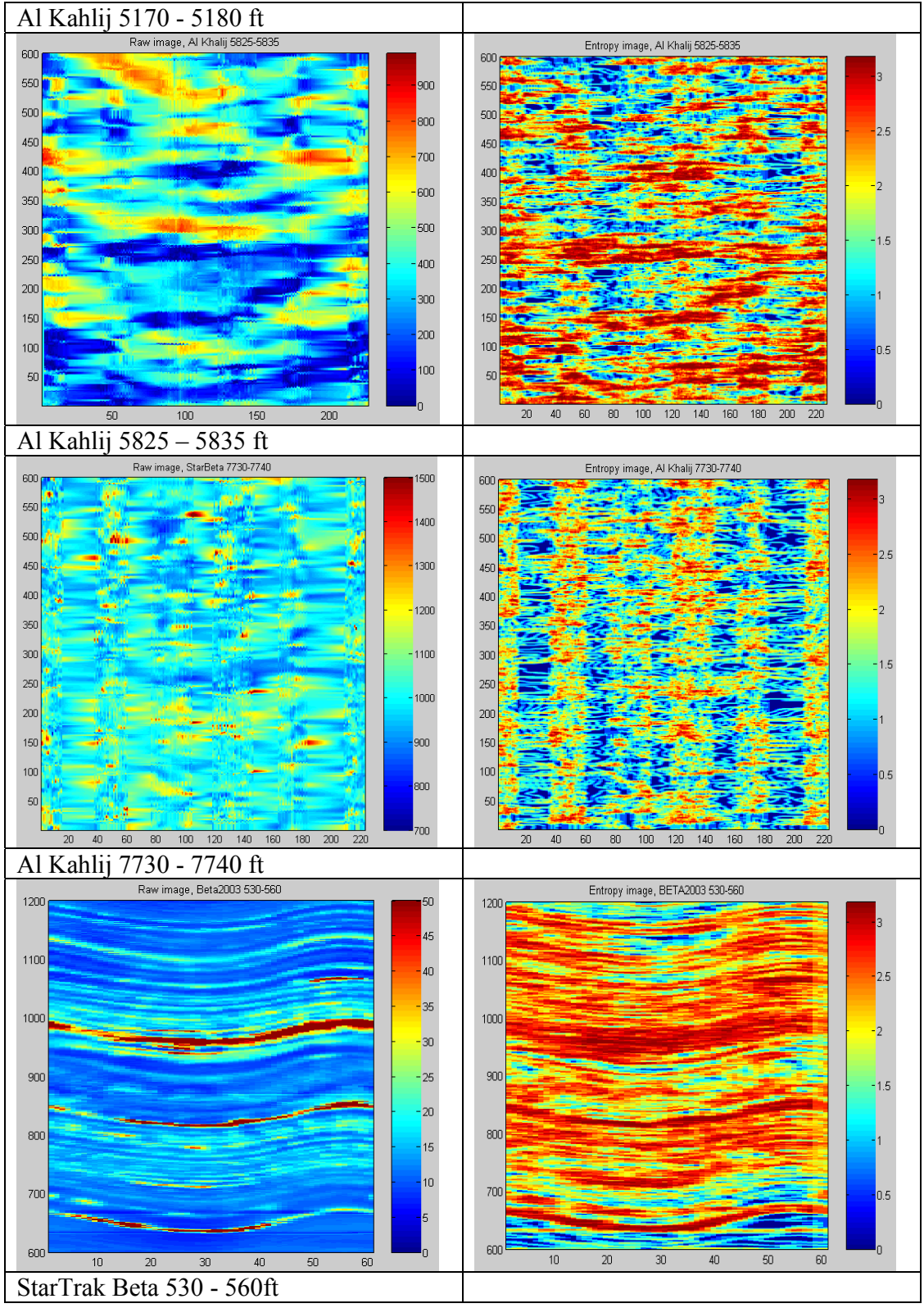**Figure 102 : Dip calculation comparison, electrical image, BETA1**

Electrical raw and IDM attribute image with
sinusoids detected by the GLCM method

Electrical raw image with
sinusoids detected by Dipex

Figure 103 : Dip calculation comparison, electrical image, BETA2

Electrical raw and IDM attribute image with sinusoids
detected by the GLCM method

Electrical raw image with
sinusoids detected by Dipex

Figure 104 : Dip calculation comparison, electrical image, BETA3

161

Nuclear raw and IDM attribute image with sinusoids detected by the GLCM method

Nuclear raw image with sinusoids detected by Dipex

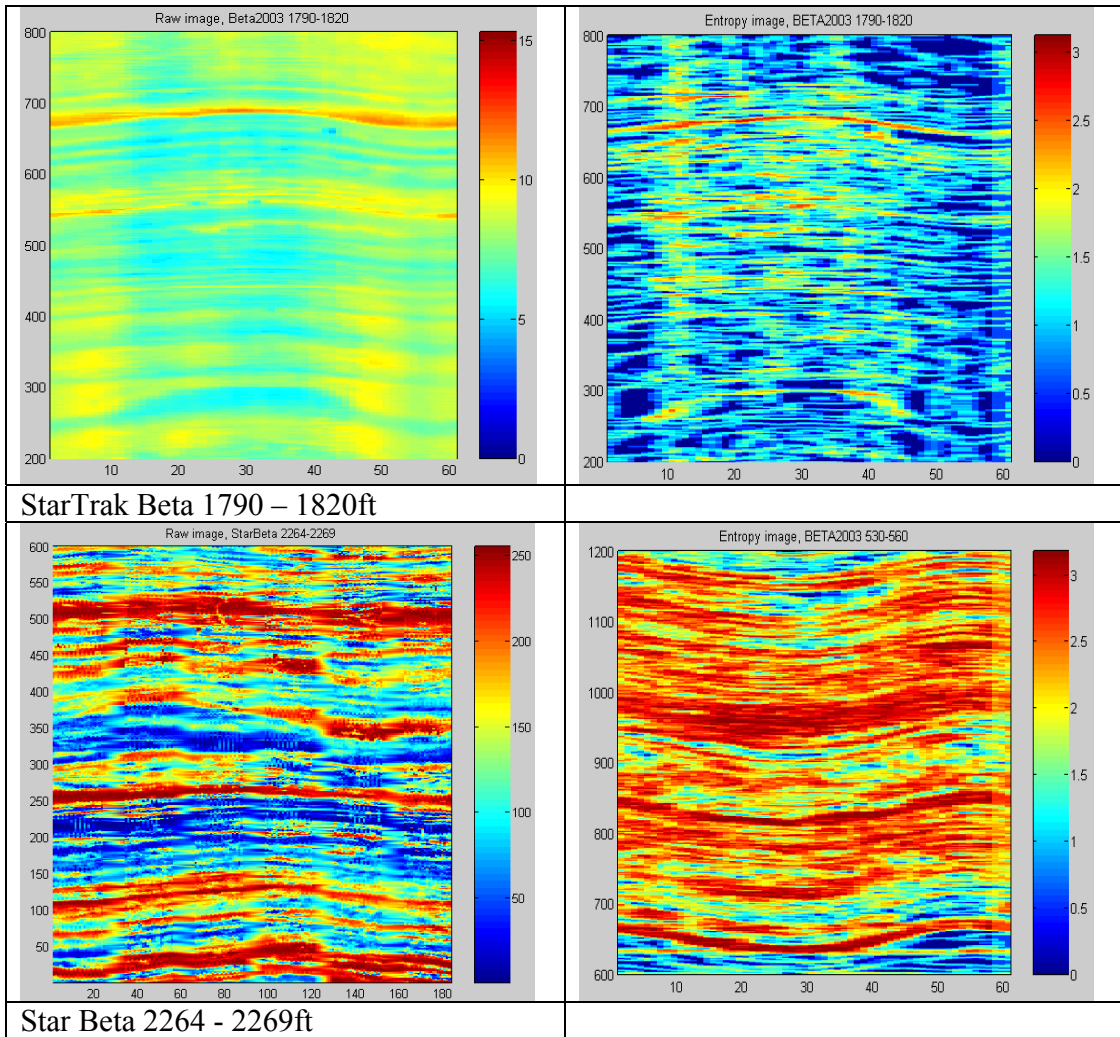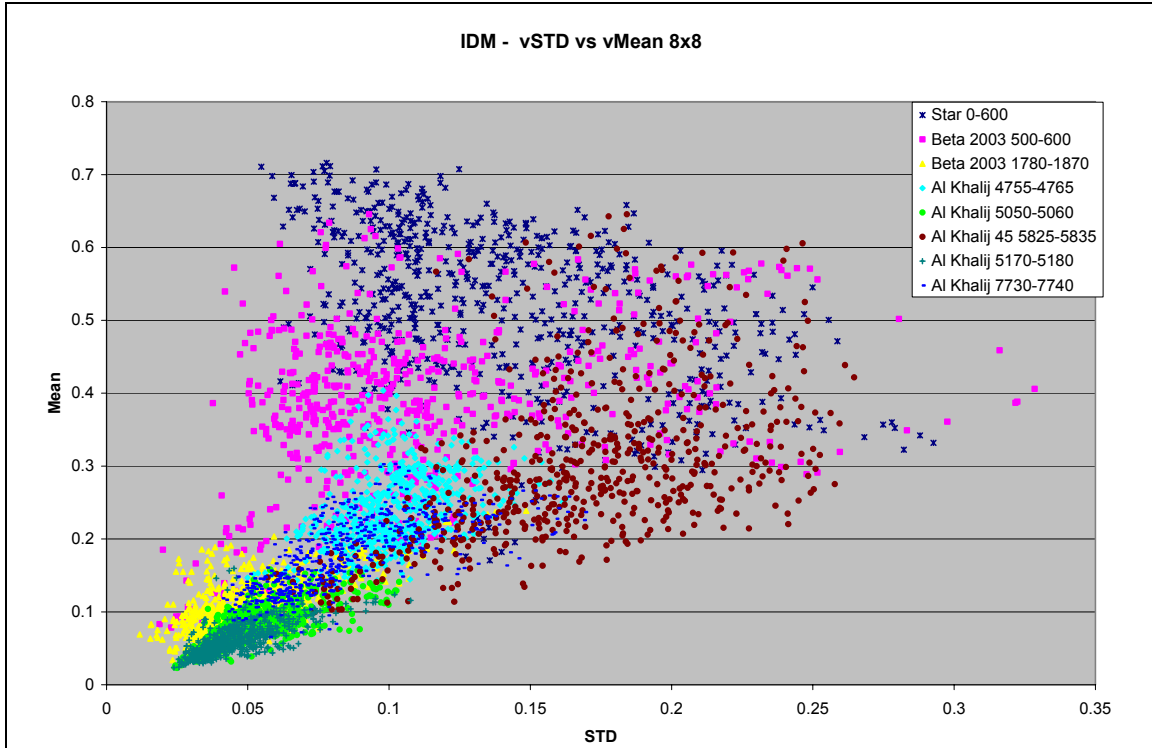**Figure 105 : Dip calculation comparison, nuclear image**

Appendix D

Raw Image	Attribute Image (Entropy, texel size 4x4. step size 1x1, vertical)
Al Kahlij 4755 - 4765 ft	
Al Kahlij 5050 - 5060 ft	

Al Kahlij 5170 - 5180 ft	
Raw image, Al Khalij 5825-5835	Entropy image, Al Khalij 5825-5835
Al Kahlij 5825 – 5835 ft	
Raw image, StarBeta 7730-7740	Entropy image, Al Khalij 7730-7740
Al Kahlij 7730 - 7740 ft	
Raw image, Beta2003 530-560	Entropy image, BETA2003 530-560
StarTrak Beta 530 - 560ft	

164

StarTrak Beta 1790 – 1820ft	
Star Beta 2264 - 2269ft	

Table 20 : Buildup of image pieces representing different texture types

1) IDM attribute build up, STD vs. Mean (both extracted from vertical evaluation), texel size 8x8
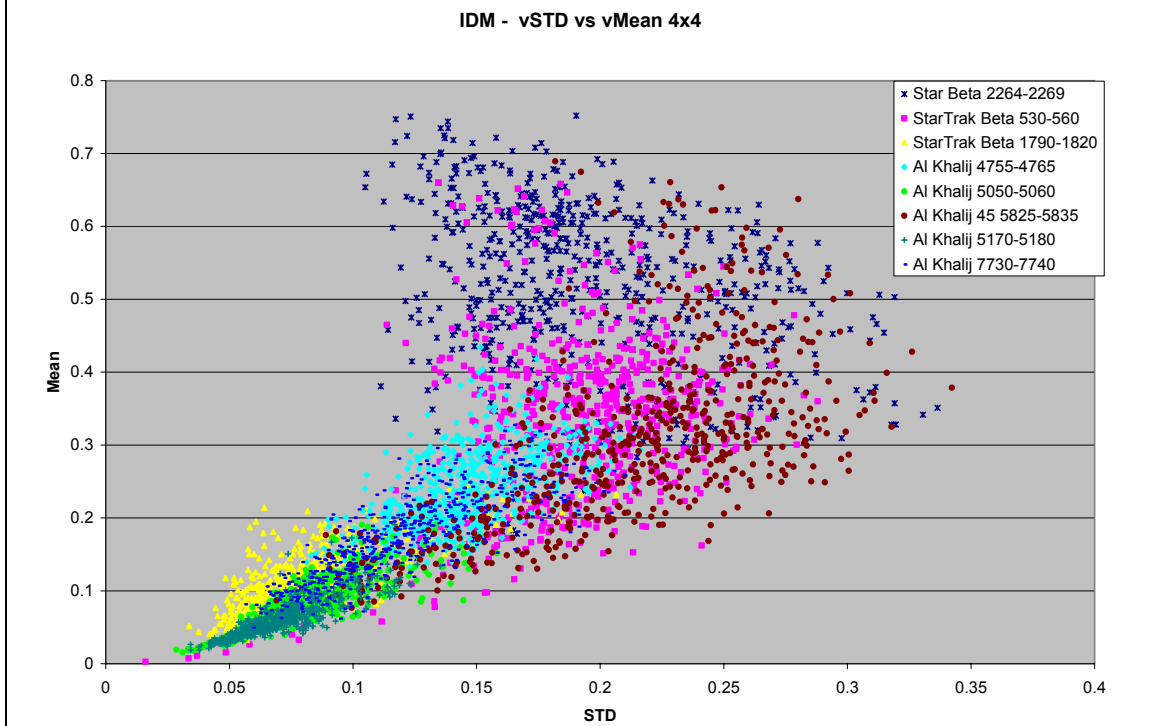
2) IDM attribute build up, STD vs. Mean (both extracted from vertical evaluation), texel size 4x4

166

IDM - hSTD vs vMean 4x4
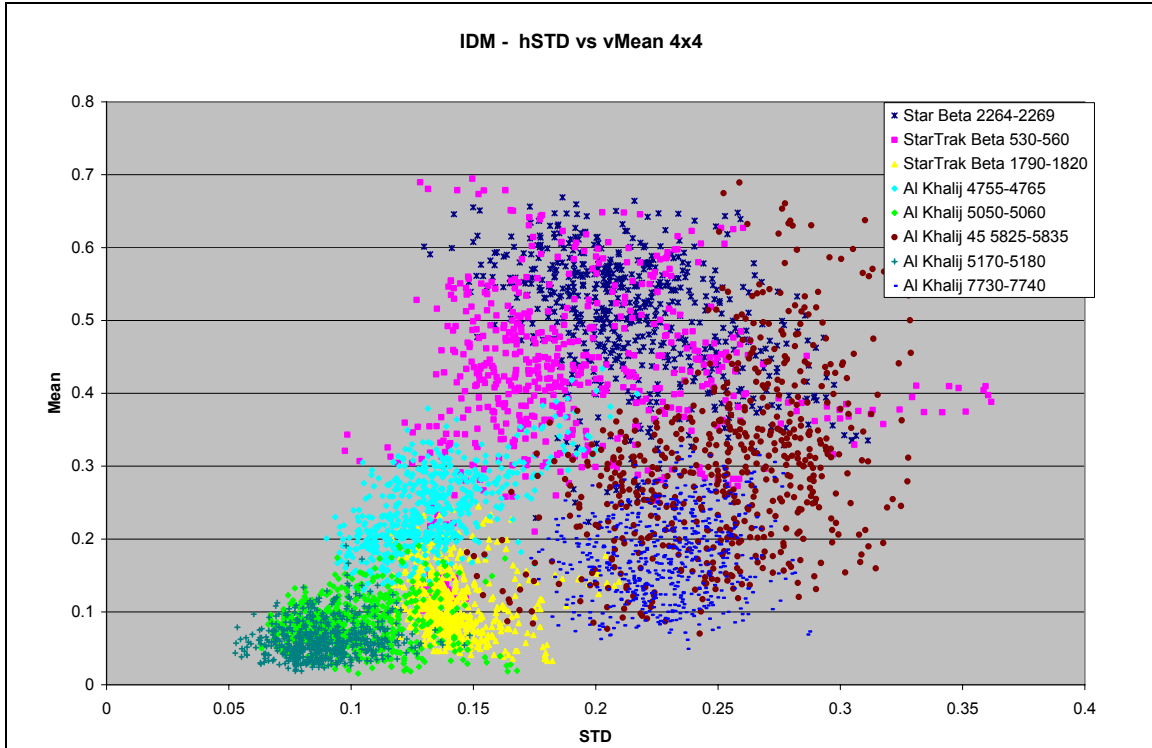
3) IDM attribute build up, STD (horizontal evaluation) vs. Mean (vertical evaluation)

IDM-hSTD vs ENT-vMean 4x4
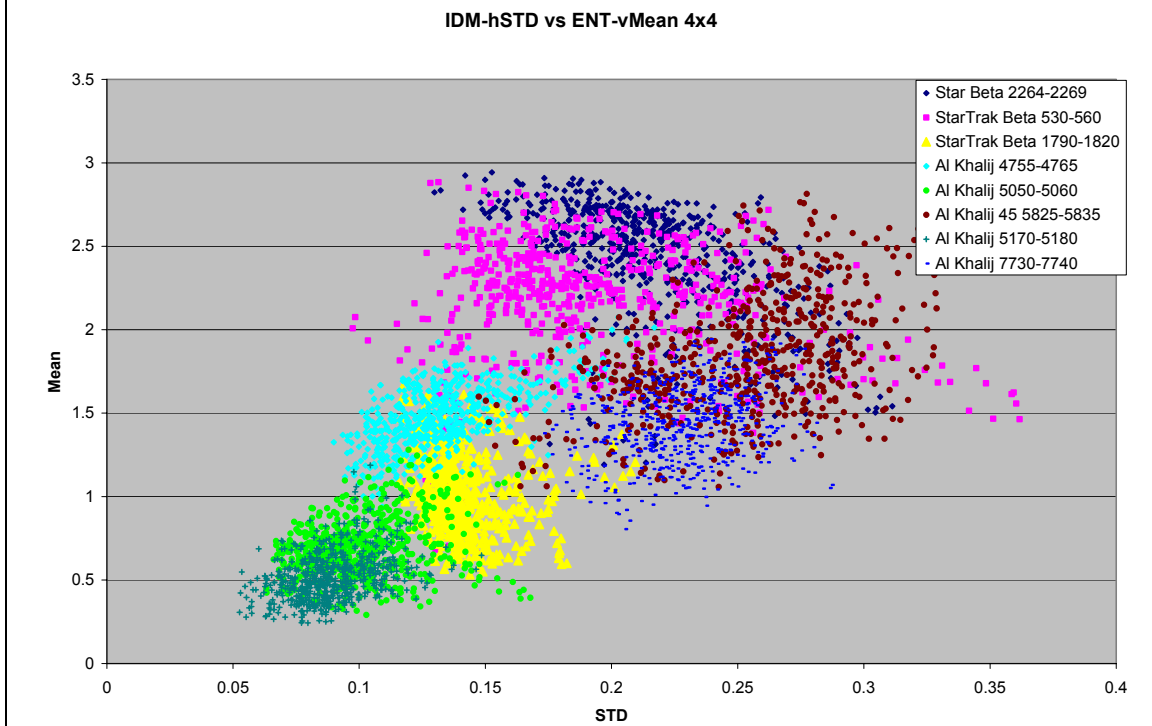
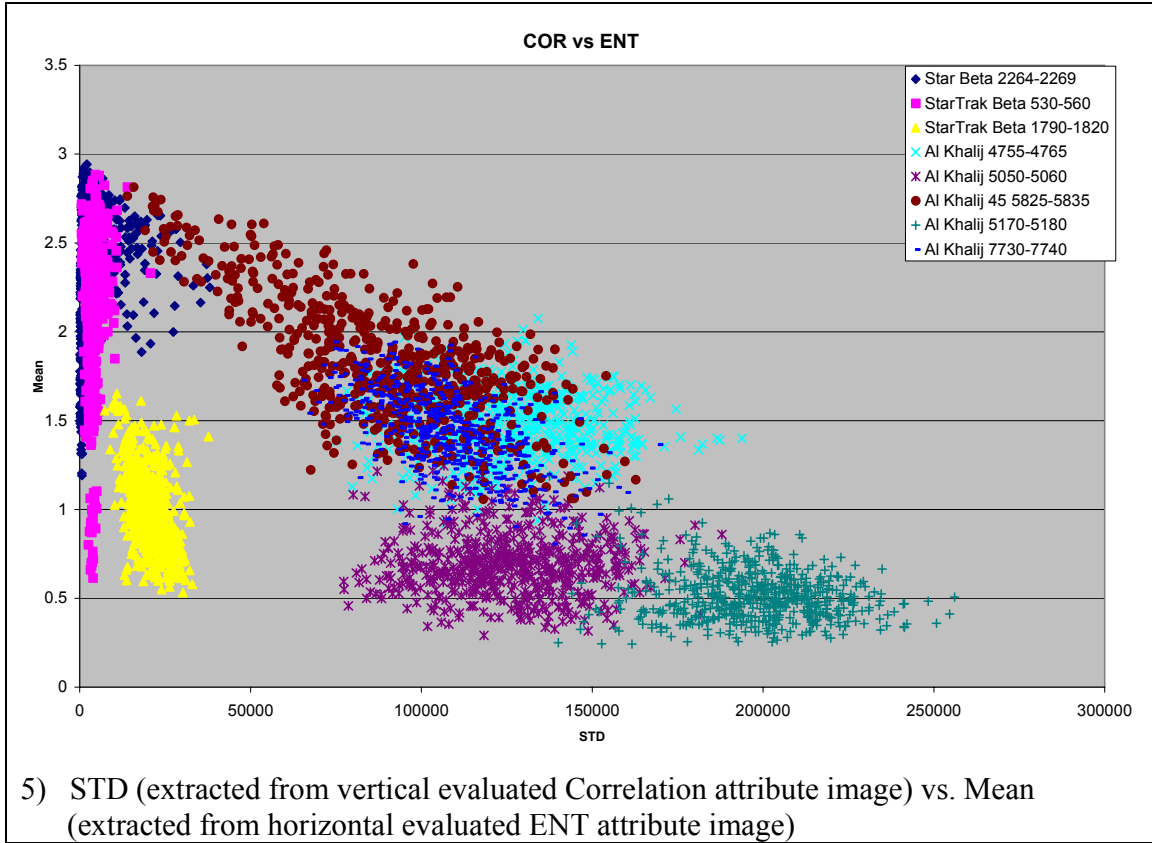4) STD (extracted from vertical evaluated IDM attribute image) vs. Mean (extracted from horizontal evaluated ENT attribute image)

167

COR vs ENT

5) STD (extracted from vertical evaluated Correlation attribute image) vs. Mean (extracted from horizontal evaluated ENT attribute image)
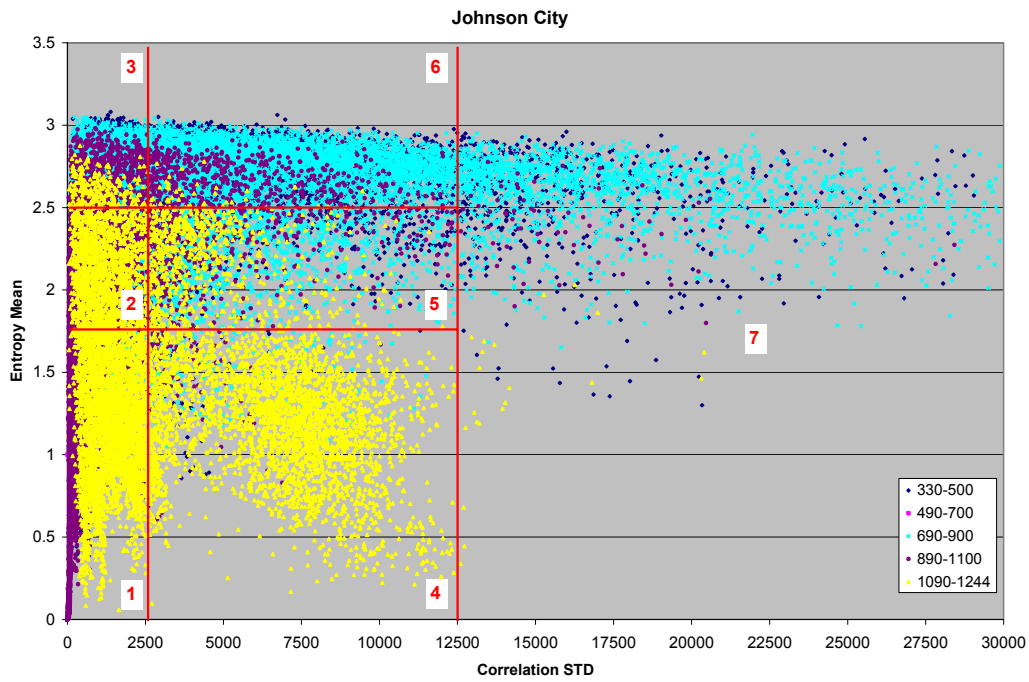
Table 21 : Facies classification evaluation

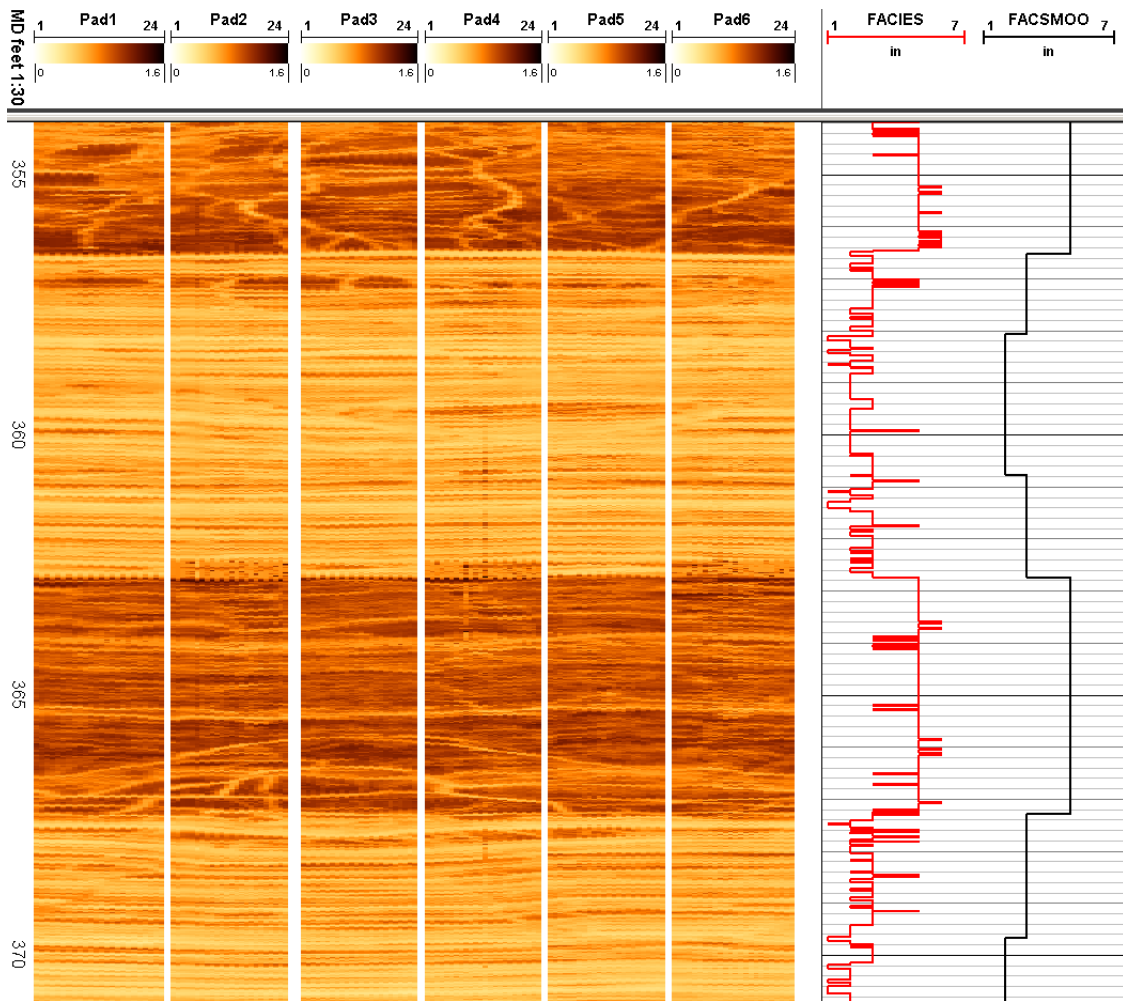**Figure 106 : Feature space from the Johnson City well (2nd subdivision approach)**
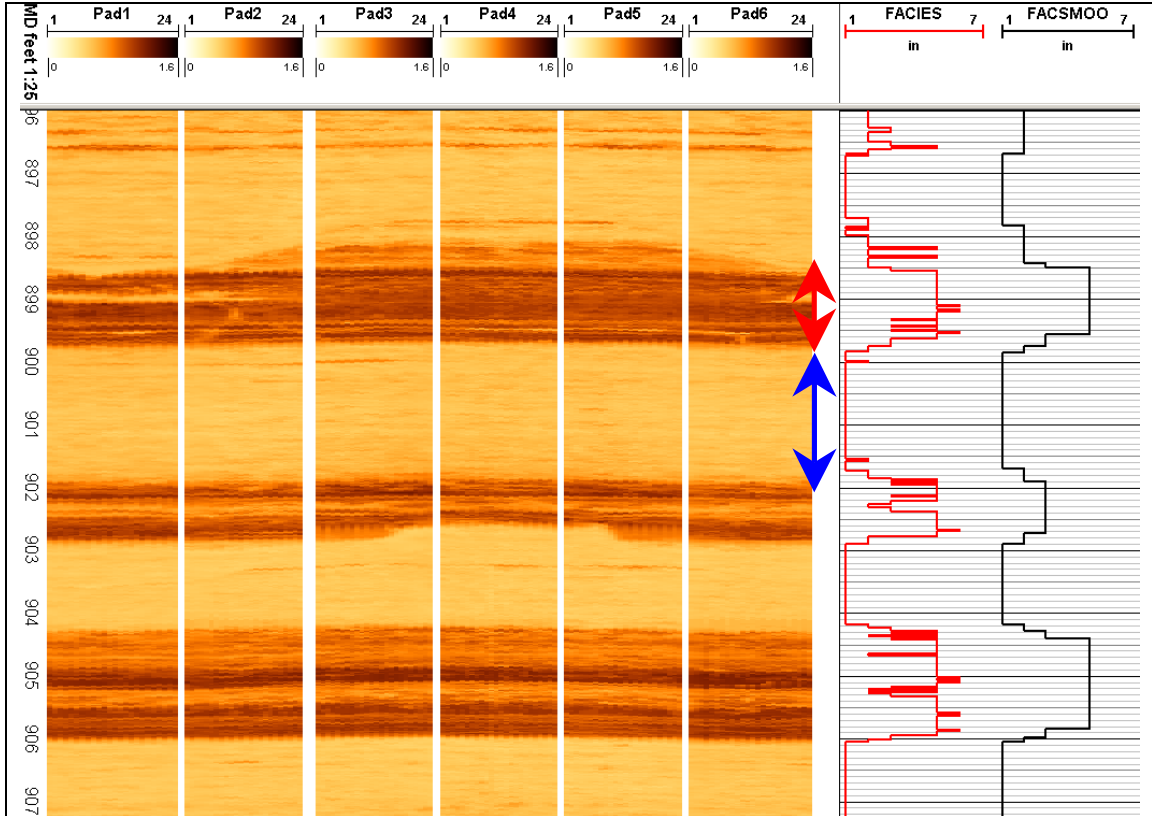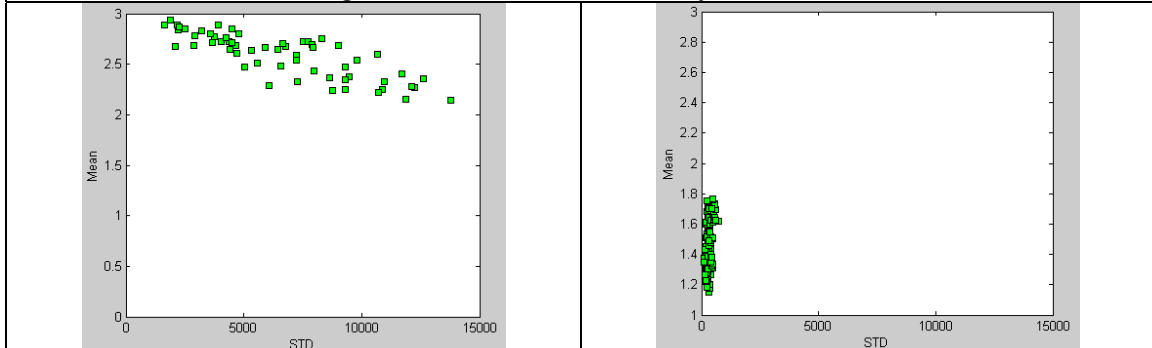
Figure 107 : Electric image log Johnson City I including facies classification curve (2nd subdivision approach)

169

Raw Image, facies curve, Johnson City well 897 – 907 ft

| 898,8-899,8 ft (red range) | 900-901,8 ft (blue range) |

Facies curve, according to subdivisions in Figure 90 (top), facies curve (middle) and smoothened facies curve (bottom) according to subdivisions Figure 106
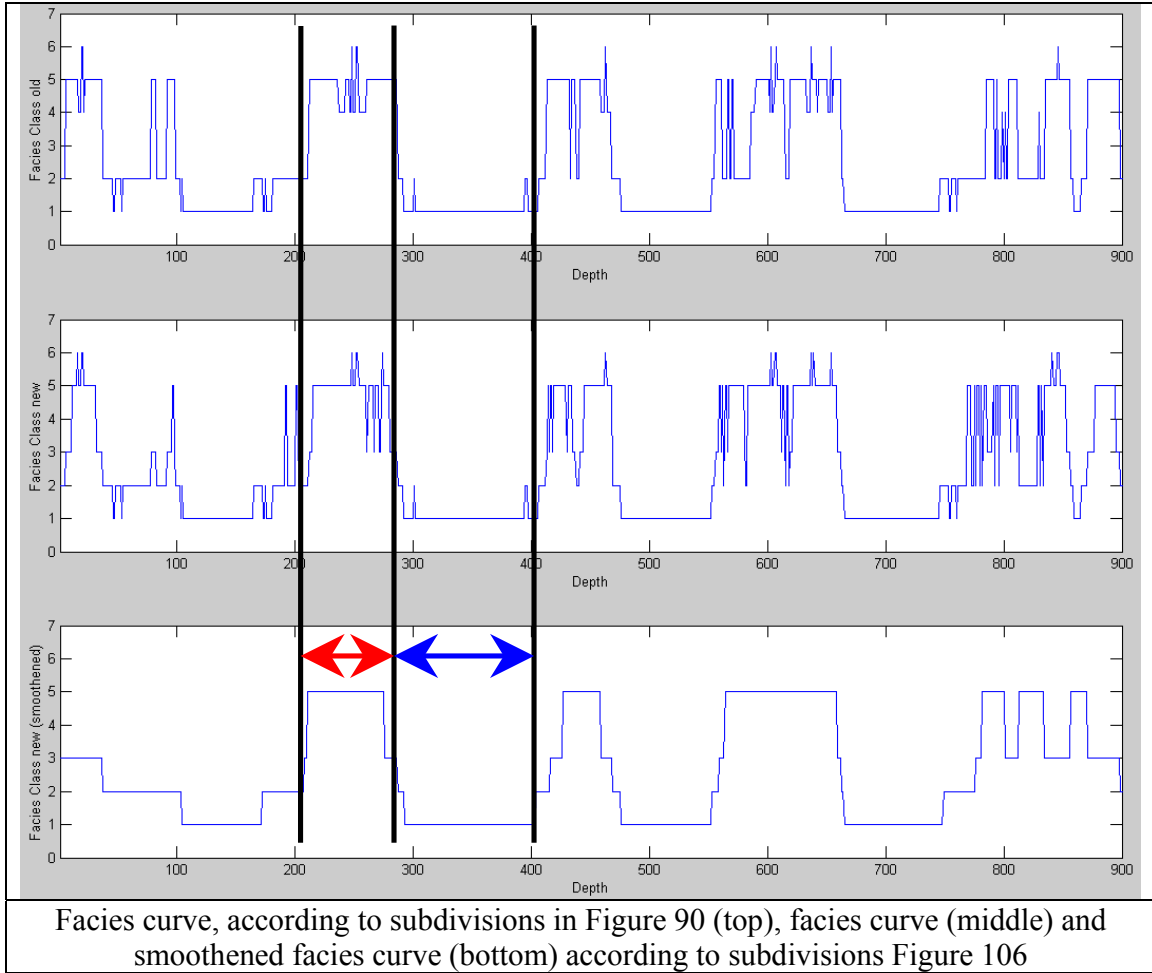
Table 22 : Facies classification example, Johnson City I